Multi-parameter optimisation of quantum optical systems

Harry James Slatyer

A thesis submitted for the degree of Doctor of Philosophy of The Australian National University.

July 2018

Declaration

This thesis is an account of research undertaken between July 2013 and December 2017 at the Department of Quantum Science, Research School of Physics and Engineering, The Australian National University, Canberra Australia.

The work described in Chapters 2 and 3 was performed in collaboration with Giovanni Guccione. The work described in Chapter 4 was performed in collaboration with Mahdi Hosseini and Giovanni Guccione. The work described in Chapter 5 was performed in collaboration with Michael R. Hush, Aaron D. Tranter and Geoff T. Campbell. All stages of the work were supervised by Ping Koy Lam and Ben C. Buchler.

Except where acknowledged in the customary manner, the material presented in this thesis is, to the best of my knowledge, original and has not been submitted in whole or part for a degree in any university.

Harry James Slatyer
July 2018

Acknowledgements

This project would not have been possible without the help and support of many people. First and foremost thank you to Ping Koy and Ben. There's too little space to describe all that you've done for the work presented in this thesis, the thesis itself, and for me personally. To choose a couple of specific points: Ping Koy, without your persistence, encouragement and confidence I never would have returned to complete the project (or, indeed, even started in the first place); Ben, the commitment and guidance you've given me, especially during the last year, have been an integral part of getting the project finished. More generally, thank you both for the unwavering support you've provided since my first day. I would not have lasted long without it.

Thank you Michael. We've only been working together on and off for about a year, but in that time you've become my go-to person for everything related to physics and thesis-writing, not to mention being another great supporting influence.

Thanks also to the colleagues I've worked with most closely. Giovanni, you taught me basically everything I know about opt(omechan)ics, and working with you was a true pleasure (except for that period of several months in which we kept breaking those force sensors). Mahdi, thank you for welcoming me into the optomechanics group, bringing me up to speed on the experiment, and becoming a great mentor. Aaron, thank you for tolerating an inordinate number of stupid GEM questions, and generally being an extremely fun person to work with (long live Skynet).

Thanks to the many proof-readers of this thesis. Aaron, Geoff, Mira, Ping Koy, Rachel, Robyn, and especially Ben and Michael: your insightful comments and suggestions have transformed the thesis, and I can't thank you enough for your time and dedication.

To Michael and Casey at Google, who gave me the chance to come back and

finish the project, thank you.

I won't try to name everybody in the ANU quantum optics group, but you are all kind and talented individuals, and it has been a privilege to work with you. A few specific shout-outs. Geoff, thank you for letting me crash your office, and for being a source of knowledge on an outrageous number of topics throughout my entire time with the group. Seiji, thank you for being an enthusiastic and positive influence, and for not being afraid to speak your mind. Amanda, thank you for your ability to get things done, your kindness, and your tolerance to the various inconveniences I've caused.

It's infeasible to thank all those who have unknowingly contributed via their software, but particular thanks to Bram Moolenaar for making the actual writing more pleasurable than it otherwise could have been, to Donald Knuth for protecting me from typesetting woes, and to John D. Hunter for saving me many hours of pixel-pushing.

I'd also like to acknowledge the financial support I've received throughout my candidature: the research presented in this thesis was supported by an Australian Government Research Training Program Scholarship, an Australian Postgraduate Award, an ANU PhD Scholarship, an ANU Supplementary Scholarship, and a Postgraduate Research Scholarship.

Thanks to my friends, who have kept me sane. You know who you are.

Of course, thank you to my family. You have been a source of inspiration my entire life, and words can't describe how lucky I feel to have your support. I never would have finished this thesis, or anything much at all, without it.

Finally, thank you Mira, for your numerous concrete contributions and most of all for putting up with me through the highs and the lows.

Abstract

Quantum optical systems are poised to become integral components of technologies of the future. While there is growing commercial interest in these systems—for applications in information processing, secure communication and precision metrology—there remain significant technical challenges to overcome before widespread adoption is possible. In this thesis we consider the general problem of optimising quantum optical systems, with a focus on sensing and information processing applications. We investigate four different classes of system with varying degrees of generality and complexity, and demonstrate four corresponding optimisation techniques.

At the most specific end of the spectrum—where behaviour is best understood—we consider the problem of interferometric sensitivity enhancement, specifically in the context of long-baseline gravitational wave detectors. We investigate the use of an auxiliary optomechanical system to generate squeezed light exhibiting frequency-dependent quadrature rotation. Such rotation is necessary to evade the effect of quantum back action and achieve broadband sensitivity beyond the standard quantum limit. We find that a cavity optomechanical system is generally unsuitable for this purpose, since the quadrature rotation occurs in the opposite direction to that required for broadband sensitivity improvement.

Next we introduce a general technique to engineer arbitrary optical spring potentials in cavity optomechanical systems. This technique has the potential to optimise many types of sensors relying on the optical spring effect. As an example, we show that this technique could yield an enhancement in sensitivity by a factor of 5 when applied to a certain gravitational sensor based on a levitated cavity mirror.

We then consider a particular nanowire-based optomechanical system with potential applications in force sensing. We demonstrate a variety of ways to improve its sensitivity to transient forces. We first apply a non-stationary feedback

cooling protocol to the system, and achieve an improvement in peak signal-to-noise ratio by a factor of 3, corresponding to a force resolution of 0.2 fN. We then implement two non-stationary estimation schemes, which involve post-processing data taken in the absence of physical feedback cooling, to achieve a comparable enhancement in performance without the need for additional experimental complexity.

Finally, to address the most complex of systems, we present a general-purpose machine learning algorithm capable of automatically modelling and optimising arbitrary physical systems without human input. To demonstrate the potential of the algorithm we apply it to a magneto-optical trap used for a quantum memory, and achieve an improvement in optical depth from 138 to 448.

The four techniques presented differ significantly in their style and the types of systems to which they are applicable. Successfully harnessing the full range of such optimisation procedures will be vital in unlocking the potential of quantum optical systems in the technologies of the future.

Contents

Chapter 1

Introduction

Quantum optical systems are on the brink of a transition from experimental platforms to core components of cutting-edge commercial technologies. This transition promises to unlock new possibilities in a range of fields, from information and communication technology to precision metrology. As quantum optical systems become integrated into applied technologies, high performance will become a key requirement. Proof-of-principal systems, while adequate in an experimental context, will not suffice; instead, components exhibiting optimal performance will be necessary. The transformation of a proof-of-principal system into a maximally-performant component suitable for a commercial device will entail system-wide optimisation.

Quantum optical systems are uniquely difficult to optimise. While quantum effects are precisely what enable the impressive capabilities of such systems, they also induce a range of challenges. For example, the Heisenberg uncertainty principle places intrinsic limits on the precision of measurements made on such systems. These limits manifest as quantum back action—the act of measurement itself perturbs the system, and this perturbation precludes precise knowledge of non-commuting observables. Improved manufacturing is not sufficient to overcome these challenges; instead, the devices must be fundamentally altered in order to sidestep the problematic quantum effects.

Not all quantum optical systems are amenable to the same styles of optimisation. The additional complexities required to model quantum behaviour render even moderately complex systems intractable to detailed theoretical analysis. In such cases optimisation must proceed via approximate analysis based on those aspects of the system that *are* understood. For some systems even this approach

is infeasible, and one must instead revert to brute-force search. More generally, as system complexity increases, the required optimisation procedures become more general and less "physical".

In this thesis we consider a selection of quantum systems sampled from this spectrum of complexity (and analytical intractability), and a corresponding collection of methods for optimising their performance.

1.1 Emerging quantum optical technologies

Optical systems have enjoyed a long history as a test bed for physical phenomena, from the famous Michelson-Morley experiment of 1887 through to the gravitational wave detectors of the present day. For quantum physics, in particular, the use of light is ubiquitous due to its general experimental convenience, its weak interaction with the environment, and the relative accessibility of quantum states and quantum effects.

The uses of quantum optical systems are not constrained to the realm of experimental physics, however. The most well-known such system with widespread commercial applications is the laser, which has formed the basis for an astonishing array of modern technologies. To name just a few, the laser underpins everyday devices such as barcode scanners, laser printers and CD drives; medical apparatus including instruments for dentistry[1] and eye surgery[2]; industrial-scale machinery for processing a variety of materials from metals[3, 4] through to plastics[5] and carbon fibre[6]; and atomic force microscopes for nanoscale imaging[7, 8].

Despite the incredible practical successes of the laser, it is far from the most interesting of quantum optical systems. In recent years the more exotic quantum properties of light have been recognised as having enormous potential for information and communication technologies and high-precision metrology. Successfully harnessing the power of quantum superposition and entanglement is expected to pave the way for a new era of computation[9–11], while exploitation of the quantum back action lies at the heart of provably secure communication via quantum key distribution[12, 13]. In metrology, similarly, the expected applications of quantum effects in the devices of the future are diverse: optical lattices form the basis of the world's most accurate clocks[14, 15]; squeezed light can enhance the sensitivity of the most sensitive displacement sensors (as we will discuss in Chapter 2); laser cooling is a prerequisite for atom interferometric gravimeters[16]; and

so on.

Already these technologies are receiving significant commercial attention, with companies today delivering quantum random number generators[17], gravimeters[18], cold atom-based atomic clocks[19] and quantum key distribution systems[20]. On the computation side the progress towards viable products is not so advanced, but if anything the interest and investment are even more intense. Large companies such as Google[21] and Lockheed Martin[22] are betting on the technology to enable breakthroughs in artificial intelligence and machine learning, while there are a wide variety of start-ups looking to carve out more specific niches in the domain.[1]

1.2 Key technical challenges

Despite this promising start, there remain significant barriers to the widespread adoption of exotic quantum optical systems as components of the technologies of the future. One fundamental problem is that quantum optical systems are inherently fragile. While photons in free space retain quantum information remarkably well, any interaction with external systems quickly leads to a loss of information via decoherence, and for information technology applications it is often exactly this type of interaction that is required.

For secure communication via quantum key distribution, for example, integration with existing fibre optic networks is desirable. However, losses in the fibre induce a loss of quantum information and lead to unacceptably low bit rates when used over large distances. Current telecom-grade low-loss optical fibre typically exhibits attenuation on the order of 0.2 dB/km[27], which limits the range of a single hop in a useful quantum network to a few hundreds of kilometers[28]. Unlike with classical communication over optical fibre, the no-cloning theorem precludes the use of simple amplification to circumvent this issue. Instead, integration of quantum repeaters into the network is expected to enable secure communication via multiple hops and thus bypass this limit[29–32], but while many of the individual components required to build a useful quantum repeater have been demonstrated, a complete system has not yet been realised. A partic-

[1] See, for example, Rigetti Computing[23] (full-stack quantum computing), h-bar[24] (general consulting on quantum information technologies), Q^{x}Branch[25] (consulting on applications to data analytics), and 1QBit[26] (hardware-agnostic software and platforms for industry).

ular subsystem that we will discuss in more detail in Chapter 5 is the quantum memory. In brief, the memory used in a quantum repeater must exhibit storage times long enough to allow entanglement to be shared between distant nodes of the network, and the time required for this sharing depends on the memory efficiency. For example, to achieve higher bit rates than direct fibre transmission over a distance of 500 km, a memory with 90% efficiency and storage time on the order of seconds is required[31]. A coherent optical memory with efficiency as high as 87% has been reported, but at this efficiency the storage time was on the order of microseconds[33]. Conversely, there are memories with storage times of seconds, but the efficiencies are below 1%[34, 35]. Indeed, the highest reported storage time for a memory with over 50% efficiency is 0.6 ms[36], indicating that there is still significant optimisation to be performed before a memory suitable for a useful quantum repeater becomes within reach.

Generally speaking the situation is not quite so intimidating for sensing applications, and this is reflected by the relative maturity of commercial sensors based on quantum optics. Such systems typically have far fewer interacting components than large-scale quantum information processing devices, which significantly relaxes the degree of internal isolation required for reducing the effect of decoherence. Indeed, in many sensing applications it is not even necessary to have long coherence times in the first place. In addition, unlike in quantum key distribution systems designed to integrate with existing fibre optic networks, a sensor can usually be delivered as a single self-contained unit, which at least allows sources of noise within the system to be controlled. Despite these mitigating factors, however, quantum optical sensors still contain delicate components and configurations susceptible to the weakest environmental disturbances, so performance is highly sensitive to external noise sources. In addition to these noises there is yet another more fundamental source, namely the quantum back action, whereby the act of measurement itself can significantly disturb the system. Even this does not enforce a hard limit, however, and with creative system design and careful optimisation it is possible to evade the effect of back action and thus further improve performance, as we will discuss in Chapter 2.

In quantum optical systems for both information and communication technologies and sensing, therefore, there is a general problem of overcoming environmental noise. For communication and computing in particular it is expected that there exist sharp thresholds of performance beyond which entirely new ca-

pabilities will emerge, such as fault-tolerant computation[37, 38] or high-speed quantum communication across multiple network nodes[29, 30], while in sensing it is more a matter of gradual sensitivity enhancement. In both cases, however, it is clear that iterative optimisation of system performance is vital for further technological development and commercial adoption.

1.3 Optimising quantum optical systems

Optimisation of quantum optical systems entails some unique challenges. Speaking very generally, one common theme is that it can be difficult to optimise individual components in isolation. Typically the underlying problem is that systems are so fragile that perturbations to one part of the system are sufficient to cause significant disturbances in others.

The Heisenberg uncertainty principle can be interpreted in this context: it is possible to decrease the noise in one observable, but doing so necessarily increases noise in any non-commuting observable.

A more concrete example, which will be the focus of Chapter 2, is found in long-baseline gravitational wave detectors. Injection of classical states of light into such devices leads to a strict sensitivity limit known as the "standard quantum limit", which arises from the phase and amplitude noise in the light. Using quantum states of light, however, the limit can be beaten: injecting suitable squeezed light can improve the sensitivity at part of the detection band, at the expense of a reduction in sensitivity over the rest of the band[39]. In order to achieve improvement across the entire band (broadband improvement) one must not only squeeze the light, but ensure that the squeezed quadrature rotates with detection frequency. If perfect quadrature rotation is not possible, the squeeze factor must also be frequency-dependent in order to reduce the negative impact of anti-squeezing at parts of the spectrum where the quadrature angle is imperfect. That is, one must optimise the squeeze factor and angle simultaneously.

Another example, which we will discuss in Chapter 3, is the class of optical spring-based sensors. One approach to sensing using optical springs is to transduce a signal of interest onto the displacement of an optical cavity mirror, and measure that displacement by monitoring the cavity output. Achieving a strong transduction onto the mirror displacement requires a soft spring constant, which corresponds to a low cavity finesse, but for optimum readout precision a high

finesse is necessary. We will show that this tension can be resolved, but only with significant changes to the system design. The fundamental difficulty in this case is that the sensing and readout systems are tightly coupled, so must be optimised as a single unit.

To summarise, for quantum optical systems consisting of multiple physical or functional components one must often optimise the entire system as a whole. This process is fundamentally more difficult than when the components are loosely coupled and can be optimised in isolation.

An additional challenge is that quantum systems are inherently difficult to model, which means that many even moderately complex systems are largely intractable to useful theoretical analysis. When dealing with such a system one must essentially revert to a combination of simplified analysis, brute-force, intuition and serendipity. Framing this observation more generally, as the complexity of the system increases there is less chance that it will be possible to perform calculated, principled improvements based on theoretical analysis, and instead optimisation must be performed more as though the system is a black box with unknown dynamics. A corollary is that for more complex systems the relevant optimisation processes become more general and applicable to a wider variety of systems.

In this thesis we consider a collection of systems of varying complexity and generality, and a corresponding suite of optimisation techniques. Our discussions range from specific systems that are sufficiently well-understood that paths to optimisation can be identified entirely by bespoke theoretical analysis, to broader classes of systems for which general but theoretically-grounded domain-specific techniques are beneficial, through to the most general case of systems that are so complex that they must be treated as unknown black boxes by the optimisation procedure. Throughout this process we thus provide a selection of specific techniques suitable in each situation, and simultaneously demonstrate the more general principle that across the spectrum of system complexity and generality one must employ vastly different styles of optimisation.

1.4 Thesis outline

The remainder of this thesis is structured as follows.

In Chapter 2 we consider the prospect of enhancing the sensitivity of optical

interferometer-based displacement detectors using non-classical light generated by optomechanical systems. Gravitational wave detectors, and interferometers in general, are limited by the quantum noise in the light used for measurement—a manifestation of the aforementioned quantum back action. At low powers and high frequencies the phase noise in the light induces photon shot noise at detection, while at high powers and low frequencies the amplitude noise randomly drives the test masses and can mask the signal. Injecting amplitude- or phase-squeezed light can thus reduce the noise floor at a particular part of the spectrum, but increases noise elsewhere due to the corresponding anti-squeezing. If the squeezed quadrature rotates with frequency then enhancement across the entire measurement band is possible. We demonstrate that the output field of optomechanical systems exhibits frequency-dependent squeezing, and investigate whether such light is suitable for use in gravitational wave detectors. Despite the complexity of the relevant systems and the technical difficulty in implementing them, this can be seen as an example of one of the cleanest approaches to optimising performance. Specifically, the system is sufficiently well-understood that a path to improving sensitivity is known, and all that remains is to identify an auxiliary system with the appropriate behaviour. Moreover, the coupling between the original system and the auxiliary system is minimal—the auxiliary system affects the behaviour of the detector solely via the light field injected into the detector, so the two systems can largely be optimised independently.

In Chapter 3 we derive a scheme for synthesising arbitrary optical spring potentials in cavity optomechanical systems by utilising polychromatic light. We focus on how the scheme may be used to optimise the sensitivity of optical spring-based gravitational sensors. This approach is applicable to any cavity optomechanical system, and has a wide variety of potential uses due to its generality. One particular fact we demonstrate is that by using this scheme one can essentially break the aforementioned coupling between the sensing and readout subsystems of optical spring sensors, by allowing the former to be manipulated arbitrarily without changing the cavity finesse. From a broad optimisation perspective the situation here is similar to the previous chapter, in the sense that the procedure is grounded on a detailed theoretical understanding of the system dynamics.

In Chapter 4 we investigate the force-sensing performance of a nanowire-based optomechanical system. We first show that by implementing a simple feedback control system one can significantly damp the nanowire's motion. We then show

that the use of this system in a non-stationary feedback cooling strategy enables an enhancement in sensitivity to transient signals. Next we present two post-processing schemes, which can be viewed as simulations of the feedback cooling process, and demonstrate that they achieve a similar enhancement in sensitivity without the need for additional experimental complexity. These techniques can be viewed as a more general approach to optimisation than those derived in the previous chapters, in the sense that they could potentially be used in arbitrary oscillator-based sensors of transient forces, without an understanding of the full system-specific dynamics and subtleties.

In Chapter 5 we take a more general approach again, and present a machine learning algorithm capable of automatically performing multi-parameter optimisation of arbitrary physical systems. The algorithm takes control of a system or experiment, and through repeated interactions learns a model of its behaviour and uses this model to determine the optimal parameter set to achieve a certain objective. This approach largely abandons all physical intuition and knowledge, since the algorithm treats the physical system as a black box. This technique enables optimisation of systems that are too complex for any useful theoretical analysis, with parameter spaces too large for brute-force search. As a proof of concept, we apply the algorithm to a magneto-optical trap with 63 tunable parameters.

In Chapter 6 we provide some concluding remarks and an outlook towards the future of optimisation in quantum optical systems.

Chapter 2

Interferometric sensitivity enhancement via optomechanical squeezing

In this chapter we demonstrate how cavity optomechanical systems may be used to generate squeezed light, and investigate the prospect of using such light to enhance the sensitivity of interferometer-based gravitational wave detectors.

In Section 2.1 we provide some background and history on interferometer-based detectors, with a focus on how their performance can be optimised with the injection of non-classical light. In Section 2.2 we derive expressions describing the squeezing characteristics of the output field of an idealised cavity optomechanics system. In Section 2.3 we use these expressions to numerically analyse some properties of optomechanically-generated squeezed light, under realistic assumptions. In Section 2.4 we investigate the possibility of using such light to improve the performance of long-baseline gravitational wave detectors. Finally, in Section 2.5 we provide some concluding remarks.

The contents of this chapter are based on the following publication:

> G. Guccione, H. J. Slatyer, A. R. R. Carvalho, B. C. Buchler, and P. K. Lam, "Squeezing quadrature rotation in the acoustic band via optomechanics", Journal of Physics B: Atomic, Molecular and Optical Physics **49**, 065401 (2016)

All stages of the research described in this chapter were performed in close collaboration between Giovanni Guccione and myself.

2.1 Background

Interferometry, the use of light interference for precision measurement, is the basis for many of the world's most sensitive detectors. General improvements in design and quality have increased the performance of these detectors over the last century, but with the effect of classical noise sources now being drastically reduced we are beginning to enter an era in which the limits imposed by quantum mechanics become significant.

Heisenberg's uncertainty principle represents the most fundamental limit to the sensitivity of a detector. In optics this principle dictates that the phase and amplitude of the light cannot simultaneously be known precisely. In an interferometric system effecting a measurement of a field quadrature, this uncertainty manifests as the well-known shot (or photon counting) noise[39, 41, 42]. The effect of shot noise can be mitigated by increasing the power of the laser; the signal increases more rapidly with laser power than the noise, meaning a higher power yields an improved signal-to-noise ratio. However, a higher laser power yields a stronger radiation pressure force, and—particularly when free masses are involved—this back action can drive the optical components of the measurement apparatus and thus increase noise[43]. That is, even in the absence of experimental limitations to the laser power there is a tradeoff to be made: a lower power reduces radiation pressure noise but increases shot noise, while a higher power decreases the effect of shot noise but increases radiation pressure noise. There is thus an optimal power at which to operate, where the combined contribution from radiation pressure noise and shot noise is minimised. This is known as the *standard quantum limit* (SQL) for interferometers[44, 45].

To be noticeably affected by the SQL requires extreme optimisation of all other noise sources, but despite the technical difficulty this regime is now being explored. The most well-known detectors operating at this level are long-baseline gravitational wave detectors (see, for example, the recent review by Holst et al.[46]). The previous generation of detectors tended to operate at a low enough power to be limited by shot noise across the detection band[47], but the current generation are limited by the SQL at the optimal detection frequency[48].

There is still potential for improvement, however, since the SQL is not a fundamental limit[49, 50]. It can be beaten by injecting squeezed light[39, 51, 52]. Specifically, one observes that the radiation pressure and shot noises do not

contribute equally across the detection band. At high frequencies the radiation pressure noise is low due to being far from the mechanical resonances, so shot noise dominates, while at low frequencies the situation is reversed. Therefore, if one can reduce the effect of either shot noise or radiation pressure noise then the noise floor at the appropriate part of the spectrum will be reduced. It is here that squeezing can be advantageous. By using phase-squeezed light, for example, the shot noise is reduced and the sensitivity at high frequencies improves. Indeed, this technique has already been used to beat the shot noise limit in interferometers[53–56]. However, such light also exhibits anti-squeezing in the amplitude quadrature, which leads to higher radiation pressure noise and thus increased noise at low frequencies, so once again there is a tradeoff. Similarly, injecting amplitude-squeezed light (or indeed light squeezed at any fixed angle) sacrifices sensitivity at some frequencies in order to improve it at others.

Achieving broadband improvement via squeezed light is possible, but requires the squeezing angle to vary with frequency[52, 57, 58]. That is, at low frequencies the light should be amplitude-squeezed in order to reduce the dominant radiation pressure noise, and the squeezed quadrature should rotate by $\pi/2$ across the frequency of optimal sensitivity ($\sim$100 Hz for gravitational wave detectors[48]) to become phase-squeezed at higher frequencies and thus reduce the shot noise[45].

There are multiple proposals for preparing this type of quadrature rotation. One approach is to start with a fixed-angle broadband squeezing source and pass it through a collection of Fabry-Pérot filter cavities, with the dispersive nature of the cavities (that is, the frequency-dependent optical path length) inducing the required rotation[45, 59]. Proof-of-principle demonstrations of these systems have been implemented[60, 61], but significant technical difficulties must be overcome before they can be effective for use in gravitational wave detectors. Specifically, filter cavities are affected by several degradation mechanisms[62], and, more fundamentally, the band over which quadrature rotation occurs is determined by the cavity linewidth. A consequence of the latter is that achieving sufficient rotation at acoustic frequencies requires storage times of up to milliseconds[63], and this regime has only recently been approached experimentally[64]. A related approach to performing frequency-dependent quadrature rotation is based on the same idea, but uses either electromagnetically-induced transparency or a cavity exhibiting optomechanically-induced transparency[65] to achieve a filter with a tunable, actively narrowed linewidth[66–68]. This approach alleviates the pri-

mary technical difficulty with traditional filter cavities, namely an extremely low linewidth.

In all of these approaches the idea is first to generate fixed-angle squeezed light using established techniques (see, for example, the review by Anderson et al.[69]) and then filter this light to achieve quadrature rotation. In this chapter we consider an alternative approach, which is to inject squeezed light generated by an optomechanical system directly into the interferometer[70–72]. As we will show, such light naturally exhibits frequency-dependent quadrature rotation due to the dispersive optomechanical interaction, and, moreover, this effect occurs over a frequency band determined by the mechanical frequency, which can quite naturally fall in the acoustic band.

We will demonstrate that with a suitable choice of parameters, within reach of current state-of-the-art systems[73–75], such a scheme can provide an alternative to filter cavities and fixed-angle squeezing for use in long-baseline gravitational wave detectors. There is a fundamental limitation, however, which is that the frequency-dependent quadrature rotation occurs in the opposite direction to that required for optimal improvement. Combined with the high anti-squeezing occurring in the orthogonal quadrature, this precludes sensitivity enhancement across the full detection band. Unlike in the case of fixed-angle squeezed light, it is possible to attain a modest improvement at both high and low frequencies simultaneously, but this would only be potentially useful in specific (unusual) modes of operation. Thus our proposal is not suitable as a general-purpose method for optimising gravitational wave detectors.

2.2 Calculation of the output spectrum for optomechanical squeezing

In this section we derive an expression for the output noise spectrum of a linear cavity with a moveable end mirror. We start by finding an expression for the output field of the cavity as a function of its inputs, and then from this we determine the spectra of its individual quadratures.

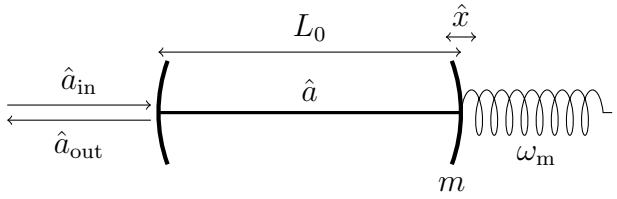

Figure 2.1: Basic optomechanical system. The left-hand cavity mirror is fixed, while the right-hand mirror is moveable and lies in a harmonic potential. The labels are defined in the text.

2.2.1 Output field

We consider a linear optical cavity of equilibrium length L_0 with one fixed mirror and one moveable mirror with natural mechanical frequency ω_{m} and mass m, as shown in Fig. 2.1.

For simplicity we consider the limit in which the natural mechanical frequency is significantly slower than the cavity free spectral range (the spacing between cavity modes, given by $\omega_{\text{FSR}} := \frac{\pi c}{L_0}$). This allows us to ignore the scattering of photons into different cavity modes stimulated by the optomechanical interaction, and thus confine the analysis to a single cavity mode[76, 77].

Let the input laser frequency be ω_{opt} and the equilibrium cavity resonance frequency be ω_0, and define the equilibrium cavity detuning $\Delta_0 := \omega_{\text{opt}} - \omega_0$. Let $\hat{a}$ and $\hat{a}^\dagger$ be the respective annihilation and creation operators for the field inside the cavity. Let $\hat{x}$ be the displacement of the moveable mirror from its equilibrium position, let $\hat{p}$ be the mirror momentum, and let $\omega(\hat{x})$ be the cavity resonance frequency for a given displacement.

Basic equations of motion

It will be convenient to work in a frame rotating at the optical frequency ω_{opt}, so we have the Hamiltonian

$$\hat{H} = \hbar(\omega(\hat{x}) - \omega_{\text{opt}})\left(\hat{a}^\dagger\hat{a} + \frac{1}{2}\right) + \frac{\hat{p}^2}{2m} + \frac{1}{2}m\omega_{\text{m}}^2\hat{x}^2. \tag{2.1}$$

We may approximate

$$\omega(\hat{x}) \approx \omega_0 - \frac{\omega_0}{L_0}\hat{x} = \omega_0 - G_0\hat{x}, \tag{2.2}$$

where we have defined the basic optomechanical coupling strength G_0 according to

$$G_0 := -\left.\frac{\partial\omega(\hat{x})}{\partial\hat{x}}\right|_0 = \frac{\omega_0}{L_0}. \tag{2.3}$$

This term converts a mirror displacement into a shift in resonance frequency, and thus describes the strength of the optomechanical interaction. The Hamiltonian simplifies to

$$\begin{aligned}\hat{H} &\approx \hbar(-\Delta_0 - G_0\hat{x})\left(\hat{a}^\dagger\hat{a} + \frac{1}{2}\right) + \frac{\hat{p}^2}{2m} + \frac{1}{2}m\omega_{\mathrm{m}}^2\hat{x}^2 \\ &\approx -\hbar\Delta_0\hat{a}^\dagger\hat{a} - \hbar G_0\hat{x}\hat{a}^\dagger\hat{a} + \frac{\hat{p}^2}{2m} + \frac{1}{2}m\omega_{\mathrm{m}}^2\hat{x}^2,\end{aligned} \tag{2.4}$$

where in the second line we have omitted the contribution from the vacuum.

From this and the commutation relations

$$[\hat{a},\hat{a}^\dagger] = 1, \qquad [\hat{x},\hat{p}] = i\hbar, \qquad [\hat{a},\hat{x}] = [\hat{a},\hat{p}] = 0 \tag{2.5}$$

we can calculate the equations of motion for the Heisenberg-picture operators in the absence of any noise or input:

$$\dot{\hat{x}} = \frac{i}{\hbar}\left(\frac{-i\hbar\hat{p}}{m}\right) = \frac{\hat{p}}{m} \tag{2.6}$$

$$\dot{\hat{p}} = \frac{i}{\hbar}\left(-i\hbar^2 G_0\hat{a}^\dagger\hat{a} + 2i\hbar m\omega_{\mathrm{m}}^2\hat{x}\right) = \hbar G_0\hat{a}^\dagger\hat{a} - m\omega_{\mathrm{m}}^2\hat{x} \tag{2.7}$$

$$\dot{\hat{a}} = \frac{i}{\hbar}\left(\hbar\Delta_0\hat{a} + \hbar G_0\hat{x}\hat{a}\right) = i(\Delta_0 + G_0\hat{x})\hat{a}. \tag{2.8}$$

Accounting for noise and inputs

To complete the picture we must include terms accounting for the mechanical and optical losses, and the driving input field.

Let the cavity half-linewidth be κ. We consider the adiabatic limit, where $\kappa \gg \omega_{\mathrm{m}}$, which allows us to assume that the optical field responds instantaneously to changes in cavity length. Let the input field be $\hat{a}_{\mathrm{in}}$, which we take to be a steady coherent laser drive a_{in} plus vacuum fluctuations $\delta\hat{a}_{\mathrm{in}}$ (that is, $\hat{a}_{\mathrm{in}} := a_{\mathrm{in}} + \delta\hat{a}_{\mathrm{in}}$). Let γ be the mechanical damping rate and consider the mirror to be driven by a steady, zero-mean Brownian force $\hat{F}$. We will define the details of these stochastic noise terms in Section 2.2.2.

The full equations of motion, which are known as the quantum Langevin equations (see Gardiner and Zoller[78] for further discussion), are thus

$$\dot{\hat{x}} = \frac{\hat{p}}{m} \tag{2.9}$$

$$\dot{\hat{p}} = \hbar G_0 \hat{a}^\dagger \hat{a} - m\omega_{\mathrm{m}}^2 \hat{x} - \gamma \hat{p} + \hat{F} \tag{2.10}$$

$$\dot{\hat{a}} = i(\Delta_0 + G_0 \hat{x})\hat{a} - \kappa \hat{a} + \sqrt{2\kappa}\hat{a}_{\mathrm{in}}. \tag{2.11}$$

Linearising the system

We will simplify the analysis by considering only small perturbations of the operators from their steady state values. We first calculate the steady state (x, p, a) based on the mean input field a_{in} and thermal driving $F = 0$:

$$\dot{\hat{x}} = 0 \implies p = 0 \tag{2.12}$$

$$\dot{\hat{p}} = 0 \implies \hbar G_0 a^* a - m\omega_{\mathrm{m}}^2 x = 0$$

$$\implies x = \frac{\hbar G_0 |a|^2}{m\omega_{\mathrm{m}}^2} \tag{2.13}$$

$$\dot{\hat{a}} = 0 \implies i(\Delta_0 + G_0 x)a - \kappa a + \sqrt{2\kappa}a_{\mathrm{in}} = 0$$

$$\implies a = -\frac{\sqrt{2\kappa}a_{\mathrm{in}}}{i\left(\Delta_0 + G_0 x\right) - \kappa} \tag{2.14}$$

Next we introduce the perturbations from the mean steady states:

$$\delta\hat{x} := \hat{x} - x \tag{2.15}$$

$$\delta\hat{a} := \hat{a} - a \tag{2.16}$$

Plugging into Eqs. (2.9) to (2.11) (and recalling that $\hat{a}_{\mathrm{in}} = a_{\mathrm{in}} + \delta\hat{a}_{\mathrm{in}}$) we obtain

$$\dot{\delta\hat{x}} = \dot{\hat{x}} = \frac{\hat{p}}{m} \tag{2.17}$$

$$\dot{\hat{p}} = \hbar G_0 \left(a^* + \delta\hat{a}^\dagger\right)\left(a + \delta\hat{a}\right) - m\omega_{\mathrm{m}}^2 \left(x + \delta\hat{x}\right) - \gamma\hat{p} + \hat{F} \tag{2.18}$$

$$\dot{\delta\hat{a}} = \dot{\hat{a}} = i(\Delta_0 + G_0\left(x + \delta\hat{x}\right))\left(a + \delta\hat{a}\right) - \kappa\left(a + \delta\hat{a}\right) + \sqrt{2\kappa}\left(a_{\mathrm{in}} + \delta\hat{a}_{\mathrm{in}}\right), \tag{2.19}$$

which can be expanded and then simplified via Eqs. (2.12) to (2.14):

$$\begin{aligned}
\dot{\hat{p}} &= \hbar G_0 a^* a - m\omega_{\mathrm{m}}^2 x + \hbar G_0 \left(a^* \delta\hat{a} + a\delta\hat{a}^\dagger + \delta\hat{a}^\dagger\delta\hat{a}\right) - m\omega_{\mathrm{m}}^2 \delta\hat{x} - \gamma\hat{p} + \hat{F} \\
&= \hbar G_0 \left(a^* \delta\hat{a} + a\delta\hat{a}^\dagger + \delta\hat{a}^\dagger\delta\hat{a}\right) - m\omega_{\mathrm{m}}^2 \delta\hat{x} - \gamma\hat{p} + \hat{F} \qquad (2.20) \\
\dot{\delta\hat{a}} &= i\left(\Delta_0 + G_0 x\right) a - \kappa a + \sqrt{2\kappa} a_{\mathrm{in}} \\
&\quad + i\left(\Delta_0 + G_0 x\right)\delta\hat{a} + iG_0 a\delta\hat{x} + iG_0\delta\hat{x}\delta\hat{a} - \kappa\delta\hat{a} + \sqrt{2\kappa}\delta\hat{a}_{\mathrm{in}} \\
&= i\left(\Delta_0 + G_0 x\right)\delta\hat{a} + iG_0 a\delta\hat{x} + iG_0\delta\hat{x}\delta\hat{a} - \kappa\delta\hat{a} + \sqrt{2\kappa}\delta\hat{a}_{\mathrm{in}} \\
&= \left(i\Delta - \kappa\right)\delta\hat{a} + iG_0 a\delta\hat{x} + iG_0\delta\hat{x}\delta\hat{a} + \sqrt{2\kappa}\delta\hat{a}_{\mathrm{in}}, \qquad (2.21)
\end{aligned}$$

where in the last line we have defined $\Delta := \Delta_0 + G_0 x$ to be the detuning at the steady state position.

We observe that applying a phase shift to the input fields a_{in} and $\delta\hat{a}_{\mathrm{in}}$ causes a corresponding phase shift in a, and these shifts may then be absorbed into $\delta\hat{a}$. That is, by varying the phase of the input field we may arbitrarily shift the phase of the intra-cavity field fluctuations $\delta\hat{a}$. Thus for our calculations we can assume that the input phase is chosen to make a positive and real, while knowing that in practice we may shift the reference phase of $\delta\hat{a}$ arbitrarily by shifting the phase of the input field.

We now define the adjusted optomechanical coupling strength $G := G_0 a$, which converts a displacement into the combined frequency shift for the whole (mean) intra-cavity field. Assuming $a \gg 1$ (that is, the number of photons circulating in the cavity is high) we may omit the second-order perturbation terms and thus obtain the linearised equations of motion:

$$\dot{\delta\hat{x}} = \frac{\hat{p}}{m} \qquad (2.22)$$

$$\dot{\hat{p}} = \hbar G\left(\delta\hat{a} + \delta\hat{a}^\dagger\right) - m\omega_{\mathrm{m}}^2\delta\hat{x} - \gamma\hat{p} + \hat{F} \qquad (2.23)$$

$$\dot{\delta\hat{a}} = \left(i\Delta - \kappa\right)\delta\hat{a} + iG\delta\hat{x} + \sqrt{2\kappa}\delta\hat{a}_{\mathrm{in}}. \qquad (2.24)$$

Solving the system

To solve this system of equations we first apply the Fourier transform

$$\mathcal{F}(f)(\omega) := \int_{-\infty}^{\infty} f(t)\exp(-i\omega t)dt. \qquad (2.25)$$

For clarity of notation we use the same symbol for an operator and its Fourier transform, but there will be no ambiguity since from this point on we will only ever be working in the frequency domain unless explicitly stated otherwise. Similarly, we will usually drop the argument to operators when it is simply ω. For an operator f we denote $f^\dagger \equiv f^\dagger(\omega) \equiv \mathcal{F}(f^\dagger)(\omega)$; that is, the Fourier transform of the conjugate as opposed to the conjugate of the Fourier transform. The system becomes

$$i\omega\delta\hat{x} = \frac{\hat{p}}{m} \tag{2.26}$$

$$i\omega\hat{p} = \hbar G\left(\delta\hat{a} + \delta\hat{a}^\dagger\right) - m\omega_{\mathrm{m}}^2\delta\hat{x} - \gamma\hat{p} + \hat{F} \tag{2.27}$$

$$i\omega\delta\hat{a} = (i\Delta - \kappa)\,\delta\hat{a} + iG\delta\hat{x} + \sqrt{2\kappa}\delta\hat{a}_{\mathrm{in}}. \tag{2.28}$$

To solve for the cavity field $\delta\hat{a}$ we start by eliminating $\hat{p}$ from the first two equations to obtain

$$\chi_{\mathrm{m}}^{-1}(\omega)\delta\hat{x} = \hbar G\left(\delta\hat{a} + \delta\hat{a}^\dagger\right) + \hat{F}, \tag{2.29}$$

where we have defined the standard mechanical susceptibility

$$\chi_{\mathrm{m}}(\omega) := \left[m\left(\omega_{\mathrm{m}}^2 - \omega^2 + i\gamma\omega\right)\right]^{-1}, \tag{2.30}$$

which describes the response of the oscillator to a unit impulsive force in the absence of any optomechanical interaction.

The equation for $\delta\hat{a}$ can be written in the form

$$\delta\hat{a} = \chi_{\mathrm{opt}}(\omega)\left(iG\delta\hat{x} + \sqrt{2\kappa}\delta\hat{a}_{\mathrm{in}}\right), \tag{2.31}$$

where we have defined the optical susceptibility

$$\chi_{\mathrm{opt}}(\omega) := (i\omega - i\Delta + \kappa)^{-1}, \tag{2.32}$$

which describes the response of the optical cavity to an injected photon (if we fix the moveable mirror in its steady state position).

Using the identity $\mathcal{F}(f^\dagger)(\omega) = \mathcal{F}(f)(-\omega)^\dagger$ we obtain a similar expression for

$\delta\hat{a}^\dagger$:

$$\begin{aligned}\delta\hat{a}^\dagger(\omega) &= \delta\hat{a}(-\omega)^\dagger \\ &= \chi_{\rm opt}(-\omega)^*\left(-iG\delta\hat{x}(-\omega)^\dagger + \sqrt{2\kappa}\delta\hat{a}_{\rm in}(-\omega)^\dagger\right) \\ &= \chi^*_{\rm opt}(\omega)\left(-iG\delta\hat{x}(\omega) + \sqrt{2\kappa}\delta\hat{a}^\dagger_{\rm in}(\omega)\right),\end{aligned} \tag{2.33}$$

where for the last line we have used Hermiticity of $\delta\hat{x}$ and defined

$$\chi^*_{\rm opt}(\omega) := (i\omega + i\Delta + \kappa)^{-1} = \chi_{\rm opt}(-\omega)^*. \tag{2.34}$$

Now we may substitute the expressions for $\delta\hat{a}$ and $\delta\hat{a}^\dagger$ into Eq. (2.29) to obtain

$$\begin{aligned}\chi_{\rm m}(\omega)^{-1}\delta\hat{x} = \hbar G\Big[&\chi_{\rm opt}(\omega)\left(iG\delta\hat{x} + \sqrt{2\kappa}\delta\hat{a}_{\rm in}\right) \\ &+\chi^*_{\rm opt}(\omega)\left(-iG\delta\hat{x} + \sqrt{2\kappa}\delta\hat{a}^\dagger_{\rm in}\right)\Big] + \hat{F},\end{aligned} \tag{2.35}$$

which can be rearranged to

$$\begin{aligned}\left(\chi_{\rm m}(\omega)^{-1} - i\hbar G^2\left(\chi_{\rm opt}(\omega) - \chi^*_{\rm opt}(\omega)\right)\right)\delta\hat{x} = \\ \sqrt{2\kappa}\hbar G\left(\chi_{\rm opt}(\omega)\delta\hat{a}_{\rm in} + \chi^*_{\rm opt}(\omega)\delta\hat{a}^\dagger_{\rm in}\right) + \hat{F}.\end{aligned} \tag{2.36}$$

From this we can define the effective mechanical susceptibility

$$\chi_{\rm eff}(\omega) := \left[\chi_{\rm m}(\omega)^{-1} - i\hbar G^2\left(\chi_{\rm opt}(\omega) - \chi^*_{\rm opt}(\omega)\right)\right]^{-1}, \tag{2.37}$$

which describes the full response of the oscillator, in the presence of the optomechanical interaction, to an impulsive force. We observe that the optomechanical interaction causes a frequency-dependent shift in the effective mechanical frequency and linewidth[79, 80]:

$$\omega_{\rm eff}(\omega)^2 := \omega_{\rm m}^2 + \frac{\hbar G^2}{m}\Im\left[\chi_{\rm opt}(\omega) - \chi^*_{\rm opt}(\omega)\right] \tag{2.38}$$

$$\gamma_{\rm eff}(\omega) := \gamma - \frac{\hbar G^2}{m\omega}\Re\left[\chi_{\rm opt}(\omega) - \chi^*_{\rm opt}(\omega)\right]. \tag{2.39}$$

Note that for $\omega \ll \kappa$ these quantities are essentially constant with respect to ω, so usually we omit the ω argument and treat them as constants (with respect to ω).

Continuing from Eq. (2.36) we obtain

$$\chi_{\rm eff}(\omega)^{-1}\delta\hat{x} = \sqrt{2\kappa}\hbar G\left(\chi_{\rm opt}(\omega)\delta\hat{a}_{\rm in} + \chi^*_{\rm opt}(\omega)\delta\hat{a}^\dagger_{\rm in}\right) + \hat{F}. \tag{2.40}$$

Substituting into Eq. (2.31) we can express the cavity field in terms of only the inputs:

$$\begin{aligned}\delta\hat{a} = \chi_{\rm opt}(\omega)\Big(&iG\chi_{\rm eff}(\omega)\left[\sqrt{2\kappa}\hbar G\left(\chi_{\rm opt}(\omega)\delta\hat{a}_{\rm in} + \chi^*_{\rm opt}(\omega)\delta\hat{a}^\dagger_{\rm in}\right) + \hat{F}\right]\\ &+\sqrt{2\kappa}\delta\hat{a}_{\rm in}\Big).\end{aligned} \tag{2.41}$$

By invoking the input-output relation[81] $\delta\hat{a}_{\rm out} = \sqrt{2\kappa}\delta\hat{a} - \delta\hat{a}_{\rm in}$ and rearranging we obtain the output field:

$$\begin{aligned}\delta\hat{a}_{\rm out} &= \sqrt{2\kappa}iG\chi_{\rm opt}(\omega)\chi_{\rm eff}(\omega)\left[\sqrt{2\kappa}\hbar G\left(\chi_{\rm opt}(\omega)\delta\hat{a}_{\rm in} + \chi^*_{\rm opt}(\omega)\delta\hat{a}^\dagger_{\rm in}\right) + \hat{F}\right]\\ &\quad + (2\kappa\chi_{\rm opt}(\omega) - 1)\delta\hat{a}_{\rm in}\\ &= \left[2\kappa i\hbar G^2\chi_{\rm eff}(\omega)\chi_{\rm opt}(\omega)^2 + \chi_{\rm opt}(\omega)/\chi_{\rm opt}(\omega)^*\right]\delta\hat{a}_{\rm in}\\ &\quad + 2\kappa i\hbar G^2\chi_{\rm eff}(\omega)\chi_{\rm opt}(\omega)\chi^*_{\rm opt}(\omega)\delta\hat{a}^\dagger_{\rm in}\\ &\quad + \sqrt{2\kappa}iG\chi_{\rm eff}(\omega)\chi_{\rm opt}(\omega)\hat{F},\end{aligned} \tag{2.42}$$

where we have observed that $2\kappa\chi_{\rm opt}(\omega) - 1 = \chi_{\rm opt}(\omega)/\chi_{\rm opt}(\omega)^*$. Similarly, the conjugate is given by

$$\begin{aligned}\delta\hat{a}^\dagger_{\rm out} &= \left[2\kappa i\hbar G^2\chi_{\rm eff}(\omega)\chi^*_{\rm opt}(\omega)^2 + \chi^*_{\rm opt}(\omega)/\chi^*_{\rm opt}(\omega)^*\right]\delta\hat{a}^\dagger_{\rm in}\\ &\quad + 2\kappa i\hbar G^2\chi_{\rm eff}(\omega)\chi_{\rm opt}(\omega)\chi^*_{\rm opt}(\omega)\delta\hat{a}_{\rm in}\\ &\quad + \sqrt{2\kappa}iG\chi_{\rm eff}(\omega)\chi^*_{\rm opt}(\omega)\hat{F}.\end{aligned} \tag{2.43}$$

Observations

Before calculating the output spectrum, which will be our main tool for analysing the properties of this output field, we can make some initial observations from simply inspecting Eq. (2.42). This will provide intuition that can guide the choice of parameters in the subsequent sections.

First, in the case that $G \approx 0$ (that is, the mechanical motion has a negligible effect on the optical properties of the system), only the $\chi_{\rm opt}(\omega)/\chi_{\rm opt}(\omega)^*\delta\hat{a}_{\rm in}$ term remains, and the action of the cavity is simply to apply a phase shift of

$2\arg(\chi_{\rm opt}(\omega)) = 2\arctan((\Delta-\omega)/\kappa)$ to the input field. In particular, if this input field is squeezed then the cavity will perform a frequency-dependent rotation of the squeezed quadrature, which is the basis of approaches to generating quadrature rotation based on filter cavities (see Section 2.1). We can also see one reason why these schemes are challenging: to achieve a significant phase shift over a 100 Hz band we must have a linewidth $\kappa/2\pi$ on the order of 50 Hz (or even lower), which corresponds to a cavity storage time of several milliseconds. Such cavities have only just started to become within reach of experimental realisation[64].

When $G \not\approx 0$ the dynamics become significantly more interesting. Specifically, one may observe that the output field depends on both the noise in the input field and its conjugate, so *a priori* we may be able to choose parameters to make these terms interfere destructively. By doing this we would reduce the noise in one component of the output field and thus generate squeezed light. Moreover, since the coefficients are frequency-dependent, the maximally-squeezed quadrature would rotate with frequency. Finally, since the coupling terms are proportional to the mechanical susceptibility, this suggests that any generated squeezing will be near the mechanical frequency.

In fact, we can extract further insight by inspecting the first two terms of Eq. (2.42), which we denote $\delta\hat{a}^{\rm sqz}_{\rm out}$, in more detail. One may notice that the first two terms resemble the action of the *squeeze operator* on the input field. The squeeze operator[82, 83],

$$\hat{S}(r,\phi) := \exp\left[\frac{r}{2}\left(e^{-2i\phi}\hat{a}^2 - e^{2i\phi}\,\hat{a}^{\dagger\,2}\right)\right], \tag{2.44}$$

acts on the vacuum (or any coherent state) to reduce the noise in the ϕ quadrature by a factor of e^{-2r} and increase the noise in the orthogonal quadrature by e^{2r}. We refer to r as the *squeeze factor* and ϕ as the *squeeze angle*. The action of the squeeze operator on the field operator $\hat{a}$ is given by

$$\hat{S}(r,\phi)^\dagger \hat{a} \hat{S}(r,\phi) = \cosh r\hat{a} - e^{2i\phi}\sinh r\hat{a}^\dagger. \tag{2.45}$$

Thus we see that, if an appropriate choice of squeeze factor r and angle ϕ can be made, $\delta\hat{a}^{\rm sqz}_{\rm out}$ indeed describes a (scaled) squeeze of the input vacuum fluctuations.[1]

[1]If the reader is unfamiliar with the squeeze operator, for the sake of intuition one can consider the case that $\Delta = 0$ and $\omega \ll \kappa$, since then we have $\chi_{\rm opt}(\omega) = \chi^*_{\rm opt}(\omega) \approx \chi_{\rm opt}(\omega)^*$

Specifically, abbreviating the coefficients of the first two terms in Eq. (2.42) as

$$\alpha(\omega) := 2\kappa i\hbar G^2 \chi_{\text{eff}}(\omega)\chi_{\text{opt}}(\omega)^2 + \chi_{\text{opt}}(\omega)/\chi_{\text{opt}}(\omega)^* \tag{2.46}$$

$$\beta(\omega) := 2\kappa i\hbar G^2 \chi_{\text{eff}}(\omega)\chi_{\text{opt}}(\omega)\chi^*_{\text{opt}}(\omega), \tag{2.47}$$

we may write

$$\begin{aligned}\delta\hat{a}^{\text{sqz}}_{\text{out}} &= \alpha(\omega)\delta\hat{a}_{\text{in}} + \beta(\omega)\delta\hat{a}^\dagger_{\text{in}} \\ &= c(\omega)\left(\cosh r(\omega)\delta\hat{a}_{\text{in}} - e^{2i\phi(\omega)}\sinh r(\omega)\delta\hat{a}^\dagger_{\text{in}}\right),\end{aligned} \tag{2.48}$$

where we take

$$\begin{gathered}r(\omega) := \coth^{-1}\left(\left|\frac{\alpha(\omega)}{\beta(\omega)}\right|\right), \qquad \phi(\omega) := \frac{\pi}{2} + \frac{\arg(\beta(\omega)) - \arg(\alpha(\omega))}{2}, \\ c(\omega) := \frac{\alpha(\omega)}{\cosh r(\omega)}.\end{gathered} \tag{2.49}$$

For some choices of parameters this identification is not possible. Indeed, it is clear from the definitions that a sufficient condition is $|\alpha| > |\beta|$, and if we recall that the hyperbolic functions satisfy $\cosh^2 x - \sinh^2 x = 1$ we see that $|\alpha|^2 - |\beta|^2 = |c|^2$ and thus this condition is also necessary. Some computation yields

$$|\alpha(\omega)|^2 - |\beta(\omega)|^2 = 1 + 4\kappa G^2\hbar\,|\chi_{\text{opt}}(\omega)|^2\,|\chi_{\text{eff}}(\omega)|^2\, m\gamma\omega, \tag{2.50}$$

so it is not hard to convince oneself that the condition could be violated, for example by considering frequencies within a linewidth of the effective mechanical frequency in systems with low mechanical damping rates. We will discuss this further when considering a specific system in Section 2.3.

Assuming we can indeed achieve the representation in Eq. (2.48), and continuing to ignore the contribution of the thermal spectrum to the output field, we can gain intuition about the magnitude and quadrature of the squeezing effect by considering the values of r and ϕ. Specifically, let us consider the case where $\kappa \gg \omega$, which is the most interesting one for our purposes, since otherwise we

---

and the form of $\delta\hat{a}^{\text{sqz}}_{\text{out}}$ reduces to $d(\omega)(\delta\hat{a}_{\text{in}} + \delta\hat{a}^\dagger_{\text{in}}) + \delta\hat{a}_{\text{in}}$ (for some $d(\omega)$). This represents a projection of the complex field onto the real axis (which could be seen as a type of degenerate "squeeze"), a scaling by $d(\omega)$, and then addition to the original field. If $d(\omega)$ is negative and real, for example, the net effect of this combined action is to shift the real parts of the input field towards zero and thus squeeze the field along the real axis.

could simply use the cavity as a filter (as mentioned above). In this limit we can consider $\chi_{\rm opt}$ to be independent of ω, and we also have $\chi^*_{\rm opt}(\omega) \approx \chi_{\rm opt}(\omega)^*$. We can therefore approximate

$$\beta(\omega) \approx 2\kappa i\hbar G^2 \chi_{\rm eff}(\omega) \left|\chi_{\rm opt}\right|^2 \tag{2.51}$$

$$\begin{aligned}\alpha(\omega) &\approx 2\kappa i\hbar G^2 \chi_{\rm eff}(\omega)\chi^2_{\rm opt} + \chi_{\rm opt}/\chi^*_{\rm opt} \\ &= \frac{\chi_{\rm opt}}{\chi^*_{\rm opt}} \left(2\kappa i\hbar G^2 \chi_{\rm eff}(\omega) \left|\chi_{\rm opt}\right|^2 + 1\right) \\ &\approx \frac{\chi_{\rm opt}}{\chi^*_{\rm opt}} \left(\beta(\omega) + 1\right). \end{aligned} \tag{2.52}$$

If we further assume $\gamma \ll \omega_{\rm m}$, which is to say the mechanical resonator is of high quality, then we see that the effective susceptibility $\chi_{\rm eff}$ is almost purely real (except when very close to the effective mechanical frequency), meaning β is essentially purely imaginary. A depiction of how α and β lie in the complex plane is shown in Fig. 2.2. It will be illustrative to consider how this picture varies as the frequency ω is increased from 0 to $\omega \gg \omega_{\rm eff}$. Initially the susceptibility $\chi_{\rm eff}$ increases and thus the magnitude of β increases, with very little change in phase. As the effective mechanical frequency is approached the magnitude becomes very large (proportional to $1/\gamma$), until near the effective mechanical frequency β rotates through the positive real half-plane to lie on the negative imaginary axis. After this point the dynamics are reversed, and as ω increases further the magnitude of β decreases back towards 0. With this picture we can gain some intuition into how the squeezing of the system varies with parameters.[2]

Looking first at the definition of the squeeze factor r given in Eq. (2.49), we see that to maximise the squeeze factor we must bring the ratio $|\alpha/\beta|$ as close to unity as possible, which, given our approximations, is simply a case of maximising $|\beta|$. This suggests that the maximum attainable squeezing level, which should be achieved near the effective mechanical frequency, will increase by decreasing any of the mechanical damping, optical linewidth κ or detuning $|\Delta|$.

Now let us consider the angle of squeezing, where in particular we will be concerned with the change in squeezed angle as ω varies. First note that following

[2]We also refer the reader to an elegant alternative approach to visualising the behaviour of optomechanical squeezing, presented by Corbitt et al.[84]: applying a rotation to the quadratures can simplify the input-output relationship (Eqs. (2.42) and (2.43)) to a form depending only on a single parameter, and significant insight can be extracted simply by considering the value of that parameter in the various regimes of interest.

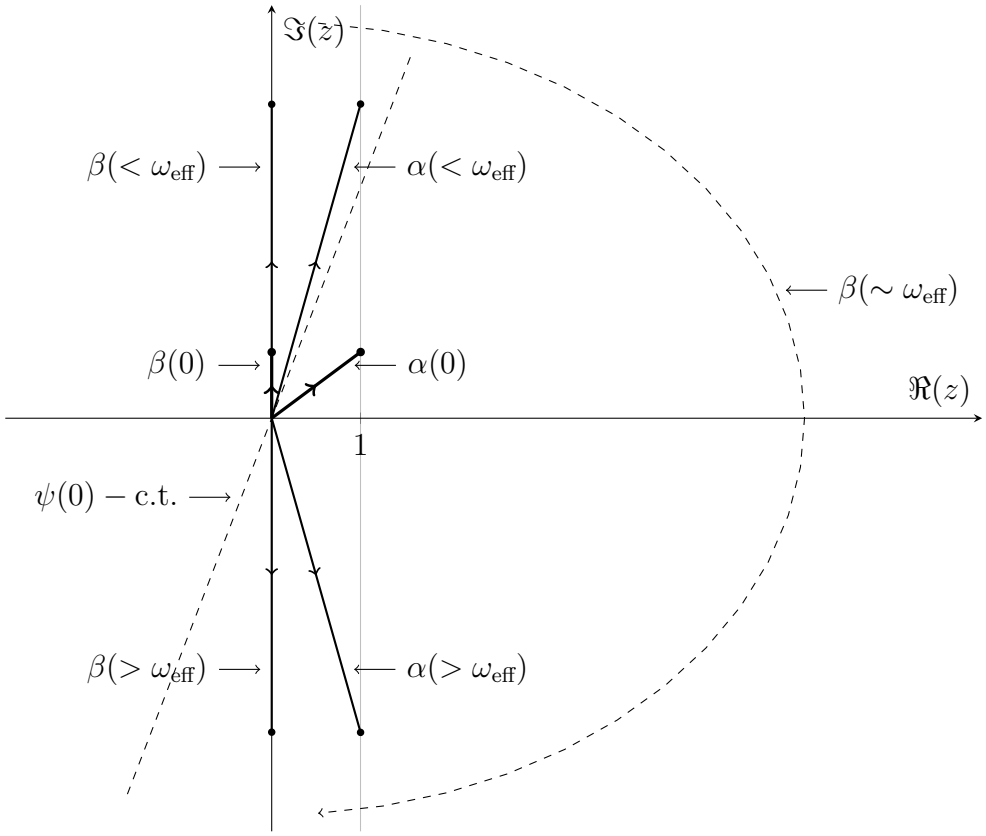

Figure 2.2: Illustration of coefficients α and β in the limit of large optical linewidth and small mechanical linewidth. For simplicity we have considered the case where χ_{opt} is approximately real (that is, $\Delta = 0$); in the general case α would be rotated by $2\arg(\chi_{\text{opt}})$. We have $\alpha(\omega) = \beta(\omega) + 1$ for all ω. As ω increases from 0, both $\alpha(\omega)$ and $\beta(\omega)$ move upwards parallel to the imaginary axis. When ω becomes very close to the effective mechanical frequency the vectors rotate around the positive real half-plane back to the negative imaginary axis, after which they move back up towards the real axis as ω further increases. The squeeze factor $r(\omega)$ is the ratio between the lengths of $\alpha(\omega)$ and $\beta(\omega)$, while the total squeeze angle $\psi(\omega)$ is the average argument of $\alpha(\omega)$ and $\beta(\omega)$ (plus a constant term, denoted "c.t." in the plot).

the squeeze $S(r(\omega), \phi(\omega))$ there is a scale by $c(\omega)$, which may be complex and thus effect a rotation of the squeezed field, so the squeezed angle $\psi(\omega)$ of the output field is given by

$$\begin{aligned}\psi(\omega) &= \arg(c(\omega)) + \phi(\omega) \\ &= \arg(\alpha(\omega)) + \phi(\omega) \\ &= \frac{\pi}{2} + \frac{\arg(\beta(\omega)) + \arg(\alpha(\omega))}{2} \\ &= \frac{\pi}{2} + \arg(\chi_{\text{opt}}) + \frac{\arg(\beta(\omega)) + \arg(\beta(\omega) + 1)}{2}. \end{aligned} \tag{2.53}$$

The first two terms are independent of ω, so to achieve a large amount of squeezing angle rotation we must cause the average phase of β and $\beta + 1$ to vary as much as possible. Thinking of this in terms of the picture described above we see that, ignoring the constant terms, the initial squeezing angle is determined by the initial magnitude of β: for a small magnitude we will have an angle close to $\pi/4$, while for a larger magnitude this will increase towards $\pi/2$. As ω increases the angle tends to $\pi/2$, until the effective mechanical frequency is reached at which point the picture is reflected and the angle jumps to $-\pi/2$. Then as we increase ω further the angle will tend back towards $-\pi/4$. Thus the factor determining the total amount of quadrature rotation across the spectrum is the magnitude of β at the start and end of the spectrum. We may decrease this magnitude, and thus increase the total amount of quadrature rotation towards $\pi/2$, by increasing the mechanical frequency, optical linewidth κ or detuning $|\Delta|$. Note the contrast to the squeezing factor, which *decreases* as κ and $|\Delta|$ increase.

To conclude our initial observations, we note an interesting property of the system's action on commutation relations. Since the squeezing operator is unitary, and thus preserves commutation relations, it may appear from Eq. (2.48) that if $|c| < 1$ the system could effect an increase in commutativity between the input field and its conjugate, and thus violate the Heisenberg uncertainty principle. Put another way, if $|c| < 1$ then the total size of the uncertainty ellipse could decrease below the shot noise level. However, we find that if we include the thermal term of Eq. (2.42), and specifically the exact thermal spectrum as defined below in Eq. (2.58), the deviation of $|c|$ from unity is exactly corrected by the temperature-independent term of the thermal spectral density. Thus, as required by the uncertainty principle, the uncertainty does not drop below the shot noise

level.

2.2.2 Output spectrum

To explore the behaviour of the output field (given by Eq. (2.42)) in more detail we may calculate the power spectra for its individual quadratures.

Noise correlation functions

The first step is to specify the details of the driving noise terms, namely the input vacuum fluctuations $\delta\hat{a}_{\mathrm{in}}$ and the force from the thermal bath $\hat{F}$. We assume that the optical drive is at room temperature, so $\hbar\omega_{\mathrm{opt}} \gg k_{\mathrm{B}}T$ and thus the mean thermal photon occupation $n_{\mathrm{o}}^{\mathrm{th}}$ is negligible. Moreover, the field fluctuations are essentially Markovian for a small bandwidth about optical frequencies[81, 85], meaning the correlation functions are

$$\begin{aligned}\left\langle \delta\hat{a}_{\mathrm{in}}^{\dagger}(\omega)\delta\hat{a}_{\mathrm{in}}(\omega')\right\rangle &= 2\pi\delta(\omega+\omega')n_{\mathrm{o}}^{\mathrm{th}} \\ &\approx 0 \qquad (2.54)\\ \left\langle \delta\hat{a}_{\mathrm{in}}(\omega)\delta\hat{a}_{\mathrm{in}}^{\dagger}(\omega')\right\rangle &= 2\pi\delta(\omega+\omega')(n_{\mathrm{o}}^{\mathrm{th}}+1) \\ &\approx 2\pi\delta(\omega+\omega') \qquad (2.55)\\ \langle\delta\hat{a}_{\mathrm{in}}(\omega)\delta\hat{a}_{\mathrm{in}}(\omega')\rangle &= \left\langle \delta\hat{a}_{\mathrm{in}}^{\dagger}(\omega)\delta\hat{a}_{\mathrm{in}}^{\dagger}(\omega')\right\rangle = 0, \qquad (2.56)\end{aligned}$$

where $\langle\cdot\rangle$ denotes the expected value and δ is the Dirac delta function.

For the mechanical noise the situation is less straightforward, since in the quantum case Brownian forces are non-Markovian[78, 85, 86]. Specifically, we have the correlation function

$$\left\langle \hat{F}(\omega)\hat{F}(\omega')\right\rangle = 2\pi\delta(\omega+\omega')S_{\mathrm{th}}(\omega), \qquad (2.57)$$

where the thermal noise spectrum S_{th} is defined, following the analysis in [85], to be

$$S_{\mathrm{th}}(\omega) := m\gamma\hbar\omega\left[\coth\left(\frac{\hbar\omega}{2k_{\mathrm{B}}T}\right)-1\right]. \qquad (2.58)$$

We shall consider the limit in which the thermal correlations are significantly faster than the mechanical timescales[78], which is to say $\hbar\omega \ll 2k_{\mathrm{B}}T$. The noise

spectrum can therefore be approximated as

$$S_{\mathrm{th}}(\omega) \approx m\gamma\hbar\omega \left[1 + \frac{2k_{\mathrm{B}}T}{\hbar\omega}\right] \approx 2m\gamma k_{\mathrm{B}}T. \tag{2.59}$$

Output spectrum for an arbitrary quadrature

We define the quadrature with angle θ as

$$\hat{X}_\theta = e^{-i\theta}\delta\hat{a}_{\mathrm{out}} + e^{i\theta}\delta\hat{a}^\dagger_{\mathrm{out}}. \tag{2.60}$$

We define the symmetrised spectral density (see Clerk et al.[87] for a comprehensive discussion of noise spectra) of such a quadrature $\hat{X}_\theta$, normalised to the shot noise, to be

$$S_\theta(\omega) := \int_{-\infty}^{\infty} \frac{d\omega'}{2\pi} \left\langle \left\{ \hat{X}_\theta(\omega), \hat{X}_\theta(\omega') \right\} \right\rangle, \tag{2.61}$$

where $\{\cdot,\cdot\}$ denotes symmetrisation: $\{f,g\} := (fg+gf)/2$.

Using Eqs. (2.42) and (2.43) for the output field $\delta\hat{a}_{\mathrm{out}}$ and its conjugate $\delta\hat{a}^\dagger_{\mathrm{out}}$, together with the noise correlation functions Eqs. (2.54) to (2.57), we can determine S_θ for an arbitrary θ. Some computation, which is rather tedious and not particularly instructive (and hence omitted), yields

$$\begin{aligned} S_\theta(\omega) = {} & 2\kappa G^2 \left|\chi_{\mathrm{eff}}(\omega)\right|^2 \left(S_{\mathrm{th}}(\omega) + \kappa\hbar^2 G^2 \left(\left|\chi_{\mathrm{opt}}(\omega)\right|^2 + \left|\chi^*_{\mathrm{opt}}(\omega)\right|^2 \right) \right) \\ & \times \left|\chi_{\mathrm{opt}}(\omega) - e^{2i\theta}\chi^*_{\mathrm{opt}}(\omega)\right|^2 \\ & + 4\kappa\hbar G^2 \Re\left[\chi_{\mathrm{eff}}(\omega)\right] \Im\left[e^{2i\theta}\chi_{\mathrm{opt}}(\omega)^*\chi^*_{\mathrm{opt}}(\omega)\right] \\ & + 2\kappa\hbar G^2 \Im\left[\chi_{\mathrm{eff}}(\omega)\right] \left(\left|\chi^*_{\mathrm{opt}}(\omega)\right|^2 - \left|\chi_{\mathrm{opt}}(\omega)\right|^2 \right) \\ & + 1. \end{aligned} \tag{2.62}$$

Squeezing angle and minimised spectrum

Fortunately the dependence of Eq. (2.62) on θ is quite simple, so some further calculations yield the quadrature angle $\theta_{\mathrm{min}}(\omega)$ minimising the spectrum (and thus maximising squeezing):

$$\theta_{\mathrm{min}}(\omega) = \frac{\pi}{2} + \frac{1}{2}\arctan 2\begin{pmatrix} (\kappa^2+\omega^2-\Delta^2)\xi(\omega) - 4\kappa\Delta\zeta(\omega) \\ -2(\kappa^2+\omega^2-\Delta^2)\zeta(\omega) - 2\kappa\Delta\xi(\omega) \end{pmatrix}, \tag{2.63}$$

where $\arctan2\binom{y}{x} := \arg(x+iy)$ and we have abbreviated the coefficients of the two θ-dependent terms in Eq. (2.62) according to

$$\zeta(\omega) := 2\kappa G^2 \left|\chi_{\text{eff}}(\omega)\right|^2 \left(S_{\text{th}}(\omega) + \kappa\hbar^2 G^2 \left(\left|\chi_{\text{opt}}(\omega)\right|^2 + \left|\chi^*_{\text{opt}}(\omega)\right|^2\right)\right) \tag{2.64}$$

$$\xi(\omega) := 4\kappa\hbar G^2 \Re\left[\chi_{\text{eff}}(\omega)\right]. \tag{2.65}$$

We can also define

$$S_{\text{min}}(\omega) := S_{\theta_{\text{min}}(\omega)}(\omega) \tag{2.66}$$

to be the value of the spectrum at the optimal angle, for each frequency. We can interpret $\theta_{\text{min}}(\omega)$ and $S_{\text{min}}(\omega)$ as the squeeze angle and factor for frequency ω.

2.3 Properties of optomechanical squeezing

With the noise spectrum Eq. (2.62) in hand we can investigate some properties of optomechanical squeezing. In particular, of course, we will focus on how the level and angle of squeezing vary with frequency in parameter regimes suitable for gravitational wave interferometry.

The parameters we use for the analysis and throughout the remainder of the chapter are shown in Table 2.1. Note that we have introduced several parameters commonly used for characterising optomechanical systems, and from which all parameters in the above analysis can be deduced. Specifically: the quality factor of the mechanical resonator, $Q_m := \omega_m/\gamma$; the total input laser power, $P_{\text{in}} := \hbar\omega_{\text{opt}} \left|a_{\text{in}}\right|^2$; the laser wavelength, $\lambda := 2\pi c/\omega_{\text{opt}}$; the cavity finesse, $\mathcal{F} = \omega_{\text{FSR}}/2\kappa$; and the single-photon optomechanical coupling strength, $g_0 := G_0\sqrt{\hbar/2m\omega_{\text{m}}}$. We have chosen to consider a cavity with medium finesse and relatively large damping rate, since this is both experimentally realistic and allows us to investigate behaviour in a regime where filter cavities would not be useful for inducing suitable quadrature rotation. We have also selected the parameters to limit the maximum attainable squeezing to 10 dB, since this allows a fair comparison with traditional squeezing techniques[45]. We note that with this choice of parameters the squeezing dilation factor $c(\omega)$ from Section 2.2.1 is extremely close to 1, except within a narrow band (with width proportional to the mechanical linewidth) about the effective mechanical frequency. This implies that we can generally consider the action of the cavity to be a pure squeeze,

Parameter	**Symbol**	**Value**	
Mechanical frequency	ω_{m}	$2\pi \times 150$	Hz
Mechanical quality factor	Q_{m}	5×10^6	
Mirror mass	m	0.5	kg
Temperature	T	3	mK
Input power	P_{in}	20	W
Wavelength	λ	1064	nm
Free spectral range	ω_{FSR}	$2\pi \times 1$	GHz
Cavity damping	κ	$2\pi \times 0.5$	MHz
Finesse	$\mathcal{F}$	1000	
Single-photon OM coupling	g_0	$2\pi \times 0.63$	mHz
Test masses (LIGO)	m_{gw}	40	kg
Cavity length (LIGO)	L_{gw}	4	km
Cavity damping (LIGO)	κ_{gw}	$2\pi \times 100$	Hz

Table 2.1: Parameters used for the analyses of optomechanical squeezing and interferometric sensitivity enhancement.

followed by a rotation, followed by the addition of thermal effects.

With these parameters fixed we may calculate the spectrum in a few different scenarios. Specifically, we are looking to achieve squeezing in the acoustic band below around 300 Hz and ideally a quadrature rotation through an angle of $\pi/2$ across this band, since this is the behaviour required for optimising long-baseline gravitational wave detectors.

We start by considering the squeezing factor (the spectral density of the maximally-squeezed quadrature) as a function of frequency and cavity detuning, as shown in Fig. 2.3. We first observe that squeezing is generally strongest when the detuning is within a single cavity linewidth; outside this region the optical susceptibilities become low and thus the strength of the optomechanical non-linearity reduces, precluding the generation of significant squeezing. For suitable detunings, a high squeezing factor is obtained across the full band of interest, peaking at approximately 10 dB as the effective mechanical frequency is approached. However, in a narrow band about the effective mechanical frequency, where the frequency response inverts, there is a reduction in squeezing (the width of this feature is proportional to the mechanical linewidth). We also

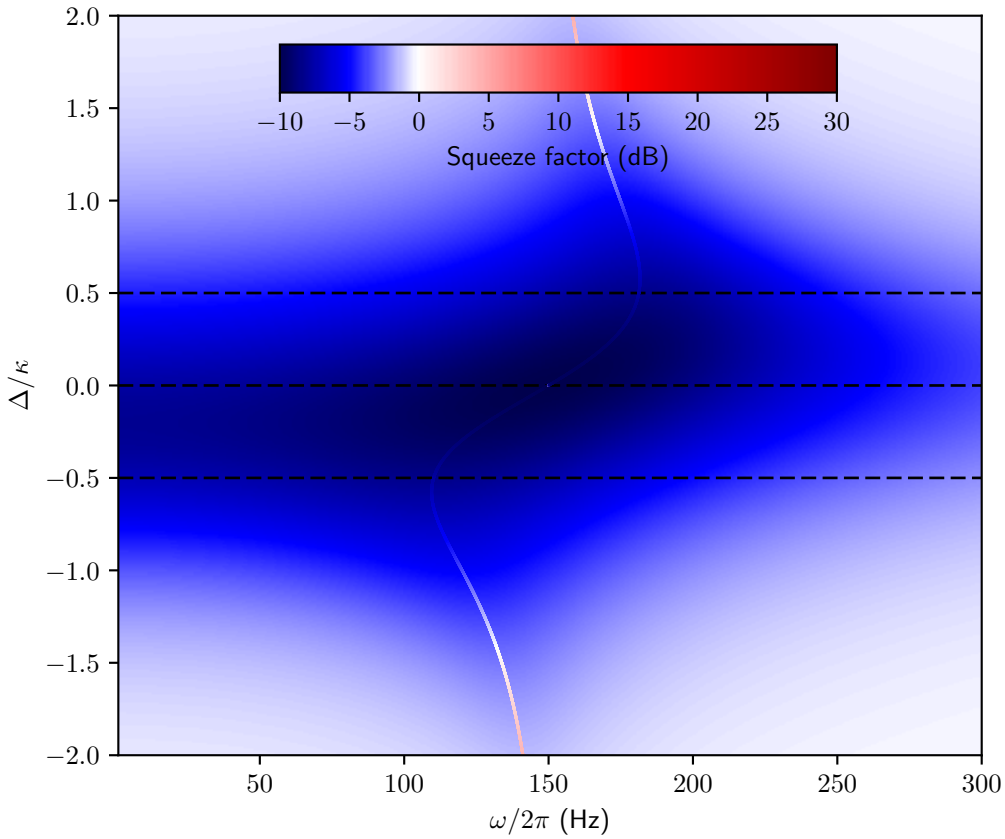

Figure 2.3: Squeezing factor $S_{\min}(\omega)$ for various detunings. Three specific detunings $\Delta = -0.5\kappa, 0, 0.5\kappa$ are marked. Note the sharp feature tracking the effective mechanical frequency, where the frequency response of the system reverses and the squeezing reduces in a very narrow band. In reality the width of this band is proportional to the mechanical damping rate and too narrow to see, but it is artificially increased here.

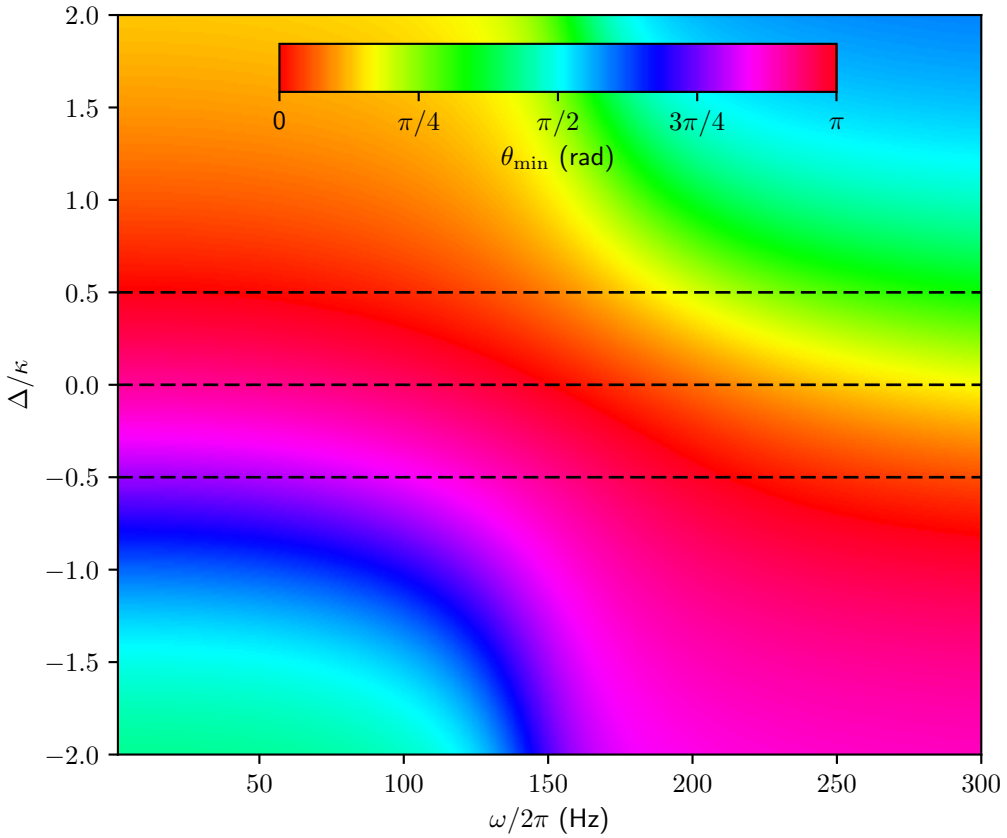

Figure 2.4: Squeezing angle $\theta_{\min}(\omega)$ for various detunings. Three specific detunings $\Delta = -0.5\kappa, 0, 0.5\kappa$ are marked.

see that the squeezing factor diminishes as the frequency becomes too far from the mechanical frequency, again because the effect of the optomechanical interaction is attenuated by the low mechanical susceptibility.

We can similarly view the squeezing angle as a function of frequency and detuning, as shown in Fig. 2.4. As with the squeezing factor, the rotation of the squeezed angle generally tends to occur in the vicinity of the mechanical frequency. Unlike with the squeezing factor, however, a stronger rotation effect (that is, rotation through a larger angle) occurs with larger detunings. That is, there is a tradeoff to be made between the squeeze factor and the amount of quadrature rotation: detuning further from the cavity resonance increases the amount of rotation but decreases the squeeze factor across the band.

To see more detail we consider three specific detunings $\Delta = -0.5\kappa, 0, 0.5\kappa$, and plot their squeezing factors and phases in Fig. 2.5. Comparing the three

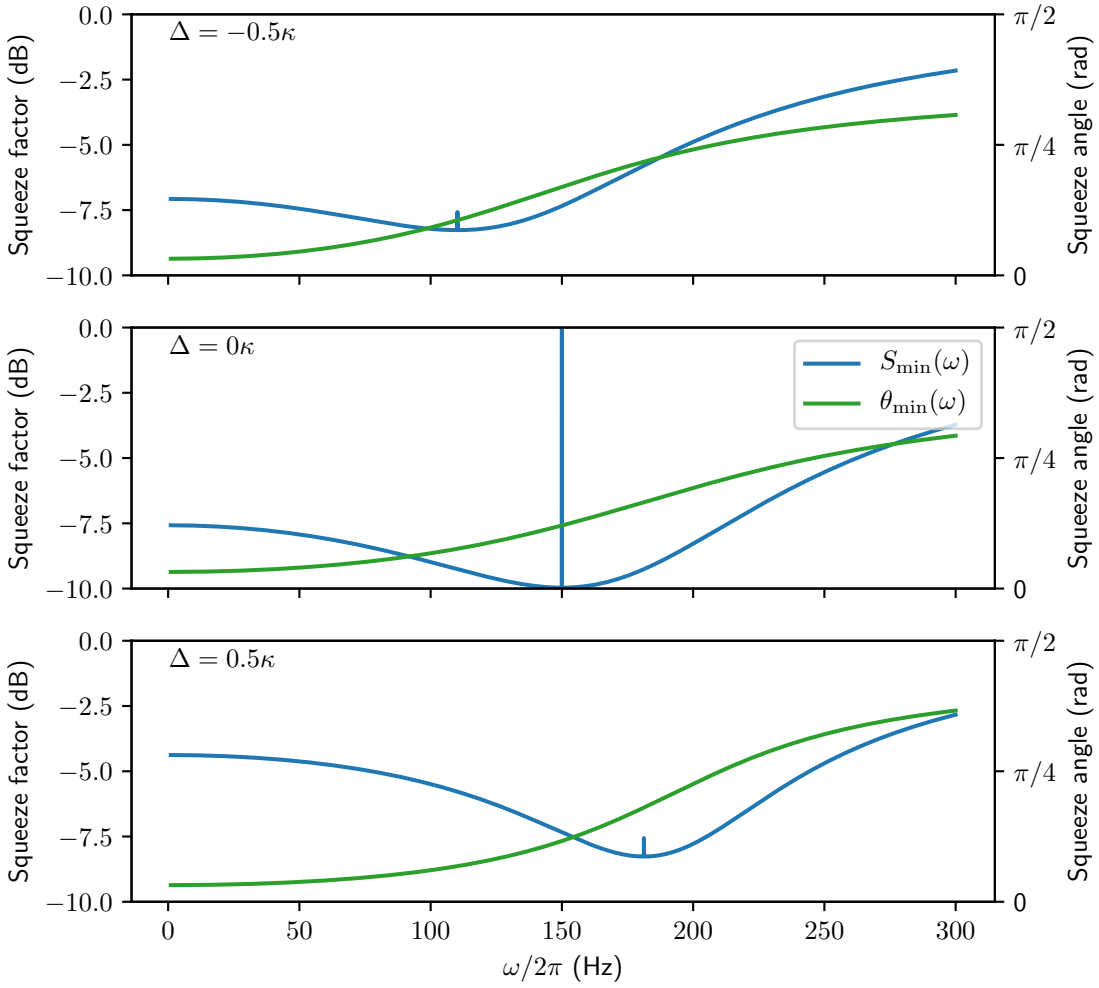

Figure 2.5: Squeezing factor $S_{\min}(\omega)$ and angle $\theta_{\min}(\omega)$ for specific detunings $\Delta = -0.5\kappa, 0, 0.5\kappa$. We have applied constant phase shifts to the squeezing angles (which, as discussed in Section 2.2.1, is possible by simply shifting the phase of the input field) in order allow the frequency dependence for different detunings to be compared more easily.

plots we again see the tradeoff between squeeze factor and the total amount of quadrature rotation. Similarly, we can see more clearly that the interesting dynamics—high squeezing and quadrature rotation—both occur in the vicinity of the mechanical frequency, meaning if one desires good squeezing then one must also deal with the steady rate of quadrature rotation (and conversely). This observation will be important in the next section when we consider the use of optomechanically-squeezed light for gravitational wave detectors.

As discussed in Section 2.2.1 the light ejected from the cavity is not purely squeezed—there is additional noise due to the thermal effects (and, at least in a very narrow band about the effective mechanical frequency, due to the optomechanical interaction too). Therefore it is important to understand the full spectrum of noise, not only that in the squeezed quadrature. In Fig. 2.6 we plot the spectra of all quadratures as a function of angle for specific detunings. We see that, especially near the effective mechanical frequency (where the noise is resonantly amplified), significant anti-squeezing occurs. Combined with the observation above, that in order to have squeezing one must be near the mechanical frequency and thus also have quadrature rotation, this suggests a difficulty with the use of optomechanically-generated squeezed light in practice: unless the quadrature rotation is perfectly matched to the appropriate system, significant contamination could occur from the anti-squeezing and thus degrade performance.

2.4 Enhancement of LIGO sensitivity via optomechanical squeezing

In this section we investigate how we expect the sensitivity of the Laser Interferometer Gravitational-Wave Observatory (LIGO) to be affected by the injection of optomechanically-generated squeezed light.

We consider a setup as shown in Fig. 2.7, with optomechanical squeezing injected into the dark port of the interferometer. The main parameters of the system that will concern us are the arm length L_{gw}, test mirror mass m_{gw}, cavity half-linewidth κ_{gw} and input power P_{gw}. Standard values for these parameters are given in Table 2.1 (with the exception of P_{gw}, the choice of which we will explain in the next section).

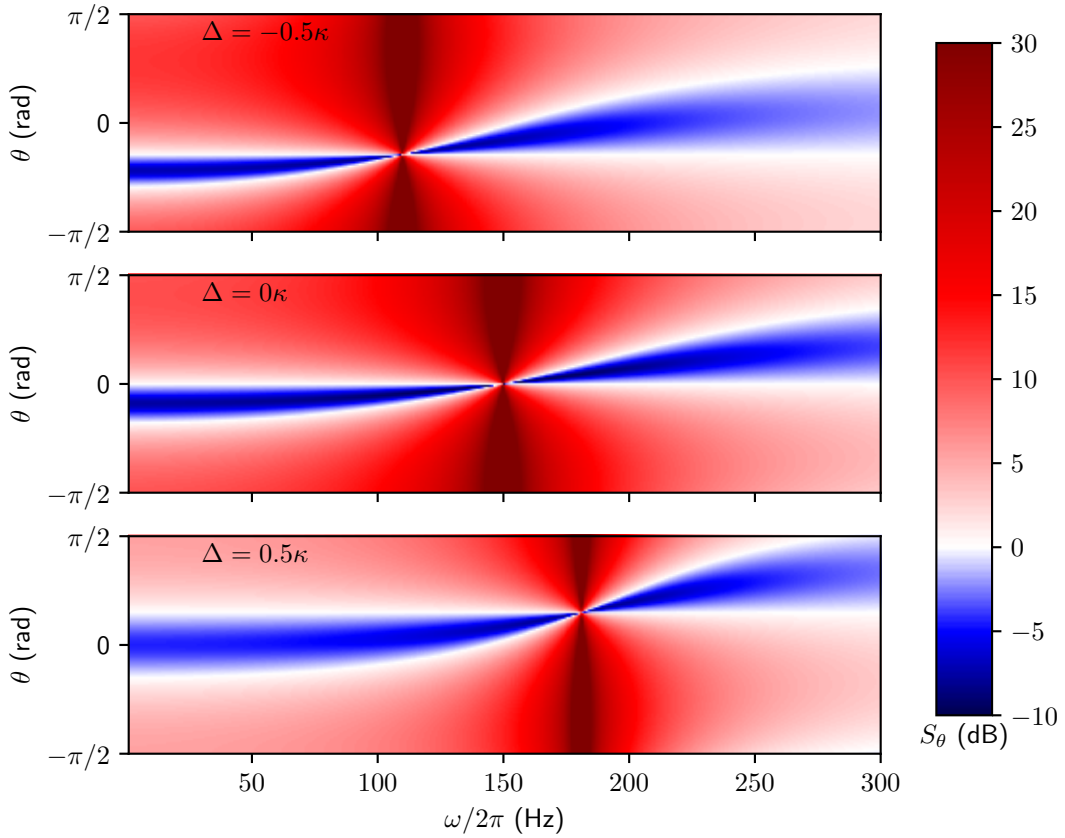

Figure 2.6: Quadrature spectrum $S_\theta(\omega)$ for all angles and specific detunings. Notice that there is significant anti-squeezing in the vicinity of the effective mechanical frequency.

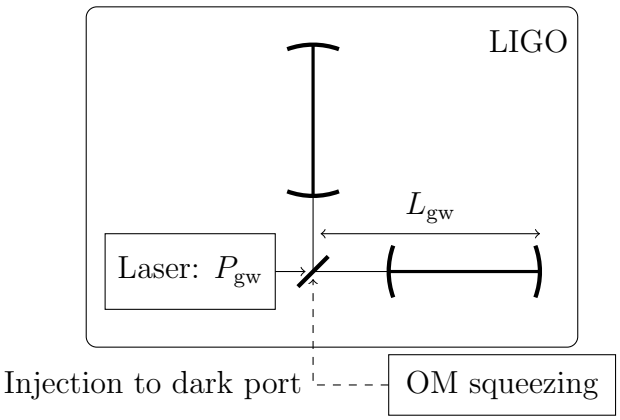

Figure 2.7: Proposed setup for LIGO with optomechanical squeezing. The output from the optomechanical system is injected into the dark port of the interferometer.

2.4.1 The standard quantum limit

As discussed in Section 2.1, the sensitivity of the current LIGO detectors is limited by quantum noise across much of the detection band. This limit arises from shot noise—which introduces fluctuations in the detected output field—at high frequencies, and from radiation pressure noise—which randomly drives the test masses—at low frequencies.

For each given frequency there is an optimal power at which the contributions from these two noise sources agree and their sum is minimised: further increasing the power increases the contribution of radiation pressure noise and increases the total noise, while decreasing the power increases the shot noise and also leads to an increase in total noise. This point is the standard quantum limit (SQL). To see more quantitatively how the limit arises, we note that the noise spectrum for the conventional LIGO interferometer when vacuum is injected into the dark port, assuming all non-quantum noise to be negligible, is[45]

$$S_{\mathrm{LIGO}}(\omega) = \frac{8\hbar}{L_{\mathrm{gw}}^2 m_{\mathrm{gw}} \omega^2} \times \frac{1}{2}\left(\frac{1}{\mathcal{K}(\omega)} + \mathcal{K}(\omega)\right), \tag{2.67}$$

where $\mathcal{K}$ is a coupling constant describing how input fluctuations are coupled to output fluctuations via the radiation pressure force and the test masses, given by

$$\mathcal{K}(\omega) := P_{\mathrm{gw}} \times \frac{4\omega_{\mathrm{opt}}}{L_{\mathrm{gw}}^2 m_{\mathrm{gw}} \kappa_{\mathrm{gw}}^4} \times \frac{2\kappa_{\mathrm{gw}}^4}{\omega^2(\kappa_{\mathrm{gw}}^2 + \omega^2)}. \tag{2.68}$$

Looking at the expression in parentheses of Eq. (2.67), the $\mathcal{K}$ term describes the contribution of radiation pressure noise (as the optomechanical coupling increases, the fluctuations in the light are more strongly imprinted onto the test mass motion), while the $1/\mathcal{K}$ term describes the shot noise (the signal increases with higher optomechanical coupling, and thus the effect of shot noise decreases[88]). If we fix all parameters except the input power P_{gw} then it is clear that the spectrum is minimised, and thus the SQL is attained, when we have $\mathcal{K}(\omega) = 1$. That is (defining $P_{\mathrm{SQL}}(\omega)$ to be the appropriate operating power), we have

$$P_{\mathrm{SQL}}(\omega) := \frac{L_{\mathrm{gw}}^2 m_{\mathrm{gw}} \kappa_{\mathrm{gw}}^4}{4\omega_{\mathrm{opt}}} \times \frac{\omega^2\left(\kappa_{\mathrm{gw}}^2 + \omega^2\right)}{2\kappa_{\mathrm{gw}}^4}, \tag{2.69}$$

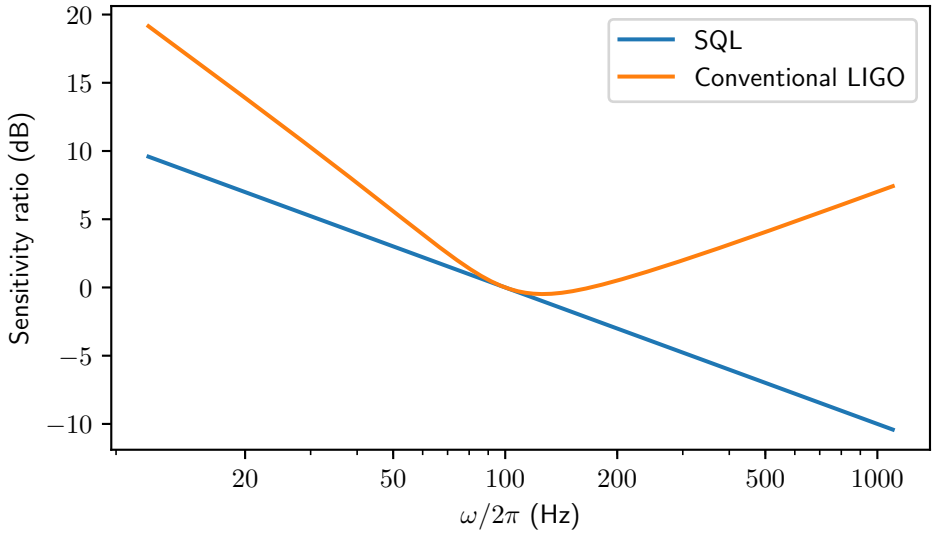

Figure 2.8: Sensitivity of conventional LIGO interferometer when configured to reach the SQL at the optimal detection frequency, compared to the full spectrum of the SQL. The sensitivity ratio is defined as the square root of the appropriate spectral density normalised to the square root of the spectral density at the optimal detection frequency ($S_{\mathrm{SQL}}(\kappa_{\mathrm{gw}})$).

and the spectrum of the SQL is then given by

$$S_{\mathrm{SQL}}(\omega) = S_{\mathrm{LIGO}}(\omega)\big|_{P_{\mathrm{gw}}=P_{\mathrm{SQL}}} = \frac{8\hbar}{L_{\mathrm{gw}}^2 m_{\mathrm{gw}}\omega^2}. \tag{2.70}$$

We will typically be interested in optimising the performance for signals in the vicinity of the linewidth κ_{gw}, which we refer to as the *optimal detection frequency* ($\kappa_{\mathrm{gw}} = 2\pi \times 100\,\mathrm{Hz}$ for LIGO), so we henceforth assume P_{gw} to be the operating power required to reach the SQL at this point:

$$P_{\mathrm{gw}} = P_{\mathrm{SQL}}(\kappa_{\mathrm{gw}}) = \frac{L_{\mathrm{gw}}^2 m_{\mathrm{gw}} \kappa_{\mathrm{gw}}^4}{4\omega_{\mathrm{opt}}}. \tag{2.71}$$

For the parameters given in Table 2.1 we have $P_{\mathrm{gw}} \approx 1.4\,\mathrm{kW}$. The sensitivity of the conventional LIGO setup, given these parameters, is shown in Fig. 2.8.

2.4.2 LIGO spectrum for arbitrary input

We have seen the LIGO noise spectrum when unsqueezed vacuum is injected, but to determine the effect of injecting optomechanically-squeezed light we must

calculate the spectrum $S^b_{\rm LIGO}$ for an arbitrary input field $\delta\hat{b} \equiv \delta\hat{b}(\omega)$. Defining the quadratures $\hat{Y}_\theta$ of the input field as in Eq. (2.60), the raw quantum noise in the LIGO measurement is given by[45]

$$h(\omega) := \sqrt{\frac{S_{\rm SQL}(\omega)}{2\mathcal{K}(\omega)}} e^{i\beta(\omega)} \left(\hat{Y}_{\pi/2}(\omega) - \mathcal{K}(\omega)\hat{Y}_0(\omega) \right), \tag{2.72}$$

where $\beta(\omega) := \arctan(\omega/\kappa_{\rm gw})$.

Defining $\Phi(\omega) := -\operatorname{arccot}(\mathcal{K}(\omega))$, and noting that $\mathcal{K}(\omega) > 0$ and thus $\Phi(\omega) \in (-\pi/2, 0)$, we have

$$1 = -\sqrt{1+\mathcal{K}(\omega)^2}\sin\Phi(\omega), \qquad \mathcal{K}(\omega) = \sqrt{1+\mathcal{K}(\omega)^2}\cos\Phi(\omega), \tag{2.73}$$

so we can write

$$\begin{aligned}
\hat{Y}_{\pi/2}(\omega) - \mathcal{K}(\omega)\hat{Y}_0(\omega) &= \sqrt{1+\mathcal{K}(\omega)^2}\left(-\sin\Phi(\omega)\hat{Y}_{\pi/2}(\omega) - \cos\Phi(\omega)\hat{Y}_0(\omega) \right) \\
&= \sqrt{1+\mathcal{K}(\omega)^2}\Big((-\cos\Phi(\omega) + i\sin\Phi(\omega))\,\delta\hat{b} \\
&\qquad + (-\cos\Phi(\omega) - i\sin\Phi(\omega))\,\delta\hat{b}^\dagger \Big) \\
&= -\sqrt{1+\mathcal{K}(\omega)^2}\hat{Y}_{\Phi(\omega)}(\omega),
\end{aligned} \tag{2.74}$$

and thus

$$h(\omega) = -\sqrt{S_{\rm SQL}(\omega)}\sqrt{\frac{1+\mathcal{K}(\omega)^2}{2\mathcal{K}(\omega)}} e^{i\beta(\omega)} \hat{Y}_{\Phi(\omega)}(\omega). \tag{2.75}$$

Let $S^b_\theta(\omega)$ denote the spectral density of the θ quadrature of the input field $\delta\hat{b}$ (as in Eq. (2.61)). Using the fact that $S_{\rm SQL}$, $\mathcal{K}$ and Φ are even functions of ω, and β is an odd function, we can thus write the noise spectrum for LIGO with input $\delta\hat{b}$ as simply

$$\begin{aligned}
S^b_{\rm LIGO}(\omega) &= S_{\rm SQL}(\omega) \times \frac{1}{2}\left(\frac{1}{\mathcal{K}(\omega)} + \mathcal{K}(\omega) \right) S^b_{\Phi(\omega)}(\omega) \\
&= S_{\rm LIGO}(\omega) S^b_{\Phi(\omega)}(\omega).
\end{aligned} \tag{2.76}$$

Therefore we can think of the effect of LIGO as simply reading out the Φ quadrature of the input field and then scaling by $S_{\rm LIGO}$. With this in mind we refer to Φ as the *readout angle* (although note that in reality a fixed-phase homodyne

detection is performed, and it is the Φ quadrature of the input field that contributes to the noise in that measurement because of the nature of the squeezing performed by the arm cavities[45]).

We see that to minimise the noise at a certain frequency ω_0 the input field must be squeezed along the $\Phi(\omega_0)$ quadrature. If the squeezed quadrature is frequency-independent there will also be an improvement at nearby frequencies, but further away from ω_0 there will be an increase in noise due to anti-squeezing. If the squeezed quadrature rotates with frequency, and in particular varies exactly with $\Phi(\omega)$, then broadband improvement is possible.

Interestingly, if the squeezing angle is perfect then the LIGO sensitivity will not be affected by the orthogonal quadrature at all, regardless of how much anti-squeezing occurs. On the other hand, if the angle has even a slight deviation then the anti-squeezing does contribute to the noise—in fact, for any deviation from the optimum angle there will be an ideal squeezing factor beyond which the noise actually increases due to the excess noise from anti-squeezing overcoming the reduction due to the squeezing.

2.4.3 Comparison of LIGO performance for different input fields

We are now in a position to compare the performance of LIGO with different input fields. We consider unsqueezed vacuum, fixed angle squeezing, optomechanical squeezing, and, for reference, ideal squeezing with perfect quadrature rotation.

With Eq. (2.76) in hand it is simple to determine the spectra in each of these cases. Light squeezed by a factor of e^{-2r} at angle ν has spectral density[83]

$$S_{\mathrm{sqz}}(\omega) = e^{2r}\sin^2(\Phi(\omega)-\nu) + e^{-2r}\cos^2\left(\Phi(\omega)-\nu\right), \tag{2.77}$$

which is easily simplified to

$$S_{\mathrm{sqz}}(\omega) = \cosh 2r - \cos\left[2(\nu-\Phi(\omega))\right]\sinh 2r. \tag{2.78}$$

Therefore for fixed angle squeezing the LIGO spectral density becomes

$$S^{\mathrm{fixed}}_{\mathrm{LIGO}}(\omega) = S_{\mathrm{LIGO}}(\omega)\left(\cosh 2r - \cos\left[2(\nu-\Phi(\omega))\right]\sinh 2r\right). \tag{2.79}$$

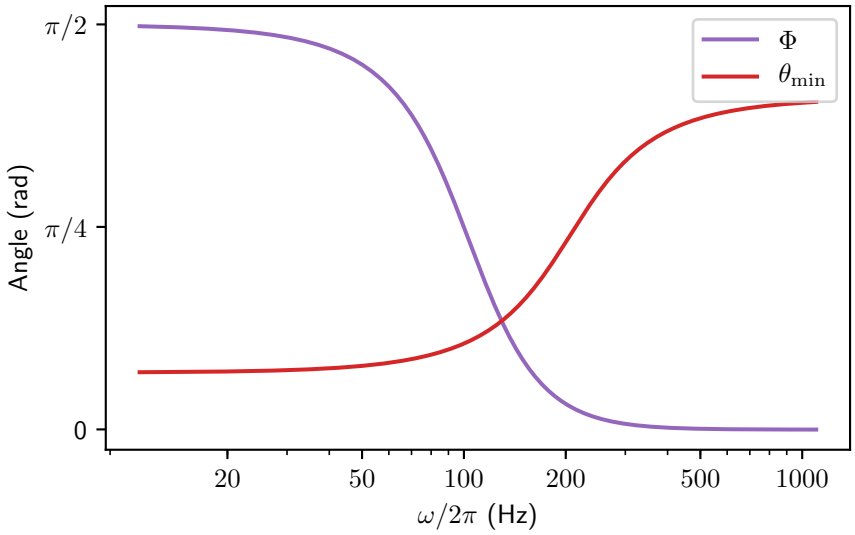

Figure 2.9: Comparison of optomechanical squeezing angle $\theta_{\min}$ and LIGO readout angle Φ, for zero detuning $\Delta = 0$. Note that we have applied constant offsets to Φ and $\theta_{\min}$, and restricted all angles to $[-\pi/2, \pi/2)$.

Similarly, when light with squeezing factor e^{-2r} and ideal squeezing angle $\Phi(\omega)$ is used we simply have

$$S_{\text{LIGO}}^{\text{ideal}}(\omega) = S_{\text{LIGO}}(\omega)e^{-2r}, \tag{2.80}$$

while for optomechanically-squeezed light we have

$$S_{\text{LIGO}}^{\text{OM}}(\omega) = S_{\text{LIGO}}(\omega)S_{\Phi(\omega)}(\omega), \tag{2.81}$$

with S_θ as defined in Eq. (2.62).

It is clear that the performance of optomechanical squeezing will depend heavily on how well the squeezed angle $\theta_{\min}(\omega)$ matches the LIGO readout angle $\Phi(\omega)$. These quantities are compared in Fig. 2.9. We notice that the angles vary in opposite directions, suggesting we will not be able to achieve a sensitivity enhancement across the full detection band using optomechanics without further filtering (this was also recognised in footnote 15 of Kimble et al.[45]). This fact is not surprising. The cavities of LIGO are themselves optomechanical systems and thus cause a frequency-dependent squeeze of the input field. The point of injecting squeezed light is to partially *counteract* this effect in order maintain a consistently-squeezed output field. However, we would expect the squeezing

generated by an auxiliary optomechanical system to exhibit the *same* frequency dependence as that generated by the interferometer arms, since they are both due to the same fundamental physical mechanisms. Despite this drawback, since both angles vary by roughly $\pi/2$ their initial and final angles can be made roughly similar (modulo π), so improvement on either side of the mechanical frequency should be possible.

The expected performance of LIGO with different input fields is compared in Fig. 2.10. As expected, squeezing with perfect quadrature rotation yields an enhancement in sensitivity across the spectrum. With fixed angle squeezing, improvement is restricted to a particular part of the spectrum (depending on the angle), with a decrease in sensitivity elsewhere. This corresponds to minimising low-frequency radiation pressure noise by utilising amplitude squeezing ($\nu = 0$) through to minimising high-frequency shot noise by using phase squeezing ($\nu = \pi/2$).

With optomechanical squeezing the situation is less straightforward. We see that, as expected, the opposite quadrature rotation around the mechanical frequency combined with the strong anti-squeezing in this area precludes sensitivity enhancement across the full band and in particular near the mechanical frequency. However, on both sides of this band improvement is possible. Generally speaking, detuning the cavity further from $\Delta = 0$ reduces the total amount of squeezing available, but shifts the effective mechanical frequency (depending on the sign of the detuning) and increases the rate and magnitude of quadrature rotation, which has the effect of reducing the width of the band in which sensitivity is reduced and potentially improving performance at either side of the band.

Indeed, looking at the plots for $\Delta = \pm 0.5\kappa$ we see that, unlike with fixed angle squeezing, optomechanical squeezing allows the sensitivity to be improved at either high or low frequencies without a significant reduction at the other end of the spectrum (in fact it is possible to choose the phase offset to achieve enhancement over conventional LIGO at both ends of the spectrum, but the enhancement factor is quite small). To achieve this we must choose the phase offset of the optomechanical squeezing so that $\theta_{\min}$ (roughly) matches Φ at both ends of the spectrum, as shown in the insets. However, as discussed above this necessarily means that the angles must disagree in the middle of the spectrum, and when combined with the high anti-squeezing this leads to a large decrease in sensitivity.

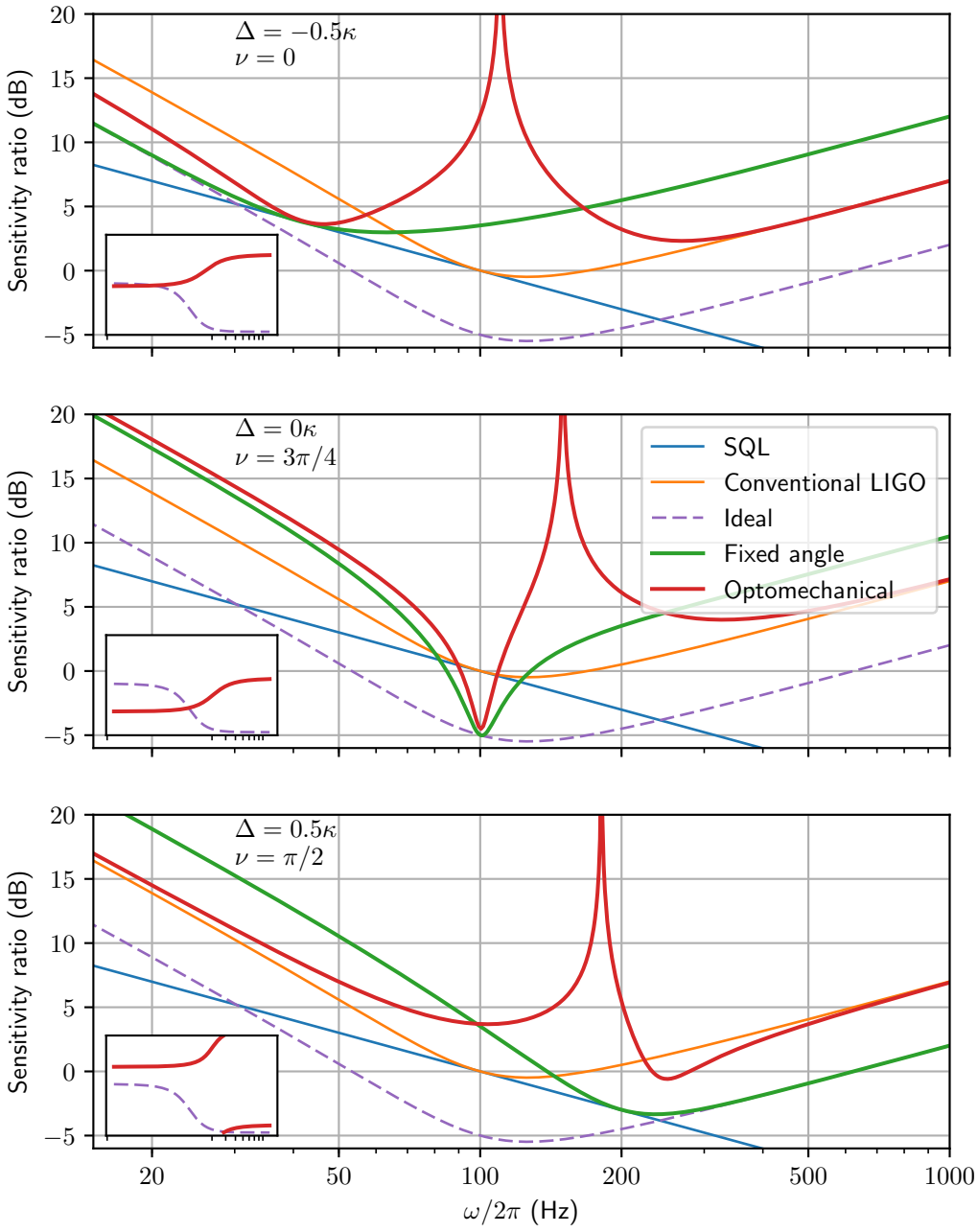

Figure 2.10: Comparison of LIGO performance for different input fields. For each detuning Δ we have chosen a certain phase offset to give good performance in some part of the spectrum, and then chosen an angle ν for the fixed angle source to give an advantage in the same area. The squeeze factor r for ideal and fixed angle squeezing is chosen so that $e^{-2r} = 0.1$. The insets show how the offset optomechanical squeezing angle and LIGO readout angle (restricted to $[-\pi/2, \pi/2)$) vary with frequency.

Alternatively, if we require particularly high sensitivity at a certain area and performance elsewhere is less important, we may use zero detuning and choose the phase offset to match $\theta_{\min}$ with Φ at the point of desired maximum sensitivity (as shown in the $\Delta = 0$ plot). This achieves an improvement comparable to that of fixed angle squeezing, but the improvement drops off more quickly due to the quadrature rotation exposing the system to anti-squeezing. However, in this case we observe that at the high end of the spectrum the phases partially re-align and the squeezing factor (and hence anti-squeezing factor) reduces, leading to a smaller sensitivity reduction than with fixed angle squeezing.

This observation highlights an aspect of optomechanical squeezing that could prove advantageous over fixed-angle squeezing, namely the frequency dependence of the squeezing factor. Once we move far enough away from the mechanical frequency the amount of squeezing becomes low, meaning the negative effect of a suboptimal squeezing angle is reduced and the performance converges to that of conventional LIGO. However, it is not clear whether this would be beneficial in practice, since significant sensitivity must still be sacrificed near the optimal detection frequency.

2.5 Conclusion

We have derived expressions describing the output field of an idealised optomechanical system. Using these we have shown that the squeezing induced by the optomechanical interaction could potentially have applications in gravitational wave detectors (and interferometers in general), although whether or not a net advantage can be gained is unclear.

In particular, we have focused on the frequency-dependent squeezing factor and angle of optomechanical squeezing, and found that the angle varies in the opposite direction to that required by gravitational wave detectors. Combined with the high anti-squeezing that occurs near the mechanical frequency, this almost invariably leads to a reduction in sensitivity in a band near the mechanical frequency. Despite this, we have demonstrated that there could still be an advantage over fixed angle squeezing, which is that sensitivity can be simultaneously improved (or at least not reduced) at several distinct parts of the spectrum, with only the performance in the aforementioned band reduced. These properties could potentially make optomechanical squeezing suitable for certain modes of

operation of gravitational wave detectors if a narrow band in which high noise is acceptable can be identified.

We note that while we believe this scheme is within current state-of-the-art systems, it would still entail significant technical challenges; for instance, the strict thermal requirements necessary to avoid washing out the squeezing with noise could prove challenging to meet.

To conclude, while in theory optomechanical squeezing could prove beneficial for certain unusual modes of operation of gravitational wave detectors, it appears to be unsuitable as a comprehensive, general-purpose approach to interferometric sensitivity enhancement.

Chapter 3

Synthesis of custom optical spring potentials

In this chapter we present a scheme for synthesising custom optical spring potentials in cavity optomechanical systems. This is a general method, applicable to any optomechanical system based on linear cavities, that could be used to optimise performance or even explore new parameter regimes. To demonstrate the utility of the scheme we show how it could be used to significantly enhance the sensitivity of a proposed optomechanical gravitational sensor.

In Section 3.1 we provide background on levitated optomechanics and the optical spring effect, with a focus on applications in metrology. In Section 3.2 we develop our scheme for synthesising custom optical spring potentials in cavity optomechanical systems. As a concrete example of an application of this technique, in Section 3.3 we consider a gravitational sensor based on an optomechanical levitation system and show how the sensitivity can be enhanced. We give some concluding remarks, with an outlook towards related future work, in Section 3.4.

The work presented in this chapter was published as:

> H. J. Slatyer, G. Guccione, Y.-W. Cho, B. C. Buchler, and P. K. Lam, "Synthesis of optical spring potentials in optomechanical systems", Journal of Physics B: Atomic, Molecular and Optical Physics **49**, 125401 (2016)

All stages of the research described in this chapter were performed in close collaboration between myself and Giovanni Guccione.

3.1 Background

Optomechanics is fast becoming established as a powerful, flexible and practical tool in quantum physics. We have already seen in Chapter 2 that the two-way interaction between optical and mechanical resonators lies at the heart of gravitational wave detectors, and that this interaction can be used to generate non-classical states of light. In terms of sensing and metrology, the applications are far broader than gravitational wave detection; cavity optomechanical systems have also been used for displacement[90], force[91, 92], mass[93, 94] and magnetic field[95–97] sensing, for example. There are also applications in quantum information and communication technologies, including single photon generation[98, 99], quantum information processing[100] and quantum memories[101–103]. In a different vein, optomechanical systems have been proposed as a means of testing the fundamentals of quantum mechanics. For instance, it has been predicted that signatures of semiclassical gravity[104] and spontaneous wave-function collapse[105] could be observed in such systems.

The optomechanical interaction is not confined to the textbook example of a linear cavity with a spring-mounted end mirror. In addition there are a wide variety of less conventional systems exhibiting the same fundamental phenomena, such as picogram-scale photonic crystal "zipper" cavities[106], micro-toroids supporting whispering gallery modes[107, 108] and microwave cavities containing superfluid helium[109], to name a few. A particularly promising class of optomechanical systems involves optically-levitated mechanical oscillators[110–113], since the near-complete isolation from the environment can result in extremely low mechanical dissipation rates.

A Gaussian beam incident on a micron-scale dielectric particle tends to trap the particle; opposite sides of the particle refract light of different intensities, and this force differential drives the particle towards the region of highest optical intensity[114, 115]. This can be used for levitation[116] and is also the basis of optical tweezers, which have become an important tool for micro- and nano-scale manipulation[117, 118]. Recent work has also explored the optomechanical properties of particles in such traps[119, 120]. The optical potential experienced by the trapped particle can be tuned by shaping the transverse mode of the levitating lasers[121], or using an optical cavity[111, 122] to modify the longitudinal mode of the light. Ultimately, however, the performance of these systems in cooling

and sensing applications will be limited by the incoherent scattering of light that is inherent to their operation.

An alternative approach to levitation, which eliminates incoherent scattering, is to levitate the end mirror of a high-finesse optical cavity[123, 124]. In this case the mechanical resonator is coupled to the environment only via background gas collisions and the coherent interaction with the optical field, which leads to extremely low damping rates. For example, the system of Guccione et al.[124] is predicted to exhibit a quality factor on the order of 10^{10} when operated at high vacuum.

A further feature of these systems is that the behaviour of the mechanical oscillator is determined almost entirely by the so-called optical spring effect[125–127]. When the input field is blue-detuned from the cavity resonance, a decrease in cavity length due to motion of the mechanical resonator induces an increase in intra-cavity power, which increases the radiation pressure on the resonator and thus leads to a restoring force. Motion from the equilibrium position causing an increase in cavity length induces the opposite effect. This optical restoring force can be interpreted as a shift in the effective mechanical spring constant, hence the term "optical spring".

The optical spring effect enables precise control of the optical potential experienced by the resonator, which in turn enables tuneability of the mechanical properties of its oscillation[128]. Although this control is possible, however, there is little flexibility; a high-finesse cavity invariably leads to a very stiff spring constant, which may not always be the desired outcome. For example, in a sensing application where the position of a levitated mirror is used to measure some force, a large mechanical response is required to maximise the signal. Ideally, therefore, one desires an optical spring of lower stiffness, while still using a high-finesse cavity to maintain optimum interferometric sensitivity of the position readout. As another example, an alternative use of the optical spring effect for sensing purposes is to transduce a small shift in optical cavity resonance frequency (resulting, for example, from the binding of a single molecule to the optical resonator) as a shift in mechanical resonance frequency, and then measure that shift[129]. If the mechanical frequency depends sensitively on the optical resonance frequency (or, equivalently, the mechanical displacement) then this transduction significantly improves the detection sensitivity. Therefore, in this case, the ideal mechanical potential exhibits a mechanical spring constant that varies significantly with even

small changes in displacement.

Phrasing these requirements more generally, the performances of optomechanical systems could be improved by customising the optical spring potentials experienced by the mechanical oscillators in an application-specific manner, and achieving this without compromising the properties of the optical resonators.

In 2007 it was suggested[130] that certain potentials could be engineered all-optically via an optomechanical system consisting of two coupled micro-ring resonators. By detuning the input laser, or even by injecting an additional laser, the potential experienced by one of the resonators may be engineered in certain non-trivial ways. It was later shown that generalising this approach, to engineer other kinds of potentials by utilising the extra degrees of freedom made available by more general polychromatic light sources, is feasible[131].

In this chapter we extend this work by presenting an explicit scheme for determining exactly which polychromatic light sources are necessary to generate approximations of arbitrary optical spring potentials. We then demonstrate how the scheme could be used to improve the sensitivity of a levitation-based gravitational sensor.

3.2 Synthesis of optical spring potentials

In this section we present our general method for improving flexibility and performance in cavity-based optomechanical systems by showing how customised force functions (and hence also customised potentials) may be approximately realised by injecting suitable input fields. The general idea is to use the standard Lorentzian peak of an optical cavity in the presence of a single mode as a building block, and combine several such modes in order to sculpt suitable force profiles. The ideal required input fields may be difficult or impossible to generate in practice, since they require detailed shaping of broadband pulses, so we also show that approximation via suitable frequency comb inputs is possible.

In Section 3.2.1 we review the physics behind the optomechanical force from a conventional single input. Before extending these principles to multiple inputs we consider the implications of interference terms in Section 3.2.2, which will allow us to assume a superposition principle whereby multiple input fields do not interact with each other. With this principle in place we may then proceed in Section 3.2.3 to describe how to determine the input field required to synthesise a

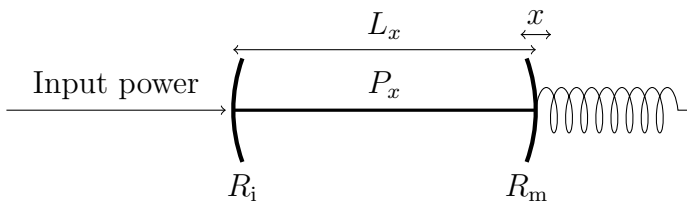

Figure 3.1: Basic optomechanical system. The left-hand cavity mirror is fixed, while the right-hand mirror is moveable and lies in a harmonic potential. The reflectivities of the mirrors are R_i and R_m respectively, the displacement of the moveable mirror from the equilibrium position is x, the cavity length corresponding to that displacement is L_x, and the power circulating in the cavity is P_x.

desired arbitrary force profile. In Section 3.2.4 we explain how these input fields may be approximated by frequency comb inputs.

3.2.1 Force from a single frequency

We first derive the force experienced by the end mirror in a standard optical cavity as a function of its position and the frequency of the input mode, which will form the basis of the main analysis. Unlike in Chapter 2, where the focus was on the effect of the optomechanical interaction on the output field, here we are concerned only with the optical force applied to the mechanical resonator.

We consider the standard simple linear cavity with a moveable end mirror, as shown in Fig. 3.1. Let the reflectivities of the fixed input mirror and moveable end mirror be R_i and R_m respectively, and let $L_x := L_0 + x$ denote the length of the cavity for a displacement x of the moveable mirror from its mean position.[1] Let the laser frequency be $\omega_\delta := \omega_0 + \delta$, where δ is the detuning from an equilibrium cavity resonance frequency ω_0. The laser wavelength is then given by $\lambda_\delta = \frac{2\pi c}{\omega_\delta}$ (and note that L_0 is a multiple of $\lambda_0/2$, since the cavity is on resonance when there is no detuning and no displacement).

From standard arguments (see Siegman[132], for example) the power circu-

[1] Note that throughout this chapter we often use a subscript variable to denote a function of that variable, with the interpretation that we are interested in the behaviour of the function even when that variable is fixed. For example, L_x is a function of x, but often we are interested in only the value of L_x for certain fixed values of x (for instance L_0).

lating in the cavity per unit input power, $P_x(\delta)$, is

$$P_x(\delta) = \frac{1 - R_\mathrm{i}}{1 + R_\mathrm{i}R_\mathrm{m} - 2\sqrt{R_\mathrm{i}R_\mathrm{m}}\cos\left(2\pi\frac{L_x}{\lambda_\delta/2}\right)}. \tag{3.1}$$

We may expand the argument of the cosine term to

$$2\pi\frac{L_x}{\lambda_\delta/2} = 2\pi\frac{L_0}{\lambda_0/2} + 2\pi\frac{x}{\lambda_0/2} + 2\frac{L_0\delta}{c} + 2\frac{x\delta}{c}. \tag{3.2}$$

Since L_0 is a multiple of $\lambda_0/2$ the first term may be removed. Next we assume that the dynamics are restricted to a small area within the cavity free spectral range $\omega_\mathrm{FSR} := \frac{\pi c}{L_0}$, which implies that $|x| \ll \lambda_0/2$ and $|x\delta| \ll L_0\,|\delta| \ll c$. The last term is thus negligible and the middle two are small. We may therefore apply the small angle approximation, and the cosine can be approximated as

$$\begin{aligned}
\cos\left(2\pi\frac{L_x}{\lambda_\delta/2}\right) &\approx 1 - \frac{1}{2}\left(2\pi\frac{x}{\lambda_0/2} + 2\frac{L_0\delta}{c}\right)^2 \\
&= 1 - \frac{1}{2}\frac{4\pi^2}{\omega_\mathrm{FSR}^2}\left(\frac{x\omega_\mathrm{FSR}}{\lambda_0/2} + \delta\right)^2 \\
&= 1 - \frac{1}{2}\frac{4\pi^2}{\omega_\mathrm{FSR}^2}\left(\delta + G_0 x\right)^2,
\end{aligned} \tag{3.3}$$

where we have introduced the optomechanical coupling strength

$$G_0 := \frac{2\omega_\mathrm{FSR}}{\lambda_0} = \frac{\omega_0}{L_0} \tag{3.4}$$

which, as discussed in Chapter 2, converts a displacement of the mirror into a shift in cavity resonance frequency. From this we define $\delta_x := \delta + G_0 x$, which is the detuning of the laser frequency ω_δ from the shifted cavity resonance frequency. The intra-cavity power (per unit input power) can now be written as

$$P_x(\delta) = \frac{1 - R_\mathrm{i}}{\left(1 - \sqrt{R_\mathrm{i}R_\mathrm{m}}\right)^2 + \sqrt{R_\mathrm{i}R_\mathrm{m}}\frac{4\pi^2}{\omega_\mathrm{FSR}^2}\delta_x^2}. \tag{3.5}$$

The half-linewidth κ of the cavity, defined so that $P_0(\kappa) = P_0(0)/2$, is given by

$$\kappa = \frac{1 - \sqrt{R_\mathrm{i}R_\mathrm{m}}}{2\pi\sqrt[4]{R_\mathrm{i}R_\mathrm{m}}}\omega_\mathrm{FSR} = \frac{\omega_\mathrm{FSR}}{2\mathcal{F}}, \tag{3.6}$$

where $\mathcal{F}$ is the cavity finesse. Substituting into the expression for $P_x(\delta)$ we have

$$P_x(\delta) = \frac{1 - R_\mathrm{i}}{\left(1 - \sqrt{R_\mathrm{i} R_\mathrm{m}}\right)^2} \frac{\kappa^2}{\kappa^2 + \delta_x^2}. \tag{3.7}$$

The radiation pressure force $F_x(\delta)$ on the end mirror, per unit input power, is therefore

$$\begin{aligned} F_x(\delta) &= \frac{1 + R_\mathrm{m}}{c} P_x(\delta) \\ &\approx \frac{2}{c} \frac{1 - R_\mathrm{i}}{\left(1 - \sqrt{R_\mathrm{i} R_\mathrm{m}}\right)^2} \frac{\kappa^2}{\kappa^2 + \delta_x^2}, \end{aligned} \tag{3.8}$$

where in the last line we have approximated $1 + R_\mathrm{m} \approx 2$, assuming the mirror reflectivity R_m to be close to unity as required for a cavity of reasonable finesse.

The optical spring effect can be seen from this expression. In particular, we notice that in the blue-detuned regime, where $\delta_x > 0$, if the position x increases then δ_x^2 also increases, leading to a reduction in force F_x and thus a tendency for x to reduce. Conversely, if the displacement decreases then the force will increase and push the mirror back towards its equilibrium position. Indeed, the spring constant for displacement x and detuning δ (measured, as usual, per unit input power) is given by

$$\begin{aligned} k_\mathrm{os} &= -\frac{dF_x(\delta)}{dx} \\ &= \frac{2}{c} \frac{1 - R_\mathrm{i}}{(1 - \sqrt{R_\mathrm{i} R_\mathrm{m}})^2} \frac{2 G_0 \delta_x \kappa^2}{(\kappa^2 + \delta_x^2)^2} \\ &= \frac{2 P_x(\delta)}{c} \frac{2 G_0 \delta_x}{\kappa^2 + \delta_x^2}. \end{aligned} \tag{3.9}$$

We note that a smaller linewidth κ, corresponding to a higher finesse cavity, yields a stiffer optical spring. As we will discuss in more detail in Section 3.3, this becomes problematic when we require a soft spring to increase the signal size but a high finesse to maximise precision of the position readout.

3.2.2 The interaction of multiple optical springs

The force profile described by Eq. (3.8) is valid only for a single-mode input. If multiple fields of different frequencies are injected into the cavity they will in-

terfere and cause a component of the intra-cavity power to beat. For example, if two fields are injected then the force experienced by the mirror will be equal to the sum of the forces it would have experienced had each field been used independently, plus a term oscillating at the beat frequency of the two fields. We will demonstrate how this beating term can be removed, and thus how we may assume a superposition principle in which the force profile due to a polychromatic input field can be obtained by summing the forces due to each individual monochromatic field.

Let us consider the response of the mechanical resonator to the beating component of the field. In general, a resonator's response to an oscillating signal is a time-delayed oscillation at that frequency, with the magnitude of the oscillation determined by the resonator's susceptibility at that frequency. In particular, a strong response occurs only in the vicinity (determined by the damping rate) of the resonator's natural frequency. Outside this band the magnitude of the response drops off with the square of the driving frequency. That is, the response of the resonator to the beating component of the field can be made arbitrarily small by increasing the beat frequency sufficiently.[2]

Next we observe that, due to the periodicity of Eq. (3.1), any given input field can be further detuned by a multiple of the free spectral range ω_{FSR} without affecting the response of the system to that individual field. However, if there is an additional field injected into the cavity then detuning one field by a multiple of ω_{FSR} will shift the beat frequency by ω_{FSR}. That is, frequency shifting particular components of a polychromatic input field by multiples of ω_{FSR} can effect an increase in beat frequencies without changing the response of the system to each field component in isolation. Combined with the previous observation—that a sufficiently high beat frequency has negligible effect on the system—this indicates the path towards removing the effect of beating: apply frequency shifts of input field components by ω_{FSR} until all beat frequencies are sufficiently large to be ignored.

We can define the scheme more precisely. Consider a frequency comb input field with spacing Δ between modes of the comb and total bandwidth small relative to the cavity free spectral range. Suppose that, as discussed above,

[2]In fact, for many applications it would not even be necessary to achieve a negligibly small oscillator response to the beating; as soon as the beat frequency became higher than other relevant frequencies the effect could simply be filtered away. Indeed, readout via an optical cavity would achieve this automatically for beat frequencies higher than the cavity linewidth.

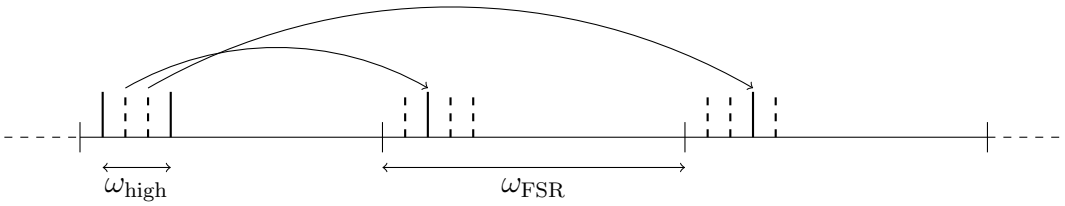

Figure 3.2: Illustration of frequency shifting to remove relevant interference effects. A comb with four modes is shown, with the second and third modes shifted to adjacent free spectral ranges to ensure that the separation between any pair of modes is at least ω_{high}.

beat frequencies higher than some ω_{high} can be ignored (either due to their small effect on the mechanical response or because they can be filtered away). For simplicity we also assume that $\omega_{\text{FSR}} > \omega_{\text{high}}$—a reasonable assumption given that for $L_0 = 5\,\text{cm}$ we have $\omega_{\text{FSR}} \approx 20\,\text{GHz}$, which is far larger than any likely mechanical frequency for a macroscopic resonator—although this is not necessary, since if it does not hold then we simply shift each mode by a higher multiple of ω_{FSR}.

With these assumptions we proceed as follows. We identify a sufficiently large integer N such that $N\Delta > \omega_{\text{high}}$, and then shift the nth mode of the comb by (n modulo N) multiples of ω_{FSR}. In this way we spread the modes of the comb between N separate free spectral ranges, so that all modes within a single free spectral range are separated sufficiently to have negligible beating. An illustration of this procedure is shown in Fig. 3.2.

To reiterate, given any frequency comb input, we can perform frequency shifting so that interference effects become negligible and the sum of the forces due to each individual mode gives a good approximation of the effective force experienced by the mirror. In other words, we can simply assume that for *any* frequency comb input field this superposition property holds, with the understanding that any necessary frequency shifting is included implicitly.

In theory this method extends to the case of general continuous power spectral density (PSD) input fields. In this case there is a continuum of modes that must be frequency-shifted, so we must divide the field into "slices" of width less than that of the bandwidth of the experiment, and then perform frequency shifting on these slices as above. The idea is that interference effects due to individual slices are too slow to affect the experiment on the appropriate timescales, while

the beating between slices is fast enough to be attenuated by the mechanical resonance. This scheme requires a fine degree of control over the input fields and is thus infeasible with current technologies, so in practice one would always use a comb input field. However, the use of arbitrary continuous PSD inputs is still a useful theoretical tool, since it allows us to argue in terms of integrals rather than sums, and also means we do not need to concern ourselves with choosing a suitable comb spacing in high-level discussions. Therefore we typically introduce our methods and results with reference to continuous PSD inputs under the assumption that no interference effects occur, and then explain how comb inputs provide a practical approximation to this ideal situation.

3.2.3 Approximation of an arbitrary force function

Suppose we desire a theoretical force function $F_{\mathrm{th}}(x)$. We wish to find the PSD $p(\delta)$ of an input laser that will cause the total radiation pressure force $F_{\mathrm{rp}}(x)$ experienced by the mirror to be as close to $F_{\mathrm{th}}(x)$ as possible. For convenience, we consider the PSD to be a function of the detuning from the central frequency ω_0, and we will assume that the PSD is localised within the particular free spectral range around ω_0. As mentioned in the previous section, we will also assume that no interference effects occur between the different frequency components of the input field. Under these assumptions the force on the end mirror due to the input field $p(\delta)$ is

$$F_{\mathrm{rp}}(x) = \int_{-\infty}^{\infty} F_x(\delta) p(\delta)\, d\delta, \tag{3.10}$$

which can be written

$$\begin{aligned} F_{\mathrm{rp}}(x) &= \int_{-\infty}^{\infty} F_0(\delta + G_0 x) p(\delta)\, d\delta \\ &= (F_0 * p)(-G_0 x), \end{aligned} \tag{3.11}$$

where $F_0 * p$ is the convolution of the force at zero displacement (given by Eq. (3.8)) and the PSD. Our goal is therefore to choose $p(\delta)$ so that $F_{\mathrm{th}}(x) \approx F_{\mathrm{rp}}(x) = (F_0 * p)(-G_0 x)$.

One might hope that this could be achieved via Fourier transforming, since this would convert the convolution into a product which can be easily inverted.

However, we found that this does not work particularly well in practice because the equation most often does not have an exact solution.

Instead it is instructive to consider more qualitatively the action of the cavity. We first write the convolution in the equivalent form

$$F_{\mathrm{rp}}(x) = (F_0 * p)(-G_0 x) = (F_0/\beta * \beta p)(\delta)\big|_{\delta=-G_0 x}, \tag{3.12}$$

where

$$\beta := \int_{-\infty}^{\infty} F_0(\delta)\, d\delta = \frac{2\kappa}{c} \frac{1 - R_{\mathrm{i}}}{\left(1 - \sqrt{R_{\mathrm{i}} R_{\mathrm{m}}}\right)^2} \tag{3.13}$$

is a normalising factor. This expression suggests that we may view the action of the cavity as a transformation from the input field p into the radiation pressure force function F_{rp} as follows: first a scaling of the input field by β, then a smoothing by the normalised Lorentzian F_0/β, and then a change of variable $\delta \to x = -\delta/G_0$. The smoothing, which is analogous to a Gaussian blur, will blur out any features smaller than the linewidth of the cavity, but will preserve larger features. For example, in the standard case of a single-mode input we start with a single sharp Lorentzian peak and blur this out to the width of the cavity linewidth, yielding exactly the usual Lorentzian force profile.

With this interpretation in mind, it is clear that theoretical force functions with features smaller than the linewidth of the cavity cannot be well-approximated regardless of the input field, since any true force function output from the cavity cannot have such fine features. On the other hand, if the theoretical force function F_{th} has only larger features then it *can* be reliably approximated. More formally, the requirement is that the function be blurred by the normalised Lorentzian F_0/β without significant effect:

$$F_{\mathrm{th}}(-\delta/G_0) \approx (F_0/\beta * F_{\mathrm{th}}\big|_{x=-\delta/G_0})(\delta). \tag{3.14}$$

With the above assumption, we simply need to choose

$$p(\delta) = F_{\mathrm{th}}(-\delta/G_0)/\beta \tag{3.15}$$

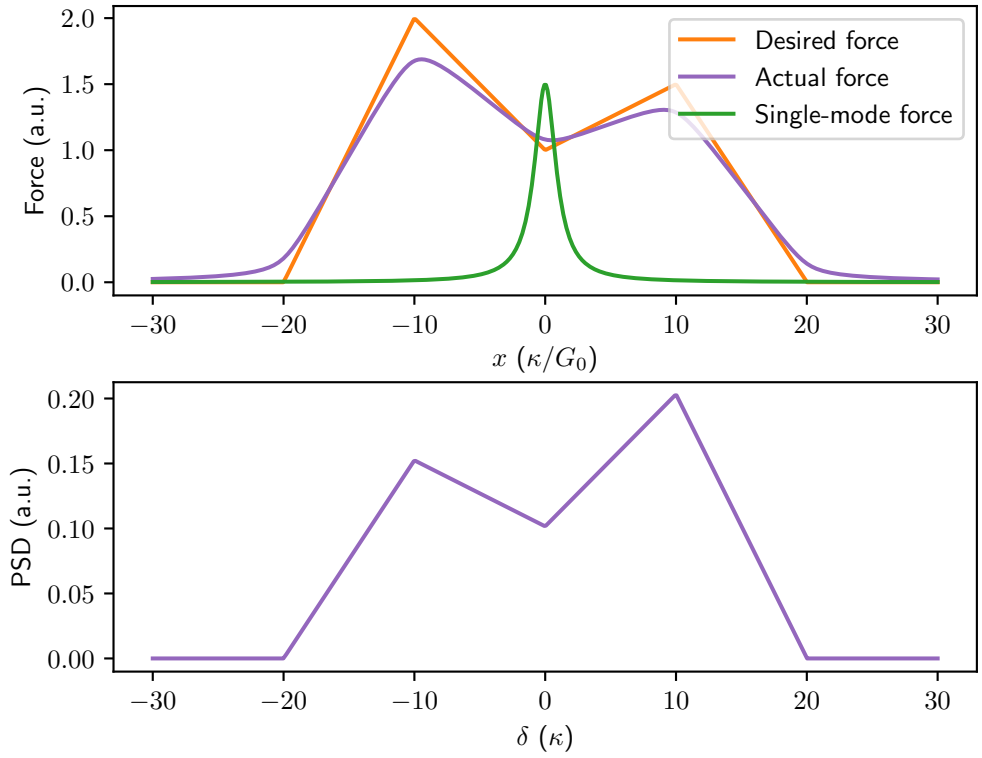

Figure 3.3: Comparison of a particular desired force function and the actual force function we would obtain using our method, with the PSD of the input field required to generate the actual force function. The force profile resulting from a single-mode input is shown for reference.

and then by Eq. (3.12) we have

$$\begin{aligned} F_{\mathrm{rp}}(x) &= (F_0/\beta * F_{\mathrm{th}}\big|_{x=-\delta/G_0})(\delta)\big|_{\delta=-G_0 x} \\ &\approx F_{\mathrm{th}}(-\delta/G_0)\big|_{\delta=-G_0 x} \\ &= F_{\mathrm{th}}(x). \end{aligned} \tag{3.16}$$

That is, choosing the input field according to Eq. (3.15) will cause the force experienced by the mirror to be approximately F_{th}, as required, and the resolution of this approximation is the linewidth of the cavity.

As an example, in Fig. 3.3 we plot a particular desired force function F_{th}, the actual force function we could achieve with the above method F_{rp}, and the required PSD. We see that the sharp features of the profile are blurred out, but the general shape is well approximated by the actual force function.

We stress again that this result hinges on the lack of interference effects between the different frequency components of the input field, which is impractical to achieve in general. We resolve this issue in the next section.

3.2.4 Practical considerations

In this section, we show that the use of a frequency comb centred at ω_0 with some given spacing Δ can be used instead of a continuous PSD input to achieve the required approximation. Applying the appropriate rectangle approximation to Eq. (3.10) we have

$$\begin{aligned} F_{\mathrm{rp}}(x) &= \int_{-\infty}^{\infty} F_x(\delta) p(\delta)\, d\delta \\ &\approx \sum_{n\in\mathbb{Z}} F_x(n\Delta) p(n\Delta)\Delta, \end{aligned} \tag{3.17}$$

and choosing the PSD according to Eq. (3.15) yields

$$F_{\mathrm{rp}}(x) = \sum_{n\in\mathbb{Z}} F_x(n\Delta) \frac{F_{\mathrm{th}}(-n\Delta/G_0)\Delta}{\beta}. \tag{3.18}$$

The right-hand side corresponds precisely to the force acting on the mirror if the input field is a frequency comb such that the component at frequency $\omega_0 + n\Delta$ has power $F_{\mathrm{th}}(-n\Delta/G_0)\Delta/\beta$, assuming interference effects are eliminated. As discussed in Section 3.2.2, this elimination can be performed by frequency shifting components of the comb by multiples of the free spectral range. It follows that a suitable frequency comb yields an approximation of F_{rp}, which is itself an approximation of the desired force function F_{th}. Note that, unsurprisingly, a smaller spacing Δ leads to a better approximation. The error tends to zero when $\Delta \ll \kappa$, since at this point $F_x(\delta)$ is well-approximated by its appropriate rectangle approximation.

For many types of force function the required frequency comb can be generated by modulation of a single mode. Specifically, the components of the comb can be realised as sidebands of the central frequency, with their power determined by the amplitude of the modulation. A combination of phase and amplitude modulation can be used to enforce any asymmetries in the required comb. The width of the comb (the maximum difference between the central frequency and a component

of the comb) determines the maximum modulation frequency necessary, and is thus the factor limiting the class of PSDs that can be approximated with a single modulator. Applying a sequence of modulators would allow wider combs to be created, at the expense of simplicity and flexibility. Alternatively, the modes of the frequency comb might be generated by commercial multi-channel laser systems, capable of independently tuning the central frequency of each channel by up to a few tens of terahertz.

3.3 Optimisation of an optomechanical gravitational sensor via synthesised potentials

In this section, we consider a particular optomechanical system and show how the techniques developed above could optimise its performance as a gravitational sensor.

3.3.1 A simple levitated optomechanics system for gravitational sensing

We consider a simplified version of the levitation system of Guccione et al.[124], where the top mirror of a single vertical cavity is supported by the radiation pressure from the intra-cavity field and constrained to move vertically (see Fig. 3.4). Variations in either the gravitational field or the mirror mass induce a shift in the mean mirror position, which can be probed very precisely via the reflected (or transmitted) optical field[133].

Levitation ensures complete mechanical isolation of the top mirror from the environment and allows the detection to be unaffected by many sources of external noise. The stability of the levitated system is due to the optical spring effect as described in Section 3.2.1 (also see Braginsky et al.[125], Sheard et al.[126] and Corbitt et al.[127]). With an input laser blue-detuned from resonance, a decrease in cavity length induces a rise in intra-cavity power. The additional radiation pressure will then push the mirror back towards equilibrium. Conversely, an increase in cavity length reduces the power and causes the radiation pressure force to drop, which causes the mirror to fall back towards equilibrium. Associated with the positive restoring force there is also negative damping that can induce

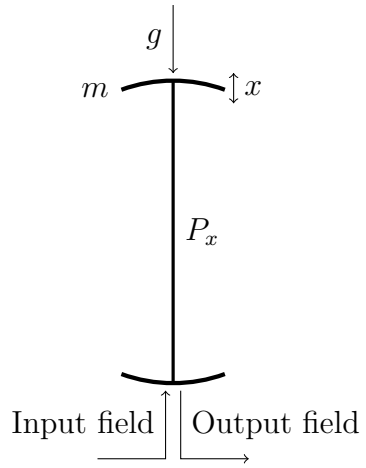

Figure 3.4: Schematic of the simplified levitation system. The top mirror is constrained to move vertically, and levitates via radiation pressure from the intracavity field with power P_x. Changes in the acceleration due to gravity g or mass m shift the mirror position x and are thus transduced to the phase of the output field.

parametric instability of the oscillator[134]. The instability can be eliminated with the addition of a second, red-detuned laser at much lower power[127].

For mechanically-clamped oscillators, the addition of an optical spring perturbs the original mechanical frequency and stiffness, and the effective spring constants produced can be extremely stiff. The levitated system we consider here is even more extreme, since in the absence of any rigid support the oscillation relies entirely on the optical spring, and the stiffness is determined entirely by the optical potential. This property makes the system a particularly illustrative and simple example to consider, but the methods we will apply for its analysis could easily be adapted to far more general systems.

Throughout this section we use the following fiducial system parameters: $\omega_{\mathrm{FSR}} = 2\pi \times 750\,\mathrm{MHz}$ (corresponding to $L_0 = 20\,\mathrm{cm}$), $\lambda_0 = 1064\,\mathrm{nm}$ and $R_{\mathrm{m}} = 99.99\%$. The finesse is adjusted by varying the reflectivity of the input mirror, R_{i}. We shall express forces in terms of the oscillator weight, which we denote $f_0 := mg$, input powers in terms of the minimum power required for levitation in the absence of any cavity, $p_0 := cf_0/2$, and spring constants in terms of $k_0 := 2f_0/\lambda_0$.

3.3.2 Sensitivity

As we have mentioned, the basic idea of the system is that a weight fluctuation induces a shift in mean mirror position, and this mirror position can be precisely read out optically. It is clear, then, that sensitivity can be increased if the same weight fluctuation can induce a larger change in position, and this is attained by having a smaller (softer) optical spring constant. We note that decreasing the spring constant also makes the system more susceptible to radiation pressure noise introduced by quantum amplitude fluctuations, but feedback and sensing methods[135] or injection of non-classical light (exactly as in Chapter 2) can push the measurement sensitivity beyond this limitation[135]. For the remainder of the chapter, therefore, we assume the sensitivity to be limited by the detection noise, rather than force noise affecting the mirror position. In the course of minimising the spring constant—and thus improving sensitivity—we must ensure that conditions for stable levitation still hold, since if the spring constant becomes too low then the mirror could fall out of the trap with even the slightest of fluctuations. Thus we consider only methods to reduce the spring constant that allow the trap threshold, defined to be the maximum weight supported (or equivalently the maximum value of the force function), to remain sufficiently large. We also generally look to maintain a constant spring stiffness, which is to say a linear force profile, in the vicinity of the trapping point.

The simplest way to lower the optical spring constant is to reduce the finesse of the cavity, but unless the input power is increased this causes a reduction in the trap threshold, as illustrated in Fig. 3.5. We see that at the equilibrium position, which is the point where the radiation pressure force F_{rp} matches the mirror weight $f_0 = mg$, the low-finesse cavity has a significantly softer spring constant. However, with a low-finesse cavity a higher input power is necessary in order to maintain a sufficiently deep trap.

Indeed, this tradeoff holds more generally. Appealing to geometric intuition it is clear that, regardless of the specific shape of the force function, maintaining the depth of the trap (that is, the maximum value of the force function) and linearity in the vicinity of the equilibrium position while reducing the spring constant (the slope of the force function) necessitates an increase in the physical length of the trap and thus in the integral of the force function. Moreover, we may verify that the integral of the force function is proportional to the total input power to the

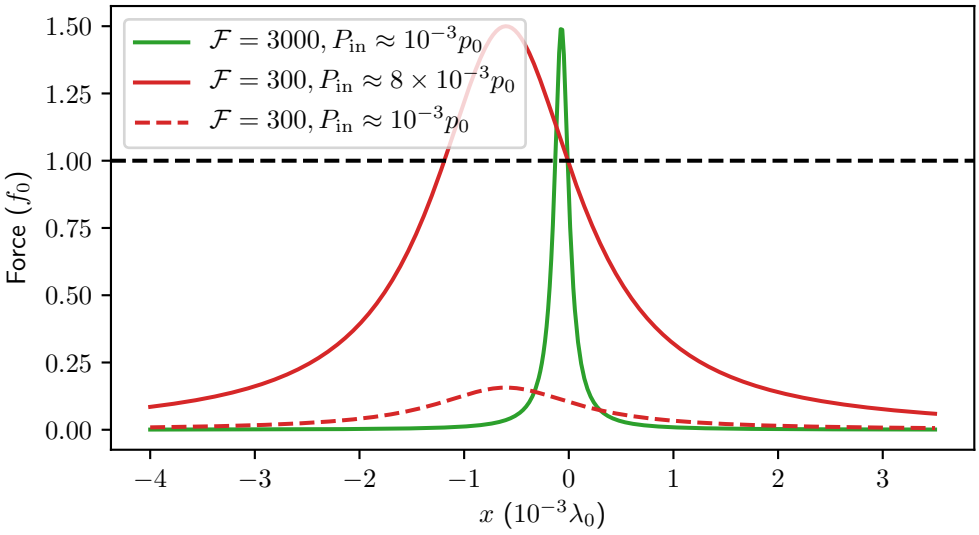

Figure 3.5: Comparison of force functions obtained with single-mode inputs in high (3000) and low (300) finesse cavities. P_{in} is the input power. The input fields have been detuned in order to shift the equilibrium position in the presence of gravity to $x = 0$.

cavity. Integrating both sides of Eq. (3.10) and switching the order of integration:

$$\begin{aligned}
\int_{-\infty}^{\infty} F_{\text{rp}}(x)dx &= \int_{-\infty}^{\infty}\int_{-\infty}^{\infty} F_x(\delta)p(\delta)d\delta\, dx \\
&= \int_{-\infty}^{\infty}\int_{-\infty}^{\infty} F_x(\delta)dx\, p(\delta)d\delta \\
&= \int_{-\infty}^{\infty}\int_{-\infty}^{\infty} F_0(\delta + G_0 x)dx\, p(\delta)d\delta \\
&= \frac{\beta}{G_0}\int_{-\infty}^{\infty} p(\delta)d\delta, \qquad (3.19)
\end{aligned}$$

which demonstrates the required relationship.[3] Note that integrating Eq. (3.17) and rearranging yields the same result. It follows that to reduce the spring constant without reducing the depth of the trap requires a higher input power. Put another way, for a given trap depth there is a tradeoff between reducing the spring constant to improve the sensitivity and keeping the input power low due to availability or to avoid damaging the optics.

[3]The "constant" of proportionality here is G_0/β, which actually depends on the cavity finesse, but it is readily verified that if the reflectivity of the moveable mirror is held constant at a value close to 1 then β is essentially constant for the relevant range of finesses.

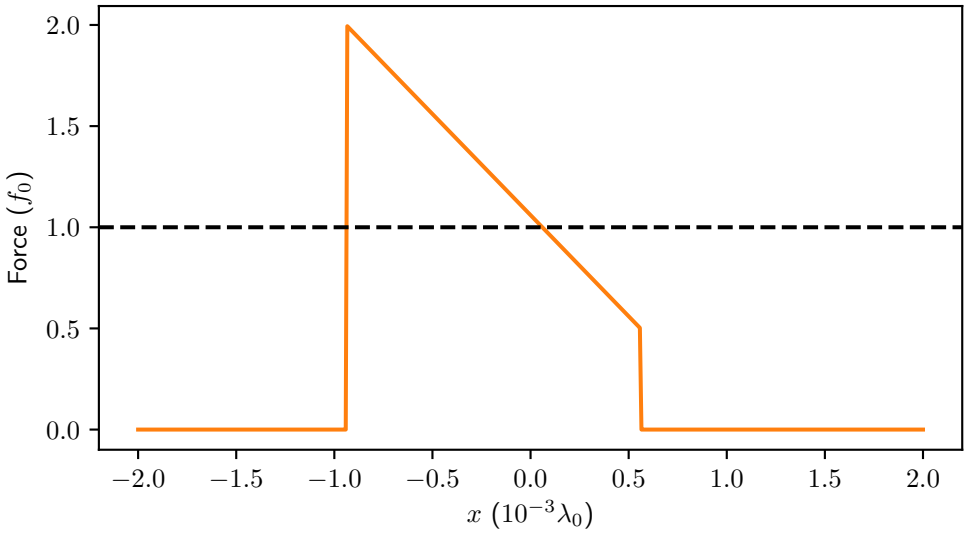

Figure 3.6: Ideal force function shape for optimising the tradeoff between sensitivity and input power.

There is one more factor to consider, which is the effect of cavity finesse on the precision of the position measurement. The simplest method for achieving a high-precision readout of the mirror position is to measure the phase shift in the field reflected or transmitted from the cavity, but the sensitivity of this approach scales with cavity finesse: a higher finesse causes photons to accumulate a larger phase shift (for a given mirror displacement) before leaving the cavity. That is, lowering the finesse to reduce the spring constant could potentially have a negative impact on the overall sensitivity of the system.

As we will see, the method presented above for synthesising custom potentials allows us both to overcome this problem and optimise the aforementioned tradeoff between stiffness and input power beyond what is achievable by simply changing the cavity finesse.

3.3.3 Sensitivity optimisation

With the above observations in mind, the ideal force function for the task at hand would have a consistent spring constant in the vicinity of the equilibrium position and drop sharply to zero outside that region to avoid unnecessary input power, as shown in Fig. 3.6.

In Fig. 3.7 we show how such an ideal function could be approximated using

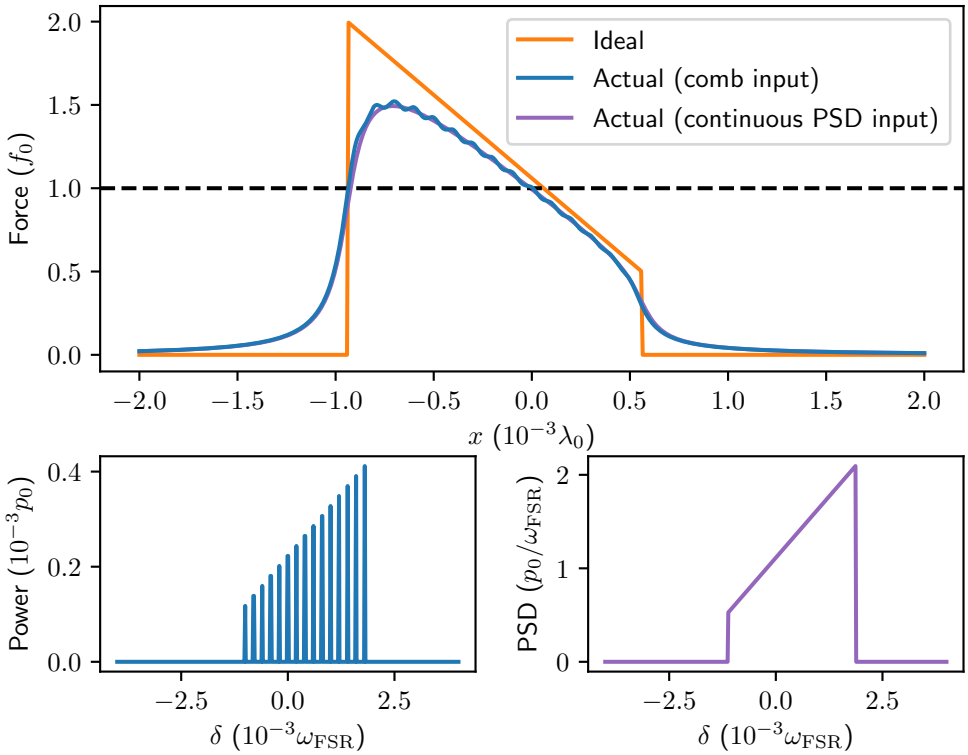

Figure 3.7: Approximation of the ideal force function obtainable using a multi-mode frequency comb input with a high-finesse cavity, with the force function obtained with an impractical continuous PSD input field shown for reference. The input fields required to attain these functions are also shown, where the height of each peak in the comb input represents the total power in that peak. Note that, in practice, some peaks of the comb or slices of the continuous input field would need to be shifted by multiples of the free spectral range ω_{FSR} in order to remove interference effects, so this plot shows the detunings modulo the free spectral range.

the method detailed in Sections 3.2.3 and 3.2.4. We first note that the use of a comb input rather than an unrealistic continuous PSD evidently does not seriously degrade the quality of the approximation. Indeed, the only effect is to induce slight fluctuations in spring constant across the linear regime, but depending on the specific application the impact of these could most likely be eliminated via appropriate scanning and filtering.

Next we can compare the approximated ideal force function with what we could obtain using single-mode inputs, as shown in Fig. 3.8. We see that an appropriate choice of multi-mode input field injected into a high-finesse cavity

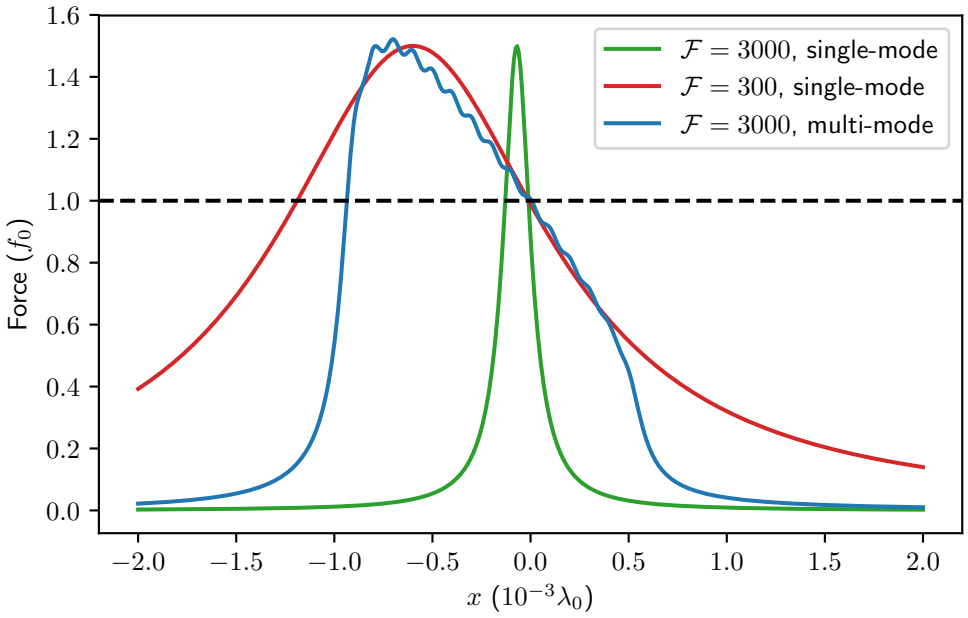

Figure 3.8: Comparison between force functions obtained in various scenarios: single-mode inputs into low- and high-finesse cavities, and a multi-mode input into a high-finesse cavity designed to approximate an ideal force function for gravitational sensing.

can yield a spring constant below that of even a low-finesse cavity, but with significantly lower power requirements. Specifically, the total power required by the multi-mode input is the sum of powers in each peak (or, in the case of a continuous PSD input field, the integral of the PSD), which in this case is $\sim 0.004 p_0$, compared to $\sim 0.008 p_0$ for the single-mode input into a low-finesse cavity. That is, the use of a multi-mode input field allows one to soften the spring constant of the sensor—and thus improve sensitivity—with a significantly lower input power than what would be necessary to achieve the same softening via reduction of the cavity finesse. Moreover, since the cavity finesse can remain high, readout precision of the mirror displacement is unaffected.

We have chosen an ideal force function that achieves a comparable spring constant to the low-finesse cavity without the same power requirements. However, the tradeoff may be optimised along other axes. To compare the two approaches more completely we therefore consider the minimum attainable spring constant as a function of total input power and cavity finesse, for both single- and multi-mode input fields.

In the single-mode case, specifying the power and finesse is sufficient to determine the spring constant at the cavity equilibrium position—it is simply the slope of the familiar Lorentzian profile at the equilibrium position. For sufficiently low powers or finesses the trap will be unable to support fluctuations in the mirror weight (or, indeed, even the mirror weight itself), so we consider only parameters causing the trap depth, or maximum weight supported, to be at least 1.5 times the mirror weight ($1.5f_0$).[4]

In the multi-mode case the situation is less simple, because we are afforded an extra degree of freedom by the ability to shape the trap. Since we seek the minimum spring constant, for each power and finesse we choose the shape of the trap to yield the lowest possible spring constant, again under the condition that the trap depth remain at least $1.5f_0$ (although in practice we always choose a depth of exactly $1.5f_0$, since a higher depth would waste power that could instead be used to further reduce the spring constant). This is realised as a ramp with maximum value $1.5f_0$, minimum (non-zero) value $0.5f_0$ (to ensure linearity near the equilibrium position), and the maximal length permitted by the available input power.

To summarise, we consider the smallest achievable spring constant (at the cavity equilibrium position) as a function of input power and cavity finesse, for single- and multi-mode input fields, under the condition that the resulting traps can support a weight of at least $1.5f_0$. This is plotted in Fig. 3.9, with cross-sections shown in Fig. 3.10. Note that for the sake of simplicity we have performed the calculations using a continuous PSD input field, but the results would be almost identical for sufficiently fine combs.

We see that for any given power and finesse, significantly softer spring constants are obtained with a suitable multi-mode input field as compared to a single-mode field. As finesse increases, the quality of the approximation improves and thus the relative advantage of using a multi-mode field is enhanced. As input power increases, the ideal ramp function to be approximated lengthens and differs more drastically from the typical Lorentzian profile, leading again to a larger advantage. When the input power and/or finesse become low enough

[4]Of course, in applications we would not expect a weight variation of anywhere near $0.5f_0$. However, the exact threshold is largely irrelevant for our comparison of single- and multi-mode inputs, since it does not affect the relationship between the methods (in fact, the only effects of decreasing the threshold are to improve the relative performance of multi-mode inputs and to expand the domain of allowable parameter values).

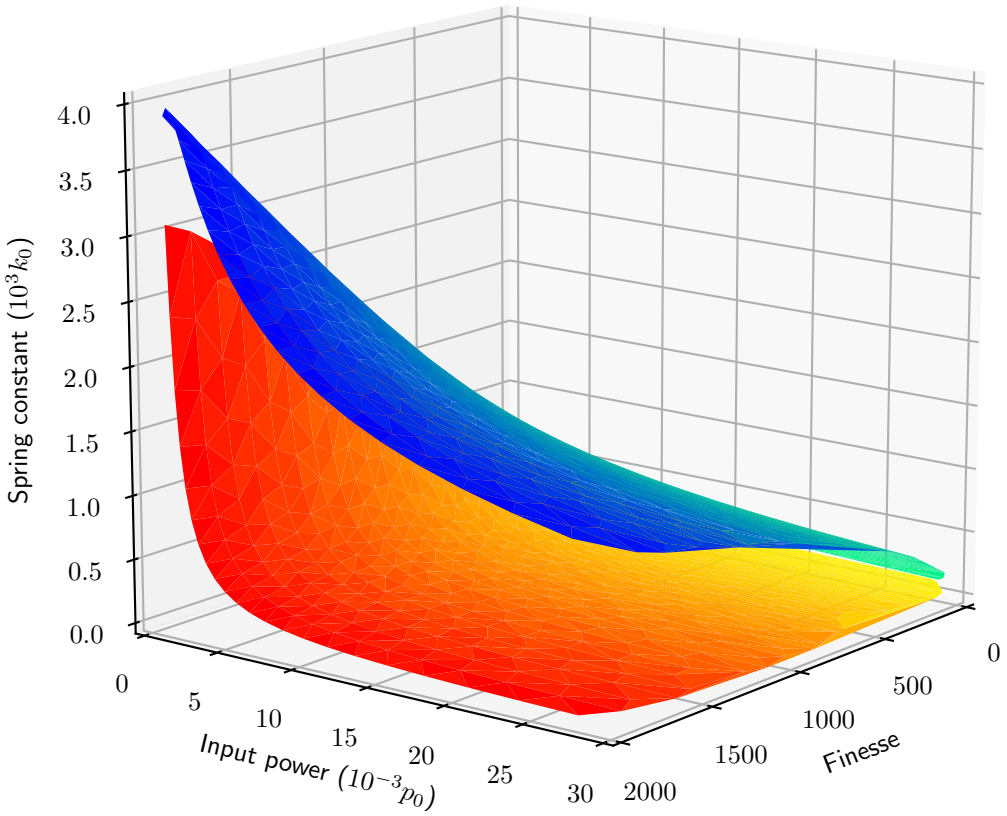

Figure 3.9: Smallest achievable spring constant as a function of input power and cavity finesse, for single-mode (upper, blue) and multi-mode (lower, orange) input fields, under the condition that the trap depth is at least $1.5f_0$. The surfaces are shaded according to finesse. Note that with additional sampling the two surfaces would meet at the low-finesse, low-power boundary of the domain.

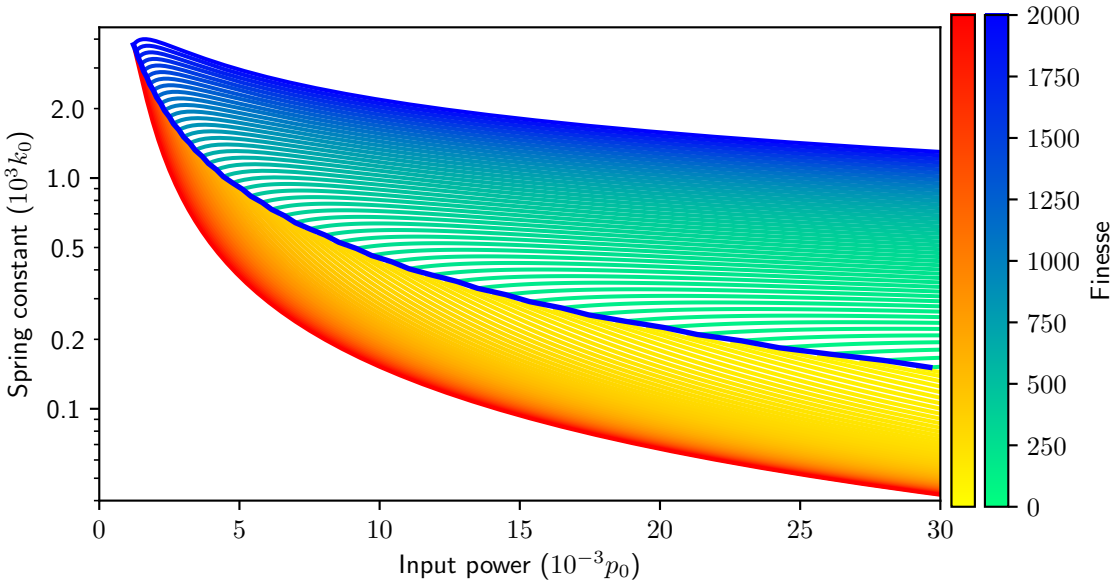

Figure 3.10: Cross-sections showing the smallest achievable spring constant as a function of input power for a selection of finesses, for single-mode (upper) and multi-mode (lower) input fields. The solid blue curve gives, for each input power, the minimum attainable spring constant using a single-mode input field (that is, the minimum is taken across all valid finesses).

that the multi-mode ramp input field has bandwidth small relative to the cavity linewidth, the cavity effectively perceives the input field as a single-mode input and the performances of the two approaches converge.

We also observe that for a given power it is always advantageous to use a multi-mode ramp input, regardless of the finesse used for each method. That is, a multi-mode input to a high-finesse cavity is superior to a single-mode input to a low-finesse cavity. The implication of this is that the conflict between reducing finesse in order to decrease spring constant and increasing finesse in order to improve readout precision may be resolved: using a multi-mode input field, a softer spring constant is attainable with a higher finesse cavity, and thus it is always advantageous to use the highest possible finesse.

As a concrete example we may calculate the expected enhancement in sensitivity for the system of Guccione et al.[124], where the mirror has mass $m = 0.3\,\mathrm{mg}$, the cavity finesse is 1000 and the available input power is 3 W. In this case the multi-mode input yields a spring constant of $1.9\,\mathrm{kN\,m^{-1}}$, while for the single-mode input the spring constant is $9.6\,\mathrm{kN\,m^{-1}}$. This corresponds to an improvement in

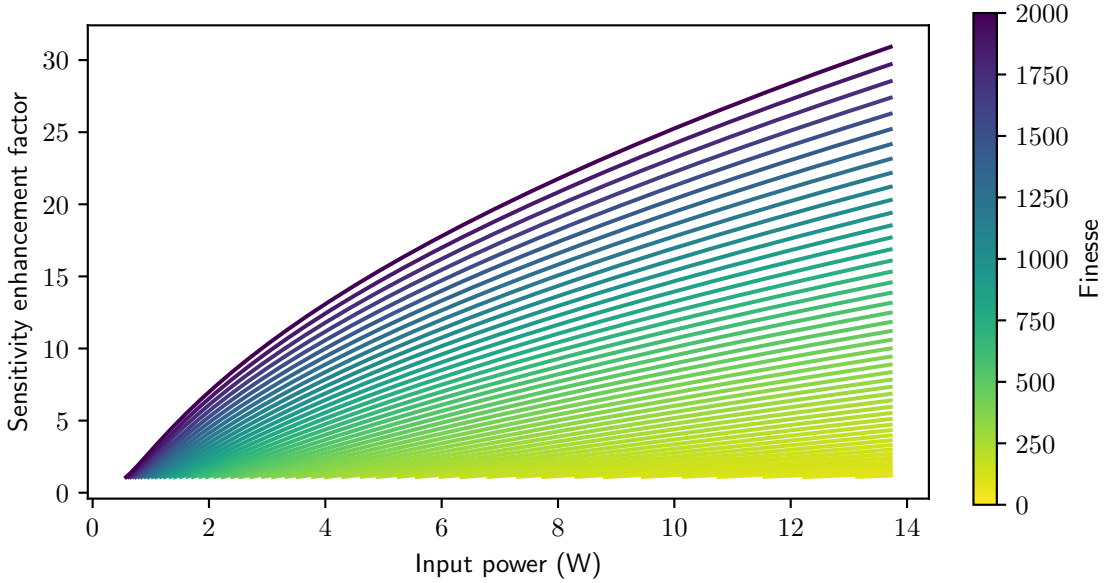

Figure 3.11: Sensitivity enhancement factor (defined as the ratio of spring constant with a single-mode input field to spring constant with an ideal multi-mode input field) as a function of input power for a range of finesses, assuming a mirror mass of $m = 0.3\,\mathrm{mg}$[124].

sensitivity by a factor of over 5 (where again we have assumed that the sensitivity is limited by detection noise, as opposed to force noise that perturbs the actual mirror position). As shown in Fig. 3.11 this factor would increase significantly with higher input powers or finesses.

Thus we see that even for the very simple system and corresponding class of force functions considered in this example, the extra flexibility made possible by our method can allow for significant enhancements in performance.

3.4 Conclusion

We have presented a simple analysis demonstrating that, by judicious choice of input field, the potential experienced by a moveable end mirror of a linear cavity can be tailored to perform more effectively for the task of interest. This tailoring is possible whenever the desired potential possesses features no finer than the cavity linewidth, and the cavity length varies by amounts small relative to the wavelength of the light. Given the practical difficulty in obtaining arbitrary continuous PSD input fields, we have further shown that the use of a frequency comb

is a viable alternative in terms of the quality of the approximation, and that with appropriate frequency shifting the interference effects due to interacting modes of the comb may be ignored. We have also given a simple example demonstrating how the ability to synthesise custom potentials can significantly improve the performance of cavity optomechanical sensors. For a gravitational sensor based on a levitated cavity mirror[124] we predict an immediate enhancement in sensitivity by a factor of over 5.

In addition to performing a proof-of-concept implementation of this method, there are several follow-up theoretical studies that could yield interesting results. One would be to adapt the results to more general optomechanical systems (for example the zipper cavities or whispering gallery mode resonators mentioned in Section 3.1); it seems likely that similar results would hold, given that such systems can often be modelled as linear cavities, but this needs confirmation. More generally, the analysis could be extended to account for the finite speed of light, or to a full quantum mechanical treatment. The former, in particular, is interesting for the case of sensors. For a single blue-detuned input mode, the delayed response of the system to shifts in cavity length manifests as an anti-damping force on the mechanical resonator[134, 136]. This can be counteracted by injecting an additional red-detuned mode at lower power, which removes the anti-damping but does not significantly perturb the optical spring frequency shift induced by the original blue-detuned beam[127, 137]. In our case, however, there could be several blue-detuned beams contributing anti-damping, so one would expect that a corresponding ensemble of low-power red-detuned beams would be necessary to eliminate the anti-damping. For example, associated to the ramp inputs of Section 3.3 we may require additional ramps—at significantly lower power—reflected about the resonance frequency. While this approach seems intuitive, however, a proper analysis would be necessary before declaring it a potential solution to the problem—the typical anti-damping analysis assumes small displacements relative to the optical linewidth[136], which is certainly not the case in our proposed system. Finally, it would be interesting to explore practical mechanisms by which the appropriate input fields could be produced. For simple fields, phase and amplitude modulation of a single beam would be sufficient, but for more precise control or more intricate fields a different approach may be necessary.

Chapter 4

Feedback cooling and retrospective filtering for nanomechanical sensors

In this chapter we consider the problem of signal-to-noise ratio enhancement for measurements made using nanomechanical systems. We discuss three methods, based on both physical modifications to the system (feedback cooling) and numerical post-processing (virtual feedback cooling and Kalman filtering). We apply these methods to a nanowire-based optomechanical force sensor and achieve significant improvements in sensitivity. In the process we demonstrate the relationships between the methods and some of their advantages and disadvantages.

In Section 4.1 we give some history on the use of nanomechanical resonators for sensing purposes, and highlight recent discussions associated with the efficacy of active cooling for optimisation purposes. In Section 4.2 we introduce the optomechanical system that will provide the platform for the subsequent investigation and analysis. In Section 4.3 we introduce the three different approaches to improving the performance of the system as a force sensor, and present the results of applying them to the system. In Section 4.4 we provide some concluding remarks and suggest avenues for further investigation associated with this work.

The contents of this chapter are based on material published in:

> M. Hosseini, G. Guccione, H. J. Slatyer, B. C. Buchler, and P. K. Lam, "Multimode laser cooling and ultra-high sensitivity force sensing with nanowires", Nature Communications **5**, 4663 (2014)

The design and setup of the experiment described in Section 4.2, along with the stationary feedback cooling analysis, were performed primarily by Mahdi Hosseini and Giovanni Guccione. The development of the Kalman filter, the implementation of the virtual cooling, and the force sensing analyses were performed in close collaboration between myself, Mahdi Hosseini and Giovanni Guccione.

4.1 Background

Micro- and nano-mechanical resonators provide a promising platform for high-precision sensing, metrology and imaging. Generally speaking, the combination of low effective masses and high quality factors in such devices enables strong transduction of a signal of interest onto the mechanical behaviour of the resonator, which can then be precisely read out via electrical[139] or optical means[140, 141]. For example, this theme lies at the heart of atomic force microscopy[142], which has seen widespread applications including force sensing[143] and biological imaging[144, 145], and magnetic resonance force microscopy[146, 147], which has been used for subsurface detection of spin centres at the single-electron level[148, 149] and imaging of individual virus particles[150]. Similarly, ultra-sensitive mass detection is possible by measuring the shift in resonance frequency resulting from depositing a sample onto the resonator[151], and the shift in equilibrium position due to nearby charge can form the basis for high-sensitivity electrometers[139].

The sensitivity limit in many of these technologies is set by the unavoidable impact of thermal noise—even though miniaturising the oscillators allows an improvement in signal-to-noise ratio (SNR)[152], the fact remains that a strong response to external forces entails susceptibility to thermal noise. Typically the impact of this noise is reduced by operating at cryogenic temperatures or employing long averaging times (for example, the system of Rugar et al.[149] operated at 1.6 K and still required 13 h of integration time per spatial point), but these techniques are infeasible in many cases. The use of cryogenics both adds technical complexity and is unsuitable for applications requiring specific environmental conditions, such as liquid property measurements[153] or biomaterial sensing[154]. Long averaging times are undesirable whenever a high measurement bandwidth is necessary, for example when detecting transient signals or in high-resolution imaging applications.

An alternative to passive cryogenic cooling is *active* cooling, for example via

electrical[155] or optical[140, 141, 156, 157] feedback cooling, laser cooling[158] or cavity cooling[159]. These approaches all work by actively damping the motion of the oscillator. While it is clear that such a scheme reduces the oscillator's response to thermal noise, for a linear system it also necessarily reduces the response to the signal (the cooling has no way to distinguish between noise and signal), meaning there is no improvement in SNR[160]. Note that for non-linear systems this is not the case. For example, if a system exhibits a poorly-understood non-linearity at high amplitudes then active cooling can be used to ensure that measurements are taken within the linear regime, which can lead to a fundamentally improved SNR[161]. However, in this chapter we concern ourselves only with linear systems, for which no improvement in SNR is possible via stationary active cooling.

There has been much debate as to whether or not this form of stationary cooling has any benefit at all for sensing applications with linear systems[91, 162, 163]. Even though no SNR improvement is possible, the use of active cooling means that the oscillator's energy changes more quickly in response to both the signal and noise, which appears to reduce the necessary averaging times and thus increase measurement bandwidth[91]. However, this is true only if the signal is estimated by averaging the oscillator energy; if the signal is instead extracted from the raw oscillator response via a different process then it is not clear that the necessary averaging time is reduced. Indeed, it turns out that using an algorithm such as Wiener[164] or Kalman[165] filtering on the raw measurement record yields an optimal estimator whose bandwidth is unaffected by the presence or absence of active cooling[162]. In fact it has been shown that, for a linear system with known dynamics, an arbitrary linear feedback protocol can actually be *simulated* by post-processing the measurement data[92]. This is actually quite intuitive: in the feedback cooling case we make measurements and feed those back into the system, but if we know the dynamics of the system then we could instead simply keep track of how the oscillator *would have* responded to feedback. Put another way, for a given averaging time we will obtain a certain amount of information from the system regardless of whether we use feedback. Provided we extract that information appropriately, the use of feedback is thus irrelevant. In theory, therefore, feedback cooling cannot yield any fundamental advantage over simply using a different estimation scheme. On the other hand, these filtering and simulation techniques require knowledge of system parameters, which may be difficult to determine precisely and, especially in nanomechanical systems,

may actually vary during the measurement process[163, 166]. To summarise the arguments, it is not clear whether stationary active cooling yields any bandwidth advantages for linear nanomechanical sensors in practice, but it is well-accepted that regardless of estimation strategy no enhancement of SNR is possible.

Outside the stationary regime, however, the SNR obtained with a basic energy averaging technique *can* be enhanced via feedback cooling. A non-stationary scheme, in which the cooling is turned off immediately before the signal arrives, causes the oscillator to respond to the signal while still in the process of rethermalising. Provided the averaging time is short relative to the rethermalisation time of the oscillator, this scheme yields a significant reduction in noise with little effect on the signal[160]. That is, for short, impulsive signals it is in theory possible to improve SNR by employing a non-stationary feedback cooling scheme.[1] However, once again it is expected that an equivalent enhancement of SNR can be attained simply by using a different estimation strategy—even a non-stationary feedback scheme applied to a linear system can be simulated via post-processing[92].

In this chapter we investigate the issue of SNR enhancement using non-stationary feedback and estimation schemes. We consider a nanomechanical system consisting of a nanowire that can be precisely detected and actuated optically. We use this system as an ultra-sensitive force sensor, and compare its performance in several different scenarios: with a basic energy averaging estimator in the presence and absence of physical non-stationary feedback cooling, with the same estimator applied to the measurement record obtained from simulating that cooling scheme during post-processing (we refer to this simulation as *virtual cooling*), and using a non-stationary Kalman filter-based estimator. We find that feedback cooling, virtual cooling and Kalman filtering all provide a comparable and significant enhancement in SNR over the basic energy averaging approach.

4.2 A nanowire-based optomechanical force sensor

In this section we introduce the system used for the analysis. A schematic of the full system, including the feedback control, is shown in Fig. 4.1. We will discuss

[1] Note that by employing a cyclic cooling strategy—where cooling is frequently turned on and off—one can achieve an improvement in SNR even if the arrival time of the signal is unknown, because on average the reduction in noise is greater than the reduction in signal[160].

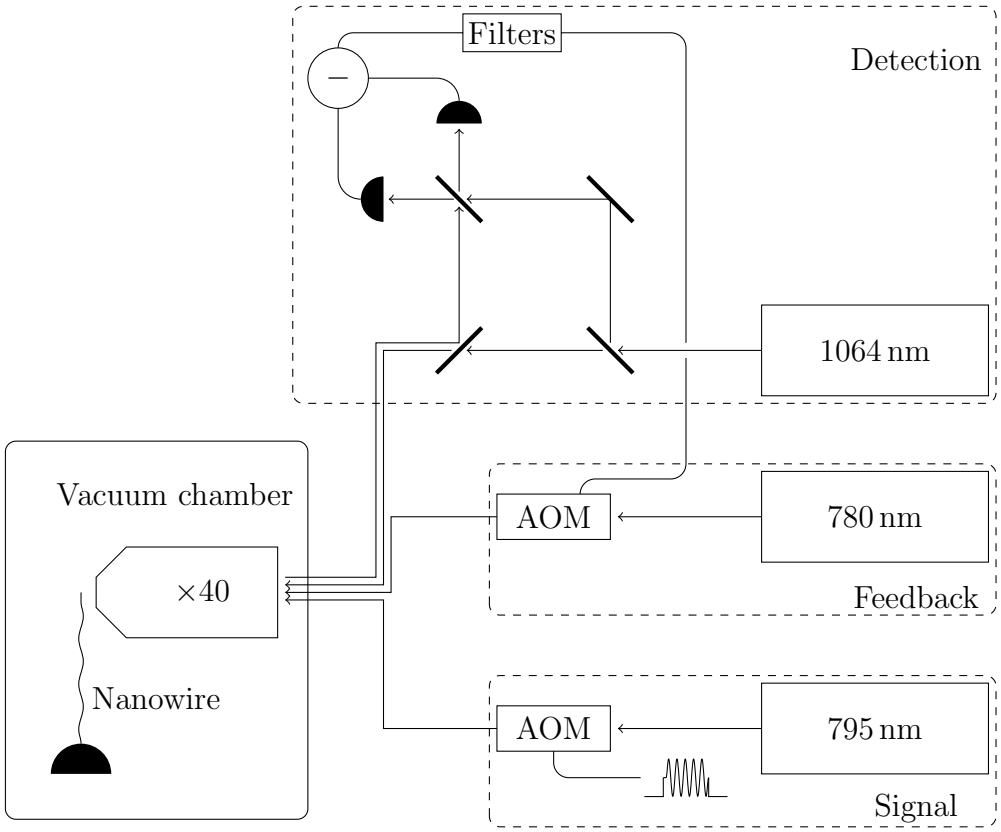

Figure 4.1: Schematic of nanowire-based optomechanical force sensor. The nanowire, which is attached to a tungsten needle, is mounted on a nanopositioning stage inside a vacuum chamber. A microscope objective (×40, NA = 0.65) is used to focus the detection, feedback and signal lasers on the nanowire. The detection laser is focused on the tip of the nanowire and is reflected with negligible impact on its position, while the feedback and signal lasers are focused closer to the mounting point and drive the nanowire. The detection arm performs homodyne measurement of the nanowire deflection by interfering the beam reflected from the nanowire with a local oscillator. The homodyne signal is passed through analog filters to adjust the phase before being fed to an acousto-optic modulator (AOM) in the feedback arm, which modulates the power of the feedback beam. In the signal arm an impulse signal modulated at the mechanical resonance frequency is applied to an AOM, which modulates the power of the signal beam and thus drives the nanowire.

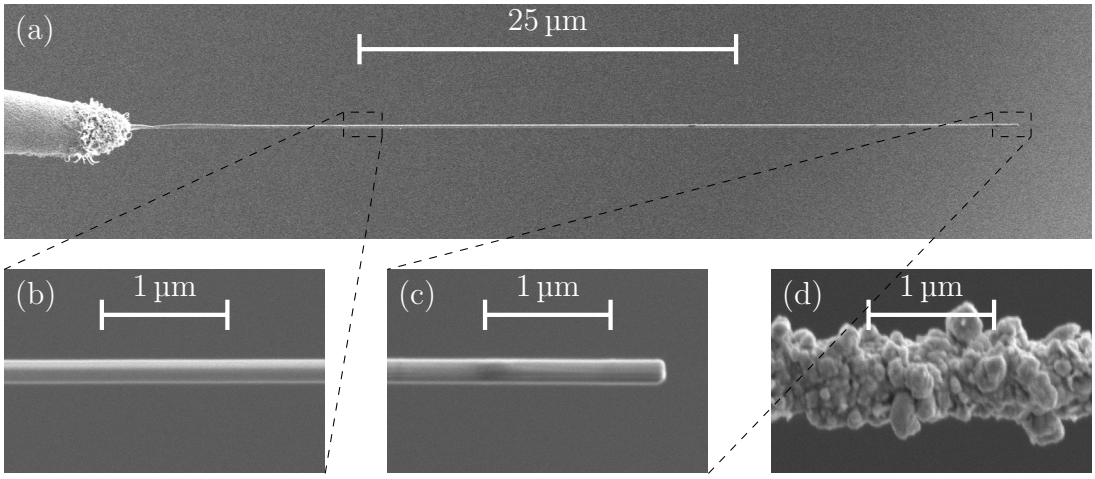

Figure 4.2: Scanning electron microscope images of (a–c) a regular Ag_2Ga nanowire and (d) a gold-coated nanowire. Gold-coated nanowires were used for the force sensor due to their higher scattering efficiency. In the sensor, the detection beam is focused on the tip of the nanowire (shown in (c)), while the feedback and signal beams are focused closer to the mounting point (shown in (b,d)).

each component of this setup in more detail in the following sections.

4.2.1 Nanowires

The mechanical oscillators used in our system are gold-coated silver-gallium (Ag_2Ga) nanowires manufactured by NaugaNeedles LLC[167]. The nanowires are grown by dipping a silver-coated tungsten needle into a drop of liquid gallium at room temperature, retracting the needle slightly, and then waiting for a period of seconds to minutes while the gallium meniscus drains away[168]. This process yields a silver-gallium nanowire with size ranging from around 20 µm to 60 µm in length and 50 nm to 200 nm in diameter. To improve detection efficiency, which depends on the amount of light scattered from the surface, the nanowires are then coated with around 50 nm of gold. Scanning electron microscope images of two nanowires are shown in Fig. 4.2.

The gold-coated nanowires used in the system typically had effective masses on the order of picograms, mechanical frequencies of roughly 300 kHz and damping rates ranging from 10 kHz at ambient pressure down to 0.8 kHz in vacuum. The latter corresponds to a mechanical quality factor of almost 400. See Guccione et al.[169] for a thorough characterisation of these nanowires.

4.2.2 Detection

The nanowire deflection is determined by illuminating the tip of the nanowire with a weak "detection" laser and measuring the phase shift of the reflected beam via homodyne detection[156]. Any vibration of the nanowire along the optical axis causes a change in path length experienced by the detection laser, and thus a phase shift relative to the reference beam. The sensitivity of this scheme depends on the angle of vibration relative to the optical axis: as the oscillation becomes further misaligned from the optical axis the detection sensitivity decreases, until the axes are orthogonal at which point the vibration cannot be detected at all.

4.2.3 Actuation

To perform feedback control and to apply an impulsive signal to be measured we actuate the nanowire by illuminating it with a $\sim$1 mW laser. Incidence of such a laser on the nanowire causes two main effects: a radiation pressure force due to the transfer of momentum from photons to the nanowire, and a rise in bulk temperature due to absorption of photons. We estimated the temperature rise to be on the order of 10 K, which is sufficient to cause thermally-induced bending of the nanowire due to the different thermal expansion rates of the gold and silver-gallium layers[170]. This bending is an instance of the *bolometric effect*[171]. Using the aforementioned detection process we determined the deflection to be $\sim$20 nm for a 1 mW incident beam, which implies a bolometric force of $\sim$10 nN. This is orders of magnitude higher than the radiation pressure force, which is on the order of 5 pN. Consequently, the dominant force exerted by the laser on the nanowire is from the thermal response to photon absorption.

While photothermal forces are typically slow due to finite thermal conductivities, they can be significantly faster in nanoscale objects than bulk materials[172]. Specifically, the response time for a long cylinder is given by $r^2/4\kappa$, where r is the radius and κ is the thermal diffusivity[173]. Estimating $\kappa \approx 10^{-4}\mathrm{m}^2\,\mathrm{s}^{-1}$ (as per Takata et al.[174]) yields a thermal response time of nanoseconds, which is significantly faster than the timescale of the mechanical oscillations (which are on the order of microseconds).

4.2.4 Feedback control

As discussed above, actuation of the nanowire via the bolometric force is significantly faster than the mechanical oscillations. Consequently, within a single oscillation we can detect the nanowire displacement, apply a gain and phase shift to the measurement, and feed the result back to the nanowire via the feedback laser. Choosing the gain and phase appropriately allows us to modify the effective oscillator parameters.

Note that the only factors limiting the bandwidth of the feedback are the speed of the electronics and the response time of the bolometric force, both of which are significantly faster than the nanowire's mechanical resonances. A consequence of this is that many mechanical resonances can be addressed simultaneously.

Cooling

Our primary interest in feedback control is in using it to cool the motion of the nanowire and thus reduce the effect of thermal noise. To achieve this we employ the *cold damping* technique[157], in which the feedback phase is chosen to apply a force proportional to the oscillator velocity. Specifically, let us consider the behaviour of a single mode of oscillation under the influence of feedback with a fixed gain. Writing the effective gain (taking into account electronic gain, losses in the feedback loop, and so on) as $-g\gamma m$, where g is a dimensionless gain factor that is effectively constant within the feedback bandwidth, γ is the linewidth of the mode and m is the effective mass, the force applied to the nanowire is

$$F_{\mathrm{fb}}(\omega) := -g\gamma m \times i\omega x(\omega), \tag{4.1}$$

where $x(\omega)$ is the displacement in the frequency domain, and we have recalled that the quantity $i\omega x(\omega)$ gives the velocity in the frequency domain. Let us now consider the nanowire to be acted on by an additional external force F_{ext}, so its motion is given by

$$x(\omega) = \chi_{\mathrm{m}}(\omega)\left(F_{\mathrm{ext}}(\omega) + F_{\mathrm{fb}}(\omega)\right), \tag{4.2}$$

where

$$\chi_{\mathrm{m}}(\omega) := \left[m\left(\omega_{\mathrm{m}}^2 - \omega^2 + i\gamma\omega\right)\right]^{-1} \tag{4.3}$$

is the mechanical susceptibility. Using Eq. (4.1) we may rewrite this in the form

$$x(\omega) = \chi_{\text{eff}}(\omega) F_{\text{ext}}(\omega), \tag{4.4}$$

where the effective susceptibility χ_{eff} is given by

$$\chi_{\text{eff}}(\omega) := \left[m \left(\omega_{\text{m}}^2 - \omega^2 + i(1+g)\gamma\omega \right) \right]^{-1}. \tag{4.5}$$

That is, the presence of feedback causes a gain-dependent shift in the mode's linewidth. For example, a positive g causes an increase in effective damping (that is, cooling) while a negative g causes a decrease (heating).

In practice we achieve cooling by manually adjusting the gain (by varying the laser power) and phase (using an adjustable analog bandpass filter on the detected displacement signal) of the feedback loop in order to minimise the power spectrum of the nanowire at its resonances.

In Fig. 4.3 we show the power spectral density (PSD) of the measured displacement for a nanowire with two proximate fundamental modes, as a function of feedback gain (laser power). This plot demonstrates that the feedback system is indeed able to cool the vibration significantly, and moreover that multiple modes can be cooled simultaneously.[2]

We can also estimate the effective temperature of the modes under the influence of feedback cooling. For a gain factor g small enough that the amount of measurement noise fed back into the system is negligible, the PSD of the measured displacement for a single mode is approximately given by[175]

$$S(\omega) = \frac{2\gamma k_{\text{B}} T_0}{m} \frac{1}{(\omega_{\text{m}}^2 - \omega^2)^2 + (1+g)^2\gamma^2\omega^2}, \tag{4.6}$$

where ω_{m}, γ and m are as defined above and T_0 is the initial temperature. These parameters are known, so we may plug them into the expression and then estimate the gain g required to match the predicted PSD S to the observed PSD. Next we observe that

$$S(\omega) = \frac{2\gamma(1+g) k_{\text{B}} T_0 (1+g)^{-1}}{m} \frac{1}{(\omega_{\text{m}}^2 - \omega^2)^2 + ((1+g)\gamma)^2\omega^2}, \tag{4.7}$$

[2] In fact, modes as high as 2 MHz can be affected, but for the purposes of sensitivity enhancement this is irrelevant since those parts of the spectrum are filtered out. See Hosseini et al.[138] for more details on broadband cooling in this system.

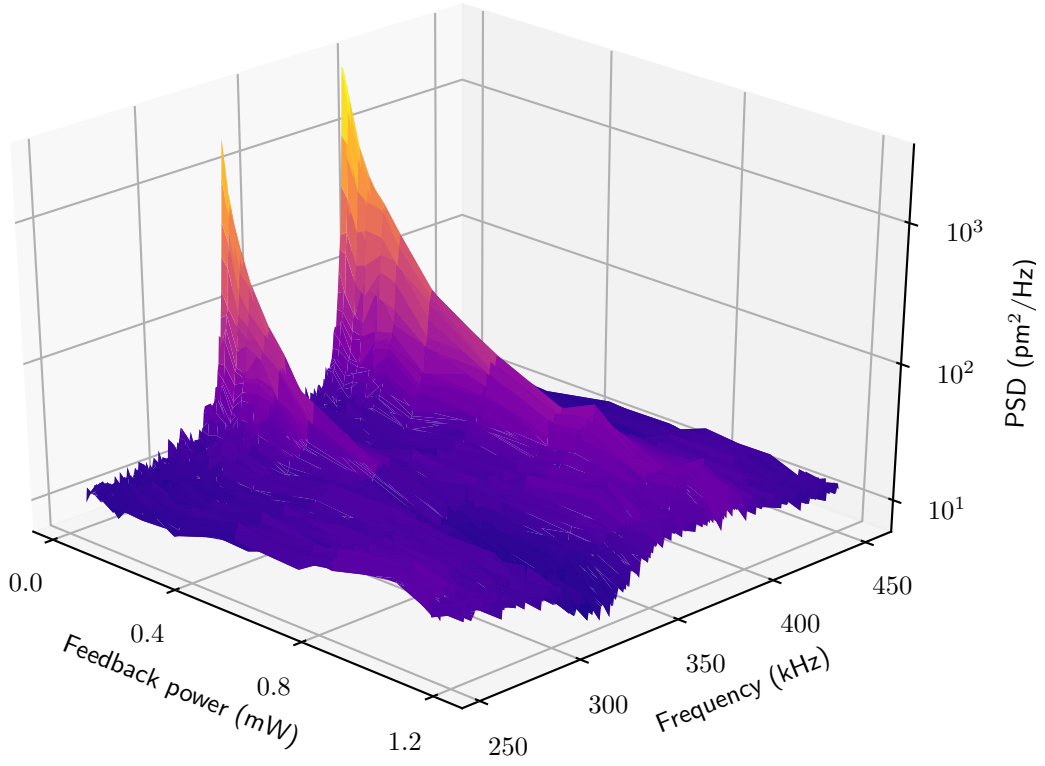

Figure 4.3: Power spectral density (PSD) of the nanowire displacement for varying feedback laser power. The normalisation factor for the spectrum, which converts the arbitrary measured units into physical units shown here, was determined by integrating the area under the spectrum in the absence of any feedback and comparing it with the result expected from the equipartition theorem.

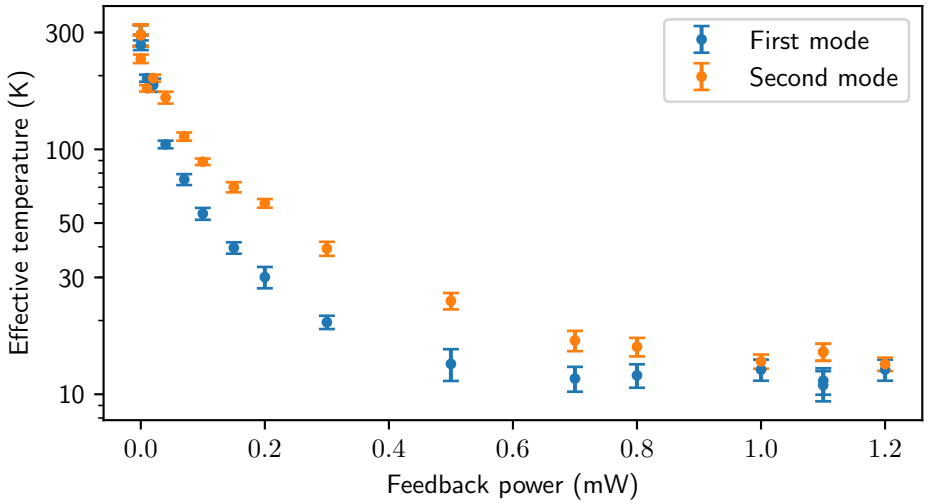

Figure 4.4: Effective temperature versus feedback laser power for the two fundamental modes. The error bars are calculated by propagating the estimated uncertainty in the gain g.

which is to say that the spectrum for gain g, temperature T_0 and damping γ is the same as that for an oscillator without feedback but at temperature $T_0(1+g)^{-1}$ and damping $\gamma(1+g)$. That is, applying a gain g effectively reduces the temperature of the oscillator to $T_0(1+g)^{-1}$. Using this observation we may determine the effective temperature as a function of laser power, as shown in Fig. 4.4. Thus we see that cooling down to an effective temperature of $\sim$10 K is possible with the feedback system.

4.2.5 Force sensing

To test the basic system's performance as a sensor for impulsive forces we use the signal laser to apply a 0.1 ms signal pulse modulated at the mechanical frequency ($\sim$340 kHz for the specific nanowire used, which, unlike the nanowire used for the cooling plots above, has a single distinguished fundamental mode), while tracking the oscillator displacement via the detection system. From this measurement we estimate the energy at each timestep after the pulse arrival. The signal quantity is then given by the average of this energy over the time since the pulse was applied. This approach to signal extraction is known as energy averaging. For a sensor the figure of merit is the SNR, so to obtain the noise we apply exactly the same procedure in the absence of any impulsive force. The SNR is then given by

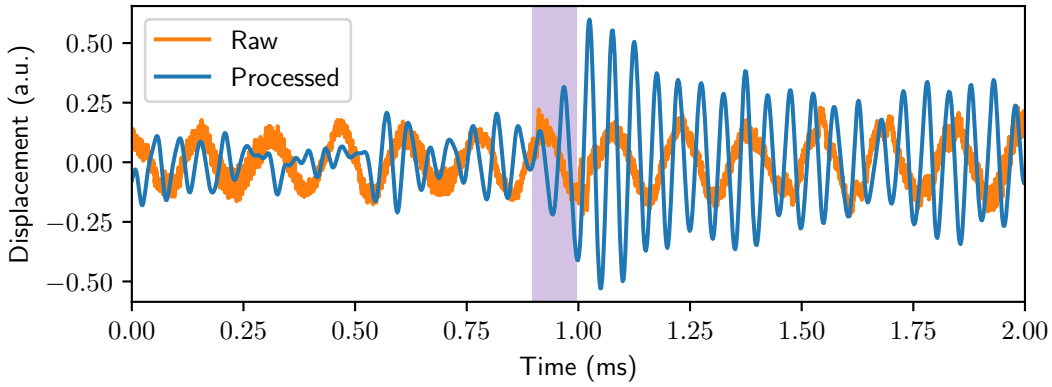

Figure 4.5: Comparison of raw and processed (bandpassed and downshifted) measurements for a randomly-chosen trace (with signal). The displacement units are arbitrary. The shaded area indicates when the signal is applied.

the ratio of these two quantities.

Note that, in practice, before performing the energy averaging we numerically filter the raw displacement to a bandwidth of 40 kHz about the mechanical frequency (that is, between 320 kHz and 360 kHz), and downshift to the 0 kHz–40 kHz band. The effect of this processing is shown in Fig. 4.5. We see that the low-frequency locking noise is eliminated, and that the resulting trace oscillates at the downshifted mechanical frequency ∼20 kHz.

Sample processed traces with and without a signal are shown in Fig. 4.6. The behaviour changes abruptly when the signal is applied after ∼0.9 ms: the oscillator energy quickly increases until the signal is turned off after 0.1 ms, after which the energy gradually decays back to its equilibrium value.

Fig. 4.7 shows the sensitivity results for the basic system, in the absence of any feedback cooling or more advanced estimation techniques. We see that, as expected, the signal and thus SNR increase as the force is being applied, because this increases the energy of the oscillator (note that the increase continues for a short time afterwards due to the fact that we use the *average* energy). As the energy decays after the force has been turned off, the signal and SNR both gradually decrease. The noise curve remains effectively constant across the full averaging period, since in this case the oscillator is being driven only by stationary thermal noise.

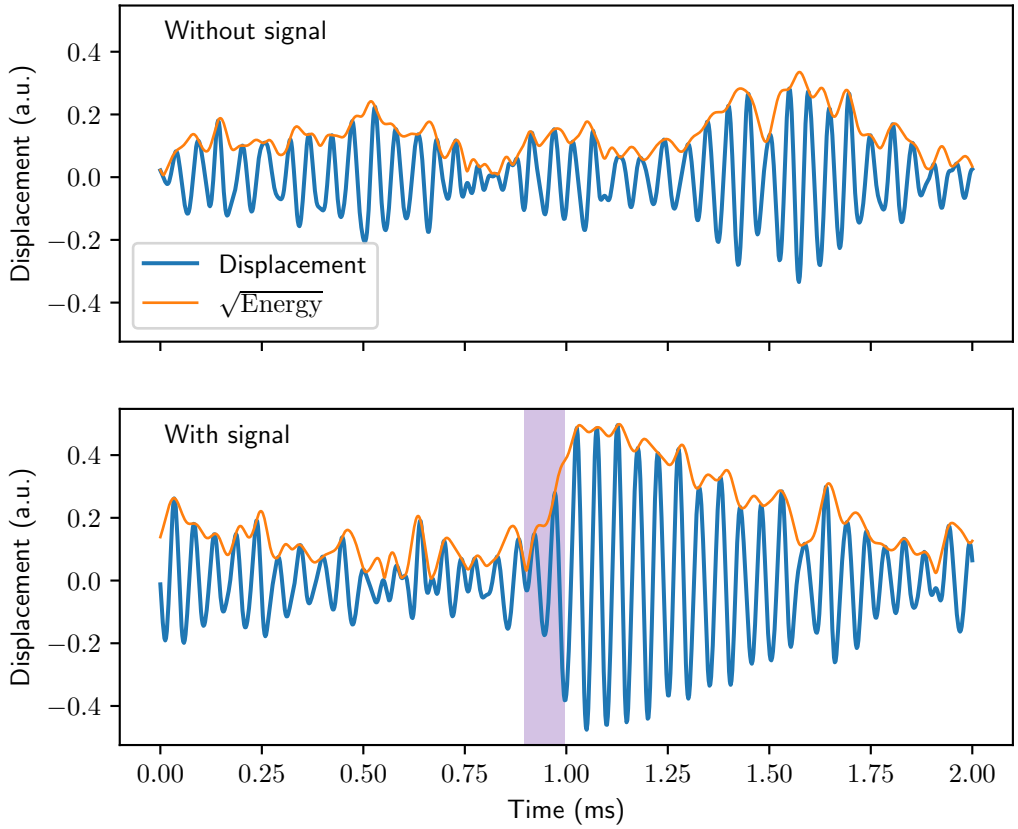

Figure 4.6: Sample traces without and with signal, showing both the displacement and estimated energy. The units are arbitrary, and the square root energy is scaled to displacement units.

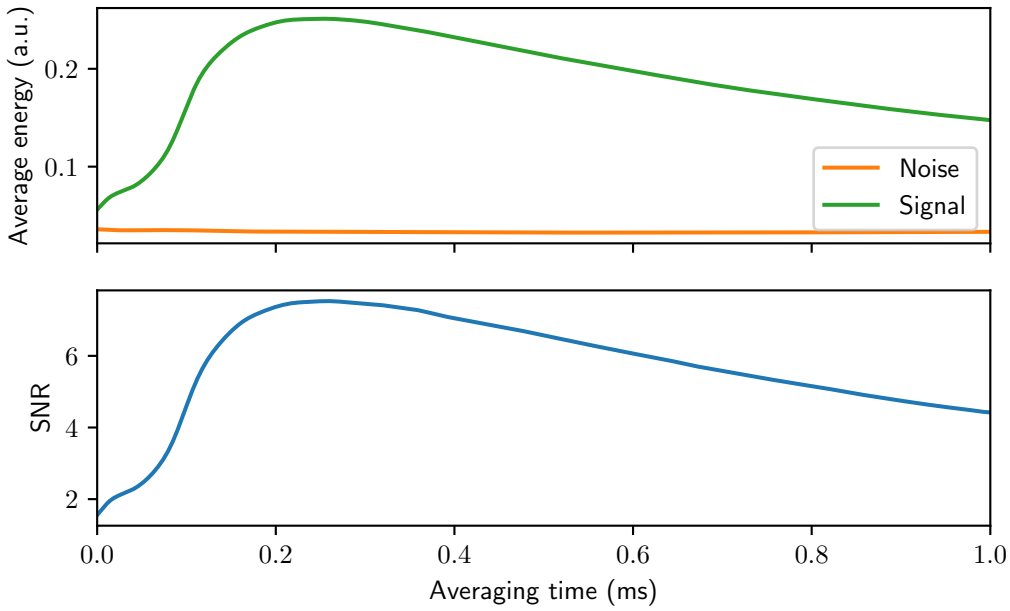

Figure 4.7: Signal, noise and SNR for the basic sensor using energy averaging in the absence of feedback cooling. The signal and noise give the average values over 150 individual runs. The SNR is simply the ratio of the signal and noise curves. The signal and noise are shown in the same arbitrary energy units.

Force resolution

By calibrating appropriately we can determine the actual force resolution of the sensor.

Let us consider the displacement $x(t)$ of the oscillator in the presence of thermal noise and an impulsive monochromatic signal $F(t)$ of magnitude F_0, duration t_F and frequency ω_{m}. We seek to determine the minimum F_0 such that this force is detectable.

Denote by $\langle\cdot\rangle_\tau$ the average of some quantity over the time τ since the signal was applied, further averaged over several independent traces. Denote by $\mathrm{std}\,[\cdot]_\tau$ the standard deviation of that average in the distribution over the traces. We will show how F_0 can be extracted from the statistics of x^2 (which is an unbiased estimator for the oscillator energy).

We may write $x(t) = \tilde{x}(t) + x_F(t)$, where $\tilde{x}(t)$ describes the motion due only to thermal forces and $x_F(t)$ describes the response to $F(t)$. Assuming we average

over sufficiently many traces we have $\langle \tilde{x} x_F \rangle_\tau \approx 0$ and thus

$$\left\langle x^2 \right\rangle_\tau \approx \left\langle \tilde{x}^2 \right\rangle_\tau + \left\langle x_F^2 \right\rangle_\tau . \tag{4.8}$$

We therefore consider the signal to be detectable via energy averaging if $\langle x_F^2 \rangle_\tau$ is at least $\mathrm{std}\,[\tilde{x}^2]_\tau$. That is, the minimum-detectable signal satisfies

$$\left\langle x_F^2 \right\rangle_\tau = \mathrm{std}\left[\tilde{x}^2\right]_\tau . \tag{4.9}$$

We can now determine the force required to trigger such a response. The time response x_F of the system to the force F is given by

$$x_F(t) = \frac{F_0}{\sqrt{2\pi}} \int_0^{t_F} \chi_\mathrm{m}(t-t') \sin \omega_\mathrm{m} t' dt', \tag{4.10}$$

where

$$\chi_\mathrm{m}(t) := \mathcal{F}^{-1}\left(\chi_\mathrm{m}(\omega)\right)(t) = \mathcal{F}^{-1}\left(\left[m\left(\omega_\mathrm{m}^2 - \omega^2 + i\gamma\omega\right)\right]^{-1}\right)(t) \tag{4.11}$$

is the mechanical susceptibility in the time domain. Therefore

$$\left\langle x_F^2 \right\rangle_\tau := \frac{1}{\tau}\int_0^\tau x_F(t)^2 dt = \frac{1}{\tau}\int_0^\tau \frac{F_0^2}{2\pi}\left(\int_0^{t_F} \chi_\mathrm{m}(t-t')\sin\omega_\mathrm{m} t' dt'\right)^2 dt. \tag{4.12}$$

Rearranging, we obtain

$$F_0 = \sqrt{\frac{2\pi\tau \left\langle x_F^2 \right\rangle_\tau}{\int_0^\tau \left(\int_0^{t_F} \chi_\mathrm{m}(t-t')\sin\omega_\mathrm{m} t' dt'\right)^2 dt}}. \tag{4.13}$$

From Eq. (4.9) we thus see that the force resolution (that is, the smallest F_0 such that the signal is detectable) for energy averaging is given by

$$F_0 = \sqrt{\frac{2\pi\tau\, \mathrm{std}\left[\tilde{x}^2\right]_\tau}{\int_0^\tau \left(\int_0^{t_F} \chi_\mathrm{m}(t-t')\sin\omega_\mathrm{m} t' dt'\right)^2 dt}}. \tag{4.14}$$

This yields the results shown in Fig. 4.8, and suggests an optimal force resolution of $\sim 3 \times 10^{-16}\,\mathrm{N}$. The existence of an optimal averaging time (in this case $\sim 0.2\,\mathrm{ms}$) can be understood as follows. The ability to resolve a perturbation

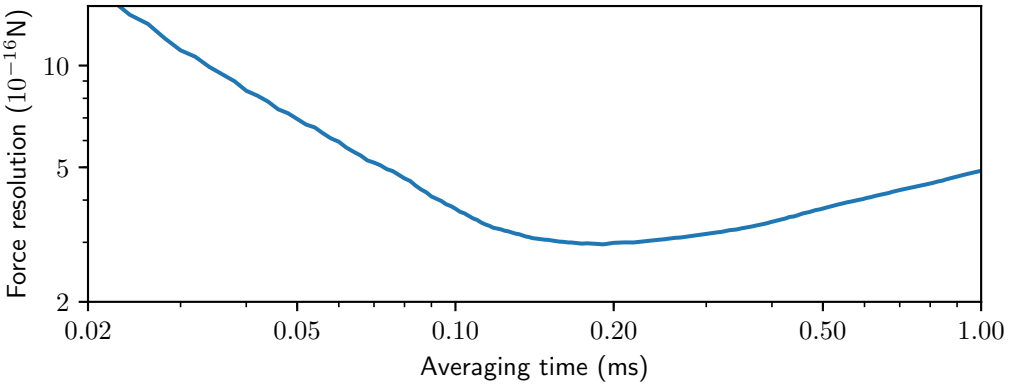

Figure 4.8: Estimated force resolution for the basic sensor.

above the noise floor improves monotonically with averaging time (since more noise can be averaged away), so one may expect very long averaging times to be advantageous. However, the energy of the oscillator increases for 0.1 ms while the signal is applied, and then starts decreasing back to its thermal equilibrium value. It follows that the *average* energy increases for slightly longer than 0.1 ms, but then starts to decrease asymptotically towards the equilibrium value. We find that this decay in signal is faster than the reduction in noise floor, which is to say that the benefits of a low noise floor associated with long averaging times are outweighed by the limitations of a small signal. It follows that sensitivity is optimised at intermediate averaging times, in the vicinity of the peak average signal energy.

4.3 Sensitivity enhancement

The system described in Section 4.2 is considered as the basic force sensor. In this section we consider three methods for improving its performance. We first describe each of the methods, and then present and discuss the results of applying them to the system. We will see that all three methods yield a significant improvement in sensitivity.

4.3.1 Physical feedback cooling

As discussed in Section 4.1, it is well-known that stationary feedback cooling cannot enhance the SNR of a sensor, since the cooling cannot distinguish between

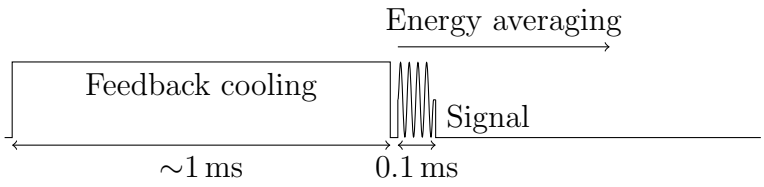

Figure 4.9: Scheme for sensitivity enhancement via non-stationary feedback cooling. The oscillator is cooled for ∼1 ms, then the cooling turned off and a 0.1 ms pulse (modulated at the mechanical frequency) applied. The oscillator energy is averaged from the moment the pulse is applied.

signal and noise and thus must reduce the two together. However, it has been suggested[160] that a non-stationary strategy can provide an advantage, at least in the context of the basic energy averaging estimator. Specifically, if the feedback cooling is turned off just before the signal arrives then the signal is largely unaffected but, until the oscillator completely rethermalises, the noise is reduced. Thus if the averaging time is short relative to this rethermalisation time (which is described by the oscillator linewidth—roughly 0.8 kHz in our case, corresponding to a rethermalisation time on the order of 1 ms) then an enhancement in SNR should be possible.

We tested this proposal. For each experimental run we used the same energy averaging procedure as above, but applied feedback cooling for ∼1 ms before the pulse arrived. The scheme is shown in Fig. 4.9, and sample traces in Fig. 4.10. We note the small oscillations and corresponding low energy when the feedback cooling is being applied. When the cooling is turned off in the absence of the signal, the energy slowly increases towards its equilibrium point. In the case that the signal is applied, the energy first increases rapidly and then decays back towards the usual value, as in the basic system. It is in the initial post-cooling period of low noise and high signal that we expect an enhancement in SNR over the basic system.

4.3.2 Virtual feedback cooling

The second approach we consider is to simulate the physical feedback cooling discussed in the previous section by post-processing the measurement data obtained in the absence of any feedback. This approach is based on the idea presented by Harris et al.[92], that, for a linear system with known dynamics and satisfying the

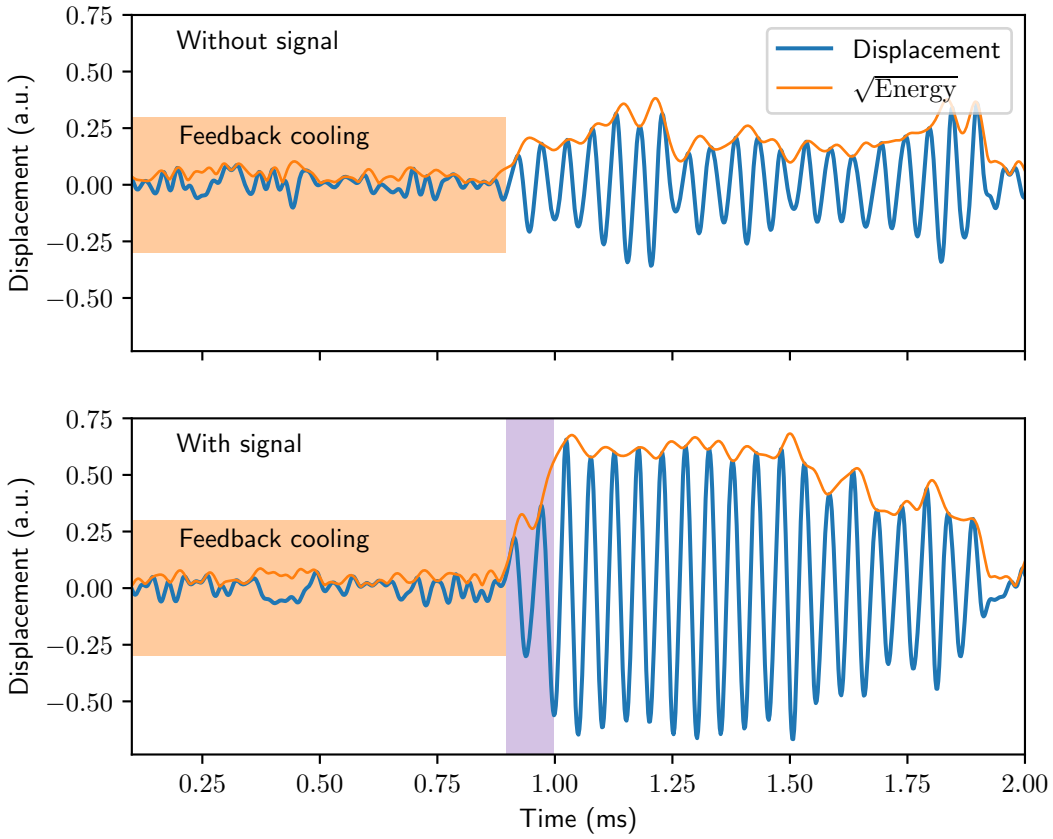

Figure 4.10: Sample traces without and with signal in the presence of feedback cooling, showing both the displacement and estimated energy. The units are arbitrary, and the square root energy is scaled to displacement units. The shaded orange and purple areas indicate when feedback cooling and signal are applied, respectively.

property that all unknown forces are independent of position, any linear feedback protocol can be simulated via post-processing.

We refer the reader to Harris et al.[92] for the full derivation of the possibility of this simulation, but as mentioned in Section 4.1 it can be understood intuitively. Consider the simplified case where we apply a single impulsive feedback signal at a particular time, based on some prior measurements of the system. Rather than actually applying this feedback, we could instead simply calculate the feedback we *would have* applied, and predict the response of the system to that feedback in the absence of all other forces. By linearity and the assumption of position-independence of unknown forces, we can then simply add this response to the observed trajectory to obtain the exact trajectory we *would have* observed had feedback been applied. For more realistic feedback protocols involving more than a single pulse we apply the same argument, but now when calculating the feedback we would have applied at each timestep we also take into account the response of the system to feedback applied at previous timesteps.

More precisely, let $x(t)$ be the position of the oscillator at time t in the absence of any feedback. Let $y(t)$ be the trajectory we would have observed had feedback been applied. We will show how y can be determined from x.

Since we are interested in simulating the cold damping described in Section 4.2.4 we consider the particular case of a linear feedback protocol depending only on the oscillator velocity at the current time, and assume without loss of generality that the mean oscillator position is 0. The feedback force at time t can thus be written as $F_{\mathrm{fb}}(t) = G(t)\dot{y}(t)$, where $G(t)$ is the gain at time t. To apply the theory of Harris et al.[92] we rewrite this in the kernel form

$$F_{\mathrm{fb}}(t) = \int_0^t -G(t)\dot{\delta}(\tau - t)x(\tau)d\tau, \tag{4.15}$$

where we have introduced the derivative of the delta function $\dot{\delta}$.

Denoting by $\chi_{\mathrm{m}}(t)$ the (Fourier transform of) the mechanical susceptibility as in Section 4.2.5 we may now define the transfer function

$$h(t,\tau) := \int_{-\infty}^{\infty} -G(t')\dot{\delta}(\tau - t')\chi_{\mathrm{m}}(t - t')dt', \tag{4.16}$$

which describes the response of the oscillator at time t to the feedback force resulting from its position at time τ. The theory of Harris et al.[92] now asserts

the following relationship between x and y:

$$y(t) - \int_0^t h(t,\tau)y(\tau)d\tau = x(t). \tag{4.17}$$

Again, this result is quite intuitive: it simply states that the signal in the absence of feedback can be obtained by considering the signal with feedback and subtracting the combined response of the system to all prior feedback. In practice we must solve this Fredholm equation for y (given x), and the simplest way to achieve this is by temporal discretisation. Specifically, we sample x, y and h at some large number of timesteps (in our case we use 1000), and collect the values into vectors $\mathbf{x}$ and $\mathbf{y}$ and a matrix H, which yields the matrix equation

$$\mathbf{y} - H\mathbf{y} = \mathbf{x} \tag{4.18}$$

$$\mathbf{y} = (I - H)^{-1}\mathbf{x}, \tag{4.19}$$

where I is the appropriate identity matrix. This equation allows us to determine $\mathbf{y}$, the measurement record we would have obtained had we used feedback, from $\mathbf{x}$, the measurement record we actually observed in the absence of feedback.

To apply this method in our scenario we simply need to specify the feedback gain $G(t)$ for our particular feedback protocol. As in Section 4.2.4 we consider an effective gain of the form $-g\gamma m$, where g is a fixed gain factor, but now we switch off the feedback after a particular time t_0. That is,

$$G(t) = \begin{cases} -g\gamma m & t \leq t_0 \\ 0 & t > t_0. \end{cases} \tag{4.20}$$

With this choice, the transfer function h becomes

$$\begin{aligned} h(t,\tau) &= \int_{-\infty}^{t_0} g\gamma m\dot{\delta}(\tau - t')\chi_{\mathrm{m}}(t - t')dt' \\ &= \begin{cases} -g\gamma m\dot{\chi}_{\mathrm{m}}(t - \tau) & \tau \leq t_0 \\ 0 & \tau > t_0. \end{cases} \end{aligned} \tag{4.21}$$

From this we may determine the matrix H and thus the transformation mapping the uncooled measurement record $\mathbf{x}$ to the virtually cooled record $\mathbf{y}$. From $\mathbf{y}$ we determine the SNR via energy averaging, exactly as in the physical feedback

cooling case.

The only remaining step is to specify values for the relevant parameters, namely ω_{m}, γ and g. We determined these as follows. First, the parameters ω_{m} and γ were roughly estimated from the raw data, and then the gain g was varied in order to maximise the associated SNR. The estimates of ω_{m} and γ were then repeatedly adjusted, interleaved with optimisation of g, in order to maximise the peak SNR. The final values we used were $\omega_{\mathrm{m}}/2\pi = 339.61\,\mathrm{kHz}$, $\gamma/2\pi = 0.54\,\mathrm{kHz}$ and $g = 55$.

Sample traces filtered with this method are shown in Fig. 4.11. We see that the virtual cooling is effective at damping the motion while turned on. After the cooling is turned off we observe similar behaviour to the physical feedback cooling case: with no signal the oscillations gradually increase in amplitude back to what we would observe with no cooling, while with signal the oscillator quickly responds to the force and the oscillations closely match what we would have observed without any feedback. Therefore, as with physical feedback cooling, we expect an enhancement in SNR in the period immediately after the cooling is switched off, since this corresponds to reduced noise but largely unaffected signal.

4.3.3 Kalman filtering

The final approach to sensitivity enhancement that we consider takes a slightly different approach.

Estimation via prediction

Feedback cooling attempts to improve the sensitivity of energy averaging by reducing the energy of the oscillator in the absence of a signal and thus reducing the noise. An alternative method for improving sensitivity is to integrate a quantity other than the raw oscillator energy. Indeed, it is not surprising that simply integrating the raw energy is suboptimal, since this approach makes no use of the knowledge of the prior state of the system—in particular, it ignores the fact that the oscillator will continue to oscillate in the same manner (with a gradual decay in amplitude) unless acted on by an external force. This observation suggests that an alternative approach to detecting a force is to predict how we expect the oscillations to continue, and track the difference between these and the actual

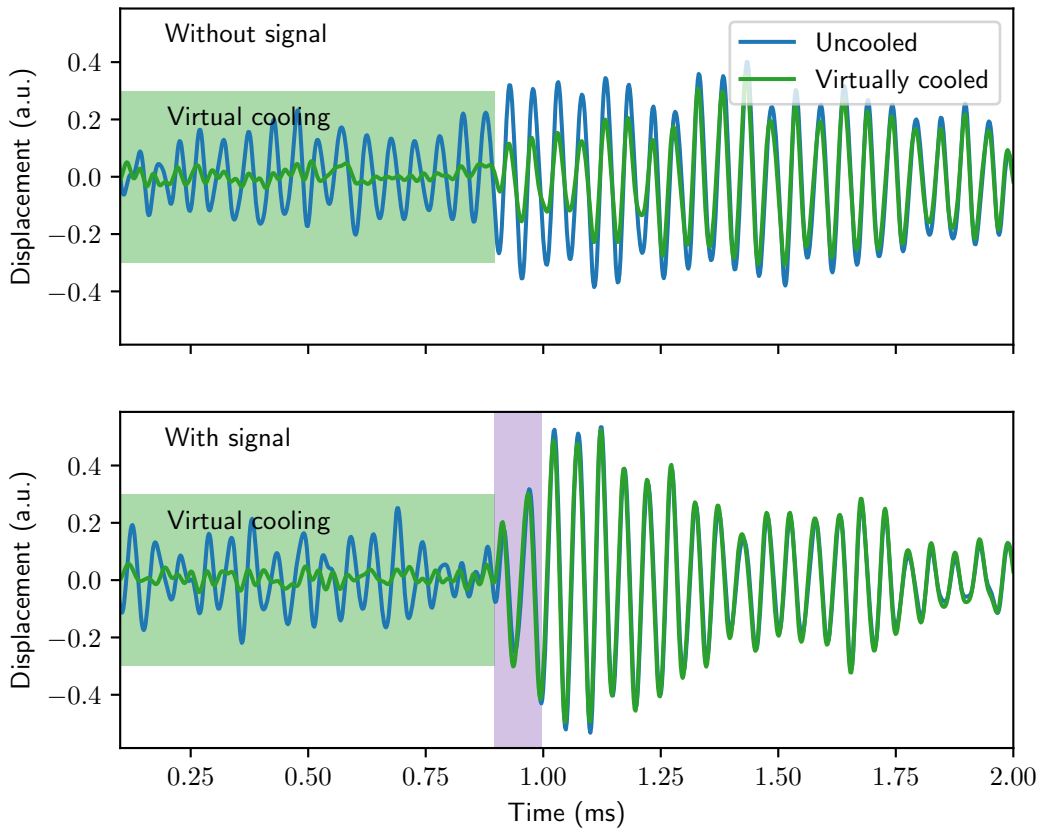

Figure 4.11: Sample traces without and with signal for virtual cooling, showing both the unfiltered and filtered measurement records. The green shading indicates when virtual cooling is applied.

oscillations.

More quantitatively, let us consider the displacement $x(t)$ of the oscillator in the presence of thermal noise and (potentially) an impulsive force. As in Section 4.2.5 we may write $x(t) = \tilde{x}(t) + x_F(t)$, where $\tilde{x}$ describes the motion due only to thermal forces and x_F describes the response of the oscillator to the impulsive force. We observe x, and our goal is to determine x_F.

If we use feedback cooling then $\tilde{x}(t) \approx 0$ (for suitable t) and thus $x(t) \approx x_F(t)$, which is to say the observed signal is a good proxy for the signal of interest.

Instead let us suppose that $\tilde{x}(t)$ is large but we have some prediction $\tilde{x}'(t)$ of $\tilde{x}(t)$, and consider the observed prediction error $\Delta(t) := x(t) - \tilde{x}'(t) = (\tilde{x}(t) - \tilde{x}'(t)) + x_F(t)$. In particular, if the prediction accurately models $\tilde{x}(t)$ at some time t then we have $\Delta(t) \approx x_F(t)$ and, just like with feedback cooling, the known signal $\Delta(t)$ is a good estimator for $x_F(t)$. That is, by predicting the oscillations we would expect in the absence of any signal, and then comparing this prediction to what we actually observe, we obtain a better estimate of the contribution of the signal.

To apply this scheme in our situation, then, based on the measurements over the initial $\sim$1 ms prior to the pulse arrival we must build up a prediction of the oscillator's future trajectory (assuming that it continues to experience only thermal noise). Then, after the time of the pulse arrival, we track the phase-space distance between this prediction and the measurement. When no pulse is applied we expect the prediction to be accurate, leading to low noise, while if there is a pulse then we expect a large prediction error and correspondingly large signal.[3] To determine this prediction we use a *Kalman filter*[165].

Kalman filters

The Kalman filter is an algorithm that processes a noisy sequence of measurements of a linear system with known dynamics in order to keep track of a statistically-optimal estimate of its underlying state. In this section we give the basic ideas behind the Kalman filter as they pertain to our implementation, and refer the reader to one of the many introductory works on the topic for addi-

[3] We can actually consider feedback cooling to be a special case of this prediction scheme—by pre-cooling the oscillator its predicted trajectory becomes simply $\tilde{x}'(t) \equiv 0$, so the observed trajectory is identical to the "prediction error". Indeed, the fundamental idea behind both methods is the same: the knowledge gained by measuring the system prior to the signal arrival can be used to partially eliminate the noise contribution from the pre-existing oscillations.

tional background (see, for example Lewis et al.[176], Welch and Bishop[177] or Haykin[178]). The treatment given here is based on Lewis et al.[176].

We consider a system described at each timestep k by some underlying state vector $\mathbf{x}_k \in \mathbb{R}^n$, evolving linearly in time according to

$$\mathbf{x}_{k+1} = F_k \mathbf{x}_k + \mathbf{w}_k, \tag{4.22}$$

where F_k is the state transition matrix and $\mathbf{w}_k$ is the process noise term, which is taken to be Gaussian with mean 0 and covariance Q_k. Measurements of the state are made by observing a vector

$$\mathbf{z}_k = H_k \mathbf{x}_k + \mathbf{v}_k, \tag{4.23}$$

where H_k maps states into actual observations (which may not reveal all the information about the state) and $\mathbf{v}_k$ is the measurement noise term, taken to be Gaussian with mean 0 and covariance R_k. The Kalman filter tracks an estimate $\hat{\mathbf{x}}_k$ of the underlying state together with a covariance P_k describing the estimated accuracy of the state estimate $\hat{\mathbf{x}}_k$. As a concrete example, in a harmonic oscillator system the state vector might consist of the particle's location in phase-space, with the observation matrix extracting the displacement. The Kalman filter produces estimates of the phase-space location at each point in time (together with an estimate of the uncertainty in that estimation).

At each timestep the filter typically proceeds in two stages. In the first, the "predict" stage, it makes an *a priori* prediction $\hat{\mathbf{x}}^-_{k+1}$ about the system state (together with an *a priori* covariance P^-_{k+1}) based on the previous estimate and the known dynamics. More precisely, it computes the quantities

$$P^-_{k+1} := F_k P_k F_k^T + Q_k \tag{4.24}$$

$$\hat{\mathbf{x}}^-_{k+1} := F_k \hat{\mathbf{x}}_k. \tag{4.25}$$

In the second, the "update" stage, the filter receives a new measurement $\mathbf{z}_{k+1}$ and combines this with the *a priori* prediction $(\hat{\mathbf{x}}^-_{k+1}, P^-_{k+1})$ to obtain an *a*

posteriori estimate $(\hat{\mathbf{x}}_{k+1}, P_{k+1})$. That is,

$$K_{k+1} := P^-_{k+1} H^T_{k+1} \left(R_{k+1} + H_{k+1} P^-_{k+1} H^T_{k+1}\right)^{-1} \tag{4.26}$$

$$P_{k+1} := \left(I - K_{k+1} H_{k+1}\right) P^-_{k+1} \tag{4.27}$$

$$\hat{\mathbf{x}}_{k+1} := \hat{\mathbf{x}}^-_{k+1} + K_{k+1} \left(\mathbf{z}_{k+1} - H_{k+1} \hat{\mathbf{x}}^-_{k+1}\right), \tag{4.28}$$

where K_{k+1} is known as the *Kalman gain*. The Kalman gain determines the weighting applied to the measurement error, taking into account the uncertainties in both the prediction and the measurement, so that a highly certain prediction or measurement is weighted more strongly (and conversely). The filter proceeds iteratively, with the *a posteriori* estimate computed in one timestep being used as the initial state for the next.

Importantly, while these two stages usually alternate it is not necessary that they do so. In particular, at any point we may disable the update stage (Eqs. (4.26) to (4.28)) and instead start using the filter as a pure predictor:

$$P_{k+1} := P^-_{k+1} \tag{4.29}$$

$$\hat{\mathbf{x}}_{k+1} := \hat{\mathbf{x}}^-_{k+1}. \tag{4.30}$$

That is, to use the Kalman filter in the force sensor we perform alternating predict/update stages up until the time of signal arrival, and after that perform only predictions.

Implementation of the Kalman filter

Our code is available on GitHub[179], and we refer the reader there for the full implementation details. Here we describe the most important points.

We consider the system to be a standard damped harmonic oscillator, so as mentioned in the previous section the state consists of the position x and velocity $\dot{x}$. We discretise to 1000 timesteps of duration $dt := 2\,\mu\text{s}$ each, meaning

$$\mathbf{x}_k := \left[x(k\,dt)\ \dot{x}(k\,dt)\right]^T \tag{4.31}$$

for $0 \leq k < 1000$. For the initial state $\mathbf{x}_0$ we used the actual position and velocity calculated from the first two data points for each trace, although we note that in practice it was sufficient to initialise both components to 0.

The standard discretised state propagation matrices for a harmonic oscillator were used, with system parameters ω_{m} and γ initially estimated from the raw data and then repeatedly adjusted in order to maximise performance across all traces. The final values used were $\omega_{\mathrm{m}}/2\pi = 339.65\,\mathrm{kHz}$ and $\gamma/2\pi = 0.56\,\mathrm{kHz}$. Note that these values differ slightly from those used for virtual cooling ($\omega_{\mathrm{m}}/2\pi = 339.61\,\mathrm{kHz}$ and $\gamma/2\pi = 0.54\,\mathrm{kHz}$). This difference is most likely due to a small amount of over-fitting: when selecting parameters to maximise SNR calculated over noisy data, it is possible to choose parameters that exploit any biases in the noise in order to extract a higher SNR than what would be obtained with perfectly accurate parameters. Moreover, the perturbations to the parameters required for over-fitting depend entirely on the specifics of the filtering method, so it is not surprising that the Kalman filter and virtual cooling yield slightly different parameters. Indeed, the fact that the parameters still match very closely indicates that any over-fitting effect was largely negligible.

We assumed the process noise $\mathbf{w}_k$ to be a random force applied to the oscillator. Its variance was determined by simulating the behaviour of an oscillator in the presence of such a force and choosing a variance yielding traces that looked qualitatively similar to the actual traces. This value was fine-tuned to optimise performance, but we found the initial estimate to be effectively optimal.

Sample filtered traces are shown in Fig. 4.12. We see that the filter closely tracks the observed position while the updating is switched on. After the updating is turned off in the absence of signal the quality of the prediction gradually decreases as the thermal noise slowly perturbs the system. When a force is applied, however, the observed trajectory quickly deviates from the prediction, leading to a large prediction error and hence a large detected signal. We note the similarity between the prediction error of Fig. 4.12 and the cooled traces of Figs. 4.10 and 4.11.

4.3.4 Results

In this section we present the results of applying the above enhancement strategies to the basic force sensor.

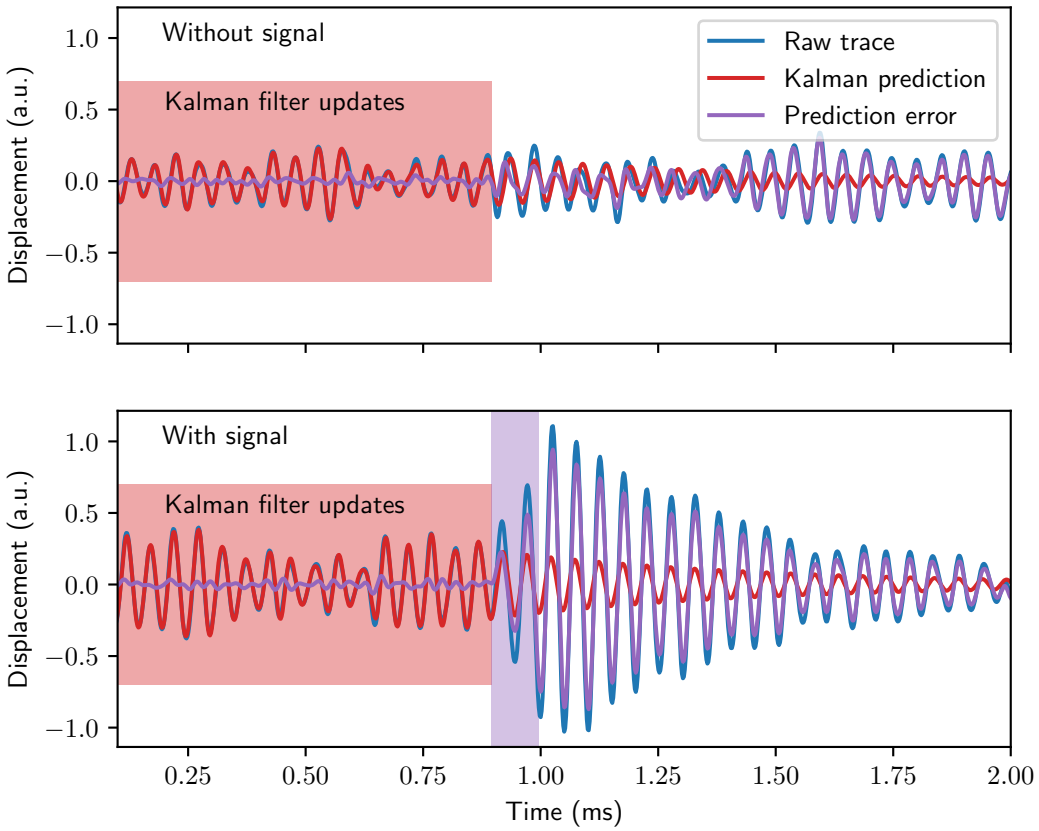

Figure 4.12: Sample traces without and with signal for Kalman filtering, showing the raw trace, the Kalman filter prediction and the prediction error. The prediction error is defined as the difference between the raw trace and the Kalman filter prediction. The red shading indicates the period in which the Kalman filter is updated with measurements. After this period no new data are passed to the filter, and it makes predictions based solely on the measurements made in the red area.

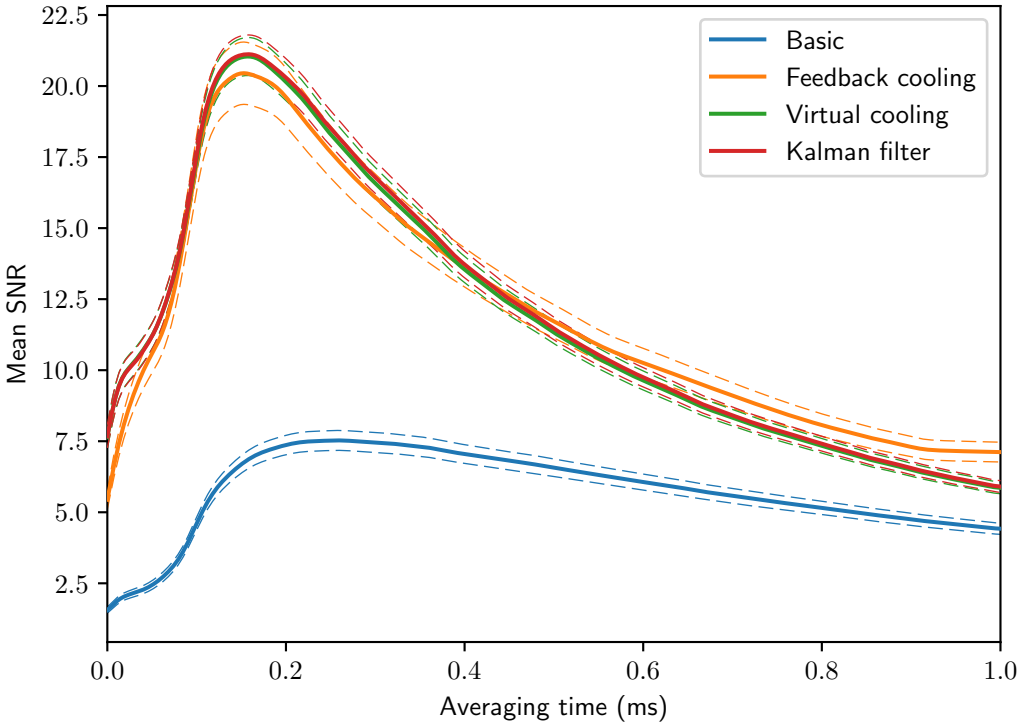

Figure 4.13: Comparison of mean SNR for different methods. The dashed lines represent the standard deviation of the mean (estimated from 150 traces).

SNR

A comparison of the SNRs obtained from the above methods is shown in Fig. 4.13. All three methods provide a significant improvement over the basic system, thus demonstrating that with non-stationary feedback and estimation strategies it is indeed possible to obtain an enhancement in SNR. We see that physical cooling, virtual cooling and Kalman filtering all achieve a peak SNR of roughly 21, compared to the 7 attained by the basic energy averaging method.

Per-trace SNR enhancement

For the filtering methods—virtual cooling and Kalman filtering—we can consider an additional measure of performance. Specifically, for each individual trace we can determine the improvement in SNR obtained by filtering that trace as compared to performing basic energy averaging. Note that we cannot calculate this quantity for physical feedback cooling, since for a cooled trace there is no corresponding "uncooled" trace. These results are shown in Fig. 4.14.

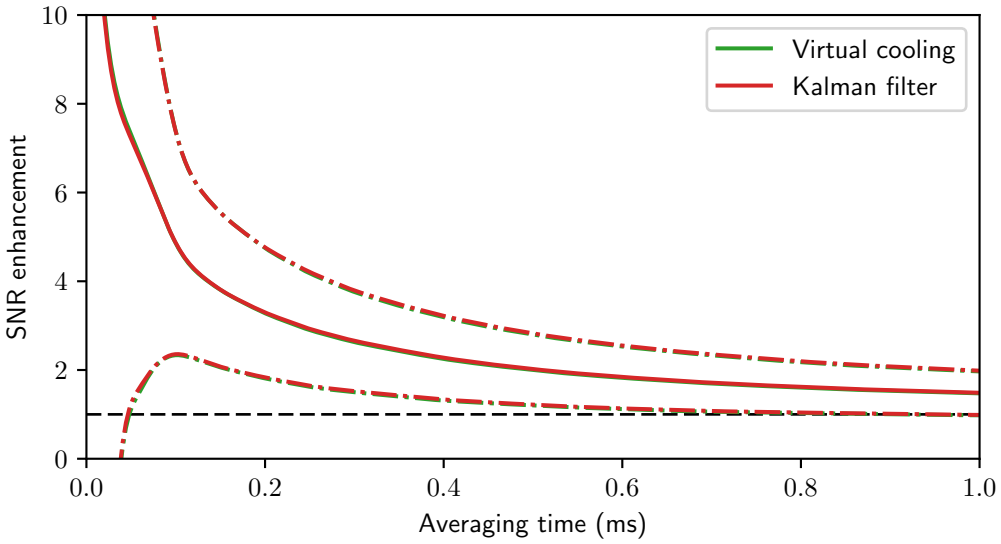

Figure 4.14: Mean SNR enhancement factor for filtering methods. For each trace, the enhancement factor is defined as the SNR for that trace obtained with the filtering method divided by the SNR for that trace obtained with basic energy averaging. The dashed lines represent the per-trace standard deviation (calculated from 150 traces).

Force resolution

To obtain the force resolution using feedback cooling, virtual cooling or Kalman filtering we simply scale down the raw force resolution (as described in Section 4.2.5) by the square root of the ratio of SNR to the basic energy averaging SNR. This process yields the results shown in Fig. 4.15, and suggests an optimal force resolution below 2×10^{-16} N for all three improved methods.

4.3.5 Discussion

We have seen that all three methods—feedback cooling, virtual cooling and Kalman filtering—provide a significant improvement in sensitivity over the basic energy averaging approach, but there are some interesting observations that warrant further discussion.

Apparent signal enhancement

We have explained why all three methods lead to a significant decrease in noise, at least for short averaging times, and we have observed a corresponding increase in

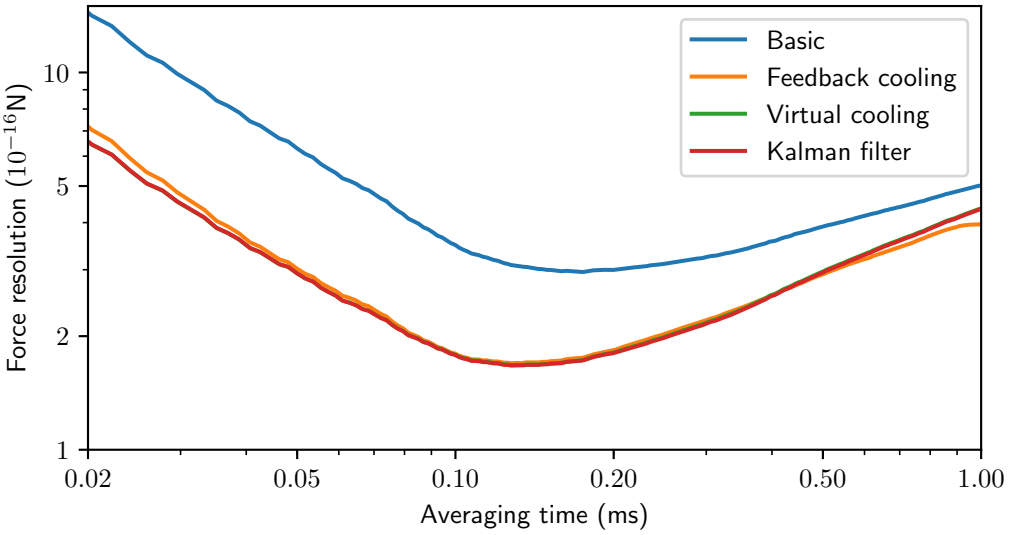

Figure 4.15: Estimated force resolution for each method.

SNR. Despite the improved SNR we would also expect a slight decrease in signal when using feedback cooling or filtering: on average, the energy of the oscillator is obtained by adding the energy due to the signal to the energy already present in the system (see Eq. (4.8)), so if the latter is minimised (either by physical cooling or filtering) then the signal should slightly decrease. SNR is still improved since the relative reduction in noise is much larger.

We may inspect the noise and signal individually, as shown in Fig. 4.16. We first see that, as expected, all three methods reduce the noise. More interestingly, they also appear to increase the size of the extracted signal. We note that the effect is particularly strong for feedback cooling, and we will discuss this further in the next section. However, even the relatively small signal increase observed for virtual cooling and the Kalman filter is somewhat surprising, since it is opposite to what we would expect.

The reason this effect is possible is interference. If the response of the system to the signal is out of phase with the existing thermal oscillations then the two contributions destructively interfere. If the effect of the existing oscillations is eliminated (either by minimising them via feedback cooling or filtering them away via prediction) then no destructive interference occurs, and a larger signal is observed. An example showing these effects is given in Fig. 4.17.

Despite this argument it is still surprising that we see the filtering methods

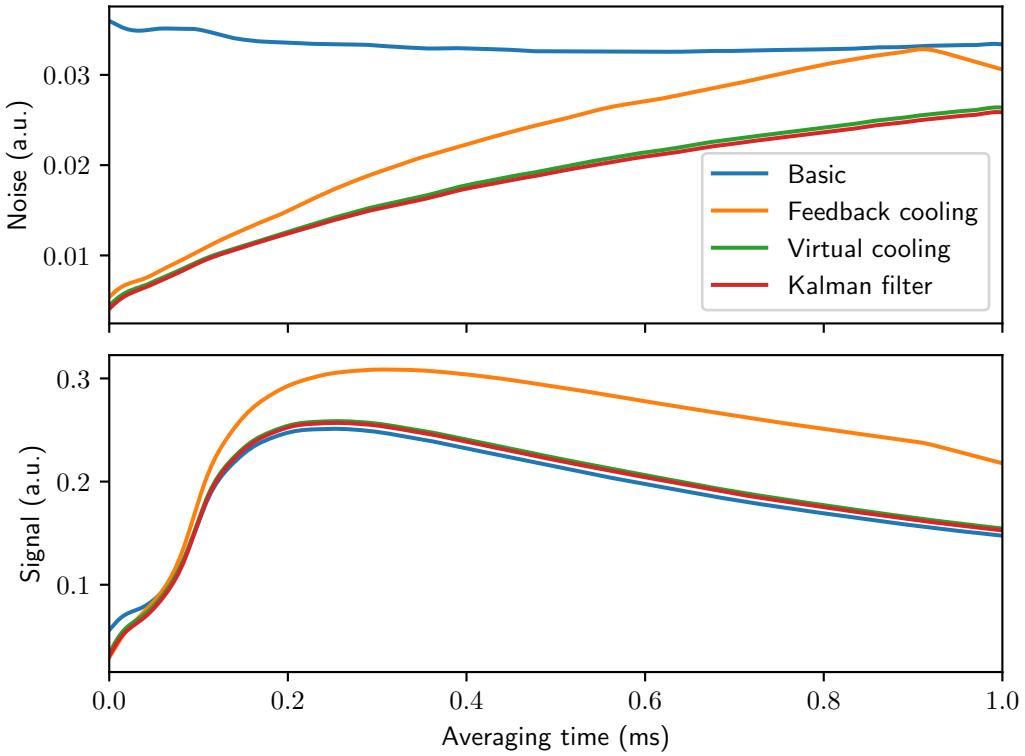

Figure 4.16: Comparison of mean noise and signal for each method, averaged over 150 traces. All quantities are measured in the same arbitrary energy units.

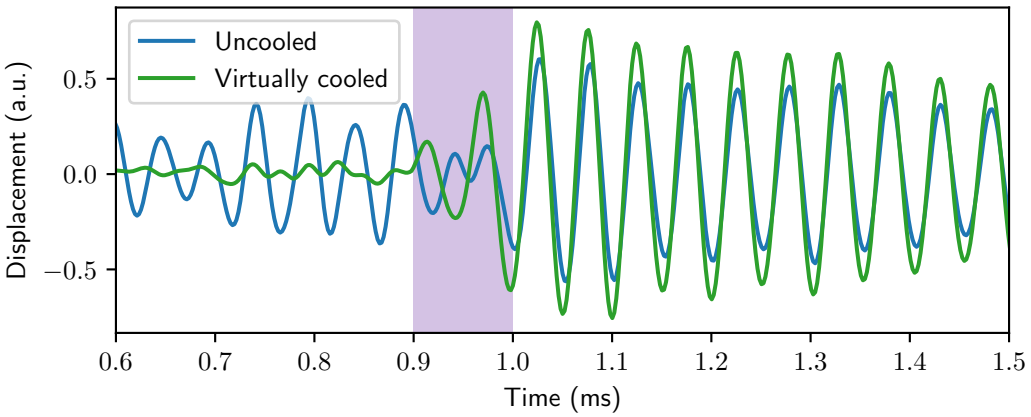

Figure 4.17: Demonstration of how destructive interference of the signal with the pre-existing thermal oscillations can be eliminated with virtual cooling (a similar effect occurs with both physical feedback cooling and Kalman filtering). The thermal oscillations prior to the signal arrival are out of phase with the signal, leading to an initial reduction in energy for the unfiltered trace. With virtual cooling, the filtered oscillator is almost at rest when the signal arrives, so no destructive interference occurs and the observed energy is larger.

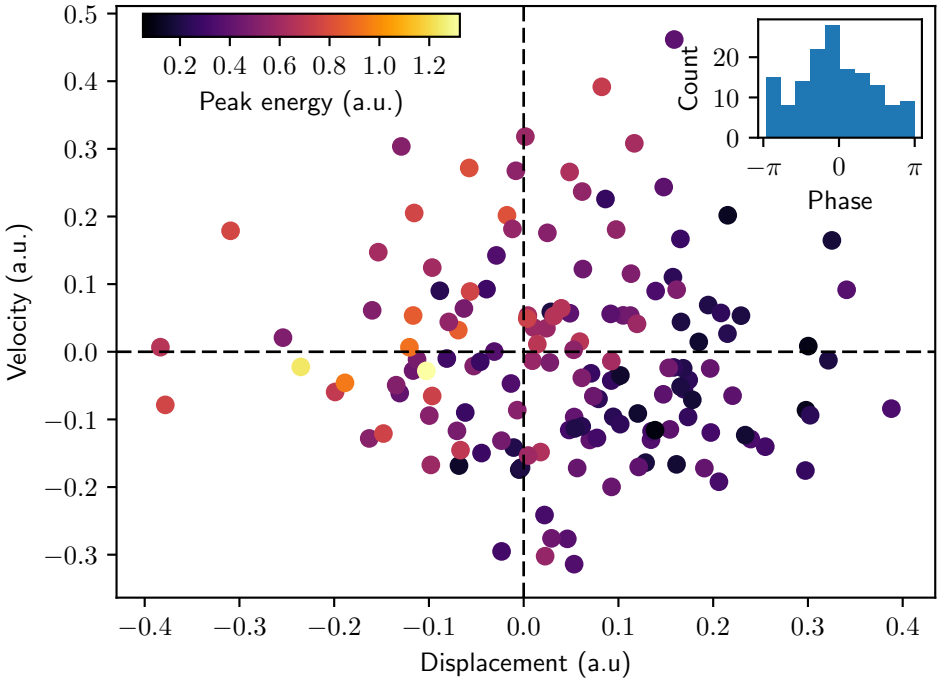

Figure 4.18: Location in phase space immediately prior to signal arrival, for unfiltered traces without feedback cooling. The colours indicate the maximum energy attained by the oscillator after signal arrival. The inset shows a histogram of the phases.

give an increased signal on average. While destructive interference is possible, we would expect *constructive* interference just as often—assuming the signal always arrives with the same phase, the type of interference depends only on the phase of the existing thermal oscillations, and we would expect that phase to be random. Thus, as described above, for random phases we would expect the signal to *decrease* if the thermal oscillations were suppressed. However, we found that in our experiment the phases of the thermal oscillations were *not* random.

To see this, we can look at the distribution of locations in phase space just before the pulse arrives, as shown in Fig. 4.18. We first observe that, generally speaking, points in the left half-plane achieve a higher energy than those in the right half-plane, suggesting that constructive interference tends to occur in the left half-plane and destructive interference occurs in the right. Moreover, the distribution of points between the half-planes is unequal—significantly more points appear in the right half-plane and thus experience destructive interference.

The reason for this discrepancy appears to be as follows. For each of the four

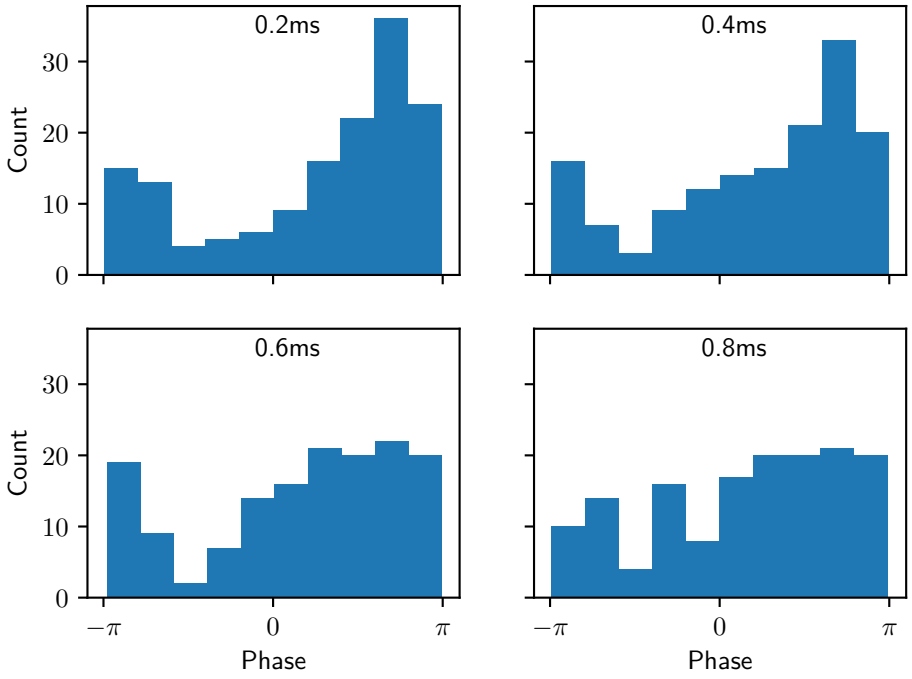

Figure 4.19: Histograms of phases at specific points in time before signal arrival for unfiltered traces without feedback cooling.

experimental configurations (determined by the presence and absence of feedback and signal) the system was set up to run in cycles: 1 ms of either no actuation or feedback, followed by 0.1 ms of either no actuation or the signal, followed by a further 0.9 ms of no actuation, and then immediately repeating from the first step. In particular, for the uncooled signal data, if insufficient phase noise built up over the 1.9 ms period between the signal of one cycle and the next (which is possible, given the linewidth of <1 kHz) then the phase of the thermal oscillations prior to signal arrival would be influenced by the phase of the signal in the previous cycle. Since the signals had a consistent phase, this would cause a bias in the phase of the thermal oscillations. To add further credence to this hypothesis we plot histograms of the phases at different times leading up to the application of the signal, as shown in Fig. 4.19. These indicate that the phase distribution spreads out over time, but there is still a noticeable bias when the signal arrives.

To estimate the effect of this discrepancy on the results we may proceed as follows. We divide the traces with signal into 10 buckets based on their phase immediately prior to signal arrival, as in the inset of Fig. 4.18. We then calculate the signal for each trace as usual, but when calculating the overall signal we first

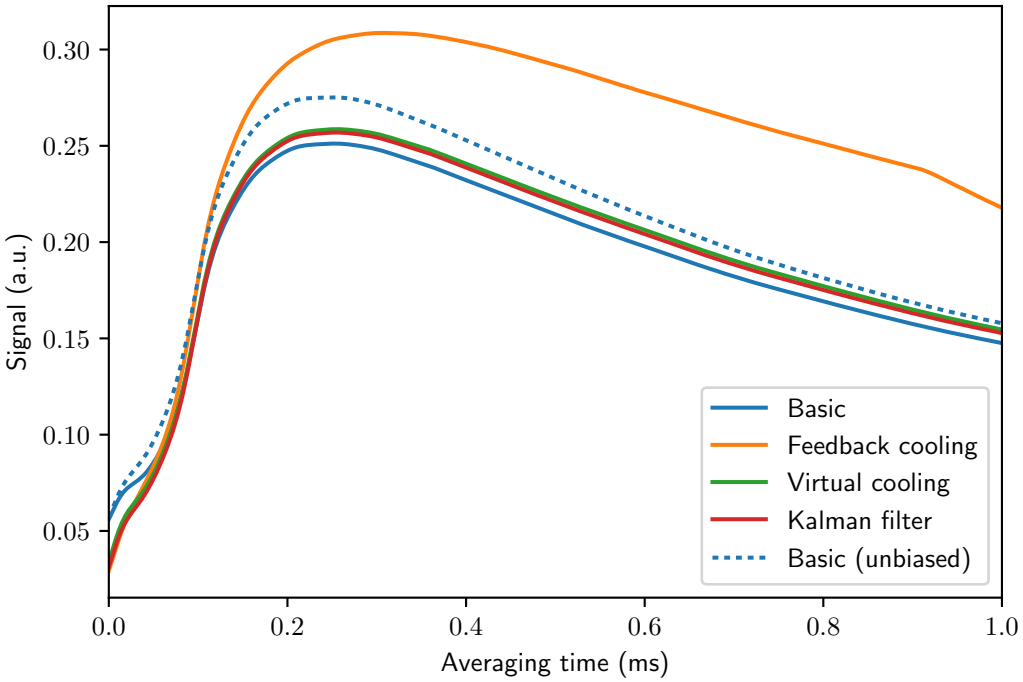

Figure 4.20: Average signals for each method, including for basic energy averaging when corrected for the phase bias.

average within each bucket and then average over the buckets. That is, we ensure that the contribution of each bucket to the overall result is equal, as opposed to the contribution of each trace being equal. The results of this procedure are shown in Fig. 4.20. We see that, as expected, when the phase bias is corrected the signal for basic energy averaging is slightly higher than that obtained with Kalman filtering and virtual cooling (we will discuss the situation for physical feedback cooling in the next section).

We note that while this effect has caused an artificial reduction in the apparent force sensing performance of basic energy averaging (Figs. 4.13 to 4.15) the effect is not major—correcting for the bias increases the peak SNR from 7 to roughly 7.5, compared to around 21 for the improved methods.

To conclude this section we observe that this issue suggests another advantage of feedback cooling and filtering methods over raw energy averaging: using these methods the system *can* be run in rapid cycles without needing to worry about the effect of one cycle on the next.

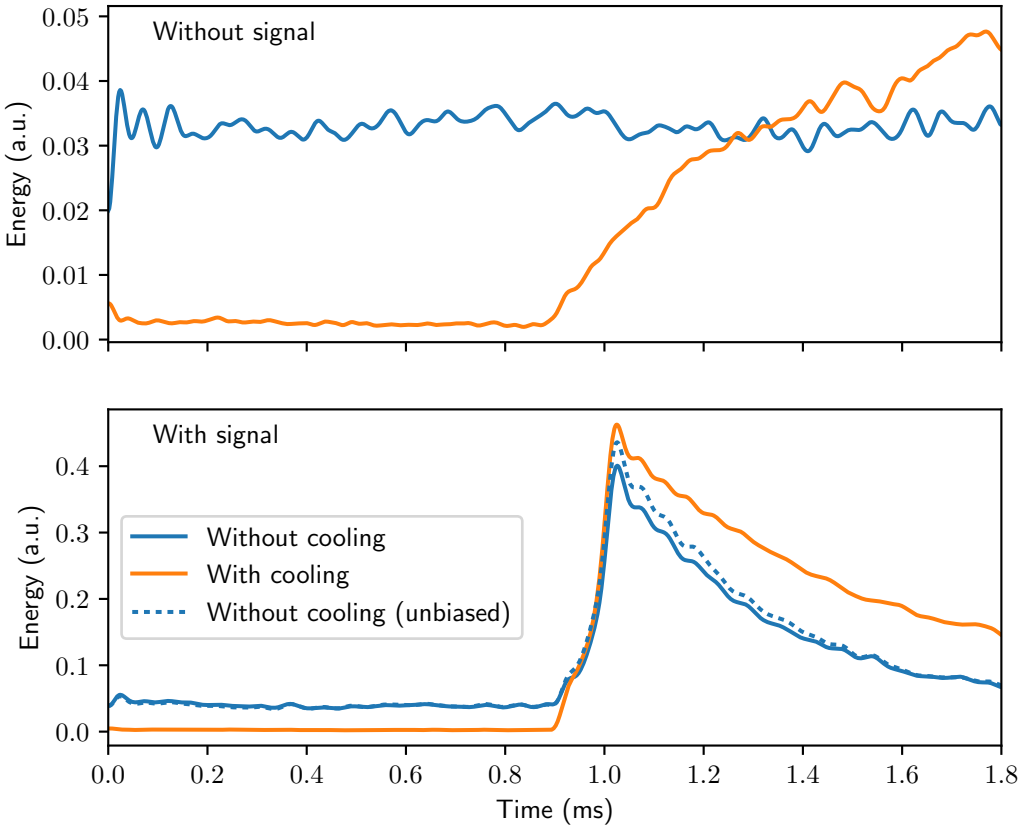

Figure 4.21: Oscillator energy in the absence and presence of signal, without and with feedback cooling. The energies at each point in time are averaged over 150 traces.

Increased steady-state noise with feedback

As we have discussed in Section 4.2.4, the feedback cooling of the nanowire's vibration occurs via the bolometric force as a result of a rise in bulk temperature of the nanowire—that is, the vibrations are cooled by heating the nanowire. We would therefore expect that, after the feedback cooling is turned off, there would be more energy in the system and thus the steady-state noise would be higher. Plotting the energy as a function of time in the presence and absence of feedback in Fig. 4.21 we see that, indeed, when the oscillator rethermalises after feedback cooling it has larger thermal vibrations (even after accounting for the aforementioned phase bias in the case of an applied signal). It is possible that this effect is what causes the virtual feedback cooling and Kalman filtering to yield slightly higher peak SNRs than physical feedback cooling.

Interestingly, it is clear from Fig. 4.21 that the discrepancy between the steady-state noises with and without feedback is significantly larger in the case of an applied signal. As with feedback, when a signal is applied there is more energy in the system and thus the steady-state noise is slightly higher, but we would not expect this to cause a larger discrepancy between the feedback and non-feedback cases. This observation indicates that there is a non-linearity in the system, whereby the steady-state heating effect of the feedback laser is magnified when there is also such an effect due to the signal laser. Further analysis and experimentation would be necessary to determine the physical source of this non-linearity.

We note that this non-linearity is likely the cause of the apparent superior performance of feedback cooling at long averaging times presented in Section 4.3.4. The relative increase in steady-state energy in the case of an applied signal would lead to a slower decrease in average energy after the signal was turned off (shown in Fig. 4.21), which in turn is consistent with the slower decay in SNR and resolution observed in Figs. 4.13 and 4.15.

These observations highlight an important advantage of filtering methods over physical feedback cooling (or, more generally, numerical post-processing methods over techniques requiring changes to the actual experimental setup): the chance of unexpected interactions between subsystems is significantly reduced.

Extended Kalman filter for tracking frequency noise

Nanomechanical oscillators, in addition to being highly susceptible to thermal noise, can exhibit low-frequency drifts of resonance frequency[180–183]. To determine whether our system was affected by such noise we implemented a second Kalman filter which, unlike the original filter, includes the oscillator's resonant frequency and linewidth in the state vector. This allows uncertainty in these parameters to be modelled, which in turn allows the parameters to be fitted by the filter for each individual trace. For oscillators under the influence of parameter drift this approach should thus yield superior results relative to those obtained with a Kalman filter using fixed parameters.

There is a complication, which is that when the state vector includes the system parameters the dynamics of the system become non-linear, and the Kalman filter is defined only for linear systems. However, by linearising about the estimated state at each timestep one obtains an algorithm capable of filtering non-

linear systems, at the expense of the optimality properties of the standard Kalman filter. This is known as the *extended Kalman filter*[176].

Our implementation of the extended Kalman filter, available on GitHub[179], is based on the descriptions by Lewis et al.[176] and Casper[184]. We refer the reader to those references for the full details.

To fit the filter we used the optimal parameters for the original linear Kalman filter described in Section 4.3.3, and then attempted to adjust the uncertainties of the resonant frequency and linewidth in order to maximise SNR. However, we found that negligible improvement was attainable over simply using uncertainties of zero (in which case the filter reduces to the standard linear Kalman filter), suggesting that the nanowire in our system was not affected by low-frequency parameter drift.

4.4 Conclusion

We have presented an ultra-sensitive nanowire-based sensor for impulsive forces, and demonstrated three distinct but related approaches to improving its sensitivity. First, by employing a non-stationary physical feedback cooling strategy—capable of cooling the effective temperature to $\sim$10 K from room temperature—the vibrations of the nanowire can be suppressed immediately prior to the arrival of the force, meaning the thermal effects are lessened while the force is being applied. This leads to a reduced noise and thus increased SNR. Next we verified the result of Harris et al.[92] in the non-stationary regime, by simulating the aforementioned physical feedback protocol during post-processing of the data obtained in the absence of any physical feedback. Finally, we implemented a Kalman filter-based estimator, again with non-stationary behaviour, which extracts a signal by predicting the future trajectory of the oscillator (under the assumption of no applied force) and comparing this prediction with the actual trajectory. All three of these methods yielded peak SNRs close to 21, a factor of roughly 3 higher than that obtained using energy averaging with no feedback cooling. We estimate that using any of these three methods the sensor can detect forces as small as 2×10^{-16} N.

We have thus demonstrated that, as predicted by Vitali et al.[160], the SNR obtained using energy averaging can be improved via a non-stationary feedback cooling protocol. In addition, a comparable enhancement can be achieved in the

absence of any feedback cooling by utilising more sophisticated estimators—such as Kalman filtering or virtual feedback cooling—during post-processing.

Comparing physical feedback cooling with the post-processing methods, the primary advantage of the former is that it requires relatively little knowledge of system dynamics and parameters—the system itself perfectly "predicts" its future behaviour—while effective post-processing requires detailed knowledge of the system dynamics and careful parameter tuning in order to perform well. However, post-processing is more flexible and has the advantage that it requires no physical changes to the system. Not only does the latter typically allow for simpler apparatus, but it can help avoid unexpected noise sources introduced by the feedback system (such as the increased nanowire temperature in our experiment, for example).

There are many avenues for further investigation associated with this work. Perhaps the most obvious potential incremental improvement is the integration of a Kalman filter into the physical feedback cooling protocol. The use of a Kalman filter could reduce the impact of measurement noise and thus potentially improve the performance of feedback cooling. More significant improvements may be possible by making more radical changes to the post-processing techniques. Specifically, all the methods we have discussed so far essentially reduce to *filtering*—that is, estimating a quantity at some time based on the prior measurements—and thus could in theory be performed in real time (indeed, the physical feedback cooling *was* performed in real time). However, if we are happy to rely on post-processing then we could instead consider *smoothing*, where we may additionally rely on future measurements when estimating the value of a quantity at a particular time[176]. A smoothing algorithm would have access to more information than a filtering algorithm, so would intuitively be able extract a higher SNR and thus achieve further performance improvements[185–187].

Chapter 5

Automated optimisation with machine learning

So far in this thesis we have considered three different classes of system, and three corresponding optimisation techniques. Generally speaking, from chapter to chapter the systems have become more intractable to useful theoretical analysis, and the optimisation procedures accordingly more general. In this chapter we extend this line of reasoning to the extreme, by considering the problem of automated optimisation of arbitrary physical systems. We introduce an algorithm to perform such optimisation, and demonstrate its potential by optimising a magneto-optical trap used for a quantum memory.

In Section 5.1 we provide some background on the general problem of automated optimisation, with a focus on quantum systems, and discuss the current state of the field. In Section 5.2 we give a brief introduction to the relevant concepts from machine learning, and then describe the algorithm we have developed. In Section 5.3 we present and discuss the results of applying the algorithm to the magneto-optical trap. Finally, in Section 5.4 we give some concluding remarks together with a brief discussion of the extensive potential for future work in this domain.

The machine learning algorithm described in Section 5.2 was developed in close collaboration between myself and Michael R. Hush. The experimental setup described in Section 5.3.2 was performed primarily by Aaron D. Tranter, Pierre Vernaz-Gris, Jesse L. Everett and Anthony C. Leung (and many others have contributed to earlier versions of the system over the course of several years). The analysis presented in Section 5.3.4 was performed in collaboration between

myself, Aaron D. Tranter, Michael R. Hush and Geoff T. Campbell.

5.1 Background

We have discussed several different approaches to optimisation of physical systems, but all of them have required some degree of detailed understanding of the system dynamics. When such understanding is not present, either because the system is particularly complex or simply because it is not yet well-understood, we must revert to a process known as *online optimisation*, where performance is improved via repeated interactions with the system.

The most basic form of online optimisation, and one which takes place in almost every experiment, is manual tuning of parameters. In optics this could be the alignment of a cavity to maximise transmission, for example. While this approach certainly has its place, when there are any more than a few independent parameters the space becomes too large to explore by manual brute force search. In this case the standard procedure is to fall back to intuition or approximate theory, and again, while this approach is often useful it tends to fall down when the system becomes moderately complex.

When neither manual tuning nor intuition is feasible, we must turn to some form of automated optimisation, where control of the system is given over to an algorithmic process that accepts inputs from the system (and/or the experimentalists) and, based on these inputs, adjusts the parameters of the system. That is, we must implement a certain type of optimising control system.

Control theory has a long and rich history, and has been successfully applied to a huge range of fields, but for concreteness we will focus our attention on its uses in optimising molecular-scale physical systems. Such systems are particularly interesting for a variety of reasons: their dynamics are usually governed by quantum mechanics, meaning theoretical treatments are often impractical for even moderately large or complex systems due to the exponential growth of the Hilbert space[188]; they are typically associated with small timescales, which means that optimisation via repeated experimentation may be relatively time-efficient; and finally, human intuition is often useless or even actively misleading. Note that simple control systems are already used in almost all such systems—laser frequency locking[189] is ubiquitous, for example, and the feedback cooling from Chapter 4 is a more specialised case—but we are interested in more complex

situations where multiple parameters must be adjusted together.

5.1.1 Quantum control

The first suggestions of control systems for quantum systems were in the 1980s, when it was shown that certain optical pulses could be used to engineer the likelihoods of particular molecular transitions[190–195]. These results were soon generalised to show that the choosing of an external control field to achieve a desired quantum state transition reduces to a minimisation problem over function spaces[196–198]. This approach is *open-loop* control—an optimal pulse sequence is first determined offline, and then later applied to the experiment. However, this requires significant knowledge of the dynamics of the system in order to determine (analytically or numerically) the optimal field accurately, so can become infeasible for even moderately complicated systems.

In the early 1990s it was suggested by Judson and Rabitz[199] that this issue could be avoided by utilising a *closed-loop* system, in which results from the experiment are fed back into the control system. The control system performs a similar optimisation procedure to that used when determining fields to use with open-loop control, but now the optimisation is performed automatically by the control system by feeding results from the experiment into a learning algorithm; that is, a form of automated online optimisation is used. In this way the experiment itself is used to exactly "evaluate" its own Schrödinger equation, thus avoiding the need to have a good theoretical understanding of the system dynamics.

The learning algorithm suggested by Judson and Rabitz[199] is a basic *genetic algorithm*. Different optical pulse sequences, "individuals", are represented by binary numbers, and an initial random population of individuals is iteratively evaluated by running the experiment and measuring a "fitness function", which determines the effectiveness of that pulse sequence and is interpreted as the fitness of that individual. Performance can be improved via "evolution": high-performing individuals are left unchanged, and the remaining individuals are divided into pairs and mixed (their binary representations split and recombined). Each individual may also undergo a small random "mutation" (that is, a bit flip) from one generation to the next. Over time the fitness of the entire population tends to increase, ideally converging towards a maximum.

Soon after that seminal proposal, control systems utilising alternative optimisation algorithms were suggested, for example gradient descent based on finite differences[200], simulated annealing[201–203], genetic algorithms with migration[204] and downhill simplex algorithms[205–207]. These were shown to be robust to many types of experimental noise[200, 208, 209].

The first experimental realisations of these protocols appeared in the late 1990s: genetic algorithms for optimising fluorescence[210], second harmonic generation[211], and branching ratios of photodissociation reactions[212]; and simulated annealing for optical pulse compression[203]. In the intervening years the same general approach has been widely applied with great success, using genetic[213–217], downhill simplex[218, 219] and gradient-based[220] algorithms.

Despite their widespread use, however, these algorithms have their drawbacks. Gradient descent is prone to becoming trapped in local minima and, when finite differences are used for evaluating the gradient, requires a large number of experiment evaluations (since each finite differences calculation requires a separate evaluation per dimension). Downhill simplex algorithms avoid the inefficiency of calculating finite differences, but are similarly susceptible to local minima, and more importantly often exhibit slow convergence for high-dimensional problems[221–224]. Genetic and simulated annealing algorithms are designed to locate global optima, but must be carefully tuned[225–227] and again can be expensive in terms of the number of evaluations[227–229]. Depending on the timescale of the experiment these algorithms thus may not be suitable.

5.1.2 Optimisation via machine-learned models

An alternative approach is to perform fewer experiment evaluations at the expense of a higher computational cost on the algorithm side. Specifically, the control system can be used to learn an input-output model describing the output of the experiment for given input parameters, and the model then analysed to determine suitable parameters[230, 231]. There are two ways the model can be used. In the first, the model is inverted, which allows one to determine the inputs necessary to cause the experiment to behave in a certain way[231, 232]. The other approach, useful in the more common scenario in which the exact behaviour of the system is unimportant and instead the goal is only to optimise some cost function, is to use the model to simulate the experiment and then determine

the optimal parameters by optimising the behaviour of that simulation[233, 234]. Optimising the simulation instead of the experiment may be more convenient (if the experiment is slow or expensive to run) or mathematically easier (Jacobians and Hessians may be calculable analytically, for instance).

Another important advantage of this type of algorithm is the construction of the model of the system, which can be inspected manually. While the model cannot (generally speaking) be used directly to extract meaningful physical parameters, it may still provide insight into the dynamics of the system[230, 233].

An alternative to learning a full input-output model of the system dynamics is to specify a certain cost function and learn a model mapping input directly to that cost function[235]. This allows the learning process to be simplified significantly. In the work of Wigley et al.[235] an algorithm based on this approach, using a Gaussian process to learn the model, was used to find optimal evaporation ramps for Bose-Einstein condensate production. With the ramps described by a 16-dimensional parameter space, the Gaussian process-based algorithm converged in only 35 experimental runs, compared to 145 required by the Nelder-Mead downhill simplex algorithm[205]. However, the time required to fit a Gaussian process scales with the cube of the number of experimental runs[236], so this approach is infeasible for experiments with large numbers of parameters (which necessarily require more experimental runs to optimise).

We have filled this gap by implementing a scalable machine learning algorithm for automatic online modelling and optimisation. The algorithm learns a model for the system using an artificial neural network, which can be quickly trained (in linear time with respect to the number of experiment runs) even for high-dimensional spaces. Through repeated interaction with the experiment the algorithm refines its model, and uses this to suggest high-performing parameter sets. We demonstrate the potential of the algorithm by using it to optimise a magneto-optical trap described by a 63-dimensional parameter space.

5.2 A scalable machine learning algorithm for automatic optimisation

In this section we present the machine learning algorithm we have developed for performing automated optimisation of quantum systems. The general form of

the algorithm is as described in Section 5.1.2: by running the experiment the algorithm learns a model of the system, which is then optimised numerically in order to determine a new set of parameters to apply, then the experiment is run with those new parameters, and the results are fed back into the algorithm and the cycle repeats. The core of the algorithm is the function approximator used to model the system, which is a type of *artificial neural network*.

The theory of artificial neural networks is extremely deep, and contains many problem-specific subtleties. Rather than attempting to discuss these in full generality, we first introduce the relevant foundational theory and definitions in the next section, before discussing our specific choices in the subsequent section. We refer the reader to one of the many introductory textbooks on artificial neural networks for a broader introduction to the field (we recommend Goodfellow et al.[237] for a comprehensive account focusing on deep learning, or Bishop[238] for a more general introduction in the context of machine learning).

5.2.1 Introduction to artificial neural networks

At the most general level, the artificial neural network is a model of computation that processes information via a network of connected *neurons*. Typically each neuron performs only a very simple function, but complex behaviour can emerge from the interaction of many neurons. The model is inspired by the brain, with the network of artificial neurons corresponding to the biological neurons connected by synapses in the brain.

While there are many different types of artificial neural network, used to perform a wide range of information processing tasks, we are concerned with only a particularly simple class, namely the *multilayer perceptron*.

Multilayer perceptrons

A multilayer perceptron is a type of artificial neural network that defines a function mapping between Euclidean spaces. It consists of a finite sequence of "layers" of neurons, with directed weighted connections from neurons in one layer to those in the next, as shown in Fig. 5.1.

The first layer is the *input* layer, where external input is applied. Computation proceeds by activating the input neurons, propagating these activations to the first *hidden* layer via the weighted connections, propagating the output of that

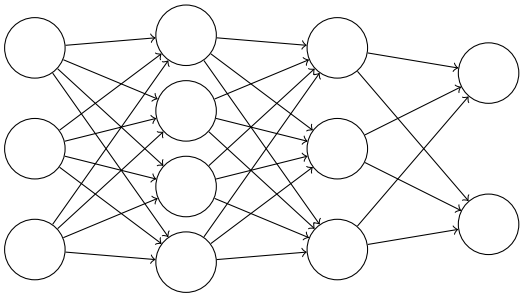

Figure 5.1: Sample multilayer perceptron architecture. The neurons are arranged in layers, and there are directed weighted connections from neurons in one layer to those in the next.

layer to the next layer, and so on until the final *output* layer is activated. The result is then read from the outputs of neurons in the output layer.

More specifically, let the number of non-input layers be $L \geq 1$, and let the dimension of layer l be $D_l \geq 1$ (where the input layer is the 0th layer). We will show how the network can define a function $\mathbf{x} \mapsto \mathbf{y} \colon \mathbb{R}^{D_0} \to \mathbb{R}^{D_L}$.

Denote by $u_i^0 \in \mathbb{R}$ the initial activation applied to the ith neuron of the input layer, and by $\mathbf{u}^0 \in \mathbb{R}^{D_0}$ the vector of these activations (so we have $\mathbf{u}^0 \equiv \mathbf{x}$). Similarly, denote by $z_i^0 \in \mathbb{R}$ the output of the ith neuron of the input layer, and by $\mathbf{z}^0 \in \mathbb{R}^{D_0}$ the vector of outputs (we will explain momentarily how the inputs and outputs are related). For each neuron i of each subsequent layer l we have a real input u_i^l and output z_i^l, and like the input layer we collect these into vectors $\mathbf{u}^l, \mathbf{z}^l \in \mathbb{R}^{D_l}$. The output of the network is simply the output of the last layer, so $\mathbf{y} \equiv \mathbf{z}^L$.

Associated with each neuron there is an *activation function* that determines how that neuron maps input to output. In general these functions can vary from neuron to neuron, but for simplicity we assume that all hidden neurons use a single activation function $\alpha \colon \mathbb{R} \to \mathbb{R}$, and that all input and output neurons use the identity function. That is, we have

$$\mathbf{z}^l = \begin{cases} \alpha(\mathbf{u}^l) & 1 \leq l < L \\ \mathbf{u}^l & l = 0, L \end{cases}, \tag{5.1}$$

where α applies element-wise.

Next we need to define how the output $\mathbf{z}^{l-1}$ of one layer relates to the input $\mathbf{u}^l$ of the next. In the multilayer perceptron model, each component u_i^l is defined

to be the weighted sum of outputs $\mathbf{z}^{l-1}$ from the previous layer plus a bias term, where the weights are taken from the appropriate connections. That is, if for neuron j of layer $l-1$ and neuron i of layer l we denote by $W^l_{ij} \in \mathbb{R}$ the weight of their connection, and we collect these weights into matrices $W^l \in \mathbb{R}^{D_l} \times \mathbb{R}^{D_{l-1}}$, then we simply have $\mathbf{u}^l = W^l \mathbf{z}^{l-1} + \mathbf{b}^l$ (where $\mathbf{b}^l \in \mathbb{R}^{D_l}$ is a vector of biases). Note that the biases can be modelled by an additional neuron with (constant) unit output in layer $l-1$, but for our purposes it is simpler to include them separately.

Putting these together, we have

$$\mathbf{z}^0 = \mathbf{u}^0 = \mathbf{x} \tag{5.2}$$

$$\mathbf{u}^l = W^l \mathbf{z}^{l-1} + \mathbf{b}^l \qquad (1 \leq l \leq L) \tag{5.3}$$

$$\mathbf{z}^l = \alpha(\mathbf{u}^l) \qquad (1 \leq l < L) \tag{5.4}$$

$$\mathbf{y} = \mathbf{z}^L = \mathbf{u}^L, \tag{5.5}$$

which shows how the perceptron yields a function $\mathbb{R}^{D_0} \to \mathbb{R}^{D_L}$, parameterised by the weights and biases.

It is instructive to present a simple example. In Fig. 5.2 we show a sample network complete with weights and biases, corresponding to a function $\mathbb{R} \to \mathbb{R}$. Using a hyperbolic tangent activation function $\alpha \equiv \tanh$, and assuming an initial network activation of $x \in \mathbb{R}$, we have also labelled the input and output for each neuron. Specifically, the input to a neuron is the weighted sum of the outputs of neurons in the previous layer (weighted by the corresponding connections), plus the bias of that neuron. The output of a neuron is obtained by applying the activation function to its input (and we recall that the activation function for the first and last layers is the identity, see Eq. (5.1)). The input to the left-most neuron is defined to be x (the initial activation of the network), and the output of the entire network is defined to be the output of the right-most neuron. Therefore the network represents the function

$$x \mapsto \tanh(0.5x) - \tanh(x - 5) - 1. \tag{5.6}$$

In terms of the formalism above, we have $L = 2$, $D_0 = D_2 = 1$ and $D_1 = 1$.

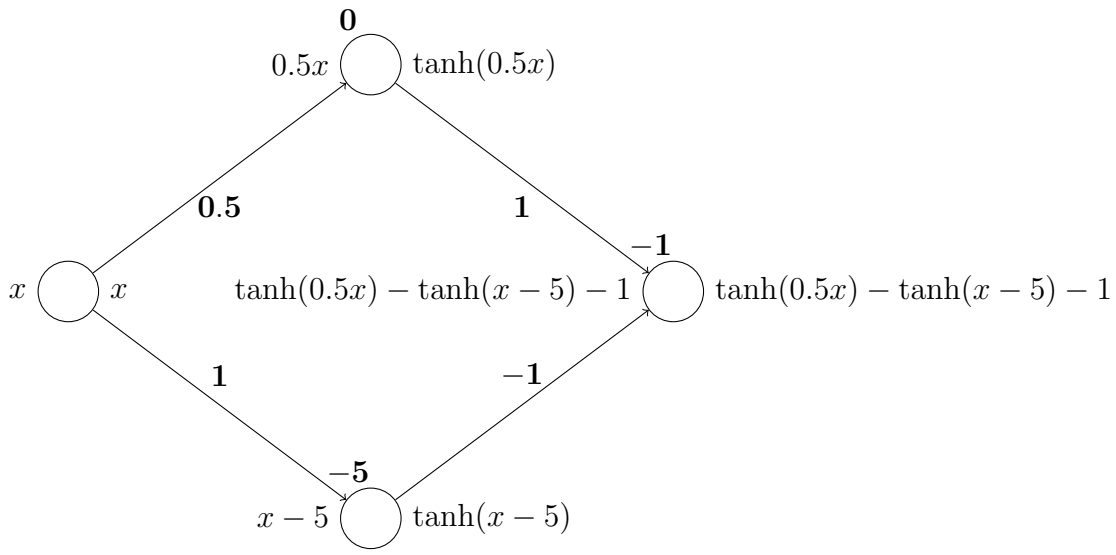

Figure 5.2: Sample multilayer perceptron. The weights are shown on each connection, and the biases shown above each neuron (all in bold). Assuming a hyperbolic tangent activation function ($\alpha \equiv \tanh$) and an initial activation $x \in \mathbb{R}$ into the network, we have shown, for each neuron, its total input on the left and its output on the right.

The weights and biases are

$$W^1 = \begin{bmatrix} 0.5 \\ 1 \end{bmatrix},\ \mathbf{b}^1 = \begin{bmatrix} 0 \\ -5 \end{bmatrix}, \quad W^2 = \begin{bmatrix} 1 & -1 \end{bmatrix},\ \mathbf{b}^2 = \begin{bmatrix} -1 \end{bmatrix}, \tag{5.7}$$

and (for a network input $x \in \mathbb{R}$) the inputs and outputs of each layer are

$$\begin{aligned} \mathbf{u}^0 &= \begin{bmatrix} x \end{bmatrix}, & \mathbf{z}^0 &= \begin{bmatrix} x \end{bmatrix}, \\ \mathbf{u}^1 &= \begin{bmatrix} 0.5x \\ x - 5 \end{bmatrix}, & \mathbf{z}^1 &= \begin{bmatrix} \tanh(0.5x) \\ \tanh(x - 5) \end{bmatrix}, \\ \mathbf{u}^2 &= \begin{bmatrix} \tanh(0.5x) - \tanh(x - 5) - 1 \end{bmatrix}, & \mathbf{z}^2 &= \begin{bmatrix} \tanh(0.5x) - \tanh(x - 5) - 1 \end{bmatrix}. \end{aligned} \tag{5.8}$$

Function approximation

The multilayer perceptron model can be used as a powerful function approximator. Suppose there is an unknown function $F\colon S \subset \mathbb{R}^k \to \mathbb{R}^m$ (often referred to as a *cost landscape* or *landscape*) that we wish to approximate based on some *train-*

ing data given by pairs $\mathcal{D} = \{(\mathbf{x}_n, \mathbf{y}_n = F(\mathbf{x}_n))\}_{n=1}^N$ (where the $\mathbf{x}_n$ are sampled from the domain of F). We may proceed as follows.

First, we choose and fix the network's *hyperparameters* (parameters describing the behaviour of the algorithm itself, as distinct from parameters determined by the algorithm): the topology (number of layers L and number of neurons per layer $\{D_l\}_{l=0}^L$, where of course we must have $D_0 = k$ and $D_L = m$) and activation function α. Once these hyperparameters are fixed, the perceptron defines a class of functions $P_{\mathcal{W}} \colon \mathbb{R}^k \to \mathbb{R}^m$ parameterised by the weights and biases $\mathcal{W} := \{W^l\}_{l=1}^L \cup \{\mathbf{b}^l\}_{l=1}^L$ of the network (these will henceforth be referred to simply as the *weights* of the network, since as we have mentioned the biases may simply be considered a particular type of weight).

Next the problem is to choose the appropriate set of weights so that $P_{\mathcal{W}}$ is as close to F as possible. The usual approach for achieving this goal, and the technique we will use here, is to choose the weights via *machine learning*: we make an initial guess for the weights, and then use the training data to iteratively update that guess. In this way we are "learning" an approximation for F from the data.

Both steps of this procedure can have a significant impact on the performance of the approximator, but they also contain many problem-specific subtleties. We briefly discuss the most general considerations in the following sections, and give more specific information in Section 5.2.2 when we discuss our algorithm. The most well-established and general part of this process is the learning of model weights once the hyperparameters are fixed.

Learning model weights

Recall that we are trying to approximate an unknown function $F \colon S \subset \mathbb{R}^k \to \mathbb{R}^m$, and to do this we have some training data $\mathcal{D} = \{(\mathbf{x}_n, \mathbf{y}_n = F(\mathbf{x}_n)\}_{n=1}^N$ and a class of candidate networks $P_{\mathcal{W}} \colon \mathbb{R}^k \to \mathbb{R}^m$ parameterised by the network weights. The problem is to choose the set of weights so that $P_{\mathcal{W}}$ is as close to F as possible.

We can frame this problem as an optimisation problem. That is, we seek to choose the weights to minimise an objective $\mathcal{O}(\mathcal{W}; \mathcal{D})$ that measures how well (or rather, how poorly, since we seek to minimise the objective) the approximating function $P_{\mathcal{W}}$ matches F. In the simplest case the objective is given by a loss function measuring the difference between the actual and approximating function values on the training data. For regression (where the function to be approxi-

mated is real-valued as opposed to binary-valued) the typical loss function is L^2. The L^2 loss on a single training example $(\mathbf{x}, \mathbf{y})$ is defined to be

$$\mathcal{L}(\mathbf{x}, \mathbf{y}; \mathcal{W}) := \left|\mathbf{y} - P_{\mathcal{W}}(\mathbf{x})\right|^2, \tag{5.9}$$

where $|\cdot| : \mathbb{R}^m \to \mathbb{R}$ is the standard L^2 vector norm. The loss on the whole training set is the average of the losses on each individual example:

$$\mathcal{L}(\mathcal{W}; \mathcal{D}) := \frac{1}{N} \sum_{n=1}^{N} \mathcal{L}(\mathbf{x}, \mathbf{y}; \mathcal{W}). \tag{5.10}$$

Typically we include an additional L^2 *regularisation* term $\mathcal{R}$ in the objective, which penalises high weights. This is a simple way to incorporate a prior belief into the optimisation procedure; the belief in this case being that the cost landscape does not vary too sharply. Specifically, we choose a positive real hyperparameter λ and define the penalty as

$$\mathcal{R}(\mathcal{W}) := \lambda \sum_{l=1}^{L} \left|W^l\right|^2, \tag{5.11}$$

where again $|\cdot|$ is the standard L^2 norm.

Thus we arrive at the objective that can be minimised in order to learn the model weights:

$$\mathcal{O}(\mathcal{W}; \mathcal{D}) := \mathcal{L}(\mathcal{W}; \mathcal{D}) + \mathcal{R}(\mathcal{W}) = \frac{1}{N} \sum_{n=1}^{N} \mathcal{L}\left(\mathbf{x}_n, \mathbf{y}_n; \mathcal{W}\right) + \lambda \sum_{l=1}^{L} \left|W^l\right|^2. \tag{5.12}$$

Even though the objective function is usually highly non-convex[239], it can typically be optimised effectively using variations of gradient descent. The most common such variation is *stochastic gradient descent*[240]. In this approach, instead of calculating the loss over the whole training set at each iteration, we consider only a single training example at a time, and cycle through the full training set over a period of N iterations (after which we shuffle the training set and cycle through again). That is, at each iteration s we update each weight

$w_i \in \mathcal{W}$ according to

$$w_i^{s+1} = w_i^s - \delta \frac{\partial \mathcal{O}\left(\mathcal{W}; \{(\mathbf{x}_n, \mathbf{y}_n)\}\right)}{\partial w_i}\bigg|_{\mathcal{W}=\mathcal{W}^s}, \tag{5.13}$$

where n iterates repeatedly over the N training examples (in a random order), δ is a step size hyperparameter and $\mathcal{W}^s$ denotes the set of weights determined at iteration s.[1] This introduces randomness into the procedure while still tending to reduce the total loss. In practice pure stochastic gradient descent can be computationally inefficient, so instead it is more common to train in *mini-batches*, where the training set is split randomly into batches of a fixed small size, and the gradient updates for each step are calculated from a single batch. Typically we also prefer a more sophisticated update over the vanilla gradient descent update of Eq. (5.13), such as AdaGrad[242] or Adam[243], since these set the step size adaptively and therefore require less manual tuning.

If too many iterations of gradient descent are performed, the learning procedure can cause the model to *over-fit*, where it starts to fit noise in the training data. In this case the quality of the approximation is actually degraded, in the sense that the model will fail to accurately predict the values corresponding to parameters outside the training data. The simplest way to avoid over-fitting is *early stopping*, where training is stopped before the weights have completely converged[244]. The inclusion of the L^2 regularisation penalty also alleviates this problem to some degree, and there are more modern techniques such as dropout[245] and batch normalisation[246] that have seen empirical success. We discuss in Section 5.2.2 the steps we take to avoid over-fitting in our algorithm.

Regardless of how effectively the weights are learned, the performance of the approximator depends on the choice of hyperparameters. We discuss the choice of activation function and topology in the following sections.

[1] Computation of the partial derivatives of the objective with respect to the network weights is typically performed using an algorithm known as *backpropagation*[241], which is a straightforward but elegant application of the chain rule. The loss of each training example is propagated backwards through the network using the weighted connections together with the inputs and outputs $\{\mathbf{u}^l, \mathbf{z}^l\}_{l=0}^L$ calculated during the forward pass. During this process, the partial derivatives with respect to each weight can be determined iteratively. We refer the reader to Rumelhart et al.[241] or Goodfellow et al.[237] for the full details.

Activation functions

The choice of activation function determines, at the most fundamental level, the *expressivity* of the network, which describes the class of functions that can be well approximated.

An initial observation is that for some choices of activation function the network is extremely lacking in expressiveness. For example, if we choose α to be the identity map then regardless of topology the network simply reduces to the affine map $\mathbf{x} \mapsto W\mathbf{x} + \mathbf{b}$, where

$$W = W^L W^{L-1} \dots W^1, \quad \mathbf{b} = \mathbf{b}^L + W^L \left(\mathbf{b}^{L-1} + W^{L-1} \left(\dots \right) \right). \tag{5.14}$$

Indeed, even if α is an arbitrary linear function then the network again reduces to an affine map.

However, if α is non-linear then the multilayer perceptron can be extremely expressive. In particular, the *universal approximation theorem* for artificial neural networks states that if α is bounded, continuous and non-constant then any compactly supported real-valued function may be uniformly approximated by a multilayer perceptron with only one hidden layer[247–249].

With this theorem in mind, it is not hard to choose an activation function that will give rise to an expressive network, but this is not the only consideration. The traditional choice is a *sigmoid* function, typically the logistic function $(u \mapsto (1 + e^{-u})^{-1})$ or hyperbolic tangent, as shown in Fig. 5.3, since these have beneficial theoretical properties (monotone, bounded, differentiable). However, in practice these functions suffer from the so-called *vanishing gradient problem*: since the gradient becomes close to zero when the input becomes too large or small, the corresponding gradient descent updates in Eq. (5.13) become small and learning slows down[250].

Instead, the *rectified linear unit* (ReLU), which is simply given by $u \mapsto \max(0, u)$ (see Fig. 5.3), is becoming more popular due to its simplicity, its similarity to models of biological neurons[251], and its tendency to greatly speed up training[252]. Note that even though the ReLU activation function is unbounded and thus does not satisfy the hypotheses of the universal approximation theorem, it is clear that the result still holds since by subtracting one ReLU from another with the same scaling but different translation we obtain a bounded step-like function.

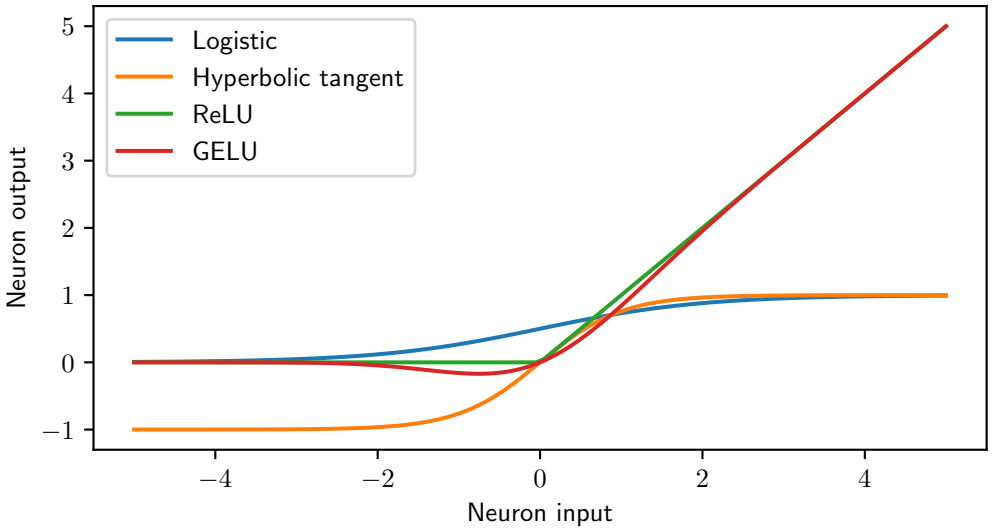

Figure 5.3: Comparison of common activation functions.

Various alternatives to ReLU have been suggested, and one that will be particularly important for our purposes is the *Gaussian error linear unit* (GELU), given by $u \mapsto u\mathcal{P}(U \leq u)$, where U is a random variable drawn from a standard normal distribution[253] (see Fig. 5.3).

We discuss our choice of activation function in Section 5.2.2.

Network topology

With the universal approximation theorem in mind, one may wonder whether there is any point using more than a single hidden layer, since each additional layer adds complexity to the training of the model[254]. The answer is that while single-hidden-layer networks can indeed approximate arbitrary functions, they may do so inefficiently in terms of the number of neurons (and therefore weights) required for that approximation[255–259]. Moreover, there is growing empirical[260–262] and theoretical[263–265] evidence to suggest that "deep" architectures (with several hidden layers) more naturally learn to *generalise*, which is to say they can perform well at regions of the domain with sparse training data by "reusing knowledge" learned from well-sampled regions.

For the sake of building intuition it will be instructive to see why the universal approximation theorem holds in the specific case of a network with one-dimensional inputs and outputs, and using the most traditional activation func-

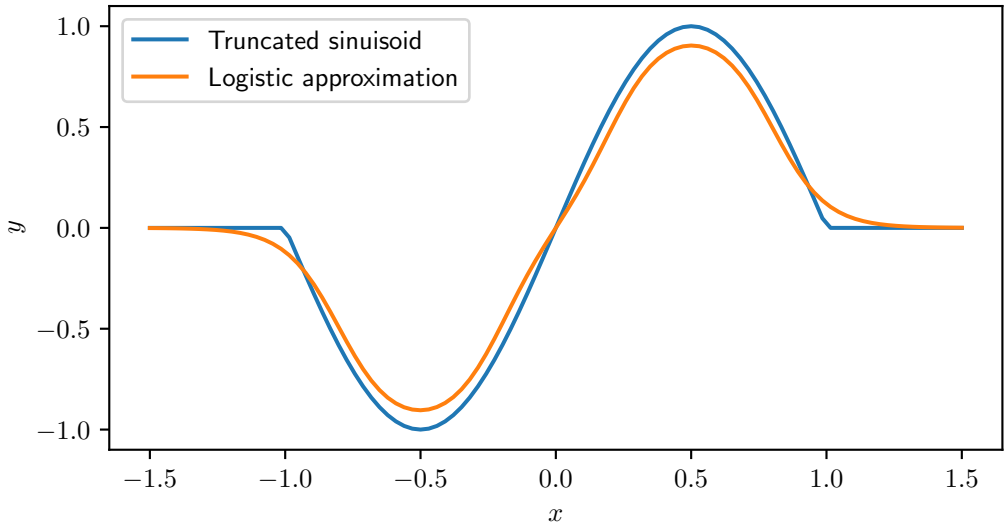

Figure 5.4: Approximation of a truncated sinusoid using a linear combination of four logistic functions.

tion, namely the logistic function:

$$\alpha(u) = \frac{1}{1 + e^{-u}}. \tag{5.15}$$

A multilayer perceptron mapping $\mathbb{R} \to \mathbb{R}$ with a single hidden logistic layer is simply a linear combination of scaled, translated logistic functions. It is clear from the shape of the logistic function that by scaling we can approximate a step function arbitrarily well, and by taking a linear combination of two step functions we get a top hat function. With a linear combination of top hat functions we can then approximate a compactly supported real-valued function. See Fig. 5.4 for a simple example, where we have approximated a truncated sinusoid using a linear combination of four logistic functions.

This argument demonstrates the high expressiveness of networks using non-linear activation functions, but also hints at a problem with shallow networks: they have no capacity to "share" learned features between different areas of the input space. With deep networks, on the other hand, the first layer can map out the general positions of features and then later layers can sculpt these features more finely, the key point being that these later layers can act on multiple parts of the input space simultaneously. This is the reason that deep networks can require fewer neurons when approximating more complex functions, and could also be

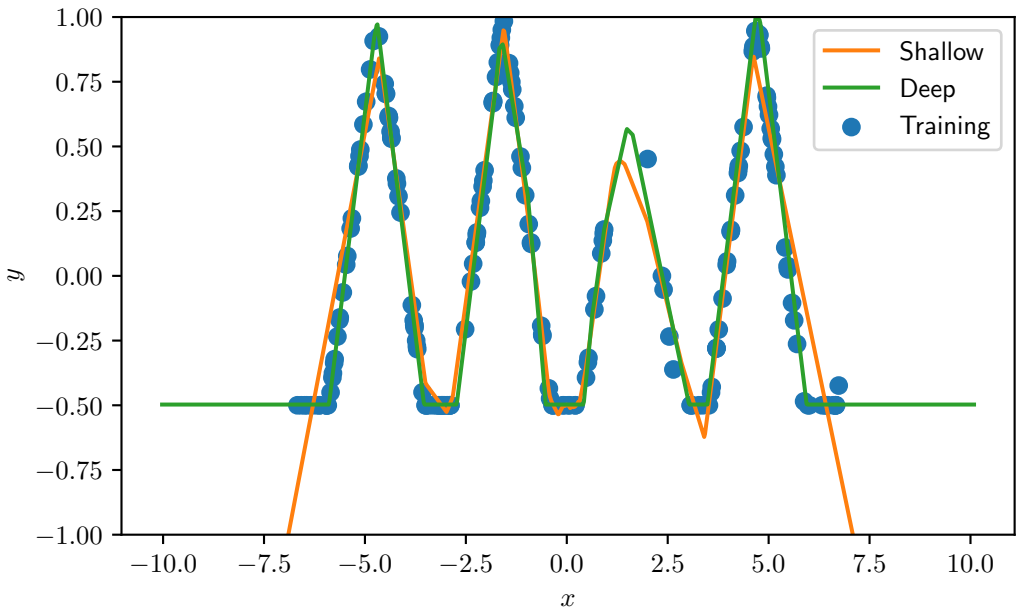

Figure 5.5: Comparison of shallow and deep neural network models for a landscape with several features. Note that for the orange and green curves, x represents the network input and y the network output. For the blue points, (x, y) pairs correspond to the training data sampled from the landscape. The plot thus shows points sampled from the landscape together with two approximate models of the landscape. We use this approach for visualising approximated landscapes throughout the remainder of this section.

responsible for the (apparent) superior generalisation ability of deep networks.

To demonstrate this feature sharing behaviour, in Fig. 5.5 we present a comparison of the fits found by shallow and deep networks for a landscape with several features. The shallow network has a single hidden layer of 128 neurons, while the deep network has a hidden layer of 32 neurons followed by a hidden layer of 4 neurons (a schematic of the deep network is shown in Fig. 5.6). Both networks use ReLU activation functions. We can see that despite having significantly fewer neurons, the deep network is able to learn a more accurate model. To explain this, we can inspect the inputs to the second hidden layer of the deep network, as shown in Fig. 5.7. Recall that these inputs will be passed to the rectified linear activation function (that is, their negative values will be truncated to zero) before being linearly combined to obtain the output of the network. We see that two neurons in the layer attain only negative values and so are essentially wasted, while the other two neurons create a sawtooth-like curve. The fact that this saw-

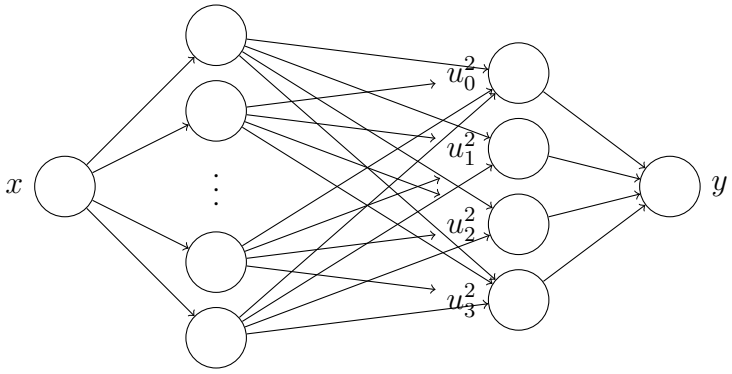

Figure 5.6: Topology of the deep network used for Fig. 5.5. The first hidden layer has 32 neurons, only 4 of which are shown. We have labelled the input x and output y of the network, and the inputs $u_0^2, u_1^2, u_2^2, u_3^2$ of the second hidden layer. Note that some arrows have been shortened to avoid clutter.

tooth drops below 0 means that the bottoms will be truncated by the activation functions in the second hidden layer. Thus we see that the deep network can share this "truncation feature" across the entire input space, which allows it to model the function accurately despite having relatively few neurons.

5.2.2 Algorithm details

With the basic ideas and techniques of multilayer perceptrons in hand we can now present the details of the machine learning algorithm (the code is available on GitHub[266]). To formalise the setting, we consider the experiment to be represented as a *cost landscape*, which is a function $\mathcal{C}\colon S \subset \mathbb{R}^k \to \mathbb{R}$ mapping a finite number of controllable parameters to a cost representing the performance of that set of parameters. In practice the cost landscape is a stochastic function (which may even vary over time), but for simplicity we approximate it as a stationary, deterministic function. We consider $\mathcal{C}$ to be a black box—the only way to determine information about $\mathcal{C}$ is to evaluate it.

With this formulation, the problem of optimising the physical system is reduced to a problem of function optimisation: determining $\arg\min_{\mathbf{x}} \mathcal{C}(\mathbf{x})$, the configuration of parameters minimizing $\mathcal{C}$.

As described in Section 5.1, we approach this problem by learning a model for the system (that is, an approximation of $\mathcal{C}$) and then optimising that model. Moreover, we extend that basic idea by making the algorithm automatically explore the domain of $\mathcal{C}$ in order to improve the model and therefore the quality of

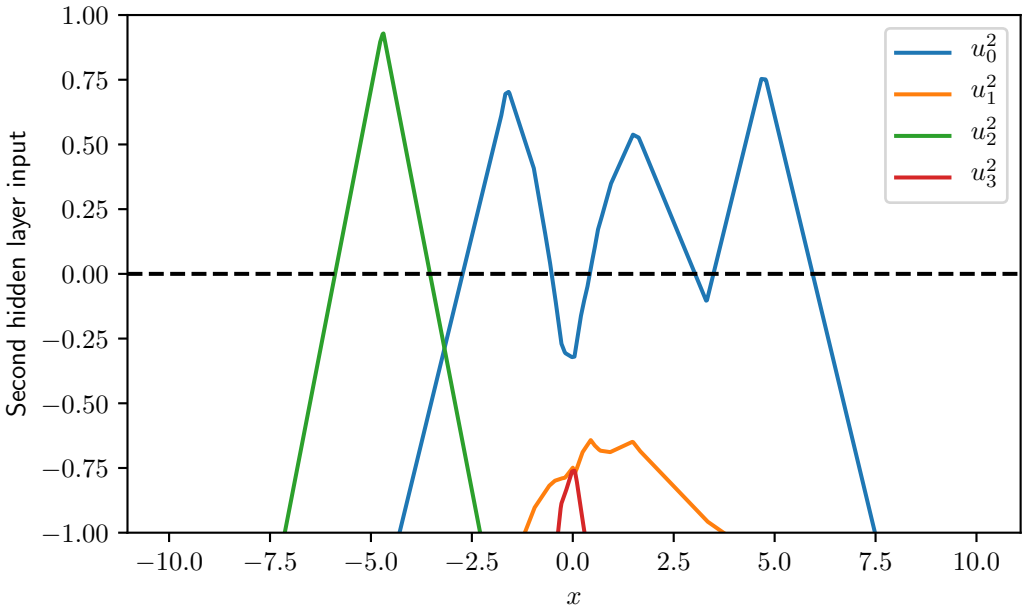

Figure 5.7: Inputs to the four individual neurons of the second hidden layer in the deep network of Figs. 5.5 and 5.6, as functions of the network input x. The curves will be truncated at 0 (dashed line) when they are passed through the ReLU activation function of the neurons.

the optimisation. The algorithm proceeds as follows:

1. Run the experiment some number of times with arbitrarily-chosen parameter sets and obtain the corresponding costs. These parameters and costs form the initial training data.

2. Fit a multilayer perceptron P to the training data.

3. Using P, find a new candidate parameter set $\mathbf{x}$.

4. Run the experiment using $\mathbf{x}$, obtain the cost $\mathcal{C}(\mathbf{x})$, and append $(\mathbf{x}, \mathcal{C}(\mathbf{x}))$ to the training data.

5. Repeat from 2 (using the larger set of training data).

6. After every three repetitions of steps 2 to 4, run the experiment once with an arbitrarily-chosen parameter set, and append the parameter set and cost to the training data.

To obtain the initial training data in step 1 we follow the approach of Wigley et al.[235], and run the experiment $2n$ times using a differential evolution[267]

algorithm. The same differential evolution algorithm is thereafter used every four runs (step 6), which adds some additional variety and exploration to the algorithm, and also enables some degree of comparison between the performances of the differential evolution and machine learning-based algorithms.

The most interesting steps of the algorithm for our purposes are 2 and 3. These steps need to be able to run quickly (otherwise we waste time that would be better spent running the experiment), but also need to model, explore and optimise the landscape effectively. This is in contrast to standard applications of multilayer perceptrons, where the focus is on function approximation alone.

Before giving the details of these steps, we note that the algorithm has many hyperparameters that determine its speed and general behaviour. For concreteness we chose initial values for hyperparameters under the assumptions that each experimental run would take on the order of one second and that the dimensionality of the landscape would be no more than around 100. We found that sometimes hyperparameters needed to be tuned simply by experimentation, and for this we used simulated random quadratic landscapes with dimensionalities ranging from 1 to 10. Ideally, hyperparameters chosen this way should work well in real experiments, since needing to fine-tune hyperparameters on a per-experiment basis partially defeats the purpose of using automatic optimisation in the first place. As we will see in Section 5.3, our approach worked: the hyperparameters chosen with this method performed well on a real experiment with significantly more parameters, and with no additional tuning.

Step 2: fitting the multilayer perceptron

The first step in fitting a multilayer perceptron is to choose the network topology and activation function.

When the domain of $\mathcal{C}$ is large and evaluations are expensive, we cannot explore all parts of the domain in detail, and therefore require our chosen model to exhibit a good generalisation ability. As discussed in Section 5.2.1, this suggests we should use a relatively deep network. We performed simple benchmarking using a simulated experiment to investigate empirically the effect of network depth on the algorithm's end-to-end performance, the results of which are shown in Fig. 5.8. This suggests that, indeed, deeper networks tend to perform better. However, deeper networks also require more time to train, so there is a tradeoff to be made. We therefore chose a 5-layer network with 64 neurons each, since

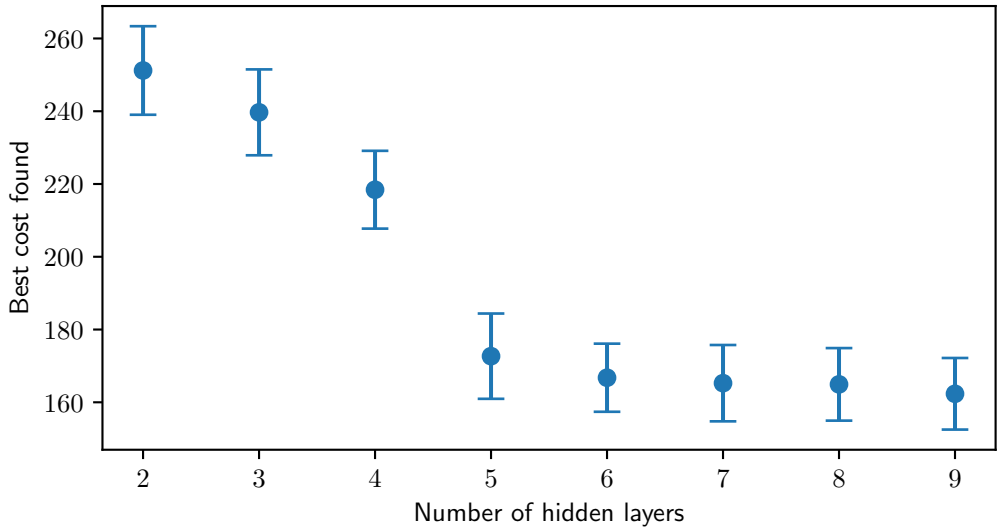

Figure 5.8: Comparison of algorithm performance for different network depths. All networks had 64 neurons per layer. Each point represents the mean (and standard deviation of the mean) estimated from a sample of 200 runs. In each individual run, the algorithm performed 100 iterations on a randomly-generated 10-dimensional quadratic landscape.

this can be trained in under one second on standard hardware but exhibited comparable performance to deeper networks on the simulated experiment.

The next choice is the activation function. We found that, as suggested by the literature, rectified linear units (ReLU) lead to significantly faster training times than sigmoids. However, we noticed that the landscapes modelled by ReLU networks occasionally exhibited large flat areas or sharp corners, which could hamper the algorithm's natural tendency to explore (see Fig. 5.9). To overcome this problem we used the Gaussian error linear unit (GELU) instead. Its linearity in the positive domain enables fast training, like ReLU, but the curvature near the origin tends to create smoother landscapes that are more easily explored and optimised (see Fig. 5.9). Moreover, by using GELU we also benefited from its minor regularisation effect[253].

As mentioned in Section 5.2.1, networks that are trained for too long can overfit the training data. The setting of our algorithm partially avoids this problem automatically, since the training data change with every iteration. To further reduce the effect, we implemented an aggressive form of early stopping where we terminate training as soon as the relative improvement in loss drops below

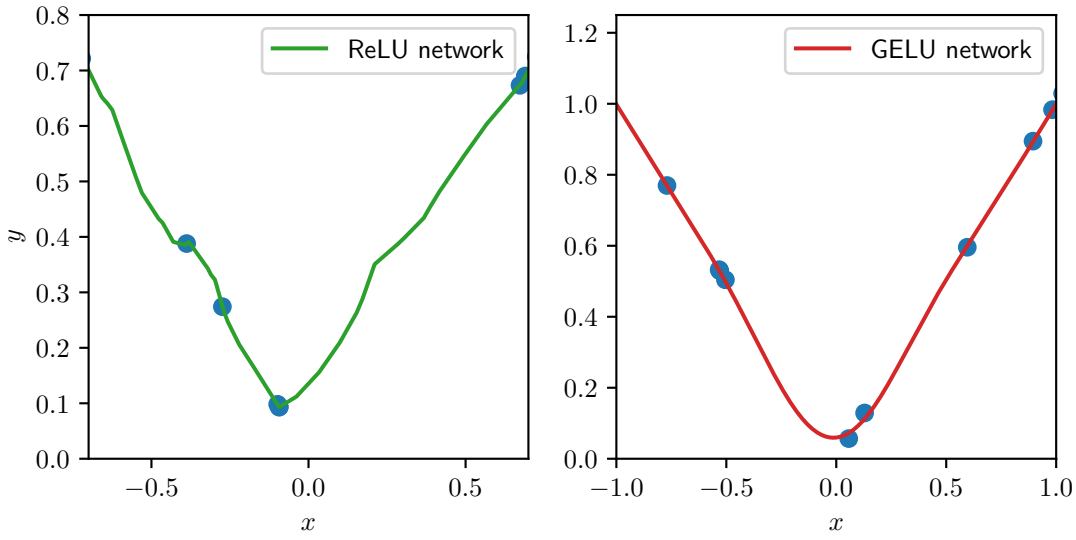

Figure 5.9: Comparison of neural network models using ReLU (left) and GELU (right) activation functions. The tendency of ReLU to create sharp corners at data points can cause the algorithm to get stuck on the edges of wells in the cost landscape. The curvature of GELU, on the other hand, tends to cause its predictions to "overshoot" the training data, and thus allows it to more naturally explore the interiors of wells.

20%. This approach additionally improves the algorithm's natural tendency to explore, since at each step the fit of the model is slightly different due to not having completely converged.

Step 3: choosing candidate parameters

Once we have the approximation P of the experimental cost landscape $\mathcal{C}$, we must use it to choose a new set of parameters.

Unlike in the typical supervised learning scenario in which a fixed set of training data is provided, here the algorithm must explore the landscape by itself, so it is suboptimal simply to return the predicted best parameters every time (since if this prediction is initially wrong then the algorithm will not be able to improve its model and potentially find even better parameters). This touches on a central problem in reinforcement learning—a subfield of machine learning in which an "agent" interacts with an unknown environment in order to generate "reward"—known as the "exploration versus exploitation" dilemma. The agent must decide whether to explore new areas of the landscape that might provide

higher reward, or exploit the best-known areas of the landscape to earn reward with high confidence. In the reinforcement learning community there are many popular approaches to resolving the exploration versus exploitation dilemma[268–270], but these tend to focus on cases where the action space (the set of choices the agent can make) is small[268]. This is certainly not true in our situation, since at any point in time the algorithm can choose to explore any point in the parameter space. For this reason we have chosen to use the theoretically well-grounded *Thompson sampling*[271], which naturally works with large action spaces.

In Thompson sampling, we have a family of potential landscapes P^θ parameterised by some θ, and a posterior $\mathcal{P}(\theta|\mathcal{D})$ giving the likelihood of the true landscape being P^θ given the training data $\mathcal{D}$. Each time we want to perform an action (that is, choose a parameter set) we sample θ from $\mathcal{P}(\theta|\mathcal{D})$ and choose the action suggested by P^θ. The idea is that all landscapes in the distribution will tend to agree on areas of the domain that have already been explored, but may exhibit very different predictions on under-sampled regions. In particular, some landscapes will predict good performance in the unknown regions, so when they are chosen they will suggest parameters from those regions and thus trigger exploration. Over time, all high-performing regions of the domain will become well-explored, so the global optimum can be identified.

To use Thompson sampling in our algorithm, we therefore need to keep track of an entire distribution of models of the landscape. Once we have this distribution, to choose the next parameter set we sample a model from the distribution and then find the minimum predicted by that model. We considered three options to track a distribution of models:

Dropout

Dropout was introduced[245, 272] as a method to help prevent over-fitting in large neural networks. In dropout, neurons are randomly dropped from the network during training (that is, their activations are set to 0). The idea is that this process prevents co-adaptation between different neurons, and thus makes the model less likely to fit noise in the data.

Traditionally, when actually evaluating the network on new inputs, all neurons are kept, and the resulting output is approximately the average over all possible "thinned" networks. However, this averaging is not necessary, and instead the neurons can be randomly dropped out during evaluation

too. This yields a distribution of models, since for each choice of neurons to drop out the network describes a different function[273].

Bayes by backpropagation

In Bayes by backpropagation[274], each network weight is normally distributed rather than deterministic. That is, corresponding to each weight there are two parameters, describing the mean and standard deviation of its distribution. An additional term is included in the training objective to discourage setting standard deviations to zero.

For each each training step, the weights are independently sampled from their distributions. With these fixed weights the gradient descent update is performed as usual, taking into account the dependence of the weights on the underlying means and standard deviations. A distribution of networks is obtained by sampling the weights prior to passing parameters through the network.

Bagging

The final method we consider, and the simplest, is bagging[275]. In this approach an ensemble of networks is created, and each network initialised independently. These networks represent the elements of the (discrete) distribution of models.

Traditionally each network is trained on its own set of data (drawn randomly with replacement from the full set of training data), but since in our case we work with relatively few data points we train each network on the full set, and rely on independent initialisations to achieve a wide variety of models.

We compare the behaviours of these three methods in Fig. 5.10, where training points have been sampled from a landscape with two wells. As we can see, the more sophisticated methods of dropout and Bayes by backpropagation are actually not particularly useful for our purposes, since most landscapes in their distributions tend to have roughly the same shape and will therefore all tend to predict minima in the same places. For example, in the case of dropout it appears that most if not all of the sampled models predict the minimum to occur in the left-hand well. With Bayes by backpropagation it appears that all models predict a very similar depth in both wells, so it is possible that the right-hand well would be identified as a potential minimum and thus explored. However,

the very strong similarities between all the models is still concerning from an exploration perspective, since it is clear that the distribution does not reflect the "true" distribution of all models fitting the data, and thus may not be useful for effectively exploring a more complex landscape. With bagging, on the other hand, not only is the fit of the training data better, but a wide variety of behaviours in the right-hand well are predicted. It is this variety that is necessary for effective exploration via Thompson sampling.

In addition to their apparently inferior exploration characteristics, dropout and Bayes by backpropagation complicate training significantly: the total training time is increased, and due to the additional randomness in the procedure it becomes harder to detect when the training has converged.

For these reasons we chose to use bagging. We found that using only three independent networks was sufficient to obtain a good level of exploration on the simulated 10-dimensional quadratic cost landscape.

The final ingredient in determining candidate parameter sets, given the distribution of networks, is locating the minimum of the sampled model. We used `SciPy`'s implementation of the `L-BFGS-B` algorithm[276, 277], starting from n randomly chosen points of the domain.

Recalling that every fourth parameter set was chosen by a differential evolution algorithm, we note that the concrete implementation of Thompson sampling using bagging reduces to the following: run the experiment three times using the best parameter sets predicted by the three networks (where the networks are trained prior to each prediction), then run the experiment once more using the parameter set suggested by the differential evolution algorithm, then run the experiment three more times using the (new) best parameters predicted by the three networks, and so on.

5.3 Optimising a magneto-optical trap with machine learning

In this section we demonstrate the potential of the algorithm by using it to automatically optimise a magneto-optical trap. We start with a general introduction to magneto-optical traps in the context of quantum memories, and a description of the particular system that we have optimised. We then present and analyse

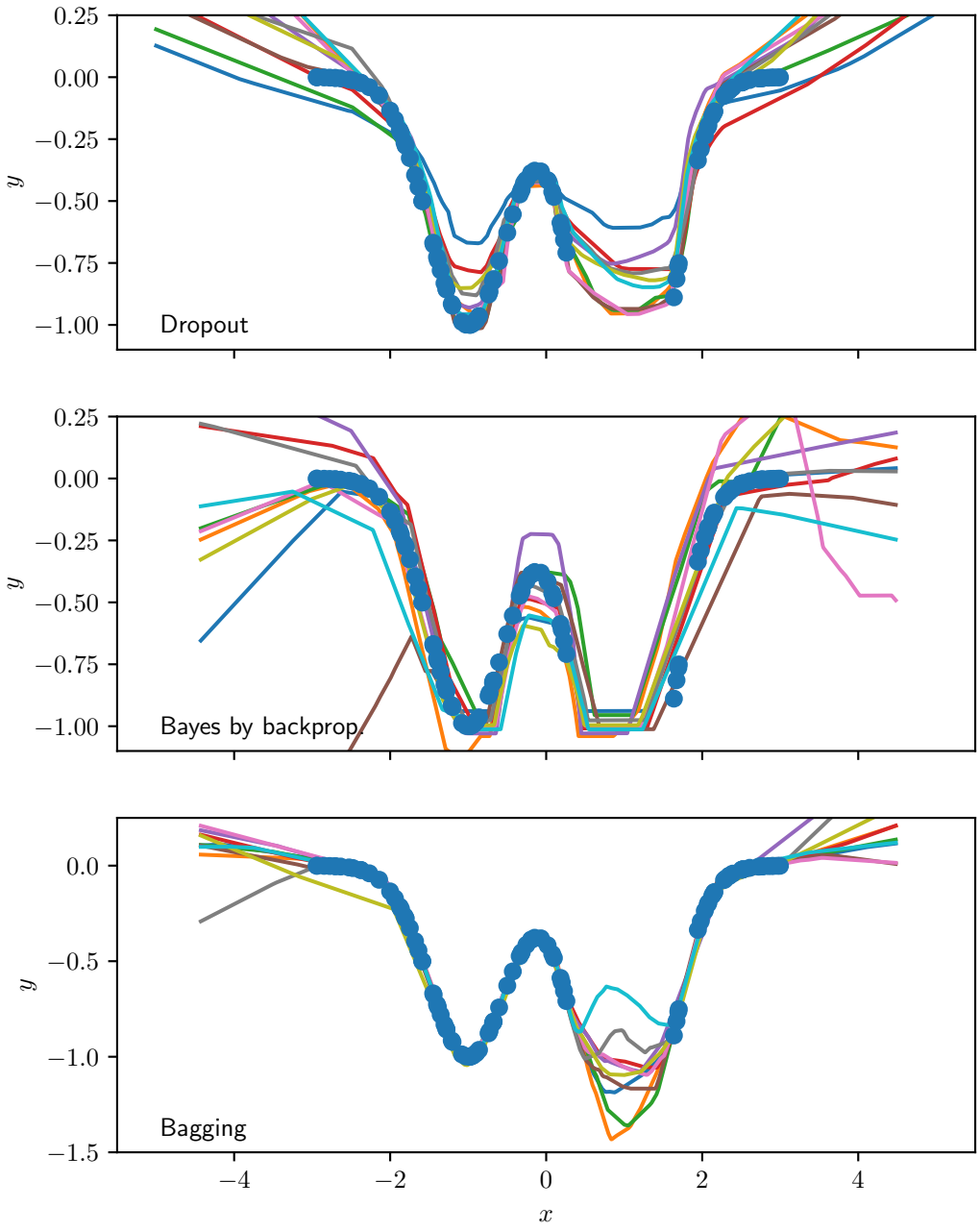

Figure 5.10: Comparison of different approaches for representing a distribution of models: dropout, Bayes by backpropagation and bagging. Each plot shows the training data together with 10 models sampled randomly from the appropriate distribution.

the preliminary results from applying the algorithm to that system.

5.3.1 Background: quantum memories and magneto-optical traps

As discussed briefly in Chapter 1, quantum memories are expected to find many applications in quantum information processing devices of the future. Generally speaking, quantum memories provide a mechanism for synchronising non-deterministic events[278]. If the outputs of multiple non-deterministic processes are required simultaneously, we may direct those outputs into a quantum memory and wait until there is a high probability that all processes have completed. If we then read out from the memory, the chances of obtaining all necessary outputs simultaneously is greatly improved.

In linear optical quantum computation, for example, it has been proposed that probabilistic gates may be prepared offline (that is, outside the path of the main computation) and teleported back into the computation when appropriate[279–281]. This removes non-determinism from the main circuit, but introduces it into the offline resource preparation. If a quantum memory is available then the resources may be prepared ahead of time and stored until they are needed, thus making the entire process more deterministic.

Another important example of a device relying fundamentally upon quantum memories is the quantum repeater, which has been proposed as a solution to the problem of slow bit rates resulting from fibre optic losses in quantum key distribution networks[29, 30]. In a network utilising quantum repeaters, nodes are placed at regular intervals along a communication line. Entanglement is swapped between pairs of adjacent nodes in a hierarchical manner, until eventually entanglement is shared between both ends of the line[31]. This entanglement may then be used as a resource for quantum key distribution[282]. Importantly, the resource and time requirements of a communication protocol based on quantum repeaters scale at most polynomially with distance, unlike direct fibre transmission which is inherently attenuated exponentially[29]. However, the scheme is not without challenges. In order for a central node to swap entangled states shared by that central node and two adjacent nodes, it must have simultaneous access to a member from each entangled pair. Since the entanglement generation is non-deterministic, simultaneous arrival cannot be guaranteed unless a quantum

memory is used to provide synchronisation.

While many schemes for optical quantum memories have been proposed and demonstrated (see, for example, the reviews by Hammerer et al.[283] or Heshami et al.[284]), the one that we are most interested in is the gradient echo memory (GEM)[285, 286]. In this scheme an ensemble of 2- or 3-level atoms is inhomogeneously broadened by the application of an electric or magnetic field gradient, such that the frequency of the appropriate transition varies monotonically along the optical path through the ensemble. An optical pulse incident on the ensemble is absorbed along its length, with Fourier components of the pulse mapped longitudinally onto the ensemble. The atomic excitation dephases as a result of the broadening, and after a period of time the sign of the gradient is switched, causing a reversal of the dephasing. After an equal period of time, when the phases realign, the pulse is re-emitted as a photon echo.

The GEM scheme was first implemented in a solid state system consisting of praseodymium-doped yttrium orthosilicate[285], soon followed by a demonstration in warm rubidium vapour[286]. Both of these systems have more recently been used to realise highly efficient memories (87% in warm vapour[287] and 69% in solid state[288]), but with storage times of only a few microseconds. For the solid state system the storage time is limited by the short coherence time of the electronic transition, while for the vapour the primary limiting factor is atomic diffusion. In the latter case, the effect of diffusion can be mitigated by switching from a warm vapour, in which atoms are fast-moving, to a dense cloud of cold atoms, which exhibits significantly lower atomic speeds[289]. Indeed, a GEM system based on cold rubidium atoms has recently been reported operating at 50% efficiency with a storage time of 0.6 ms[36], which is significantly longer than the storage time at 50% efficiency in warm vapour (10 µs[287]). A key challenge in further improving performance of this system is attaining a strong light-atom coupling, which translates to requiring that the cold atomic cloud exhibit an extremely high optical depth (OD)[285, 290–292]. The component at the core of this requirement is the *magneto-optical trap* (MOT), which is used to collect, cool and compress a cloud of atoms.

Since its introduction in 1987[293], the MOT has become an indispensable tool in cold atom experiments[294]. Perhaps most famously, production of Bose-Einstein condensates typically proceeds by first loading and compressing atoms with a MOT and then performing evaporative cooling to reduce the tempera-

tures drastically[295–297]. Other examples include quantum information processing based on neutral atoms[298–300], isotope trace analysis[301], high-resolution spectroscopy[302, 303] and cold-atom interferometry[304–306], to name just a few.

Despite its widespread and impressive successes, the MOT has evaded detailed theoretical understanding throughout its history, and as a consequence has often been a source of experimental surprises. For example, soon after the *optical molasses*—the precursor to the MOT—was first reported[307], it was noted that the minimum achievable temperatures were significantly better (by a factor of 6) than the limit predicted by the theory[308, 309]. This was later understood to be due to an unexpected cooling mechanism known as *polarisation gradient cooling*[310]. Similarly, it was found that confinement times in optical molasses could be improved by a factor of 50 by misaligning the nominally counterpropagating beams[311, 312]. This effect has since been attributed to a dynamical stabilisation of the atomic trajectories through the molasses[313].

More generally, the analytic intractability of the MOT has meant that methods to improve performance have largely been discovered via empirical means[314–316]. In addition to the aforementioned polarisation gradient cooling, notable examples are *dark spots*, where a region of the cloud is made transparent to the trapping field to eliminate the repulsive effects of reabsorption[317, 318], and the use of a *compression phase* in which the density of the cloud is transiently increased at the expense of atom number by gradually ramping the laser detunings and magnetic field gradient[319–321]. While these "tricks" are now widely used and continue to yield impressive results, the lack of a comprehensive theoretical model of the MOT—especially outside the adiabatic regime of constant or slowly-varying fields—means there is no reason to believe that these techniques are optimal[322–325].

The compression phase of a MOT, in which multiple parameters that may vary with time must be controlled simultaneously, is thus a prime candidate for optimisation via machine learning: there is little theoretical understanding of the dynamics, so the algorithm is not particularly disadvantaged compared to a human physicist; there is a huge parameter space to explore, given that for each field there are multiple parameters describing its time dependence; and the timescales of the experiment are inherently short, so iterations may be performed relatively rapidly.

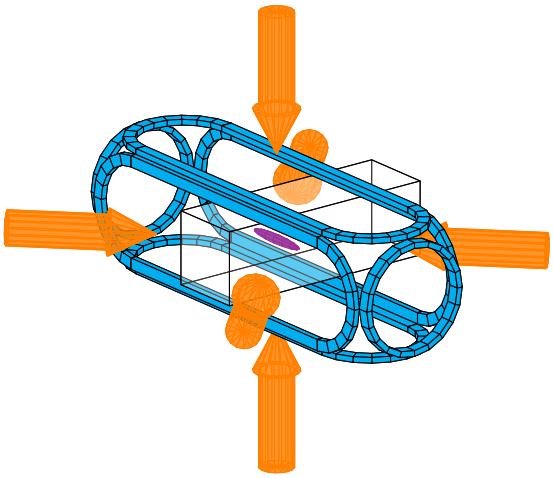

Figure 5.11: Schematic of the magneto-optical trap (MOT), showing the trapping and repump lasers (orange), ^{87}Rb atom cloud (purple) and magnetic field coils (blue). The trapping and repump lasers are combined on a polarising beamsplitter (not shown), and the copropagating fields are then split and directed into the MOT. The horizontal beams are incident at 45° in order to allow access along the long axis of the cloud for the GEM beams (not shown). The cloud is confined in a glass cell inside the coils, and is attached to a vacuum chamber (not shown).

5.3.2 A magneto-optical trap for a cold-atom gradient echo memory

In this section we introduce the specific MOT—the core component of a cold-atom gradient echo memory—that we have optimised. The system is the same as that used by Sparkes et al.[289, 292] and Cho et al.[36], and the basic schematic is shown in Fig. 5.11. The ^{87}Rb atoms are confined in a glass cell, and trapped in a cylindrical geometry (a "two-dimensional" MOT) in order to maximise OD along the optical path used by the memory. This is achieved by using elongated coils in a quadrupole configuration[326]. In addition, the horizontal trapping and repump beams are injected at 45°, which allows access along the long axis of the MOT for the memory beams[326].

Loading of the MOT with atoms proceeds as follows. There is first a ∼400 ms loading phase, in which atoms are collected into the trap from the surrounding gas. In this phase the repump is on resonance with the D2 $F = 1 \rightarrow F' = 2$ transition, the trapping is 30.8 MHz red-detuned from the D2 $F = 2 \rightarrow F' = 3$ transition, and the magnetic field gradient is $6\,\mathrm{G\,cm^{-1}}$.

After the loading phase there is a compression phase in order to transiently increase the OD[317, 319]. Over a period of 20 ms the magnetic field gradient is ramped up to 28 G cm^{-1}, and the repump is red-detuned by 30 MHz. This is followed by 1 ms of polarisation gradient cooling, in which the magnetic fields are switched off and the trapping laser is red-detuned to 70 MHz.

The exact values for the compression ramps described above were determined via manual tuning, but the general motivation is as follows. Increasing the magnetic field gradient increases the spring constant at the center of the trap and thus compresses the atoms more tightly, at the expense of collecting fewer atoms from the surrounding gas (since the Zeeman shift for atoms far from the center of the trap becomes so large that trapping photons are not absorbed). This tradeoff is acceptable since we are looking to achieve a high density and are no longer interested in collecting more atoms. Simultaneously detuning the repump means that, as the MOT becomes denser due to the increasing magnetic field gradient, fewer atoms are visible to the trapping light and thus the repulsive effect of reabsorption is minimised (this is known as a *temporal dark spot*[317]).

While this manually-optimised sequence has been successful for the system in the past[36, 289], there is no reason to believe that it cannot be improved significantly with further tuning.

Parameterisation and cost function

In order to apply the machine learning algorithm it was necessary to define a parameterisation of the compression phase, describing the control given to the algorithm, and a cost function, quantifying the performance of a given parameter set. We chose to allow the trapping frequency, repump frequency and magnetic field gradient to be varied, since there is evidence to suggest that all three of these quantities can have a large effect on the performance of the MOT[317, 319]. To give these quantities time dependence we divided the 20 ms compression followed by the 1 ms of polarisation gradient cooling into 21 timesteps of 1 ms each, and used an independent parameter for each timestep and each of the three quantities (trapping and repump frequencies, and magnetic field gradient). This yielded 63 independent parameters describing three piecewise-constant functions of time. We limited all trapping detunings between -70 MHz and 12 MHz (that is, 70 MHz red-detuned to 12 MHz blue-detuned), all repump detunings between -30 MHz and 1.3 MHz, and magnetic field gradients between 0 G cm^{-1} and 28 G cm^{-1}.

Our goal was to achieve a high OD, so we determined the cost function as follows. Immediately after the 21 ms phase controlled by the algorithm, the atoms were pumped into the $F = 2$ state for 1 ms. Then the transmission of a probe field, off-resonant from the D1 $F = 2 \rightarrow F' = 1$ transition, was measured. The cost function was defined to be the result of that measurement.

Also note that, as mentioned in Section 5.2.2, no additional tuning of the algorithm was performed based on this experiment-specific parameterisation and cost function.

5.3.3 Results

We performed five optimisation runs of the compression phase across several days using the machine learning algorithm, with each run involving between roughly 200 and 700 iterations (runs of the experiment with different parameter sets). The longest complete optimisation run took approximately 2.5 hours.

An OD of 448 was obtained using the learned compression ramps, compared to 138 for the original manually-optimised ramps. The learned compression ramps are shown in Fig. 5.12, with the original ramps shown for comparison.

Imaging of the MOT during the compression phase, using the learned ramps, is shown in Fig. 5.13. We observe the pulsed nature of the compression, consistent with what we might expect from inspecting the ramps.

5.3.4 Discussion

The algorithm was evidently able to produce a significant enhancement in performance by employing ramps that are radically different to those determined via manual optimisation. In this section we present a preliminary discussion of these results and some of their implications.

We shall make frequent reference to the five different optimisation runs we performed. We denote by R_i the run with i iterations and by p_i the best parameters found in that run, where $i \in \{702, 583, 502, 302, 272\}$ is referred to as the length of the run.

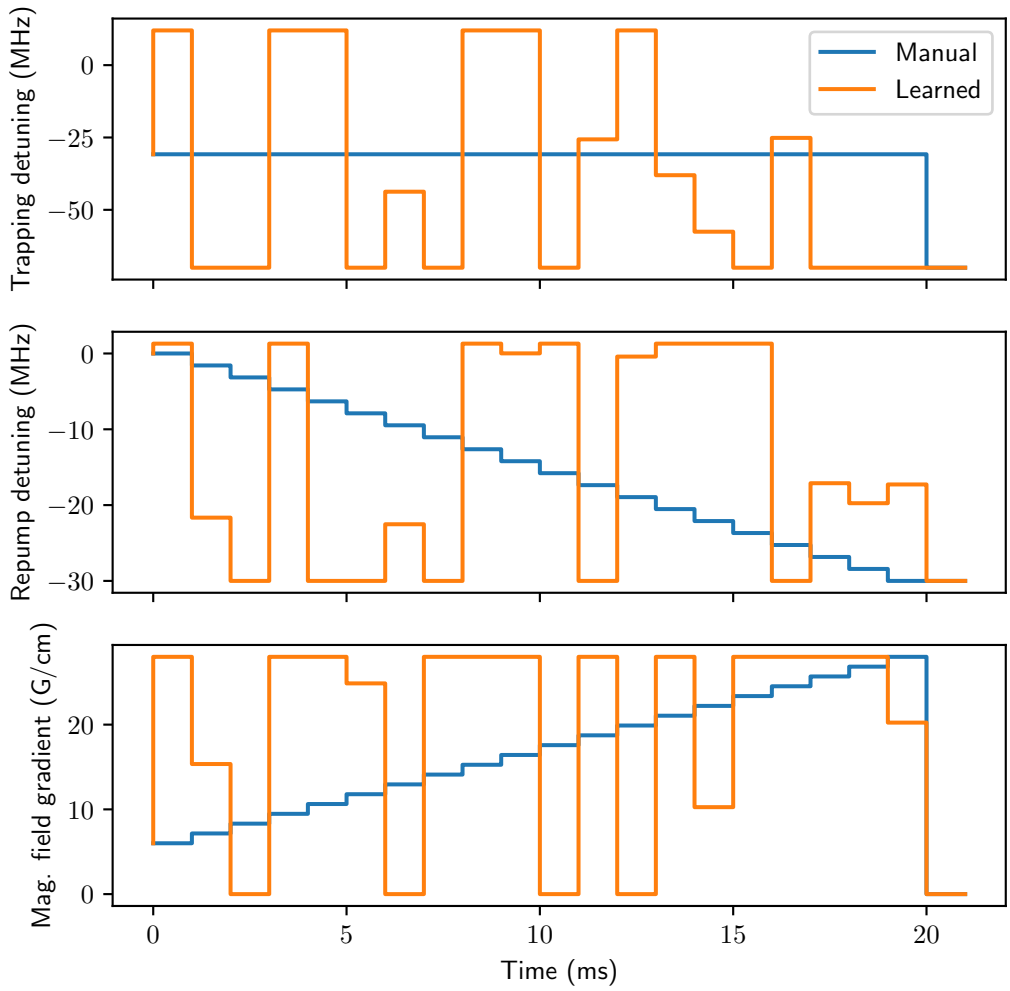

Figure 5.12: Best ramps found by a run of the machine learning algorithm compared to the best manually-tuned ramps.

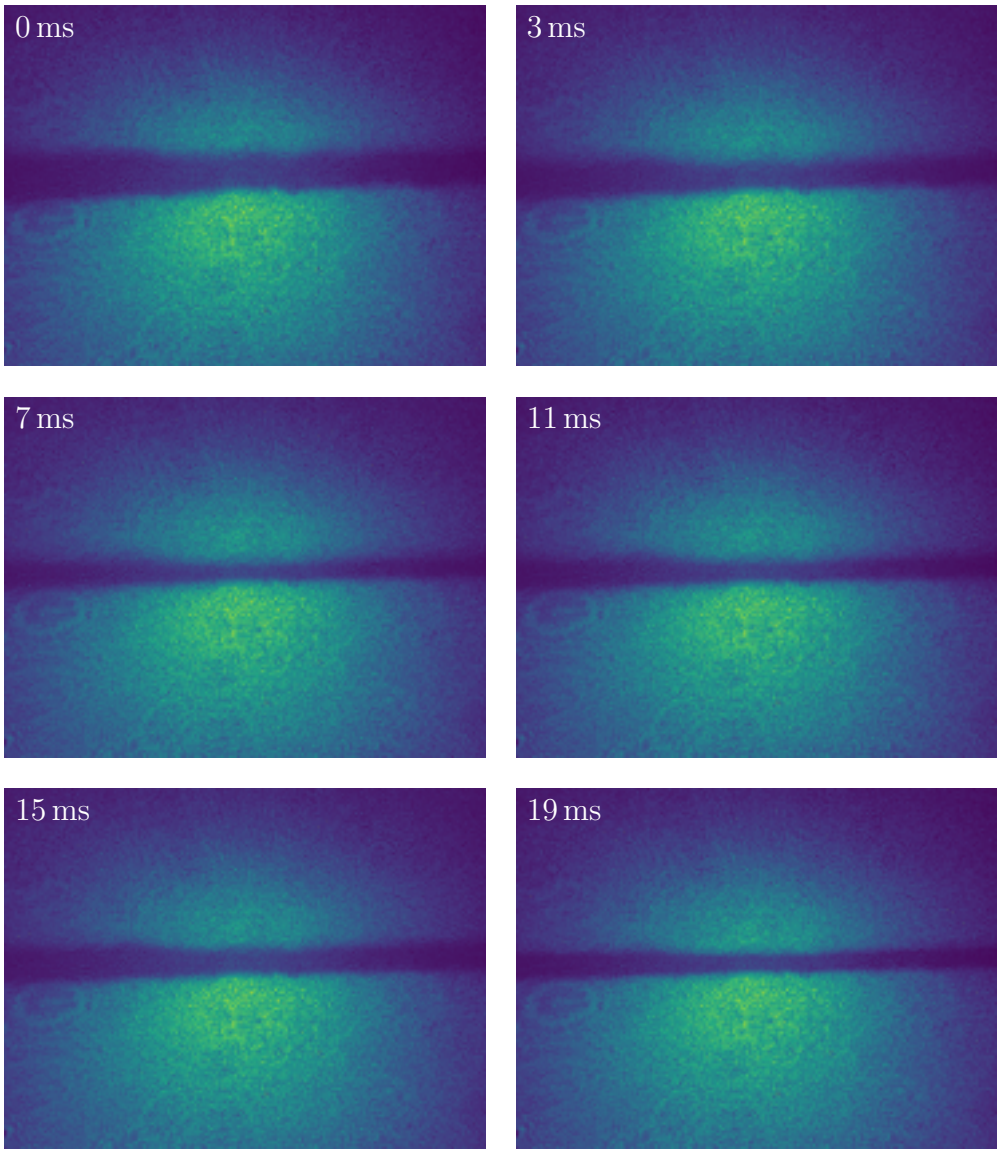

Figure 5.13: Absorption images of the MOT at various stages during compression. Note the pulsing behaviour: the cloud contracts for the first 7 ms, then expands slightly over the next 8 ms, and finally is compressed tightly.

Comparison of ramps

Since the learned ramps are extremely different to the original ramps, and indeed are quite unintuitive, it is important to understand which features of the ramps contribute to the superior performance, and which are merely artefacts of the learning process. It is not surprising that such artefacts exist: there is no incentive for the algorithm to learn ramps that are "simple" or "smooth" unless they correspond to better costs, and it seems likely that there are some parameters—or, indeed, combinations of parameters—that can be varied widely without significantly affecting cost.

One simple approach we can take to help distinguish between important features and irrelevant artefacts is to compare the high-performing ramps found by the algorithm across different optimisation runs on different days, as shown in Figs. 5.14 and 5.15 (we have split the runs across two plots to avoid excess clutter).

Inspection of these plots shows that there exist some common trends. In all cases the trapping frequency is ramped down (corresponding to becoming further red-detuned) towards the end of the phase. There has been some prior evidence to suggest that this type of ramp can be advantageous, since by further detuning the trapping light there is less absorption and thus less repulsive force due to reabsorption[319, 327]. The manually-tuned runs did not adjust the trapping frequency until the polarisation gradient cooling phase, when the magnetic fields were switched off, so it could be interesting to investigate experimentally whether increasing the trapping detuning a few milliseconds earlier has a positive effect on performance.

Similarly, all runs exhibit a clear reduction in repump frequency (corresponding to becoming further red-detuned) towards the end of the phase, which is consistent with conventional wisdom regarding the creation of a temporal dark spot. Interestingly, however, it would appear that the ramp used in the original manually-tuned scheme is unnecessarily slow, and good performance can be attained with a more abrupt reduction.

For magnetic field gradient the correlations are less clear, although in all cases there is a sustained period of maximum gradient towards the end of the phase, which is again consistent with the standard approach to MOT compression.

While these trends towards the end of the phase are quite clear, the first half

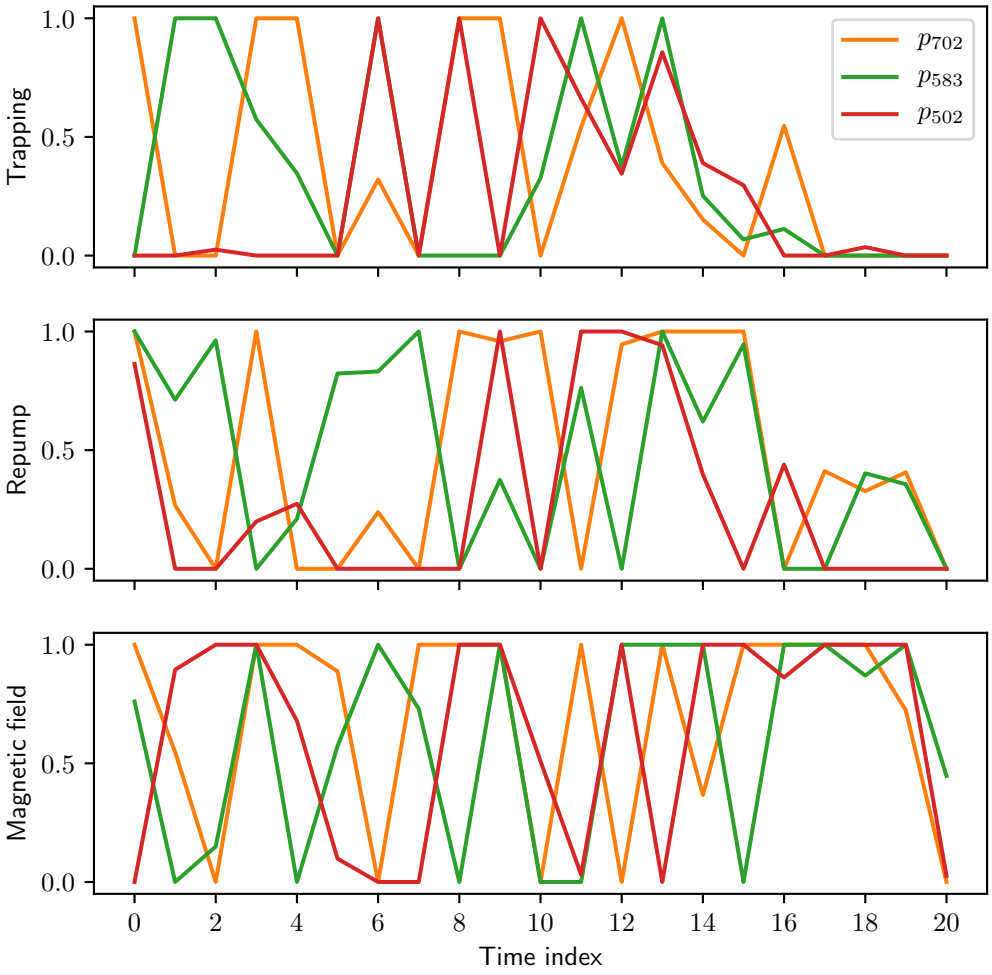

Figure 5.14: Comparison of best parameter sets found during the longest three optimisation runs. Each colour corresponds to a single parameter set. In order to simplify visualisation we have re-scaled each parameter to $[0, 1]$ (according to its bounds), and plotted parameters as points corresponding to their indices within the compression phase, rather than plotting piecewise-constant functions of time. Moreover, even though the quantities are distinct we have joined points from the same parameter set with lines, since this allows whole parameter sets to be more easily visualised. We will use this technique throughout the remainder of the chapter.

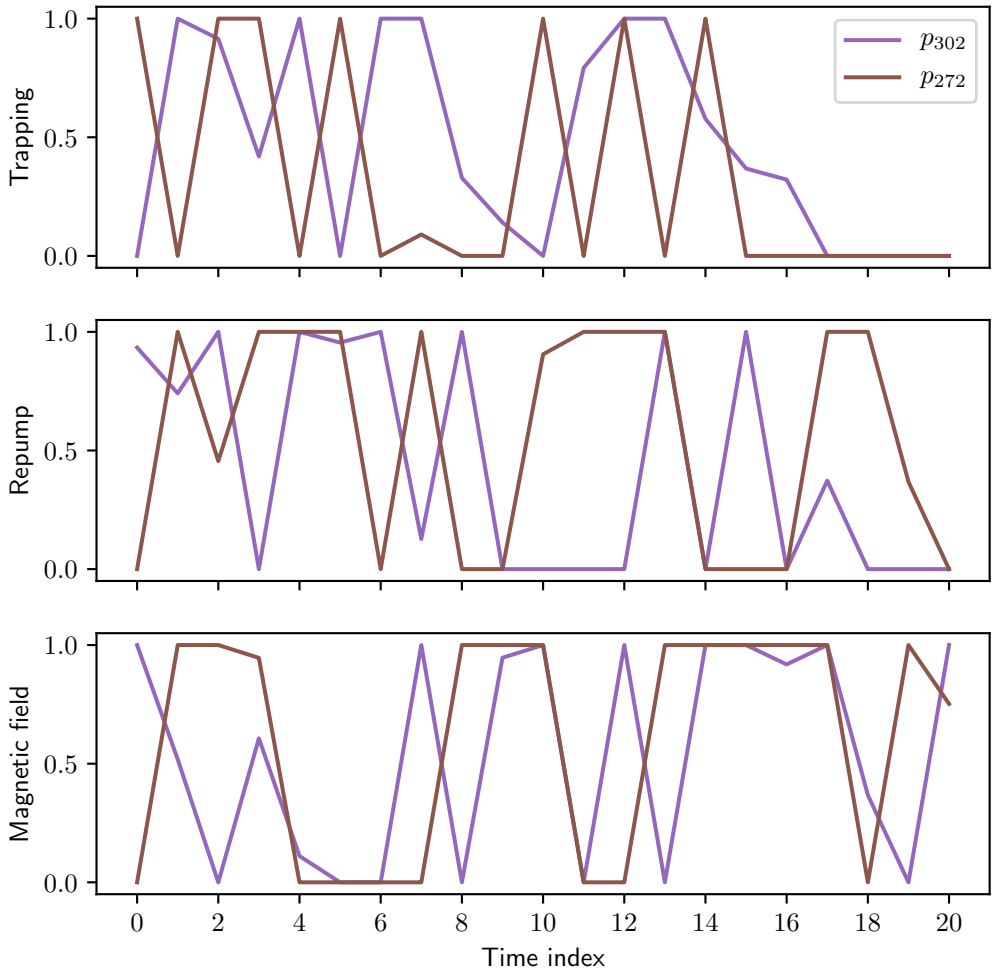

Figure 5.15: Comparison of best parameter sets found during the shortest two optimisation runs. As in Fig. 5.14, each colour corresponds to a single parameter set, and parameters have been scaled to $[0, 1]$ and plotted as lines to aid visualisation.

is more difficult to analyse, since there are no clear common features shared by all runs. This does not necessarily imply that these parameters are insignificant; instead it simply means that good performance can be attained for many different choices of these parameters. Further experimentation is required to determine exactly which features of the ramps contribute to the high performance.

Another implication of the diversity in the learned ramps from run to run is that the parameters found by the algorithm depend sensitively on inherent randomness in the optimisation procedure, since otherwise we would expect the same parameters to be found every time.

Algorithm convergence

We have seen that there is significant variability in the ramps found by the algorithm between different optimisation runs. To understand the reasons for this we may investigate in more detail the convergence behaviour of the algorithm within each run. For example, it is possible *a priori* that the runs were merely stopped prematurely, and all would have converged to the same global minimum given sufficient time. Alternatively, each run could have been converging to a different local minimum of the cost landscape depending on the initial training data. The evidence we shall present suggests the latter.

To start investigating any convergence (or lack thereof) we may look at the sampled costs from each run over time, as the algorithm explored and refined its estimates. These are shown for the longest run in Fig. 5.16. We observe that during the first $\sim$120 runs, where the parameters were being chosen by the differential evolution algorithm, a variety of costs were achieved as different parts of the space were explored. When the neural network-based algorithm was switched on, it rapidly made use of these initial training data to identify promising areas of the domain. Indeed, in this particular run the neural network algorithm took only 15 iterations before identifying a superior parameter set. Moreover, it was able to continue to improve on this choice over the next several hundred iterations, and in the process achieved far better costs than those found by the differential evolution algorithm. We also note that even after 700 iterations the algorithm was still exploring the search space (as evidenced by the variety of costs on the right-hand side of the plot), although the best obtained costs appear to be converging.

In Fig. 5.17 we plot the analogous quantities for several more optimisation

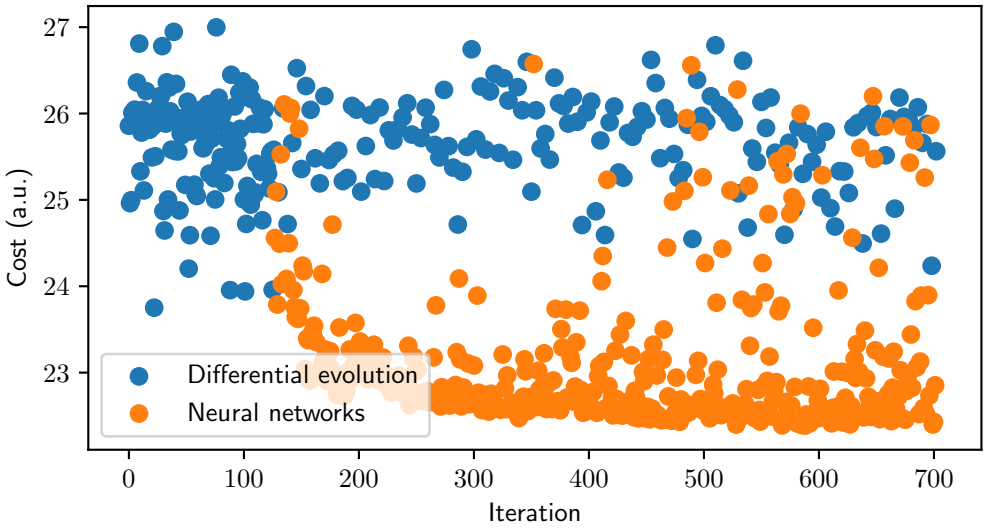

Figure 5.16: Cost as a function of iteration for the longest optimisation run. We have distinguished between parameters chosen by the differential evolution algorithm (initial training data, and subsequently every fourth iteration) and the neural networks.

runs of varying lengths, and observe similar trends. Note that the costs cannot be compared from run to run, since they depend on transient aspects of the experimental setup such as the number of atoms in the cell and the detuning of the probe field. We observe that in some instances the performance of the algorithm actually decreased as time went on. The fact that this trend also appears to affect the performance of the differential evolution indicates that it was due to a low-frequency drift in the cost measurement, rather than the algorithm "forgetting" the best parameters.

Another interesting trend evident in Figs. 5.16 and 5.17 is that as time went on the variability in the costs of parameters suggested by the neural networks increased, suggesting that the algorithm explored more and more aggressively. A possible explanation for this is that over time the landscape modelled by the neural networks would most likely have become more complex, and thus exhibited more local minima. The minimisation procedure used to select candidate parameters would then be more likely to become stuck in a local minimum away from the well-explored region. This hypothesis could be tested by taking snapshots of the modelled landscape at various points during the optimisation run, and investigating the complexity of the landscape at each such point.

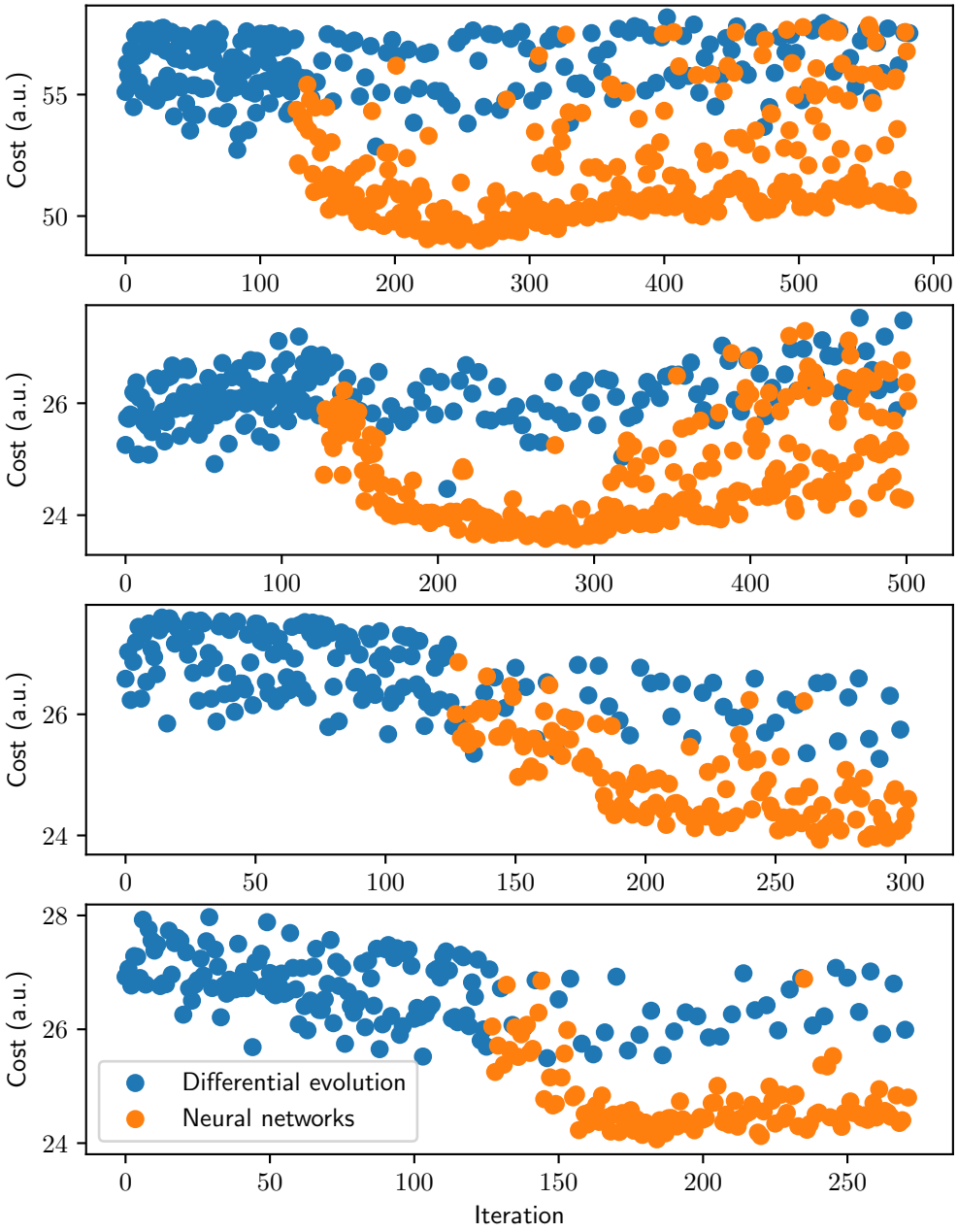

Figure 5.17: Cost as a function of iteration for several optimisation runs.

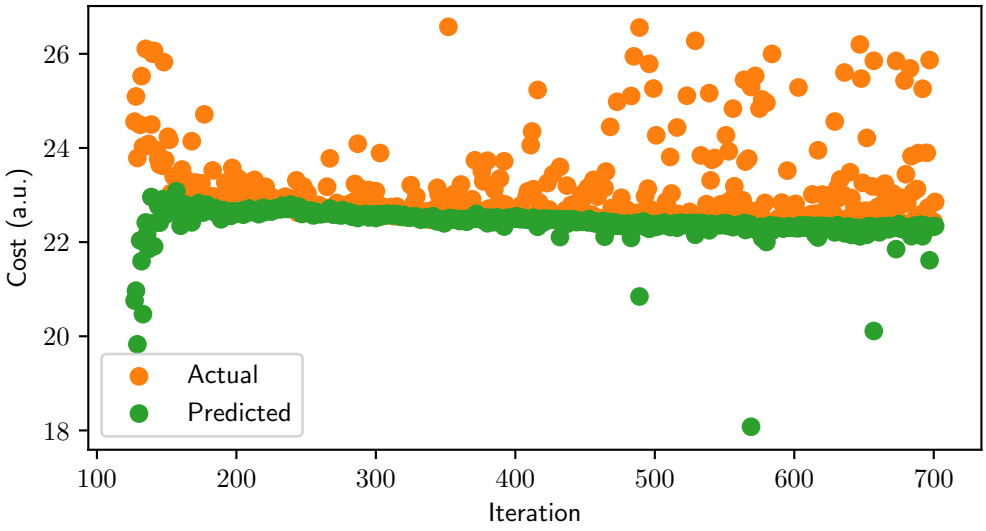

Figure 5.18: Actual and predicted costs for all parameters selected by the neural networks during the longest run.

An alternative explanation is based on the idea that the machine learning algorithm may have been generally "optimistic"; that is, it may have tended to predict unrealistically good costs for unknown parameters. After the initial training data were provided, the neural networks most likely identified an "obvious" region of good parameters (as evidenced by the rapid initial convergence to a low cost). While the neural networks explored this region, the differential evolution would have continued to explore the broader space, and may have found other similarly promising regions. If the neural networks were optimistic, after discovering that the parameters in the "obvious" region were not as good as expected, they would have incentive to explore the other regions (for which they still harboured unrealistic expectations). In Fig. 5.18 we plot the actual cost against the predicted cost for each set of parameters chosen by the neural networks, and we see that, indeed, they tended to predict unrealistically good costs. While this observation lends the hypothesis some evidence, more analysis and experimentation are required to confirm or refute it.

It is clear that the algorithm was still exploring near the end of each run, and that the costs it was able to obtain were converging. However, this does not give any information about convergence of the actual parameters. To investigate this aspect we may calculate the distances in parameter space between a certain fixed parameter set and each parameter set chosen during a run. Convergence of these

distances suggests convergence of the corresponding parameters. We use the best ramps found during the two longest runs (p_{702}, p_{583}) as fixed points, and calculate distances to each of these points for the two longest runs, as shown in Fig. 5.19 (note that we calculate distances after scaling each parameter to $[0, 1]$ based on its bounds).

The top-left and bottom-right plots demonstrate that, in each run, the parameters converge roughly towards the best parameters found in that run. The existence of some degree of convergence to the best parameters is unsurprising. The more interesting observation is that there is no additional subsequence converging to some other parameter set, which suggests that the algorithm has identified a single promising area early in the run, and—aside from some scattered exploratory samplings—has focused only on refining that guess. This observation indicates that while the algorithm was capable of effectively optimising the experiment, it is unlikely that in a single run it could find the true *global* minimum of the landscape. This is not particularly surprising, given the potential complexity of a 63-dimensional landscape, nor necessarily problematic, but still an important observation.

The top-right and bottom-left plots reinforce this picture by showing that the parameters in one run remain relatively distant from the best parameters found in a *different* run. This implies that the algorithm could not have gathered sufficient information to conclude that the region it chose to focus on was better than the region found by the other optimisation run; instead it appears that the algorithm was most likely ignorant of the alternative region altogether.

We can gain further insight into the localised convergence behaviour within a run by inspecting several of the best parameter sets from that run. These are shown for the longest run in Fig. 5.20, together with the single best parameter set from the second longest run (p_{583}) for comparison. While there is evidently some degree of variety, it is clear that most of the good parameter sets identified during the run had similar shapes and features, even though we know (from Figs. 5.14 and 5.15) that there exist highly effective ramps with very different shapes.

We have presented evidence suggesting that the general behaviour of the algorithm, within an optimisation run, was to quickly identify a promising area of the parameter space in which to search, and over time converge towards a minimum in that area. While some amount of wider exploration continued to occur until the end of each run, this was insufficient to detect the existence of other areas of

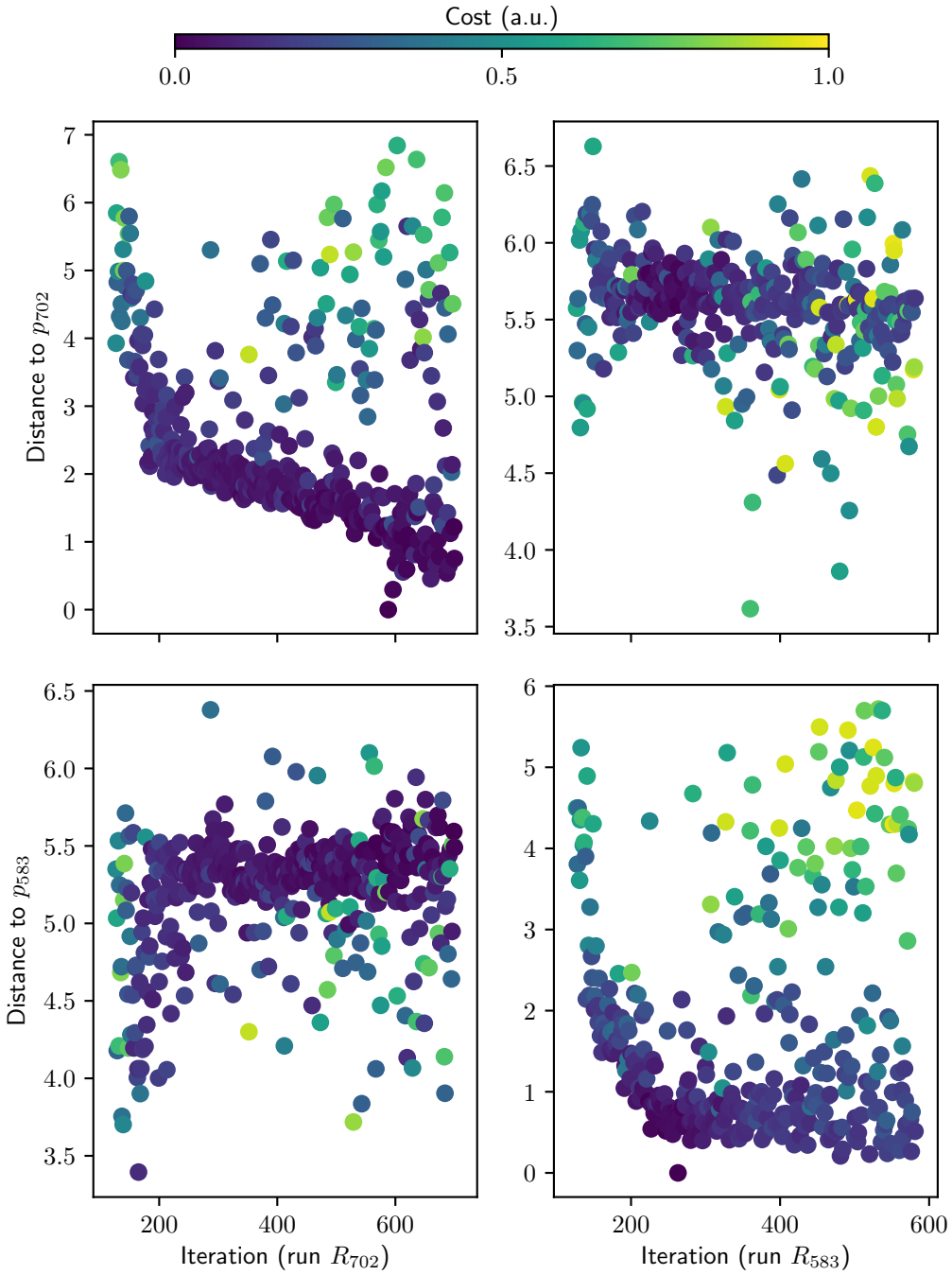

Figure 5.19: Parameter space distance to fixed point for each parameter set chosen by the neural networks, for fixed points p_{702} and p_{583} and runs R_{702} and R_{583}. The colours indicate the cost, normalised to the appropriate run.

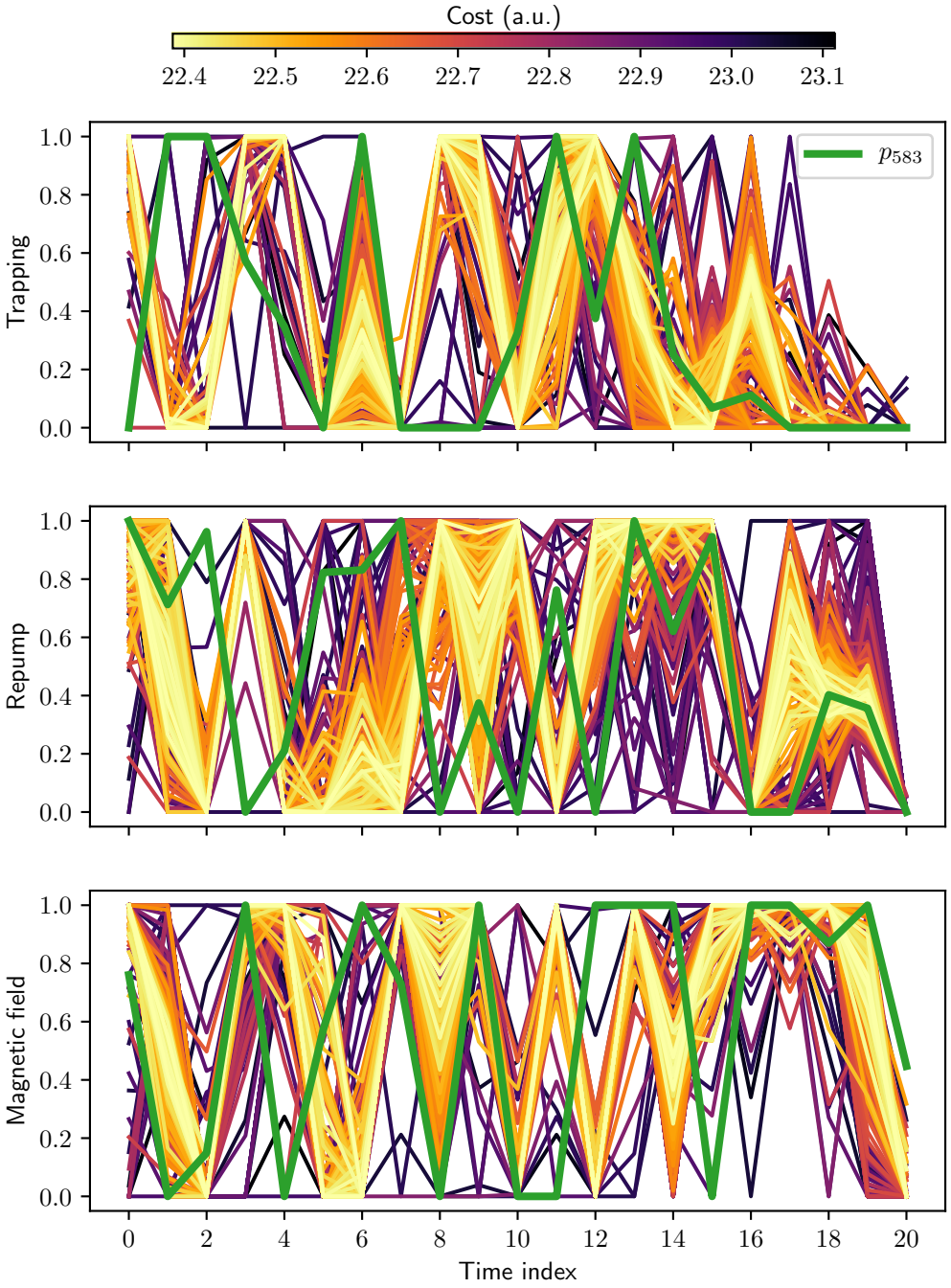

Figure 5.20: The best 300 parameters found during the longest optimisation run, with the best parameters p_{583} found during the second longest run shown for comparison. Each line represents a single parameter set. With the exception of the green line representing p_{583}, each line is coloured according to the cost of the corresponding parameter set.

the space containing good solutions.

Local landscape behaviour

We have shown that each run of the algorithm tends towards an optimal solution within a particular localised area of the parameter space, and that this solution was (unsurprisingly) close to the best parameters found for that run. An advantage of this type of convergence is that the model should be an accurate representation of the true landscape in the vicinity of those best parameters, by virtue of having sampled so many points. We can thus inspect the model in order to learn about the behaviour of the landscape in that area. In this section we focus on the longest run (R_{702}), and in particular the local behaviour about the best parameters (p_{702}).

While neural networks are notoriously opaque to the extraction of useful information[328–330], in our case we may exploit the fact that—despite any internal complexity—the networks we consider merely represent explicit real-valued functions of real variables. In particular, we may calculate the derivatives of the relevant neural network about the best parameters, and thus obtain Taylor approximations of the landscape.[2]

For example, it is useful to know whether better costs could have been attained had the bounds on the parameters been larger, since this could inform the choice of bounds used in future runs of the algorithm. Inspecting the best parameters (Fig. 5.12) suggests that this could indeed be the case, since many parameters were chosen to saturate their bounds.

Another way to attempt to answer this question is by calculating the gradient of the model: a highly non-zero partial derivative (with an appropriate sign) for a parameter that saturated its bounds would imply that, indeed, the bounds were overly restrictive. The gradient vectors for the three neural network models trained during the longest run are shown in Fig. 5.21 (note that all parameters were scaled to $[0, 1]$ based on their bounds prior to calculation of the gradient, so that gradients with respect to different physical quantities can be roughly compared). We notice that the second model exhibits significantly higher partial derivatives than the other two, meaning it predicted the landscape to be less

[2] Actual computation of derivatives proceeds via multiple applications of the chain rule; many machine learning libraries have built-in functionality to compute arbitrary mixed partial derivatives (of multilayer perceptrons) automatically[331, 332].

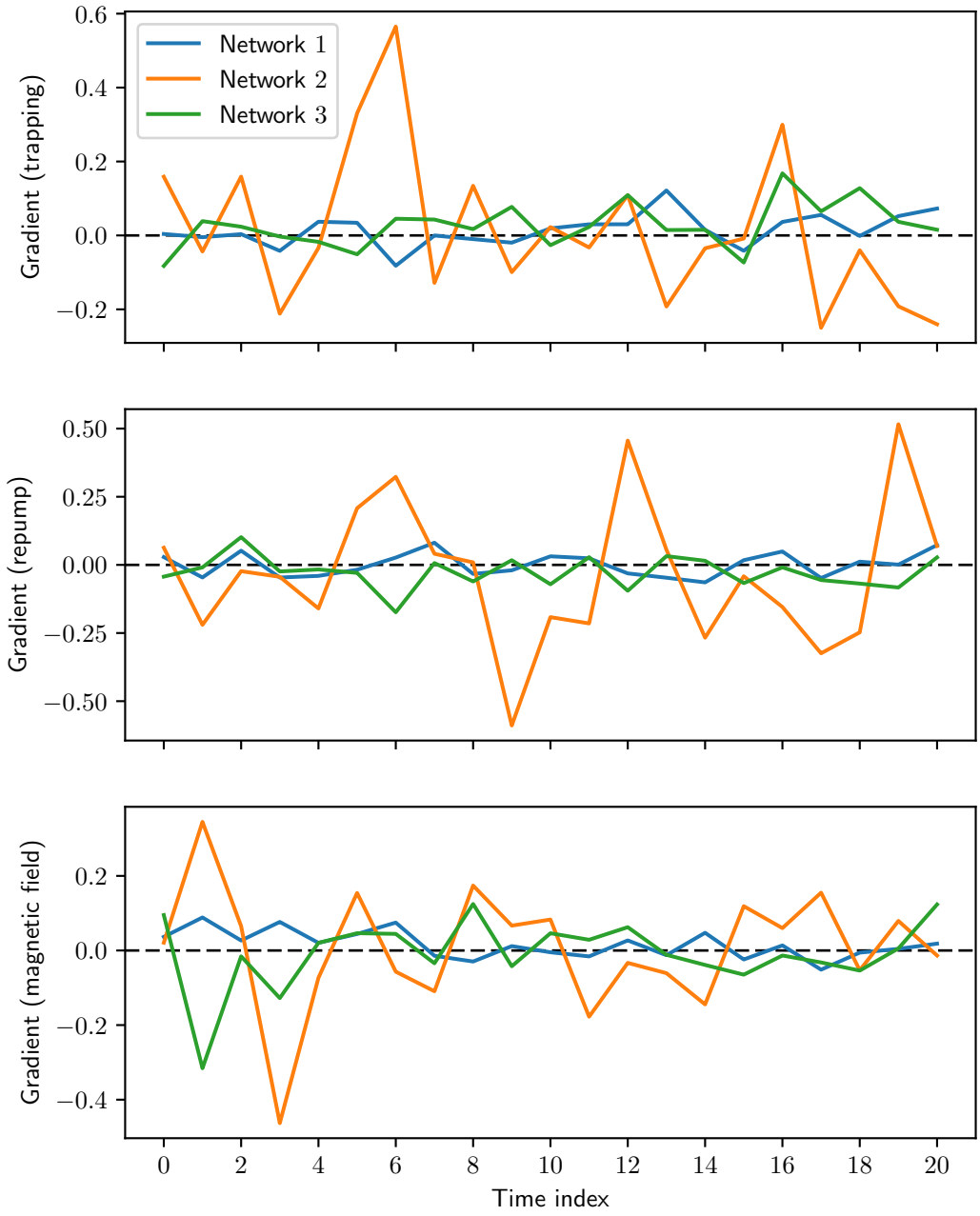

Figure 5.21: Gradients of each neural network at the best parameters, for the longest run. Each point gives the component of the gradient vector corresponding to a single parameter (the partial derivative with respect to that parameter), where the parameters are arranged in the usual manner. The units correspond to raw costs as shown in Fig. 5.16 and parameters scaled to $[0, 1]$ as usual. We have once again plotted lines to help distinguish between the different data sets, even though the quantities are discrete.

flat (in the vicinity of the best parameters). However, the fact that the model was not actually able to find a better-performing set of parameters suggests that this may simply be a result of inaccurate modelling, since over time the accuracy of each individual model fluctuates (due to the randomness in the training procedure). In any case, there do not appear to be strong correlations between saturated parameters in Fig. 5.12 and highly non-zero gradients in Fig. 5.21. The only potential candidates from a trustworthy network (namely 1 or 3) are some of the late trapping detunings and early magnetic field gradients, although in both cases the gradients are still relatively small. Thus it appears that the bounds on the parameters did not significantly hamper the algorithm's ability to optimise the chosen solution, although for a future run it could be interesting to increase the allowable magnetic field gradients and trapping detunings to see if any improvement in performance becomes possible.

Another aspect of the local landscape behaviour that we can investigate is the sensitivity of the cost function to perturbations of the parameters, which in turn could yield information about which features of the parameter set are most important. Once again we use a Taylor approximation of the model, but this time we consider only the second-order term, namely the Hessian matrix (the matrix of mixed second-order partial derivatives). This describes a paraboloid approximation of the landscape in the vicinity of the best parameters. The principal directions of this paraboloid, which are given by the eigenvectors of the Hessian, yield the directions along which the cost function's curvature is maximised (with the curvature given by the corresponding eigenvalues). That is, the eigenvectors with highest eigenvalues correspond to the directions in parameter space to which the cost is most sensitive. In Fig. 5.22 we plot the eigenvalues for the three Hessian matrices corresponding to the three networks (again, parameters were scaled to $[0, 1]$ before calculating the matrices). Interestingly, we see that for all networks the majority of eigenvalues are very close to 0, which suggests that the landscape is relatively flat except along a few specific directions. We also note again the difference in behaviour between network 2 and the others, where the former has modelled a paraboloid with significantly steeper curvatures.

We can attempt to further investigate the local landscape behaviour by plotting the principal directions (eigenvectors) themselves, as shown in Fig. 5.23 (note that we have omitted network 2 since, as discussed above, it appears to have been poorly fitted when the optimisation was stopped). We first note the large array

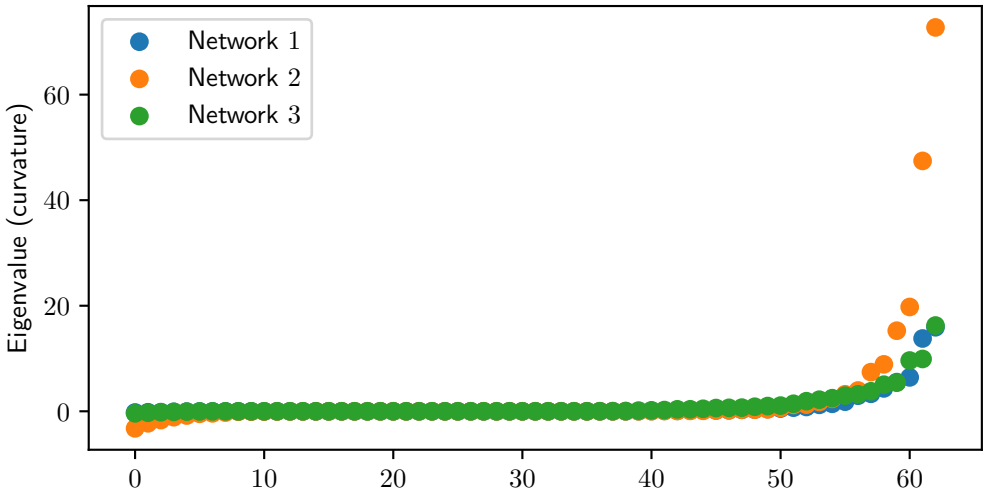

Figure 5.22: Eigenvalues of Hessian matrices at the best parameters, for the longest run. These represent the curvatures of the landscapes modelled by the networks.

of directions with low curvature in the background, corresponding to the long tail of low eigenvalues in Fig. 5.22. Looking at the directions corresponding to high curvatures, large components tentatively indicate parameters on which the cost depends sensitively. For example, this reasoning suggests that the cost is sensitive to the final few milliseconds of the repump detuning, and to the initial few milliseconds of the magnetic field gradient. The former is not surprising, since if the repump is detuned too far then any trapping or polarisation gradient cooling could be compromised, while detuning too little could cause excess reabsorption and thus outward pressure on the MOT. The latter is more unexpected, so it would be very interesting to test the sensitivity to those parameters experimentally. Unfortunately it is hard to conclude anything about the sensitivity to perturbations in the trapping frequency, or in the magnetic field gradient during the second half of the compression, due to the lack of any clear pattern. Ideally we would also be able to understand the sensitivity to combinations of parameters varying together, rather than only individual parameters in isolation, but this similarly appears infeasible at present. Longer optimisation runs could make this analysis more useful, since the networks would be closer to convergence and thus would hopefully exhibit more consistent and less noisy behaviour.

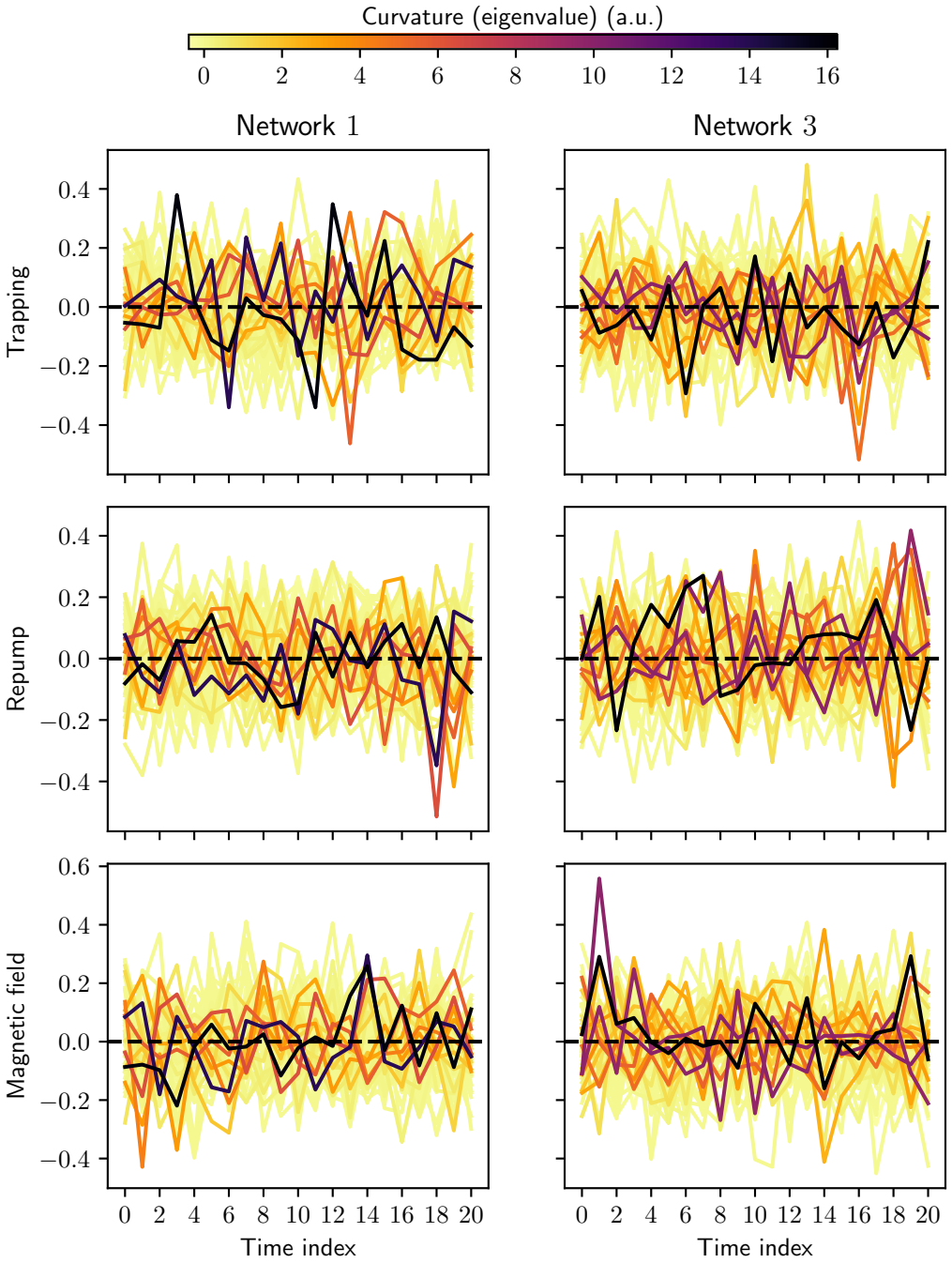

Figure 5.23: Principal directions (Hessian eigenvectors) of networks 1 and 3 at the best parameters, for the longest run. Each direction is a unit 63-dimensional vector, with components corresponding to perturbations to the usual parameters. Each direction is coloured according to the curvature of the landscape along that direction (the corresponding eigenvalue). As usual, even though the quantities are discrete they are plotted with lines for the sake of clearer visualisation.

5.4 Conclusion

We have presented a fast, scalable machine learning algorithm based on neural networks for performing automatic optimisation of arbitrary physical systems. After giving a brief introduction to the relevant theory of artificial neural networks, we described the core unique components of the algorithm. We then demonstrated the potential of the algorithm by presenting and discussing the preliminary results from applying it the MOT at the heart of a cold-atom gradient echo memory: in short, an enhancement in optical depth from 138, the best value obtained via manual optimisation, to 448.

There is significant scope for future work related to this project. For a start, the details of the MOT optimisation are still not well-understood. It would be useful to understand why the algorithm tends to explore more aggressively at later times (possibly by confirming the hypothesis presented earlier). More importantly, an analysis of the different optimal ramps found by each run of the machine learning algorithm to determine the common features would help to understand why the ramps are so effective. Similarly, while we have given a preliminary investigation into the local behaviour of the cost landscape in the vicinity of particular high-performing parameter sets, it appears that there is significantly more information to extract, and this could again help to understand the physical mechanisms at play. Another potentially interesting avenue would be to apply regularisation (as described in Section 5.2.1 for the neural network loss function) to the experiment cost function. Specifically, a small penalty could be applied to "complex" ramps exhibiting rapidly oscillating values or sharp changes, which would encourage the algorithm to find ramps that both achieve high OD and are simple. The outcome of this process would be interesting regardless of whether the optimisation became more or less effective. A reduction in performance after applying such regularisation would imply that these features are in fact important, while any other result would at least yield simpler ramps that might be amenable to simpler reasoning. Another possible approach to finding more physically meaningful compression ramps would be to use a different parameterisation, for example based on Fourier coefficients. Such a parameterisation could potentially be more efficient and yield simpler ramps.

There are also many possible improvements associated with the algorithm itself. In the short term, application to a wider variety of experiments would help

determine suitability of the chosen hyperparameters. As we have discussed, these were chosen by testing on a simple, low-dimensional, simulated experiment, but were still able to perform well when applied to the MOT. However, more data points are necessary before concluding that they work well in general.

In the medium term more significant adaptations could be beneficial. For example, a wider distribution of networks and thus improved exploration could be obtained by using bagging with more networks, or making another attempt at using dropout or Bayes by backpropagation. With specialised hardware these techniques may become more feasible than they were in this first application of the algorithm, which was performed on standard consumer hardware. Another approach to potentially improving the exploration capabilities of the algorithm, inspired by the observations in Section 5.3.4 regarding the convergence to different points based on the initial training data, would be to train each network of the ensemble on a random subset of the data, as opposed to all the data. This would most likely slow down the rate of convergence of the algorithm to low costs, but could significantly improve its ability to identify multiple spatially separate local minima.

Longer term there are many exciting fundamental improvements to the algorithm. One would be to implement a hybrid algorithm utilising different types of model for different regimes of the optimisation procedure. For instance, neural networks—which, as we have seen, can efficiently handle high-dimensional parameter spaces—could be used in the initial stages to identify promising areas of the space and principal directions along which to explore, and then control could be passed to a slower Gaussian process-based algorithm that may be capable of more accurately modelling the simplified space.

An important improvement would be to more explicitly support stochastic or time-varying cost landscapes, since these would be ubiquitous in practice. It is not entirely clear how we would approach this problem, although possibilities include artificially adjusting training data based on its staleness (by under-sampling old data during training, for instance), and using a more sophisticated loss function (that can take into account stochastic costs) while training the network[333, 334].

Another exciting prospect involves utilising a wider variety of neural networks. At present the same neural networks are used throughout the procedure, and all have the same hyperparameters. For optimisation runs involving many more evaluations of the experiment it is possible to envisage a scenario in which a much

larger ensemble of networks, with a variety of hyperparameters, are trained simultaneously, and networks are discarded and replaced if they predict poorly. If replacement networks were chosen based on the features of high-performing networks, we would essentially have implemented a genetic algorithm for automatically choosing and updating the neural networks; this is known as *neuroevolution*, and is a well-studied technique[335–337].

Chapter 6

Conclusions and outlook

In this thesis we have considered four different types of physical system, and four corresponding methods for optimising their performances. Generally speaking, the systems have become less analytically tractable from chapter to chapter, and the optimisation techniques correspondingly more general.

We first investigated, in Chapter 2, the prospect of enhancing the sensitivity of interferometer-based gravitational wave detectors by injecting squeezed light generated by a cavity optomechanical system. Broadband sensitivity enhancement requires squeezed light exhibiting specific frequency-dependent quadrature rotation. We derived an expression describing the output field of such a system, and found that while the field exhibits quadrature rotation, this rotation occurs in the opposite direction to that required by gravitational wave detectors. As a result, while sensitivity can be enhanced at high and low frequencies, there is necessarily a band of central frequencies at which sensitivity is reduced. Thus optomechanical squeezing is unsuitable in general for gravitational wave detectors, although it could potentially find uses in particular unconventional modes of operation.

In Chapter 3 we derived a general scheme for synthesising custom optical spring potentials in cavity optomechanical systems. This scheme allows one to tailor the displacement-dependent forces experienced by the cavity mirrors far beyond what is achievable merely by changing the cavity finesse, potentially yielding performance improvements or unlocking entirely new applications. As a specific example we considered a gravitational sensor based on a levitated cavity mirror, and demonstrated that by utilising the scheme an improvement in sensitivity by a factor of 5 would be expected.

In Chapter 4 we introduced a nanowire-based optomechanical sensor for transient forces. We enhanced signal-to-noise ratio by a factor of 3 by implementing a non-stationary feedback cooling protocol to damp the nanowire's motion immediately prior to the arrival of the signal. The improved sensor had a force resolution of 2×10^{-16} N. Next we considered two non-stationary post-processing techniques, one based on a Kalman filter and one based on a simulation of the physical feedback. We showed that both techniques yielded similar sensitivity enhancements to the physical feedback cooling, but did not require the additional experimental complexity.

Finally, in Chapter 5 we presented a machine learning algorithm capable of optimising arbitrary physical systems without human input. After giving some background from the theory of artificial neural networks we discussed the most interesting details of the algorithm. To demonstrate the algorithm's potential we then applied it to a magneto-optical trap (MOT) used for a quantum memory, and achieved an improvement in optical depth from 138 to 448. We then analysed the behaviour of the algorithm during the optimisation of the MOT. Our findings showed that the algorithm was not exploring the full parameter space in detail during each individual run. This suggests that even better performance—beyond the factor of 3 improvement in optical depth already observed—could potentially be attained with minor modifications to the algorithm.

From a general perspective, achieving optimal performance will become increasingly important as experimental quantum systems evolve into commercial quantum technologies. It will be necessary to optimise a variety of systems, ranging from those that are understood in detail to those whose dynamics are essentially unknown, and a corresponding range of optimisation techniques will be required.

We expect that general-purpose optimisation procedures will be particularly suitable for fine-tuning system parameters in the final stages of development. Techniques such as that presented in Chapter 5 (and, to some degree, Chapter 4) are thus likely to become ubiquitous in this setting. We also expect these techniques to grow in popularity in both experimental physics and the research and development phases of commercial technologies, but more as exploratory tools for complex systems than as methods for extracting optimal performance. For example, the results in Chapter 5 indicate that MOTs can be optimised to new levels by employing highly unexpected compression phases. However, presumably

even better performance could be achieved if the physical mechanism behind this process was understood, since then we may be able to perform principled system-specific optimisation in the style of Chapters 2 and 3. In the near future we expect this picture to evolve dramatically. The capabilities of machine learning are growing extremely rapidly at present, so it is likely that we will soon see algorithms capable of accurately modelling and optimising complex systems to an even greater degree than that presented here. If this is the case then a new challenge may emerge for physicists: trying to understand the physical mechanisms behind the performances of automatically-optimised systems. This process could provide fascinating breakthroughs from a physical perspective, and moreover is necessary in order to extract truly maximal performance via bespoke techniques.

In any case, the future of optimisation—performed by a combination of human and machine—holds many exciting opportunities and challenges, and will be instrumental in the evolution of quantum optical systems in both experimental and commercial applications.

Bibliography

[1] D. Coluzzi and R. Convissar, *Atlas of laser applications in dentistry* (Quintessence Publishing Company, Chicago, 2007), ISBN: 978-0-86715-476-4.

[2] T. Sakimoto, M. I. Rosenblatt, and D. T. Azar, "Laser eye surgery for refractive errors", The Lancet **367**, 1432–1447 (2006).

[3] P. Peyre and R. Fabbro, "Laser shock processing: a review of the physics and applications", Optical and Quantum Electronics **27**, 1213–1229 (1995).

[4] J. Tusek and M. Suban, "Hybrid welding with arc and laser beam", Science and Technology of Welding and Joining **4**, 308–311 (1999).

[5] J. Coelho, M. Abreu, and M. Pires, "High-speed laser welding of plastic films", Optics and Lasers in Engineering **34**, 385–395 (2000).

[6] D. Liu, Y. Tang, and W. Cong, "A review of mechanical drilling for composite laminates", Composite Structures **94**, 1265–1279 (2012).

[7] N. Jalili and K. Laxminarayana, "A review of atomic force microscopy imaging systems: application to molecular metrology and biological sciences", Mechatronics **14**, 907–945 (2004).

[8] F. J. Giessibl, "Advances in atomic force microscopy", Reviews of Modern Physics **75**, 949–983 (2003).

[9] D. Deutsch, "Quantum theory, the church–turing principle and the universal quantum computer", Proceedings of the Royal Society of London A: Mathematical, Physical and Engineering Sciences **400**, 97–117 (1985).

[10] R. P. Feynman, "Simulating physics with computers", International Journal of Theoretical Physics **21**, 467–488 (1982).

[11] T. D. Ladd, F. Jelezko, R. Laflamme, Y. Nakamura, C. Monroe, and J. L. O'Brien, "Quantum computers", Nature **464**, 45–53 (2010).

[12] C. H. Bennett and G. Brassard, "Quantum cryptography: public key distribution and coin tossing", in Proceedings of the IEEE international conference on computers, systems and signal processing (1984), pp. 175–179.

[13] N. Gisin and R. Thew, "Quantum communication", Nature Photonics **1**, 165–171 (2007).

[14] A. Derevianko and H. Katori, "Colloquium: physics of optical lattice clocks", Reviews of Modern Physics **83**, 331–347 (2011).

[15] B. J. Bloom, T. L. Nicholson, J. R. Williams, S. L. Campbell, M. Bishof, X. Zhang, W. Zhang, S. L. Bromley, and J. Ye, "An optical lattice clock with accuracy and stability at the 10^{-18} level", Nature **506**, 71–75 (2014).

[16] M. de Angelis, A. Bertoldi, L. Cacciapuoti, A. Giorgini, G. Lamporesi, M. Prevedelli, G. Saccorotti, F. Sorrentino, and G. M. Tino, "Precision gravimetry with atomic sensors", Measurement Science and Technology **20**, 022001 (2009).

[17] Quintessence Labs, *Quintessence Labs*, (2017) `https://www.quintessencelabs.com/` (visited on 09/18/2017).

[18] AOSense, *AOSense*, (2017) `https://aosense.com` (visited on 09/18/2017).

[19] Muquans, *Muquans*, (2017) `https://www.muquans.com/` (visited on 09/18/2017).

[20] ID Quantique, *ID Quantique*, (2017) `https://www.idquantique.com/` (visited on 09/18/2017).

[21] Google, *Quantum A.I.* (2017) `https://research.google.com/pubs/QuantumAI.html` (visited on 09/19/2017).

[22] Lockheed Martin, *Quantum*, (2017) `https://www.lockheedmartin.com.au/us/what-we-do/emerging/quantum.html` (visited on 09/19/2017).

[23] Rigetti Computing, *Rigetti Computing*, (2017) `https://www.rigetti.com/` (visited on 11/14/2017).

[24] h-bar, *h-bar: Quantum Technology Consultants*, (2017) `https://www.h-bar.com.au/` (visited on 11/14/2017).

[25] QxBranch, *QxBranch*, (2017) `http://www.qxbranch.com/` (visited on 11/14/2017).

[26] 1QBit, *1QBit*, (2017) `https://1qbit.com/` (visited on 11/14/2017).

[27] *Fiber types in gigabit optical communications*, tech. rep., `https://www.cisco.com/c/en/us/products/collateral/interfaces-modules/transceiver-modules/white_paper_c11-463661.pdf` (Cisco, 2008).

[28] M. Takeoka, S. Guha, and M. M. Wilde, "Fundamental rate-loss tradeoff for optical quantum key distribution", Nature Communications **5**, 5235 (2014).

[29] H.-J. Briegel, W. Dür, J. I. Cirac, and P. Zoller, "Quantum repeaters: the role of imperfect local operations in quantum communication", Physical Review Letters **81**, 5932–5935 (1998).

[30] L.-M. Duan, M. D. Lukin, J. I. Cirac, and P. Zoller, "Long-distance quantum communication with atomic ensembles and linear optics", Nature **414**, 413–418 (2001).

[31] N. Sangouard, C. Simon, H. de Riedmatten, and N. Gisin, "Quantum repeaters based on atomic ensembles and linear optics", Reviews of Modern Physics **83**, 33–80 (2011).

[32] E. Diamanti, H.-K. Lo, B. Qi, and Z. Yuan, "Practical challenges in quantum key distribution", npj Quantum Information **2**, 16025 (2016).

[33] M. Hosseini, B. M. Sparkes, G. Campbell, P. K. Lam, and B. C. Buchler, "High efficiency coherent optical memory with warm rubidium vapour", Nature Communications **2**, 174 (2011).

[34] J. J. Longdell, E. Fraval, M. J. Sellars, and N. B. Manson, "Stopped light with storage times greater than one second using electromagnetically induced transparency in a solid", Physical Review Letters **95**, 063601 (2005).

[35] G. Heinze, C. Hubrich, and T. Halfmann, "Stopped light and image storage by electromagnetically induced transparency up to the regime of one minute", Physical Review Letters **111**, 033601 (2013).

[36] Y.-W. Cho, G. T. Campbell, J. L. Everett, J. Bernu, D. B. Higginbottom, M. T. Cao, J. Geng, N. P. Robins, P. K. Lam, and B. C. Buchler, "Highly efficient optical quantum memory with long coherence time in cold atoms", Optica **3**, 100–107 (2016).

[37] D. Aharonov and M. Ben-Or, "Fault-tolerant quantum computation with constant error", in Proceedings of the twenty-ninth annual ACM symposium on theory of computing, edited by F. T. Leighton and P. W. Shor (1997), pp. 176–188, ISBN: 978-0-89791-888-6.

[38] A. G. Fowler, M. Mariantoni, J. M. Martinis, and A. N. Cleland, "Surface codes: towards practical large-scale quantum computation", Physical Review A **86**, 032324 (2012).

[39] C. M. Caves, "Quantum-mechanical noise in an interferometer", Physical Review D **23**, 1693–1708 (1981).

[40] G. Guccione, H. J. Slatyer, A. R. R. Carvalho, B. C. Buchler, and P. K. Lam, "Squeezing quadrature rotation in the acoustic band via optomechanics", Journal of Physics B: Atomic, Molecular and Optical Physics **49**, 065401 (2016).

[41] J. Shapiro, H. Yuen, and A. Mata, "Optical communication with two-photon coherent states—part ii: photoemissive detection and structured receiver performance", IEEE Transactions on Information Theory **25**, 179–192 (1979).

[42] H. P. Yuen and V. W. S. Chan, "Noise in homodyne and heterodyne detection", Optics Letters **8**, 177–179 (1983).

[43] C. M. Caves, "Quantum-mechanical radiation-pressure fluctuations in an interferometer", Physical Review Letters **45**, 75–79 (1980).

[44] V. B. Braginsky, "Classical and quantum restrictions on the detection of weak disturbances of a macroscopic oscillator", Soviet Journal of Experimental and Theoretical Physics **26**, 831 (1968).

[45] H. J. Kimble, Y. Levin, A. B. Matsko, K. S. Thorne, and S. P. Vyatchanin, "Conversion of conventional gravitational-wave interferometers into quantum nondemolition interferometers by modifying their input and/or output optics", Physical Review D **65**, 022002 (2001).

[46] M. Holst, O. Sarbach, M. Tiglio, and M. Vallisneri, "The emergence of gravitational wave science: 100 years of development of mathematical theory, detectors, numerical algorithms, and data analysis tools.", English, Bulletin of the American Mathematical Society **53**, 513–554 (2016).

[47] J. R. Smith (for the LIGO Scientific Collaboration), "The path to the enhanced and advanced LIGO gravitational-wave detectors", Classical and Quantum Gravity **26**, 114013 (2009).

[48] The LIGO Scientific Collaboration, "Advanced LIGO", Classical and Quantum Gravity **32**, 074001 (2015).

[49] V. B. Braginsky and Y. I. Vorontsov, "Quantum-mechanical limitations in macroscopic experiments and modern experimental technique", Soviet Physics Uspekhi **17**, 644 (1975).

[50] V. B. Braginsky, Y. I. Vorontsov, and K. S. Thorne, "Quantum nondemolition measurements", Science **209**, 547–557 (1980).

[51] W. G. Unruh, "Quantum noise in the interferometer detector", in *Quantum optics, experimental gravity, and measurement theory*, edited by P. Meystre and M. O. Scully (Springer, Boston, 1983), pp. 647–660, ISBN: 978-1-4613-3712-6.

[52] M. T. Jaekel and S. Reynaud, "Quantum limits in interferometric measurements", Europhysics Letters **13**, 301 (1990).

[53] M. Xiao, L.-A. Wu, and H. J. Kimble, "Precision measurement beyond the shot-noise limit", Physical Review Letters **59**, 278–281 (1987).

[54] P. Grangier, R. E. Slusher, B. Yurke, and A. LaPorta, "Squeezed-light enhanced polarization interferometer", Physical Review Letters **59**, 2153–2156 (1987).

[55] H. Vahlbruch, S. Chelkowski, B. Hage, A. Franzen, K. Danzmann, and R. Schnabel, "Coherent control of vacuum squeezing in the gravitational-wave detection band", Physical Review Letters **97**, 011101 (2006).

[56] The LIGO Scientific Collaboration, "Enhanced sensitivity of the LIGO gravitational wave detector by using squeezed states of light", Nature Photonics **7**, 613–619 (2013).

[57] A. Luis and L. L. Sánchez-Soto, "Multimode quantum analysis of an interferometer with moving mirrors", Physical Review A **45**, 8228–8234 (1992).

[58] A. F. Pace, M. J. Collett, and D. F. Walls, "Quantum limits in interferometric detection of gravitational radiation", Physical Review A **47**, 3173–3189 (1993).

[59] J. Harms, Y. Chen, S. Chelkowski, A. Franzen, H. Vahlbruch, K. Danzmann, and R. Schnabel, "Squeezed-input, optical-spring, signal-recycled gravitational-wave detectors", Physical Review D **68**, 042001 (2003).

[60] S. Chelkowski, H. Vahlbruch, B. Hage, A. Franzen, N. Lastzka, K. Danzmann, and R. Schnabel, "Experimental characterization of frequency-dependent squeezed light", Physical Review A **71**, 013806 (2005).

[61] E. Oelker, T. Isogai, J. Miller, M. Tse, L. Barsotti, N. Mavalvala, and M. Evans, "Audio-band frequency-dependent squeezing for gravitational-wave detectors", Physical Review Letters **116**, 041102 (2016).

[62] P. Kwee, J. Miller, T. Isogai, L. Barsotti, and M. Evans, "Decoherence and degradation of squeezed states in quantum filter cavities", Physical Review D **90**, 062006 (2014).

[63] T. Isogai, J. Miller, P. Kwee, L. Barsotti, and M. Evans, "Loss in long-storage-time optical cavities", Optics Express **21**, 30114–30125 (2013).

[64] F. D. Valle, E. Milotti, A. Ejlli, U. Gastaldi, G. Messineo, L. Piemontese, G. Zavattini, R. Pengo, and G. Ruoso, "Extremely long decay time optical cavity", Optics Express **22**, 11570–11577 (2014).

[65] S. Weis, R. Rivière, S. Deléglise, E. Gavartin, O. Arcizet, A. Schliesser, and T. J. Kippenberg, "Optomechanically induced transparency", Science **330**, 1520–1523 (2010).

[66] E. E. Mikhailov, K. Goda, T. Corbitt, and N. Mavalvala, "Frequency-dependent squeeze-amplitude attenuation and squeeze-angle rotation by electromagnetically induced transparency for gravitational-wave interferometers", Physical Review A **73**, 053810 (2006).

[67] Y. Ma, S. L. Danilishin, C. Zhao, H. Miao, W. Z. Korth, Y. Chen, R. L. Ward, and D. G. Blair, "Narrowing the filter-cavity bandwidth in gravitational-wave detectors via optomechanical interaction", Physical Review Letters **113**, 151102 (2014).

[68] J. Qin, C. Zhao, Y. Ma, X. Chen, L. Ju, and D. G. Blair, "Classical demonstration of frequency-dependent noise ellipse rotation using optomechanically induced transparency", Physical Review A **89**, 041802 (2014).

[69] U. L. Andersen, T. Gehring, C. Marquardt, and G. Leuchs, "30 years of squeezed light generation", Physica Scripta **91**, 053001 (2016).

[70] C. Fabre, M. Pinard, S. Bourzeix, A. Heidmann, E. Giacobino, and S. Reynaud, "Quantum-noise reduction using a cavity with a movable mirror", Physical Review A **49**, 1337–1343 (1994).

[71] S. Mancini and P. Tombesi, "Quantum noise reduction by radiation pressure", Physical Review A **49**, 4055–4065 (1994).

[72] A. Nunnenkamp, K. Børkje, J. G. E. Harris, and S. M. Girvin, "Cooling and squeezing via quadratic optomechanical coupling", Physical Review A **82**, 021806 (2010).

[73] D. W. C. Brooks, T. Botter, S. Schreppler, T. P. Purdy, N. Brahms, and D. M. Stamper-Kurn, "Non-classical light generated by quantum-noise-driven cavity optomechanics", Nature **488**, 476–480 (2012).

[74] A. H. Safavi-Naeini, S. Groblacher, J. T. Hill, J. Chan, M. Aspelmeyer, and O. Painter, "Squeezed light from a silicon micromechanical resonator", Nature **500**, 185–189 (2013).

[75] T. P. Purdy, P.-L. Yu, R. W. Peterson, N. S. Kampel, and C. A. Regal, "Strong optomechanical squeezing of light", Physical Review X **3**, 031012 (2013).

[76] C. K. Law, "Effective hamiltonian for the radiation in a cavity with a moving mirror and a time-varying dielectric medium", Physical Review A **49**, 433–437 (1994).

[77] C. K. Law, "Interaction between a moving mirror and radiation pressure: a hamiltonian formulation", Physical Review A **51**, 2537–2541 (1995).

[78] C. Gardiner and P. Zoller, *Quantum noise: a handbook of markovian and non-markovian quantum stochastic methods with applications to quantum optics*, Springer Series in Synergetics (Springer, Berlin, 2004), ISBN: 978-3-540-22301-6.

[79] A. A. Clerk and F. Marquardt, "Basic theory of cavity optomechanics", in *Cavity optomechanics: nano- and micromechanical resonators interacting with light*, edited by M. Aspelmeyer, T. J. Kippenberg, and F. Marquardt (Springer, Berlin, 2014), pp. 5–23, ISBN: 978-3-642-55312-7.

[80] M. Aspelmeyer, T. J. Kippenberg, and F. Marquardt, "Cavity optomechanics", Reviews of Modern Physics **86**, 1391–1452 (2014).

[81] M. J. Collett and C. W. Gardiner, "Squeezing of intracavity and traveling-wave light fields produced in parametric amplification", Physical Review A **30**, 1386–1391 (1984).

[82] D. Stoler, "Equivalence classes of minimum uncertainty packets", Physical Review D **1**, 3217–3219 (1970).

[83] P. Drummond and Z. Ficek, *Quantum squeezing*, Springer Series on Atomic, Optical, and Plasma Physics (Springer, Berlin, 2004), ISBN: 978-3-540-65989-1.

[84] T. Corbitt, Y. Chen, F. Khalili, D. Ottaway, S. Vyatchanin, S. Whitcomb, and N. Mavalvala, "Squeezed-state source using radiation-pressure-induced rigidity", Physical Review A **73**, 023801 (2006).

[85] V. Giovannetti and D. Vitali, "Phase-noise measurement in a cavity with a movable mirror undergoing quantum Brownian motion", Physical Review A **63**, 023812, 023812 (2001).

[86] K. Jacobs, I. Tittonen, H. M. Wiseman, and S. Schiller, "Quantum noise in the position measurement of a cavity mirror undergoing Brownian motion", Physical Review A **60**, 538–548 (1999).

[87] A. A. Clerk, M. H. Devoret, S. M. Girvin, F. Marquardt, and R. J. Schoelkopf, "Introduction to quantum noise, measurement, and amplification", Reviews of Modern Physics **82**, 1155–1208 (2010).

[88] H. Miao, "Quantum theory of gravitational-wave detectors", in *Exploring macroscopic quantum mechanics in optomechanical devices* (Springer, Berlin, 2012), pp. 13–49, ISBN: 978-3-642-25640-0.

[89] H. J. Slatyer, G. Guccione, Y.-W. Cho, B. C. Buchler, and P. K. Lam, "Synthesis of optical spring potentials in optomechanical systems", Journal of Physics B: Atomic, Molecular and Optical Physics **49**, 125401 (2016).

[90] G. Anetsberger, O. Arcizet, Q. P. Unterreithmeier, R. Riviere, A. Schliesser, E. M. Weig, J. P. Kotthaus, and T. J. Kippenberg, "Near-field cavity optomechanics with nanomechanical oscillators", Nature Physics **5**, 909–914 (2009).

[91] E. Gavartin, P. Verlot, and T. J. Kippenberg, "A hybrid on-chip optomechanical transducer for ultrasensitive force measurements", Nature Nanotechnology **7**, 509–514 (2012).

[92] G. I. Harris, D. L. McAuslan, T. M. Stace, A. C. Doherty, and W. P. Bowen, "Minimum requirements for feedback enhanced force sensing", Physical Review Letters **111**, 103603 (2013).

[93] J.-J. Li and K.-D. Zhu, "Nonlinear optical mass sensor with an optomechanical microresonator", Applied Physics Letters **101**, 141905 (2012).

[94] F. Liu, S. Alaie, Z. C. Leseman, and M. Hossein-Zadeh, "Sub-pg mass sensing and measurement with an optomechanical oscillator", Optics Express **21**, 19555–19567 (2013).

[95] S. Forstner, S. Prams, J. Knittel, E. D. van Ooijen, J. D. Swaim, G. I. Harris, A. Szorkovszky, W. P. Bowen, and H. Rubinsztein-Dunlop, "Cavity optomechanical magnetometer", Physical Review Letters **108**, 120801 (2012).

[96] C. Yu, J. Janousek, E. Sheridan, D. L. McAuslan, H. Rubinsztein-Dunlop, P. K. Lam, Y. Zhang, and W. P. Bowen, "Optomechanical magnetometry with a macroscopic resonator", Physical Review Applied **5**, 044007 (2016).

[97] M. Wu, N. L.-Y. Wu, T. Firdous, F. Fani Sani, J. E. Losby, M. R. Freeman, and P. E. Barclay, "Nanocavity optomechanical torque magnetometry and radiofrequency susceptometry", Nature Nanotechnology **12**, 127–131 (2017).

[98] P. Rabl, "Photon blockade effect in optomechanical systems", Physical Review Letters **107**, 063601 (2011).

[99] L. Qiu, L. Gan, W. Ding, and Z.-Y. Li, "Single-photon generation by pulsed laser in optomechanical system via photon blockade effect", Journal of the Optical Society of America B **30**, 1683–1687 (2013).

[100] K. Stannigel, P. Komar, S. J. M. Habraken, S. D. Bennett, M. D. Lukin, P. Zoller, and P. Rabl, "Optomechanical quantum information processing with photons and phonons", Physical Review Letters **109**, 013603 (2012).

[101] A. H. Safavi-Naeini and O. Painter, "Proposal for an optomechanical traveling wave phonon–photon translator", New Journal of Physics **13**, 013017 (2011).

[102] D. E. Chang, A. H. Safavi-Naeini, M. Hafezi, and O. Painter, "Slowing and stopping light using an optomechanical crystal array", New Journal of Physics **13**, 023003 (2011).

[103] V. Fiore, Y. Yang, M. C. Kuzyk, R. Barbour, L. Tian, and H. Wang, "Storing optical information as a mechanical excitation in a silica optomechanical resonator", Physical Review Letters **107**, 133601 (2011).

[104] H. Yang, H. Miao, D.-S. Lee, B. Helou, and Y. Chen, "Macroscopic quantum mechanics in a classical spacetime", Physical Review Letters **110**, 170401 (2013).

[105] S. Nimmrichter, K. Hornberger, and K. Hammerer, "Optomechanical sensing of spontaneous wave-function collapse", Physical Review Letters **113**, 020405 (2014).

[106] J. Chan, M. Eichenfield, R. Camacho, and O. Painter, "Optical and mechanical design of a "zipper" photonic crystal optomechanical cavity", Optics Express **17**, 3802–3817 (2009).

[107] H. Rokhsari, T. J. Kippenberg, T. Carmon, and K. J. Vahala, "Radiation-pressure-driven micro-mechanical oscillator", Optics Express **13**, 5293–5301 (2005).

[108] J. Hofer, A. Schliesser, and T. J. Kippenberg, "Cavity optomechanics with crystalline whispering gallery mode resonators", in Conference on lasers and electro-optics (2009), pp. 1–2, ISBN: 978-1-55752-869-8.

[109] L. A. D. Lorenzo and K. C. Schwab, "Superfluid optomechanics: coupling of a superfluid to a superconducting condensate", New Journal of Physics **16**, 113020 (2014).

[110] P. F. Barker, "Doppler cooling a microsphere", Physical Review Letters **105**, 073002 (2010).

[111] N. Kiesel, F. Blaser, U. Delić, D. Grass, R. Kaltenbaek, and M. Aspelmeyer, "Cavity cooling of an optically levitated submicron particle", Proceedings of the National Academy of Sciences **110**, 14180–14185 (2013).

[112] L. P. Neukirch and A. N. Vamivakas, "Nano-optomechanics with optically levitated nanoparticles", Contemporary Physics **56**, 48–62 (2014).

[113] V. G. Shvedov, A. R. Davoyan, C. Hnatovsky, N. Engheta, and W. Krolikowski, "A long-range polarization-controlled optical tractor beam", Nature Photonics **8**, 846–850 (2014).

[114] A. Ashkin, "Acceleration and trapping of particles by radiation pressure", Physical Review Letters **24**, 156–159 (1970).

[115] A. Ashkin, "History of optical trapping and manipulation of small-neutral particle, atoms, and molecules", IEEE Journal Of Selected Topics In Quantum Electronics **6**, 841–856 (2000).

[116] A. Ashkin and J. M. Dziedzic, "Optical levitation by radiation pressure", Applied Physics Letters **19**, 283–285 (1971).

[117] J. R. Moffitt, Y. R. Chemla, S. B. Smith, and C. Bustamante, "Recent advances in optical tweezers", Annual Review of Biochemistry **77**, 205–228 (2008).

[118] O. M. Maragò, P. H. Jones, P. G. Gucciardi, G. Volpe, and A. C. Ferrari, "Optical trapping and manipulation of nanostructures", Nature Nanotechnology **8**, 807–819 (2013).

[119] T. Li, S. Kheifets, and M. G. Raizen, "Millikelvin cooling of an optically trapped microsphere in vacuum", Nature Physics **7**, 527–530 (2011).

[120] J. Millen, T. Deesuwan, P. Barker, and J. Anders, "Nanoscale temperature measurements using non-equilibrium Brownian dynamics of a levitated nanosphere", Nature Nanotechnology **9**, 425–429 (2014).

[121] K. Dholakia and T. Čižmár, "Shaping the future of manipulation", Nature Photonics **5**, 335–342 (2011).

[122] D. E. Chang, C. A. Regal, S. B. Papp, D. J. Wilson, J. Ye, O. Painter, H. J. Kimble, and P. Zoller, "Cavity opto-mechanics using an optically levitated nanosphere", Proceedings of the National Academy of Sciences **107**, 1005–1010 (2010).

[123] S. Singh, G. A. Phelps, D. S. Goldbaum, E. M. Wright, and P. Meystre, "All-optical optomechanics: an optical spring mirror", Physical Review Letters **105**, 213602 (2010).

[124] G. Guccione, M. Hosseini, S. Adlong, M. T. Johnsson, J. Hope, B. C. Buchler, and P. K. Lam, "Scattering-free optical levitation of a cavity mirror", Physical Review Letters **111**, 183001 (2013).

[125] V. B. Braginsky, M. L. Gorodetsky, and F. Y. Khalili, "Optical bars in gravitational wave antennas", Physics Letters A **232**, 340–348 (1997).

[126] B. S. Sheard, M. B. Gray, C. M. Mow-Lowry, D. E. McClelland, and S. E. Whitcomb, "Observation and characterization of an optical spring", Physical Review A **69**, 051801 (2004).

[127] T. Corbitt, Y. Chen, E. Innerhofer, H. Müller-Ebhardt, D. Ottaway, H. Rehbein, D. Sigg, S. Whitcomb, C. Wipf, and N. Mavalvala, "An all-optical trap for a gram-scale mirror", Physical Review Letters **98**, 150802 (2007).

[128] S. W. Schediwy, C. Zhao, L. Ju, D. G. Blair, and P. Willems, "Observation of enhanced optical spring damping in a macroscopic mechanical resonator and application for parametric instability control in advanced gravitational-wave detectors", Physical Review A **77**, 013813 (2008).

[129] W. Yu, W. C. Jiang, Q. Lin, and T. Lu, "Cavity optomechanical spring sensing of single molecules", Nature Communications **7**, 12311 (2016).

[130] P. T. Rakich, M. A. Popovic, M. Soljacic, and E. P. Ippen, "Trapping, corralling and spectral bonding of optical resonances through optically induced potentials", Nature Photonics **1**, 658–665 (2007).

[131] P. T. Rakich, M. A. Popović, and Z. Wang, "General treatment of optical forces and potentials in mechanically variable photonic systems", Optics Express **17**, 18116–18135 (2009).

[132] A. E. Siegman, *Lasers* (University Science Books, Mill Valley, 1986), ISBN: 978-0-935702-11-8.

[133] M. Aspelmeyer, T. J. Kippenberg, and F. Marquard, "Cavity optomechanics", Reviews of Modern Physics **86**, 1391–1452 (2014).

[134] J. M. Aguirregabiria and L. Bel, "Delay-induced instability in a pendular fabry-perot cavity", Physical Review A **36**, 3768–3770 (1987).

[135] W. Z. Korth, H. Miao, T. Corbitt, G. D. Cole, Y. Chen, and R. X. Adhikari, "Suppression of quantum-radiation-pressure noise in an optical spring", Physical Review A **88**, 033805 (2013).

[136] V. B. Braginsky and S. P. Vyatchanin, "Low quantum noise tranquilizer for fabry-perot interferometer", Physics Letters A **293**, 228–234 (2002).

[137] H. Rehbein, H. Müller-Ebhardt, K. Somiya, S. L. Danilishin, R. Schnabel, K. Danzmann, and Y. Chen, "Double optical spring enhancement for gravitational-wave detectors", Physical Review D **78**, 062003 (2008).

[138] M. Hosseini, G. Guccione, H. J. Slatyer, B. C. Buchler, and P. K. Lam, "Multimode laser cooling and ultra-high sensitivity force sensing with nanowires", Nature Communications **5**, 4663 (2014).

[139] A. N. Cleland and M. L. Roukes, "A nanometre-scale mechanical electrometer", Nature **392**, 160–162 (1998).

[140] P.-F. Cohadon, O. Arcizet, T. Briant, A. Heidmann, and M. Pinard, "Optical monitoring and cooling of a micro-mechanical oscillator to the quantum limit", in Noise and information in nanoelectronics, sensors, and standards III, Vol. 5846, edited by J. A. Bergou, J. M. Smulko, M. I. Dykman, and L. Wang (2005), pp. 124–134, ISBN: 978-0-8194-5841-4.

[141] O. Arcizet, P.-F. Cohadon, T. Briant, M. Pinard, A. Heidmann, J.-M. Mackowski, C. Michel, L. Pinard, O. Fran çais, and L. Rousseau, "High-sensitivity optical monitoring of a micromechanical resonator with a quantum-limited optomechanical sensor", Physical Review Letters **97**, 133601 (2006).

[142] G. Binnig, C. F. Quate, and C. Gerber, "Atomic force microscope", Physical Review Letters **56**, 930–933 (1986).

[143] H. J. Mamin and D. Rugar, "Sub-attonewton force detection at millikelvin temperatures", Applied Physics Letters **79**, 3358–3360 (2001).

[144] B. Drake, C. B. Prater, A. L. Weisenhorn, S. A. Gould, T. R. Albrecht, C. F. Quate, D. S. Cannell, H. G. Hansma, and P. K. Hansma, "Imaging crystals, polymers, and processes in water with the atomic force microscope", Science **243**, 1586–1589 (1989).

[145] M. Dong, S. Husale, and O. Sahin, "Determination of protein structural flexibility by microsecond force spectroscopy", Nature Nanotechnology **4**, 514–517 (2009).

[146] J. A. Sidles, "Noninductive detection of single-proton magnetic resonance", Applied Physics Letters **58**, 2854–2856 (1991).

[147] J. A. Sidles, J. L. Garbini, K. J. Bruland, D. Rugar, O. Züger, S. Hoen, and C. S. Yannoni, "Magnetic resonance force microscopy", Reviews of Modern Physics **67**, 249–265 (1995).

[148] H. J. Mamin, R. Budakian, B. W. Chui, and D. Rugar, "Detection and manipulation of statistical polarization in small spin ensembles", Physical Review Letters **91**, 207604 (2003).

[149] D. Rugar, R. Budakian, H. J. Mamin, and B. W. Chui, "Single spin detection by magnetic resonance force microscopy", Nature **430**, 329–332 (2004).

[150] C. L. Degen, M. Poggio, H. J. Mamin, C. T. Rettner, and D. Rugar, "Nanoscale magnetic resonance imaging", Proceedings of the National Academy of Sciences **106**, 1313–1317 (2009).

[151] K. L. Ekinci, X. M. H. Huang, and M. L. Roukes, "Ultrasensitive nanoelectromechanical mass detection", Applied Physics Letters **84**, 4469–4471 (2004).

[152] T. D. Stowe, K. Yasumura, T. W. Kenny, D. Botkin, K. Wago, and D. Rugar, "Attonewton force detection using ultrathin silicon cantilevers", Applied Physics Letters **71**, 288–290 (1997).

[153] M. M. Yazdanpanah, M. Hosseini, S. Pabba, S. M. Berry, V. V. Dobrokhotov, A. Safir, R. S. Keynton, and R. W. Cohn, "Micro-wilhelmy and related liquid property measurements using constant-diameter nanoneedle-tipped atomic force microscope probes", Langmuir **24**, 13753–13764 (2008).

[154] P. Gao and Y. Cai, "Label-free detection of the aptamer binding on protein patterns using kelvin probe force microscopy (kpfm)", Analytical and Bioanalytical Chemistry **394**, 207–214 (2009).

[155] A. Hopkins, K. Jacobs, S. Habib, and K. Schwab, "Feedback cooling of a nanomechanical resonator", Physical Review B **68**, 235328 (2003).

[156] S. Mancini, D. Vitali, and P. Tombesi, "Optomechanical cooling of a macroscopic oscillator by homodyne feedback", Physical Review Letters **80**, 688–691 (1998).

[157] P. F. Cohadon, A. Heidmann, and M. Pinard, "Cooling of a mirror by radiation pressure", Physical Review Letters **83**, 3174–3177 (1999).

[158] I. Wilson-Rae, P. Zoller, and A. Imamoğlu, "Laser cooling of a nanomechanical resonator mode to its quantum ground state", Physical Review Letters **92**, 075507 (2004).

[159] C. H. Metzger and K. Karrai, "Cavity cooling of a microlever", Nature **432**, 1002–1005 (2004).

[160] D. Vitali, S. Mancini, and P. Tombesi, "Optomechanical scheme for the detection of weak impulsive forces", Physical Review A **64**, 051401 (2001).

[161] J. Gieseler, L. Novotny, and R. Quidant, "Thermal nonlinearities in a nanomechanical oscillator", Nature Physics **9**, 806–810 (2013).

[162] A. Vinante, M. Bonaldi, F. Marin, and J.-P. Zendri, "Dissipative feedback does not improve the optimal resolution of incoherent force detection", Nature Nanotechnology **8**, 470–470 (2013).

[163] E. Gavartin, P. Verlot, and T. J. Kippenberg, "Reply to 'dissipative feedback does not improve the optimal resolution of incoherent force detection'", Nature Nanotechnology **8**, 692–692 (2013).

[164] N. Wiener, *Extrapolation, interpolation, and smoothing of stationary time series* (MIT Press, Cambridge, 1964), ISBN: 978-0-262-73005-1.

[165] R. E. Kalman, "A new approach to linear filtering and prediction problems", Journal of Basic Engineering **82**, 35–45 (1960).

[166] E. Gavartin, P. Verlot, and T. J. Kippenberg, "Stabilization of a linear nanomechanical oscillator to its thermodynamic limit", Nature Communications **4**, 2860 (2013).

[167] NaugaNeedles LLC, *Nauganeedles*, (2015) `http://nauganeedles.com` (visited on 07/19/2017).

[168] M. M. Yazdanpanah, S. A. Harfenist, A. Safir, and R. W. Cohn, "Selective self-assembly at room temperature of individual freestanding ag2ga alloy nanoneedles", Journal of Applied Physics **98**, 073510 (2005).

[169] G. Guccione, M. Hosseini, A. Mirzaei, H. J. Slatyer, B. C. Buchler, and P. K. Lam, "Enhanced photothermal cooling of nanowires", Quantum Science and Technology **2**, 034005 (2017).

[170] T. Ikuno, S.-i. Honda, T. Yasuda, K. Oura, M. Katayama, J. G. Lee, and H. Mori, "Thermally driven nanomechanical deflection of hybrid nanowires", Applied Physics Letters **87**, 213104 (2005).

[171] E. Gil-Santos, D. Ramos, V. Pini, J. Llorens, M. Fernández-Regúlez, M. Calleja, J. Tamayo, and A. S. Paulo, "Optical back-action in silicon nanowire resonators: bolometric versus radiation pressure effects", New Journal of Physics **15**, 035001 (2013).

[172] S. Dhara, H. S. Solanki, A. P. R., V. Singh, S. Sengupta, B. A. Chalke, A. Dhar, M. Gokhale, A. Bhattacharya, and M. M. Deshmukh, "Tunable thermal conductivity in defect engineered nanowires at low temperatures", Physical Review B **84**, 121307 (2011).

[173] R. R. Anderson and J. A. Parrish, "Selective photothermolysis: precise microsurgery by selective absorption of pulsed radiation", Science **220**, 524–527 (1983).

[174] Y. Takata, H. Haneda, T. Mitsuhashi, and Y. Wada, "Evaluation of thermal diffusivity for thin gold films using femtosecond laser excitation technique", Applied Surface Science **189**, 227–233 (2002).

[175] D. Kleckner and D. Bouwmeester, "Sub-kelvin optical cooling of a micromechanical resonator", Nature **444**, 75–78 (2006).

[176] F. Lewis, L. Xie, and D. Popa, *Optimal and robust estimation: with an introduction to stochastic control theory*, Automation and control engineering (CRC Press, Boca Raton, 2008), ISBN: 978-0-8493-9008-1.

[177] G. Welch and G. Bishop, *An introduction to the Kalman filter*, tech. rep. TR 95-041, `https://www.cs.unc.edu/~welch/media/pdf/kalman_intro.pdf` (Department of Computer Science, University of North Carolina at Chapel Hill, Chapel Hill, 2006).

[178] S. Haykin, "Kalman filters", in *Kalman filtering and neural networks*, edited by S. Haykin (John Wiley & Sons, New York, 2002), pp. 1–21, ISBN: 978-0-471-22154-8.

[179] H. J. Slatyer, *Kalman filters for nanowires*, (2017) `https://github.com/charmasaur/kalman` (visited on 11/25/2017).

[180] A. N. Cleland and M. L. Roukes, "Noise processes in nanomechanical resonators", Journal of Applied Physics **92**, 2758–2769 (2002).

[181] K. L. Ekinci, Y. T. Yang, and M. L. Roukes, "Ultimate limits to inertial mass sensing based upon nanoelectromechanical systems", Journal of Applied Physics **95**, 2682–2689 (2004).

[182] M. I. Dykman, M. Khasin, J. Portman, and S. W. Shaw, "Spectrum of an oscillator with jumping frequency and the interference of partial susceptibilities", Physical Review Letters **105**, 230601 (2010).

[183] J. Atalaya, A. Isacsson, and M. I. Dykman, "Diffusion-induced dephasing in nanomechanical resonators", Physical Review B **83**, 045419 (2011).

[184] A. Casper, *Kalman filter*, (2012) `http://www.acasper.org/tag/kalman-filter/` (visited on 07/28/2017).

[185] K.-W. Chiang, T. T. Duong, J.-K. Liao, Y.-C. Lai, C.-C. Chang, J.-M. Cai, and S.-C. Huang, "On-line smoothing for an integrated navigation system with low-cost mems inertial sensors", Sensors **12**, 17372–17389 (2012).

[186] M. Kamil, T. Chobtrong, E. Günes, and M. Haid, "Low-cost object tracking with mems sensors, kalman filtering and simplified two-filter-smoothing", Applied Mathematics and Computation **235**, 323–331 (2014).

[187] T. A. Wheatley, M. Tsang, I. R. Petersen, and E. H. Huntington, "Improved mirror position estimation using resonant quantum smoothing", EPJ Quantum Technology **2**, 13 (2015).

[188] J. Eisert, M. Friesdorf, and C. Gogolin, "Quantum many-body systems out of equilibrium", Nature Physics **11**, 124–130 (2015).

[189] R. W. P. Drever, J. L. Hall, F. V. Kowalski, J. Hough, G. M. Ford, A. J. Munley, and H. Ward, "Laser phase and frequency stabilization using an optical resonator", Applied Physics B **31**, 97–105 (1983).

[190] D. J. Tannor and S. A. Rice, "Control of selectivity of chemical reaction via control of wave packet evolution", The Journal of Chemical Physics **83**, 5013–5018 (1985).

[191] D. J. Tannor, R. Kosloff, and S. A. Rice, "Coherent pulse sequence induced control of selectivity of reactions: exact quantum mechanical calculations", The Journal of Chemical Physics **85**, 5805–5820 (1986).

[192] P. Brumer and M. Shapiro, "Control of unimolecular reactions using coherent light", Chemical Physics Letters **126**, 541–546 (1986).

[193] S. Shi, A. Woody, and H. Rabitz, "Optimal control of selective vibrational excitation in harmonic linear chain molecules", The Journal of Chemical Physics **88**, 6870–6883 (1988).

[194] E. D. Potter, J. L. Herek, S. Pedersen, Q. Liu, and A. H. Zewail, "Femtosecond laser control of a chemical reaction", Nature **355**, 66–68 (1992).

[195] J. Herek, A. Materny, and A. Zewail, "Femtosecond control of an elementary unimolecular reaction from the transition-state region", Chemical Physics Letters **228**, 15–25 (1994).

[196] A. P. Peirce, M. A. Dahleh, and H. Rabitz, "Optimal control of quantum-mechanical systems: existence, numerical approximation, and applications", Physical Review A **37**, 4950–4964 (1988).

[197] R. Kosloff, S. Rice, P. Gaspard, S. Tersigni, and D. Tannor, "Wavepacket dancing: achieving chemical selectivity by shaping light pulses", Chemical Physics **139**, 201–220 (1989).

[198] W. Jakubetz, J. Manz, and H.-J. Schreier, "Theory of optimal laser pulses for selective transitions between molecular eigenstates", Chemical Physics Letters **165**, 100–106 (1990).

[199] R. S. Judson and H. Rabitz, "Teaching lasers to control molecules", Physical Review Letters **68**, 1500–1503 (1992).

[200] P. Gross, D. Neuhauser, and H. Rabitz, "Teaching lasers to control molecules in the presence of laboratory field uncertainty and measurement imprecision", The Journal of Chemical Physics **98**, 4557–4566 (1993).

[201] S. Kirkpatrick, C. D. Gelatt, and M. P. Vecchi, "Optimization by simulated annealing", Science **220**, 671–680 (1983).

[202] B. Amstrup, J. D. Doll, R. A. Sauerbrey, G. Szabó, and A. Lőrincz, "Optimal control of quantum systems by chirped pulses", Physical Review A **48**, 3830–3836 (1993).

[203] D. Meshulach, D. Yelin, and Y. Silberberg, "Adaptive ultrashort pulse compression and shaping", Optics Communications **138**, 345–348 (1997).

[204] B. Amstrup, G. J. Tóth, G. Szabó, H. Rabitz, and A. Lőrincz, "Genetic algorithm with migration on topology conserving maps for optimal control of quantum systems", The Journal of Physical Chemistry **99**, 5206–5213 (1995).

[205] J. A. Nelder and R. Mead, "A simplex method for function minimization", The Computer Journal **7**, 308 (1965).

[206] R. R. Barton and J. John S. Ivey, "Nelder-mead simplex modifications for simulation optimization", Management Science **42**, 954–973 (1996).

[207] G. Turinici, C. Le Bris, and H. Rabitz, "Efficient algorithms for the laboratory discovery of optimal quantum controls", Physical Review E **70**, 016704 (2004).

[208] G. J. Tóth, A. Lőrincz, and H. Rabitz, "The effect of control field and measurement imprecision on laboratory feedback control of quantum systems", The Journal of Chemical Physics **101**, 3715–3722 (1994).

[209] H. Rabitz, "Optimal control of quantum systems: origins of inherent robustness to control field fluctuations", Physical Review A **66**, 063405 (2002).

[210] C. J. Bardeen, V. V. Yakovlev, K. R. Wilson, S. D. Carpenter, P. M. Weber, and W. S. Warren, "Feedback quantum control of molecular electronic population transfer", Chemical Physics Letters **280**, 151–158 (1997).

[211] T. Baumert, T. Brixner, V. Seyfried, M. Strehle, and G. Gerber, "Femtosecond pulse shaping by an evolutionary algorithm with feedback", Applied Physics B **65**, 779–782 (1997).

[212] A. Assion, T. Baumert, M. Bergt, T. Brixner, B. Kiefer, V. Seyfried, M. Strehle, and G. Gerber, "Control of chemical reactions by feedback-optimized phase-shaped femtosecond laser pulses", Science **282**, 919–922 (1998).

[213] J. Kunde, B. Baumann, S. Arlt, F. Morier-Genoud, U. Siegner, and U. Keller, "Adaptive feedback control of ultrafast semiconductor nonlinearities", Applied Physics Letters **77**, 924–926 (2000).

[214] D. Zeidler, S. Frey, K.-L. Kompa, and M. Motzkus, "Evolutionary algorithms and their application to optimal control studies", Physical Review A **64**, 023420 (2001).

[215] B. J. Pearson, J. L. White, T. C. Weinacht, and P. H. Bucksbaum, "Coherent control using adaptive learning algorithms", Physical Review A **63**, 063412 (2001).

[216] M. Sugawara, M. Yamanouchi, and S. Yabushita, "Laser field designing by evolutionary algorithm for coherent control of molecular dynamics", Chemical Physics Letters **396**, 136–141 (2004).

[217] P. Nuernberger, G. Vogt, T. Brixner, and G. Gerber, "Femtosecond quantum control of molecular dynamics in the condensed phase", Physical Chemistry Chemical Physics **9**, 2470–2497 (2007).

[218] C. Leonard, F. Le Quere, P. Rosmus, C. Puzzarini, and M. P. de Lara Castells, "Selective vibrational excitations in the OX (X=F, Cl, Br, I) molecules", Physical Chemistry Chemical Physics **2**, 1117–1122 (2000).

[219] C. Leonard, G. Chambaud, P. Rosmus, S. Carter, and N. C. Handy, "The selective population of the vibrational levels of thioformaldehyde", Physical Chemistry Chemical Physics **3**, 508–513 (2001).

[220] J. Roslund and H. Rabitz, "Gradient algorithm applied to laboratory quantum control", Physical Review A **79**, 053417 (2009).

[221] V. J. Torczon, "Multidirectional search: a direct search algorithm for parallel machines", `http://hdl.handle.net/1911/16304`, PhD thesis (Rice University, Houston, 1989).

[222] K. I. M. McKinnon, "Convergence of the nelder–mead simplex method to a nonstationary point", SIAM Journal on Optimization **9**, 148–158 (1998).

[223] R. M. Lewis, V. Torczon, and M. W. Trosset, "Direct search methods: then and now", Journal of Computational and Applied Mathematics **124**, 191–207 (2000).

[224] R. J. Koshel, "Enhancement of the downhill simplex method of optimization", in International optical design conference, edited by P. K. Manhart and J. M. Sasian (2002).

[225] Z. Michalewicz and C. Z. Janikow, "Genetic algorithms for numerical optimization", Statistics and Computing **1**, 75–91 (1991).

[226] C. Jennison and N. Sheehan, "Theoretical and empirical properties of the genetic algorithm as a numerical optimizer", Journal of Computational and Graphical Statistics **4**, 296–318 (1995).

[227] J. Stander and B. W. Silverman, "Temperature schedules for simulated annealing", Statistics and Computing **4**, 21–32 (1994).

[228] L. Franconi and C. Jennison, "Comparison of a genetic algorithm and simulated annealing in an application to statistical image reconstruction", Statistics and Computing **7**, 193–207 (1997).

[229] M. Bhattacharya, "Evolutionary approaches to expensive optimisation", International Journal of Advanced Research in Artificial Intelligence **2**, 53–59 (2013).

[230] M. Q. Phan and J. A. Frueh, "Learning control for trajectory tracking using basis functions", in Proceedings of 35th IEEE conference on decision and control, Vol. 3 (1996), pp. 2490–2492, ISBN: 978-0-7803-3590-5.

[231] M. Q. Phan and H. Rabitz, "Learning control of quantum-mechanical systems by laboratory identification of effective input-output maps", Chemical Physics **217**, 389–400 (1997).

[232] M. Q. Phan and H. Rabitz, "A self-guided algorithm for learning control of quantum-mechanical systems", The Journal of Chemical Physics **110**, 34–41 (1999).

[233] J. M. Geremia, E. Weiss, and H. Rabitz, "Achieving the laboratory control of quantum dynamics phenomena using nonlinear functional maps", Chemical Physics **267**, 209–222 (2001).

[234] J. S. Biteen, J. Geremia, and H. Rabitz, "Closed-loop quantum control utilizing time domain maps", Chemical Physics **290**, 35–45 (2003).

[235] P. B. Wigley, P. J. Everitt, A. van den Hengel, J. W. Bastian, M. A. Sooriyabandara, G. D. McDonald, K. S. Hardman, C. D. Quinlivan, P. Manju, C. C. N. Kuhn, I. R. Petersen, A. N. Luiten, J. J. Hope, N. P. Robins, and M. R. Hush, "Fast machine-learning online optimization of ultra-cold-atom experiments", Scientific Reports **6**, 25890 (2016).

[236] D. Barber, *Bayesian reasoning and machine learning* (Cambridge University Press, Cambridge, 2012), ISBN: 978-0-521-51814-7.

[237] I. Goodfellow, Y. Bengio, and A. Courville, *Deep learning*, `http://www.deeplearningbook.org` (MIT Press, Cambridge, 2016).

[238] C. M. Bishop, *Pattern recognition and machine learning*, Information Science and Statistics (Springer, New York, 2006), ISBN: 978-0-387-31073-2.

[239] J. Šíma, "Training a single sigmoidal neuron is hard", Neural Computation **14**, 2709–2728 (2002).

[240] Y. LeCun, L. Bottou, G. B. Orr, and K.-R. Müller, "Efficient backprop", in *Neural networks: tricks of the trade*, edited by G. B. Orr and K.-R. Müller (Springer, Berlin, 1998), pp. 9–50, ISBN: 978-3-540-49430-0.

[241] D. E. Rumelhart, G. E. Hinton, and R. J. Williams, "Learning representations by back-propagating errors", Nature **323**, 533–536 (1986).

[242] J. Duchi, E. Hazan, and Y. Singer, "Adaptive subgradient methods for online learning and stochastic optimization", Journal of Machine Learning Research **12**, 2121–2159 (2011).

[243] D. P. Kingma and J. Ba, "Adam: a method for stochastic optimization", in International conference on learning representations 2015 (2015).

[244] Y. Yao, L. Rosasco, and A. Caponnetto, "On early stopping in gradient descent learning", Constructive Approximation **26**, 289–315 (2007).

[245] N. Srivastava, G. Hinton, A. Krizhevsky, I. Sutskever, and R. Salakhutdinov, "Dropout: a simple way to prevent neural networks from overfitting", Journal of Machine Learning Research **15**, 1929–1958 (2014).

[246] S. Ioffe and C. Szegedy, "Batch normalization: accelerating deep network training by reducing internal covariate shift", Computing Research Repository, abs/1502.03167 (2015).

[247] K. Hornik, M. Stinchcombe, and H. White, "Multilayer feedforward networks are universal approximators", Neural Networks **2**, 359–366 (1989).

[248] G. Cybenko, "Approximation by superpositions of a sigmoidal function", Mathematics of Control, Signals and Systems **2**, 303–314 (1989).

[249] K. Hornik, "Approximation capabilities of multilayer feedforward networks", Neural Networks **4**, 251–257 (1991).

[250] S. Hochreiter, Y. Bengio, P. Frasconi, and J. Schmidhuber, "Gradient flow in recurrent nets: the difficulty of learning long-term dependencies", in *A field guide to dynamical recurrent neural networks*, edited by S. C. Kremer and J. F. Kolen (IEEE Press, New York, 2001), ISBN: 978-0-7803-5369-5.

[251] X. Glorot, A. Bordes, and Y. Bengio, "Deep sparse rectifier neural networks", in Proceedings of the 14th international conference on artificial intelligence and statistics, Vol. 15, edited by G. Gordon, D. Dunson, and M. Dudík (2011), pp. 315–323.

[252] Y. LeCun, Y. Bengio, and G. Hinton, "Deep learning", Nature **521**, 436–444 (2015).

[253] D. Hendrycks and K. Gimpel, "Bridging nonlinearities and stochastic regularizers with gaussian error linear units", Computing Research Repository, abs/1606.08415 (2016).

[254] H. Larochelle, Y. Bengio, J. Louradour, and P. Lamblin, "Exploring strategies for training deep neural networks", Journal of Machine Learning Research **10**, 1–40 (2009).

[255] R. Pascanu, G. Montúfar, and Y. Bengio, "On the number of response regions of deep feed forward networks with piece-wise linear activations", in International conference on learning representations 2014 (2014).

[256] A. C.-C. Yao, "Separating the polynomial-time hierarchy by oracles", in Proceedings of the 26th annual symposium on foundations of computer science (1985), pp. 1–10, ISBN: 978-0-8186-0644-1.

[257] J. Håstad and M. Goldmann, "On the power of small-depth threshold circuits", Computational Complexity **1**, 113–129 (1991).

[258] A. Hajnal, W. Maass, P. Pudlák, M. Szegedy, and G. Turán, "Threshold circuits of bounded depth", Journal of Computer and System Sciences **46**, 129–154 (1993).

[259] O. Delalleau and Y. Bengio, "Shallow vs. deep sum-product networks", in Advances in neural information processing systems 24, edited by J. Shawe-Taylor, R. S. Zemel, P. L. Bartlett, F. Pereira, and K. Q. Weinberger (2011), pp. 666–674, ISBN: 978-1-61839-599-3.

[260] G. Hinton, L. Deng, D. Yu, G. Dahl, A.-r. Mohamed, N. Jaitly, A. Senior, V. Vanhoucke, P. Nguyen, T. Sainath, and B. Kingsbury, "Deep neural networks for acoustic modeling in speech recognition", IEEE Signal Processing Magazine **29**, 82–97 (2012).

[261] H. Larochelle, D. Erhan, A. Courville, J. Bergstra, and Y. Bengio, "An empirical evaluation of deep architectures on problems with many factors of variation", in Proceedings of the 24th international conference on machine learning, edited by Z. Ghahramani (2007), pp. 473–480, ISBN: 978-1-59593-793-3.

[262] M. Ranzato, C. Poultney, S. Chopra, and Y. L. Cun, "Efficient learning of sparse representations with an energy-based model", in Advances in neural information processing systems 19, edited by P. B. Schölkopf, J. C. Platt, and T. Hoffman (2007), pp. 1137–1144, ISBN: 978-0-262-25373-4.

[263] G. Montúfar, R. Pascanu, K. Cho, and Y. Bengio, "On the number of linear regions of deep neural networks", in Proceedings of the 27th international conference on neural information processing systems, edited by Z. Ghahramani, M. Welling, C. Cortes, N. Lawrence, and K. Weinberger (2014), pp. 2924–2932.

[264] Y. Bengio and Y. LeCun, "Scaling learning algorithms towards AI", in *Large-scale kernel machines*, edited by L. Bottou, O. Chapelle, D. DeCoste, and J. Weston (MIT Press, Cambridge, 2007), ISBN: 978-0-262-25091-7.

[265] Y. Bengio, "Learning deep architectures for AI", Foundations and Trends in Machine Learning **2**, 1–127 (2009).

[266] M. R. Hush and H. J. Slatyer, *M-LOOP*, (2017) `https://github.com/charmasaur/M-LOOP` (visited on 11/25/2017).

[267] R. Storn and K. Price, "Differential evolution – a simple and efficient heuristic for global optimization over continuous spaces", Journal of Global Optimization **11**, 341–359 (1997).

[268] R. S. Sutton and A. G. Barto, *Reinforcement learning: an introduction*, 1st (MIT Press, Cambridge, 1998), ISBN: 978-0-262-19398-6.

[269] P. Auer, N. Cesa-Bianchi, and P. Fischer, "Finite-time analysis of the multiarmed bandit problem", Machine Learning **47**, 235–256 (2002).

[270] M. Tokic and G. Palm, "Value-difference based exploration: adaptive control between epsilon-greedy and softmax", in Proceedings of the 34th annual German conference on advances in artificial intelligence, edited by J. Bach and S. Edelkamp (2011), pp. 335–346, ISBN: 978-3-642-24454-4.

[271] W. R. Thompson, "On the likelihood that one unknown probability exceeds another in view of the evidence of two samples", Biometrika **25**, 285–294 (1933).

[272] G. E. Hinton, N. Srivastava, A. Krizhevsky, I. Sutskever, and R. Salakhutdinov, "Improving neural networks by preventing co-adaptation of feature detectors", Computing Research Repository, abs/1207.0580 (2012).

[273] Y. Gal and Z. Ghahramani, "Dropout as a Bayesian approximation: representing model uncertainty in deep learning", arXiv:1506.02142 (2015).

[274] C. Blundell, J. Cornebise, K. Kavukcuoglu, and D. Wierstra, "Weight uncertainty in neural networks", in Proceedings of the 32nd international conference on machine learning, edited by F. Bach and D. Blei (2015), pp. 1613–1622, ISBN: 978-1-5108-1058-7.

[275] L. Breiman, "Bagging predictors", Machine Learning **24**, 123–140 (1996).

[276] E. Jones, T. Oliphant, P. Peterson, et al., *SciPy: open source scientific tools for Python*, (2001) `http://www.scipy.org/` (visited on 11/25/2017).

[277] R. H. Byrd, P. Lu, J. Nocedal, and C. Zhu, "A limited memory algorithm for bound constrained optimization", SIAM Journal on Scientific Computing **16**, 1190–1208 (1995).

[278] F. Bussières, N. Sangouard, M. Afzelius, H. de Riedmatten, C. Simon, and W. Tittel, "Prospective applications of optical quantum memories", Journal of Modern Optics **60**, 1519–1537 (2013).

[279] D. Gottesman and I. L. Chuang, "Demonstrating the viability of universal quantum computation using teleportation and single-qubit operations", Nature **402**, 390–393 (1999).

[280] E. Knill, R. Laflamme, and G. J. Milburn, "A scheme for efficient quantum computation with linear optics", Nature **409**, 46–52 (2001).

[281] P. Kok, W. J. Munro, K. Nemoto, T. C. Ralph, J. P. Dowling, and G. J. Milburn, "Linear optical quantum computing with photonic qubits", Reviews of Modern Physics **79**, 135–174 (2007).

[282] A. K. Ekert, "Quantum cryptography based on Bell's theorem", Physical Review Letters **67**, 661–663 (1991).

[283] K. Hammerer, A. S. Sørensen, and E. S. Polzik, "Quantum interface between light and atomic ensembles", Reviews of Modern Physics **82**, 1041–1093 (2010).

[284] K. Heshami, D. G. England, P. C. Humphreys, P. J. Bustard, V. M. Acosta, J. Nunn, and B. J. Sussman, "Quantum memories: emerging applications and recent advances", Journal of Modern Optics **63**, 2005–2028 (2016).

[285] G. Hétet, J. J. Longdell, A. L. Alexander, P. K. Lam, and M. J. Sellars, "Electro-optic quantum memory for light using two-level atoms", Physical Review Letters **100**, 023601 (2008).

[286] G. Hétet, M. Hosseini, B. M. Sparkes, D. Oblak, P. K. Lam, and B. C. Buchler, "Photon echoes generated by reversing magnetic field gradients in a rubidium vapor", Optics Letters **33**, 2323–2325 (2008).

[287] M. Hosseini, B. M. Sparkes, G. Campbell, P. K. Lam, and B. C. Buchler, "High efficiency coherent optical memory with warm rubidium vapour", Nature Communications **2**, 174 (2011).

[288] M. P. Hedges, J. J. Longdell, Y. Li, and M. J. Sellars, "Efficient quantum memory for light", Nature **465**, 1052–1056 (2010).

[289] B. M. Sparkes, J. Bernu, M. Hosseini, J. Geng, Q. Glorieux, P. A. Altin, P. K. Lam, N. P. Robins, and B. C. Buchler, "Gradient echo memory in an ultra-high optical depth cold atomic ensemble", New Journal of Physics **15**, 085027 (2013).

[290] N. Sangouard, C. Simon, M. Afzelius, and N. Gisin, "Analysis of a quantum memory for photons based on controlled reversible inhomogeneous broadening", Physical Review A **75**, 032327 (2007).

[291] J. J. Longdell, G. Hétet, P. K. Lam, and M. J. Sellars, "Analytic treatment of controlled reversible inhomogeneous broadening quantum memories for light using two-level atoms", Physical Review A **78**, 032337 (2008).

[292] B. M. Sparkes, J. Bernu, M. Hosseini, J. Geng, Q. Glorieux, P. A. Altin, P. K. Lam, N. P. Robins, and B. C. Buchler, "An ultra-high optical depth cold atomic ensemble for quantum memories", Journal of Physics: Conference Series **467**, 012009 (2013).

[293] E. L. Raab, M. Prentiss, A. Cable, S. Chu, and D. E. Pritchard, "Trapping of neutral sodium atoms with radiation pressure", Physical Review Letters **59**, 2631–2634 (1987).

[294] S. Chu, "Nobel lecture: the manipulation of neutral particles", Reviews of Modern Physics **70**, 685–706 (1998).

[295] M. H. Anderson, J. R. Ensher, M. R. Matthews, C. E. Wieman, and E. A. Cornell, "Observation of bose-einstein condensation in a dilute atomic vapor", Science **269**, 198–201 (1995).

[296] P. A. Altin, N. P. Robins, D. Döring, J. E. Debs, R. Poldy, C. Figl, and J. D. Close, "R85b tunable-interaction bose–einstein condensate machine", Review of Scientific Instruments **81**, 063103 (2010).

[297] H. Perrin, "Ultra cold atoms and bose-einstein condensation for quantum metrology", The European Physical Journal Special Topics **172**, 37–55 (2009).

[298] K. D. Nelson, X. Li, and D. S. Weiss, "Imaging single atoms in a three-dimensional array", Nature Physics **3**, 556 (2007).

[299] M. J. Piotrowicz, M. Lichtman, K. Maller, G. Li, S. Zhang, L. Isenhower, and M. Saffman, "Two-dimensional lattice of blue-detuned atom traps using a projected gaussian beam array", Physical Review A **88**, 013420 (2013).

[300] T. Xia, M. Lichtman, K. Maller, A. W. Carr, M. J. Piotrowicz, L. Isenhower, and M. Saffman, "Randomized benchmarking of single-qubit gates in a 2d array of neutral-atom qubits", Physical Review Letters **114**, 100503 (2015).

[301] C. Y. Chen, Y. M. Li, K. Bailey, T. P. O'Connor, L. Young, and Z.-T. Lu, "Ultrasensitive isotope trace analyses with a magneto-optical trap", Science **286**, 1139–1141 (1999).

[302] H. Wang, P. L. Gould, and W. C. Stwalley, "Photoassociative spectroscopy of ultracold ^{39}K atoms in a high-density vapor-cell magneto-optical trap", Physical Review A **53**, R1216–R1219 (1996).

[303] W. Li, I. Mourachko, M. W. Noel, and T. F. Gallagher, "Millimeter-wave spectroscopy of cold rb rydberg atoms in a magneto-optical trap: quantum defects of the ns, np, and nd series", Physical Review A **67**, 052502 (2003).

[304] F. Shimizu, K. Shimizu, and H. Takuma, "Stark phase shift and deflection in the ultracold atomic interferometer", Japanese Journal of Applied Physics **31**, L436 (1992).

[305] B. Canuel, F. Leduc, D. Holleville, A. Gauguet, J. Fils, A. Virdis, A. Clairon, N. Dimarcq, C. J. Bordé, A. Landragin, and P. Bouyer, "Six-axis inertial sensor using cold-atom interferometry", Physical Review Letters **97**, 010402 (2006).

[306] A. D. Cronin, J. Schmiedmayer, and D. E. Pritchard, "Optics and interferometry with atoms and molecules", Reviews of Modern Physics **81**, 1051–1129 (2009).

[307] S. Chu, L. Hollberg, J. E. Bjorkholm, A. Cable, and A. Ashkin, "Three-dimensional viscous confinement and cooling of atoms by resonance radiation pressure", Physical Review Letters **55**, 48–51 (1985).

[308] P. D. Lett, R. N. Watts, C. I. Westbrook, W. D. Phillips, P. L. Gould, and H. J. Metcalf, "Observation of atoms laser cooled below the doppler limit", Physical Review Letters **61**, 169–172 (1988).

[309] M. Drewsen, P. Laurent, A. Nadir, G. Santarelli, A. Clairon, Y. Castin, D. Grison, and C. Salomon, "Investigation of sub-doppler cooling effects in a cesium magneto-optical trap", Applied Physics B **59**, 283–298 (1994).

[310] J. Dalibard and C. Cohen-Tannoudji, "Laser cooling below the doppler limit by polarization gradients: simple theoretical models", Journal of the Optical Society of America B **6**, 2023–2045 (1989).

[311] S. Chu, M. G. Prentiss, A. E. Cable, and J. E. Bjorkholm, "Laser cooling and trapping of atoms", in Laser spectroscopy VIII: proceedings of the eighth international conference, edited by W. Persson and S. Svanberg (1987), pp. 58–63, ISBN: 978-3-540-47973-4.

[312] Y. Shevy, D. S. Weiss, P. J. Ungar, and S. Chu, "Bimodal speed distributions in laser-cooled atoms", Physical Review Letters **62**, 1118–1121 (1989).

[313] V. S. Bagnato, N. P. Bigelow, G. I. Surdutovich, and S. C. Zílio, "Dynamical stabilization: a new model for supermolasses", Optics Letters **19**, 1568–1570 (1994).

[314] T. Walker, D. Sesko, and C. Wieman, "Collective behavior of optically trapped neutral atoms", Physical Review Letters **64**, 408–411 (1990).

[315] K. E. Gibble, S. Kasapi, and S. Chu, "Improved magneto-optic trapping in a vapor cell", Optics Letters **17**, 526–528 (1992).

[316] C. G. Townsend, N. H. Edwards, K. P. Zetie, C. J. Cooper, J. Rink, and C. J. Foot, "High-density trapping of cesium atoms in a dark magneto-optical trap", Physical Review A **53**, 1702–1714 (1996).

[317] W. Ketterle, K. B. Davis, M. A. Joffe, A. Martin, and D. E. Pritchard, "High densities of cold atoms in a dark spontaneous-force optical trap", Physical Review Letters **70**, 2253–2256 (1993).

[318] H. J. Lee, C. S. Adams, M. Kasevich, and S. Chu, "Raman cooling of atoms in an optical dipole trap", Physical Review Letters **76**, 2658–2661 (1996).

[319] W. Petrich, M. H. Anderson, J. R. Ensher, and E. A. Cornell, "Behavior of atoms in a compressed magneto-optical trap", Journal of the Optical Society of America B **11**, 1332–1335 (1994).

[320] S. L. Winoto, M. T. DePue, N. E. Bramall, and D. S. Weiss, "Laser cooling at high density in deep far-detuned optical lattices", Physical Review A **59**, R19–R22 (1999).

[321] M. T. DePue, S. L. Winoto, D. Han, and D. S. Weiss, "Transient compression of a mot and high intensity fluorescent imaging of optically thick clouds of atoms", Optics Communications **180**, 73–79 (2000).

[322] M. Gajda and J. Mostowski, "Three-dimensional theory of the magneto-optical trap: doppler cooling in the low-intensity limit", Physical Review A **49**, 4864–4875 (1994).

[323] S. Chang, T. Y. Kwon, H. S. Lee, and V. G. Minogin, "Laser sub-doppler cooling of atoms in an arbitrarily directed magnetic field", Physical Review A **66**, 043404 (2002).

[324] S.-K. Choi, S. E. Park, J. Chen, and V. G. Minogin, "Three-dimensional analysis of the magneto-optical trap for (1+3)-level atoms", Physical Review A **77**, 015405 (2008).

[325] O. N. Prudnikov, A. V. Taichenachev, A. M. Tumaikin, and V. I. Yudin, "Magneto-optical force in a resonant field of elliptically polarized light waves", Physical Review A **77**, 033420 (2008).

[326] S. Zhang, J. F. Chen, C. Liu, S. Zhou, M. M. T. Loy, G. K. L. Wong, and S. Du, "A dark-line two-dimensional magneto-optical trap of 85rb atoms with high optical depth", Review of Scientific Instruments **83**, 073102 (2012).

[327] A. M. Steane, M. Chowdhury, and C. J. Foot, "Radiation force in the magneto-optical trap", Journal of the Optical Society of America B **9**, 2142–2158 (1992).

[328] L. Fu, "Rule generation from neural networks", IEEE Transactions on Systems, Man, and Cybernetics **24**, 1114–1124 (1994).

[329] D. Castelvecchi, "Can we open the black box of AI?", Nature **538**, 20–23 (2016).

[330] R. Shwartz-Ziv and N. Tishby, "Opening the black box of deep neural networks via information", Computing Research Repository, abs/1703.00810 (2017).

[331] Tensorflow, *Tf.gradients*, (2017) `https://www.tensorflow.org/api_docs/python/tf/gradients` (visited on 11/25/2017).

[332] Theano, *Symbolic differentiation*, (2017) `http://deeplearning.net/software/theano/library/gradient.html` (visited on 11/25/2017).

[333] V. Mnih and G. E. Hinton, "Learning to label aerial images from noisy data", in Proceedings of the 29th international conference on machine learning, edited by J. Langford and J. Pineau (2012), pp. 567–574.

[334] S. E. Reed, H. Lee, D. Anguelov, C. Szegedy, D. Erhan, and A. Rabinovich, "Training deep neural networks on noisy labels with bootstrapping", Computing Research Repository, abs/1412.6596 (2014).

[335] X. Yao, "Evolving artificial neural networks", Proceedings of the IEEE **87**, 1423–1447 (1999).

[336] K. O. Stanley and R. Miikkulainen, "Evolving neural networks through augmenting topologies", Evolutionary Computation **10**, 99–127 (2002).

[337] S. Risi and J. Togelius, "Neuroevolution in games: state of the art and open challenges", IEEE Transactions on Computational Intelligence and AI in Games **9**, 25–41 (2017).